Faculty of Science

Department of Applied Physics

The Structural Nature of Aluminosilicate Inorganic Polymers: A Macro to Nanoscale Study

Matthew Ryan Rowles

This thesis is presented for the Degree of
Doctor of Philosophy
of
Curtin University of Technology

October 2004

This thesis contains no material which has been accepted for the award of any other degree or diploma in any university. To the best of my knowledge and belief this thesis contains no material previously published by any other person except where due acknowledgment has been made.

Signed: _____

Date: _____

ACKNOWLEDGEMENTS

A PhD research project, indeed any research project, cannot be undertaken without input from a great many people. This project was no different. In presenting this thesis as my “original contribution to knowledge”, I wish to acknowledge the contribution of some of the many people who helped make this project possible.

I would like to thank my Principal Supervisor, Emeritus Professor Brian O’Connor for his support and supervision over the past few years. He has given me enough guidance with my project to keep me going forward, with enough leeway to let me make my own mistakes, most of which turned out alright in the end. Thanks are also due to my Associate Supervisors for their help in this project; Professor Arie van Riessen, for his help and guidance in some of my experimental work, and for asking some of the harder questions, Associate Professor Craig Buckley for his support for my small angle scattering experiments, Dr Shane Kennedy for his advice on neutron scattering, and to Professors Paul McCormick and Gordon Parkinson for their help in the initial stages of my project.

Further acknowledgement is due to my colleagues Subaer, Dr Nigel Kirby, Karsten Winter and most probably quite a few others, all of whom persevered through my talking at them about various aspects of my work, and helped with providing answers of some description.

I was given the ability to work on this project through an Australian Postgraduate Award, and an Australian Institute of Nuclear Science and Engineering (AINSE) Postgraduate Research Award, which provided a stipend, travel and research support at the Australian Nuclear Science and Technology Organisation (ANSTO). I would like to thank Mr John Hanna, of ANSTO, for his efforts in collecting my NMR data.

I was able to travel to the Photon Factory in Tsukuba, Japan and to the Advanced Photon Source in Chicago, USA through grants from the Australian Synchrotron Research Program. I would like to thank Drs James

Hester and Garry Foran for their assistance in the data collection at the Photon Factory. Dr Sarvjit Shastri is to be thanked for his abundant efforts in setting up, and maintaining the data collection at the Advanced Photon Source.

My deepest thanks and gratitude go my parents for helping and supporting me through my university life; for doing all those things that parents are wont to do. I would also like to thank my brother and sister for not letting me get away with everything. Now I have to go out into the real world.

ABSTRACT

Aluminosilicate inorganic polymers (AIPs) are network heteropolymers consisting of SiO_4 and AlO_4 tetrahedra linked by a shared oxygen. The use of these materials as a cementing agent, toxic waste storage and fibre reinforced material, amongst a multitude of prospective applications, has grown in recent years.

The utilisation of AIPs is hampered by a lack of knowledge about their formation and structure. In order to allow the materials to achieve their full potential, the way in which the material behaves and forms under different conditions must be elucidated.

The basic questions that this study aimed to answer were:

1) How does the structure of these AIPs change with composition? and
2) Can this change in structure explain the material properties of the AIP?

The AIPs investigated in the study covered the molar composition ranges Si:Al ratio = 1 – 3 and Na:Al ratio = 0.5 – 2. They were made by the sodium hydroxide activation of metakaolinite, derived from the dehydroxylation of kaolinite. The Si content of the AIP was altered by the addition of amorphous silica fume via the activation solution.

The study considered the structural nature of the AIPs at the macro, micro and nanoscales, and found that the structure changed at all scales and with all compositions.

The nature of the AIP structure was studied at the macroscale utilising compressive strength testing. The results from this work showed that the compressive strength of the AIPs varied systematically with the chemical composition. The strengths recorded ranged from 0.4 ± 0.2 MPa for a sample with Si:Al:Na molar ratios = 1.08:1:0.5, to 64 ± 3 MPa for a sample with

Si:Al:Na molar ratios = 2.5:1:1.3. The higher strengths measured exceed those exhibited by Portland cement pastes.

The microstructure of the AIPs was investigated by scanning electron microscopy and energy dispersive spectroscopy. Microscopy showed that the microstructure variations correlated with the compressive strength. In general, AIPs with low compressive strengths exhibited an inhomogeneous two-phase microstructure; grain and matrix. The grain phase consisted of undissolved metakaolinite, whilst the matrix was the fully formed inorganic polymer. AIPs with high compressive strengths exhibited a microstructure that was more homogeneous than the samples with low compressive strength. The compressive strength of the AIPs depended on both the chemical composition and the level of residual MK present in the microstructure. EDS microanalysis showed that the composition of the two phases was significantly different, and that the differences depended on the overall composition of the AIP. EDS results also demonstrated that the impurity elements present in the metakaolinite were affected by the polymerisation process. Soluble elements such as Ca and Mg were found primarily in the matrix, indicating that they had leached out of the metakaolinite grains, whereas insoluble elements such as Fe and Ti were found primarily in the grains.

The nanoscale structure of the AIPs was examined by solid-state nuclear magnetic resonance (NMR) and x-ray scattering (XRS). The NMR measurements revealed that the average coordination of Si varied according to the composition of the AIP, whereas the coordination of Al was constant. Na is present in the network in both hydrated and non-hydrated forms. It is postulated that the variation in the Si coordination can be explained by the formation of Si-O-Na bonds with Na forming an ionic bond with O in the polymer network. Radial distribution function (RDF) analysis of the XRS patterns revealed little difference in the structure of the different AIPs beyond ~2.5 Å. Unfortunately, the data were of insufficient resolution to allow for a full evaluation of the differences in the Si-O and Al-O bonds between different AIPs. However, the trends present in the shape and position of the RDF peak

corresponding to the Si-O and Al-O bonds do follow the composition of the AIP.

It has been shown that a variety of experimental techniques can be used in concert to obtain information on the structural nature of AIPs. To this end, it has been found that the compressive strength of AIPs can be optimised, and that the microstructure of the AIPs changes systematically with variations in the compressive strength. An improved model for the structure of AIPs has also been proposed.

TABLE OF CONTENTS

LIST OF FIGURES

LIST OF TABLES

LIST OF ABBREVIATIONS

AIP	Aluminosilicate inorganic polymer
ANBF	Australian National Beamline Facility
APS	Advanced Photon Source
AS	Australian Standard
ASTM	American Society for Testing and Materials
CP	Cross polarisation
CRAMPS	Combined Rotation and Multiple-Pulse Spectroscopy
CSH	Calcium silicate hydrate
EBSD	Electron back-scatter diffraction
ED	Electron diffraction
EDS	Energy dispersive spectroscopy
EELS	Electron energy-loss spectroscopy
EXAFS	Extended x-ray absorption fine structure
FA	Fly ash
FID	Free induction decay
FTIR	Fourier transform infra-red
IP	Inorganic polymer
IPD	Irreversible plastic deformation
IR	Infra-red
KEK	High Energy Accelerator Research Organisation
MAS	Magic-angle spinning
MCA	Multi-channel analyser
MK	Metakaolinite
MQ	Melt-quench
NBO	Non-bonding oxygen
ND	Neutron diffraction
NMR	Nuclear magnetic resonance
OPC	Ordinary Portland cement
PDF	Pair distribution function
PF	Photon Factory
PRDF	Partial radial distribution function
RDF	Radial distribution function

RE	Rare earth
rf	Radio frequency
RMC	Reverse monte-carlo
RRDF	Reduced radial distribution function
SEM	Scanning electron microscope
SF	Silica fume
SRD	Synchrotron radiation diffraction
SS	Spinning sideband
SSNMR	Solid-state nuclear magnetic resonance
TEM	Transmission electron microscope
TEOS	Tetraethoxysilane
TMS	Tetramethylsilane
WIP	Warm isostatic press
XANES	X-ray absorption near edge spectroscopy
XAS	X-ray absorption spectroscopy
XPS	X-ray photoelectron spectroscopy
XRD	X-ray diffraction
XRF	X-ray fluorescence
XRS	X-ray scattering

1.0 INTRODUCTION

1.1 Background

The most important prerequisite for an element to be able to form a polymer is to have a valency greater than two. The formation of organic polymers can be attributed to the ability of the tetrahedral carbon atoms to undergo unlimited covalent combination with other carbon atoms (Gimblett, 1963). These polymers, where all of the atoms in the chain are the same, are termed 'homopolymers'. The properties of these organic polymers can be changed by the addition of other atomic species. The regular addition of other atoms in the carbon chain forms a type of polymer termed a 'heteropolymer'. However, the basic building block of the polymer is still carbon. Inorganic polymers go a step further and utilise most elements in the periodic table as possible backbone templates.

A small number of elements are able to form inorganic homopolymers. These elements can be described as carbon analogues, and are given in Table 1.1. There are, however, a vast number of inorganic heteropolymers. In theory, most combinations of elements should be able to form a polymer material. In practice, most inorganic heteropolymers are constructed of repeating units consisting of two different atoms, where one is almost always oxygen or nitrogen (Gimblett, 1963). Inorganic polymers (IPs) are capable of forming all varieties of the structural forms found in organic polymers. These include linear and branched chains, sheets and 3-dimensional networks. As in organic polymers, the valencies of the constituent atoms control these possibilities.

IPs can be formed by a variety of methods. These include melt/ crystallisation, condensation polymerisation, sintering and cationic/anionic aggregation. The final material properties, the presence of secondary phases, crystallinity etc. are all influenced by the processing route chosen, and how that processing is carried out.

Table 1.1: Elements capable of forming homopolymers, as indicated by the shaded section (Gimblett, 1963; Hunter, 1963).

Group				
IIIb	IVb	Vb	VIb	VIIb
5 B	6 C	7 N	8 O	9 F
13 Al	14 Si	15 P	16 S	17 Cl
31 Ga	32 Ge	33 As	34 Se	35 Br
49 In	50 Sn	51 Sb	52 Te	53 I
81 Tl	82 Pb	83 Bi	84 Po	85 At

IPs have a wide range of technological uses. They can be used in the form of fibres (Bugosh, 1959) or elastomers (Lyon, 2002); and they can be used in conjunction with organic polymers to create surface coatings (Lay & Yarovsky, 2003), such as paints and antireflective glazes. In some cases, the organic polymer is a secondary phase used to disperse the IP, and is later burnt off in the manufacturing process. One potential use for these materials currently being studied, is for the immobilisation of toxic metals (van Jaarsveld, van Deventer & Lorenzen, 1997). IPs are ideal for this application, as the atomic species being contained form part of the polymer network, thus making it more difficult for toxins to leach into the environment. IPs have also been successfully used in a composite form as heat shielding on Formula One racecars (Davidovics, Martin & Davidovits, 1999). In this application in particular, IPs exhibit the properties of traditional organic polymers in terms of their ease of forming, and of ceramic materials in terms of their thermal properties. IPs have also found their way into use as a replacement for Portland cement in engineering structures such as sewage pipes and railway sleepers. In this application, IPs are used both as the sole binding agent, and in conjunction with Portland cement.

The IPs that are the focus of this work are known as aluminosilicate inorganic polymers (AIPs). This family of IPs are 3-dimensional ternary heteropolymers built on a backbone of tetrahedrally coordinated silicon and

aluminium bonded by divalent oxygen. As such, the polymer consists of alternating Al-O, Si-O bonds, with the constraint that there are no Al-O-Al bonds according to the Loewenstein Avoidance Principle (Loewenstein, 1954). This family of AIPs can be made by a variety of means including sol-gel methods (Iwahiro *et al.*, 2001) and hydrothermal condensation (Davidovits, 1989). The temperature range through which these AIPs can be manufactured ranges from room temperature to hundreds of degrees Celsius.

This project focuses on AIPs produced by the alkaline activation of aluminosilicate minerals under hydrothermal conditions. The process of alkaline activation involves mixing an aluminosilicate mineral, such as kaolinite, in an alkaline or alkaline silicate solution in order to initiate polymerisation. The composition and properties of the final polymer are controlled by the mineral and activating solution, whilst the properties of the polymer are also affected by the thermal treatment of the mixture.

1.2 Project objectives

As shown in §1.1, these polymers can be used in a variety of different applications, and the methods of producing them are equally diverse. The area of interest investigated, due to its technological and environmental importance to Australia and to the world at large, was the use of these polymers as a substitute for Portland cement. Portland cement has been in use since the mid-1800s, and no substantial technological advance has been made in its manufacture and use since that time. In the current environmental climate of global warming, nations are attempting to limit their production of greenhouse gases, of which one gas is carbon dioxide. Cement production is one of the leading contributors to CO_2 emissions. In 1987, the world production of cement equated to approximately 1 gigatonne, resulting in the emission of 1 gigatonne of CO_2. This was equivalent to 5% of the world's anthropogenic CO_2 production in that year (Davidovits, 1994a). The use of AIPs in cement applications has the potential to decrease CO_2 related to cement production emissions to 1%, due to the low-CO_2 nature of the material and processing (Davidovits, 1994a).

Within this field of cement replacement research, the scope of this project was further narrowed to study the structure/property relationships in AIPs. This was seen as a fruitful area of research, as it is simple to control the chemistry of these polymers, and changes in the composition results in changes in material properties.

In trying to understand how the chemical composition impacts the material properties, the approach taken was to examine how the composition affects the structure of the polymers and endeavour to explain the material properties in terms of this observed structure. In light of this reasoning, the principal questions this research hoped to answer were:

1) How does the structure of these AIPs change with composition? and
2) How does this change in structure influence the material properties of the AIP?

1.3 Study design

In order to answer the questions stated in the objectives, the following research plan was formulated:

1) Review literature regarding the manufacturing of AIPs,
2) Review literature regarding the methods available to characterise the structure of the AIPs at the macro, micro and nanoscales,
3) To study a physical property of the material that would give results that could be related to the material structure, and
4) To apply the structure characterisation techniques chosen in 2) to determine structural details, and to explain the properties of the AIPs in terms of their structure.

1.4 Thesis outline

This thesis begins with an introduction to IPs in general. Chapter 1 gave a general overview of the science of IPs, and concluded with a statement of objectives and the associated study design and research plan.

Chapter 2 reviews the literature on IPs in greater detail. The science of polymers in general is introduced to the reader. The Chapter then focuses on AIPs; their structure and synthesis. The Chapter then ends by reviewing the reaction chemistry and uses of AIPs.

The focus of Chapter 3 is on bonding characterisation science; what techniques can, and have, been used to look at bonding on the nanoscale. Techniques used in this project, as well as other approaches that are available have been reviewed. The theoretical basis for these techniques is also presented.

Chapter 4 presents the experimental details. The details of each experiment are given and explained. The chapter is written with the aim of providing the reader with the opportunity of reproducing the work reported in this project. The chapter focuses on the practical application of the techniques discussed in Chapter 3, and introduces the experimental techniques utilised in the current study.

Chapter 5 presents the results of a macroscale study on the influence of the chemical composition on AIP compressive strength. Chapter 6 details the results of the microscale study. The microstructure of the AIPs is reported in this chapter. Chapter 7 provides the results of the nanoscale study. The influence of chemical bonding is discussed.

The final chapter, Chapter 8, delivers the conclusions from this work, and gives recommendations for further research.

2.0 INORGANIC POLYMER SCIENCE

This chapter gives an account into the science of the structure and formation of polymers, and inorganic polymers in particular. The descriptions are designed to give the reader a working knowledge of the science of inorganic polymers.

2.1 Polymers

2.1.1 Basic polymer concepts

Polymers are ubiquitous in today's society. A *polymer* is a material whose molecules are made up of a large number of repeating units. It is from this structure that the word polymer is derived; *poly* = many, *meros* = parts. Each repeating unit is termed a *monomer* (Challa, 1993 p. 12). The polymer is formed when the monomers react to form larger structures. If the monomer is represented by **M**, then the resultant polymer can be represented by:

$$\text{- - - -M-M-M-M-M-M- - - -} \quad \text{or} \quad [\text{-M-}]_n$$

where *n* is the degree of polymerisation of the polymer molecule.

Polymers can be classified into two broad categories: organic and inorganic. Generally, organic polymers consist of polymer molecules whose main chain consists of carbon atoms, whereas inorganic polymers are polymers whose main chain consists of other atom types, such as silicon, sulphur or boron. Organometallic polymers belong to both organic and inorganic polymer categories.

Polymers can be further subdivided into different classes by their chain structure, monomer composition and polymerisation mechanism (Challa, 1993 pp. 16-19). A diagram indicating a polymer classification scheme is given in Figure 2.1.

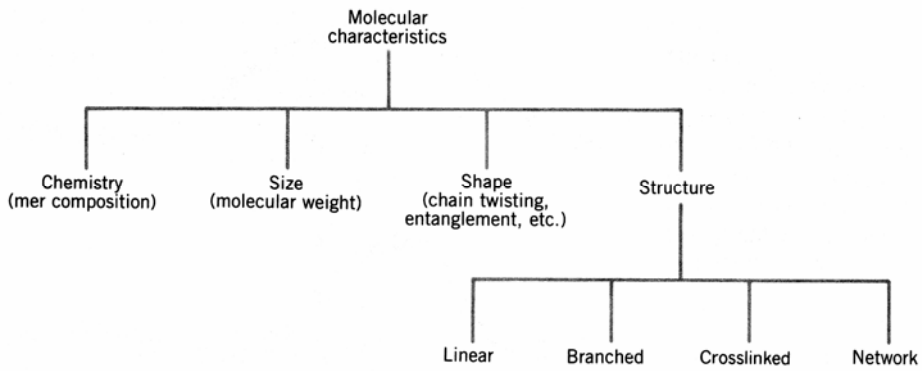

Figure 2.1: Classification scheme for the characteristics of polymer molecules (after Callister, 1997, p. 453). See text for full details of the terms used.

2.1.2 Polymer structure types

The chain structure of polymers can be divided into four different structures, as shown in Figure 2.2. *Linear polymers* are those in which the monomers are joined together end-to-end in a single chain. *Branched polymers* are linear polymers with branches of linear polymer joined to the main chain. The branches need not be of the same size. Trifunctional (or higher order) monomers that have three (or more) active covalent bonds can form *network polymers*. In *ladder*, or *crosslinked*, polymers, adjacent linear chains are joined together at various positions by polymer chains. Ladder polymers have a high degree of regularity in the crosslinking, whilst crosslinked polymers are not as ordered (Callister, 1997 pp. 449-450; Challa, 1993 p. 16).

The monomer composition of polymers can be broken down into two main families. *Homopolymers* consist of identical monomers, whilst *heteropolymers* are made of different monomers. Heteropolymers consisting of two monomers can be further divided into *random copolymers*, where two different monomers are distributed randomly along the polymer chain. *Alternating copolymers* have different monomers swapping positions along the chain. A *block copolymer* has two different monomers in the main chain clustered in groups, whilst the *graft copolymer* has the main chain made from one monomer with the second monomer forming a branch off the side. The same principles also apply to polymers made with three or more

monomers (Callister, 1997 pp.453-454; Challa, 1993 p. 19). Figure 2.3 shows some schematic diagrams of the different types of copolymer.

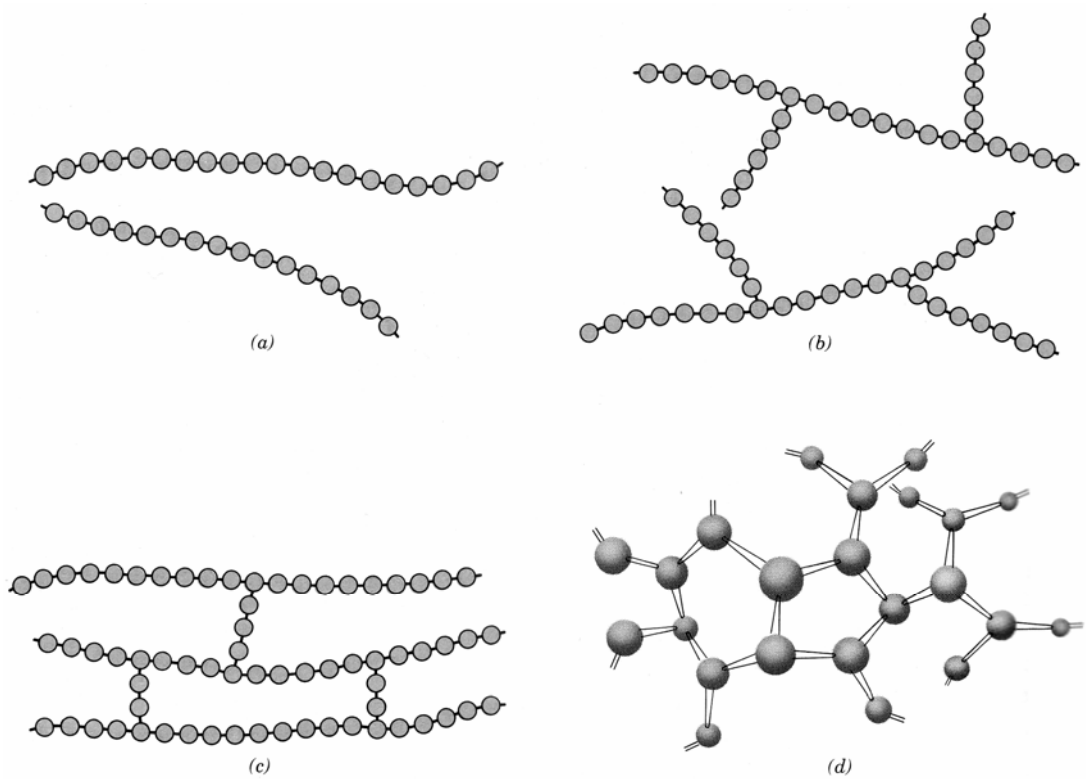

Figure 2.2: Schematic representations of **(a)** linear, **(b)** branched, **(c)** crosslinked, and **(d)** network polymer structures. Circles represent individual monomers (Callister, 1997, p. 450).

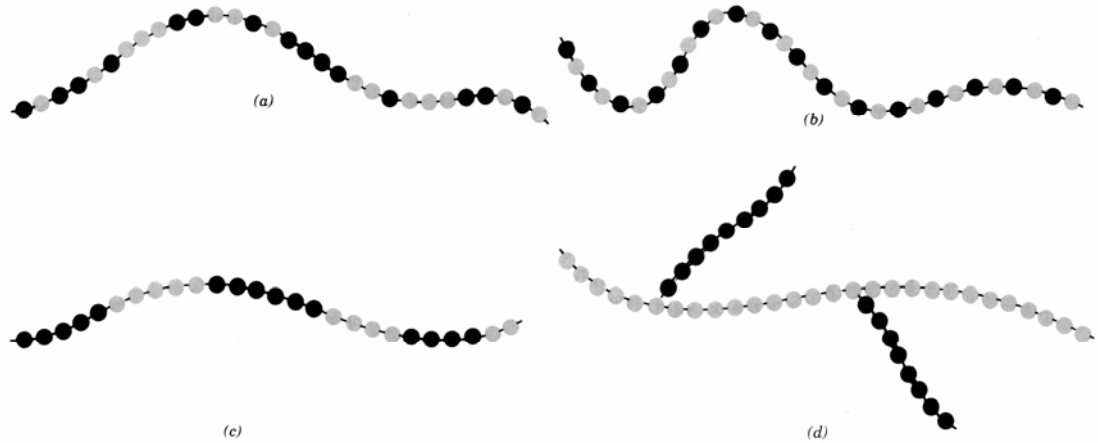

Figure 2.3: Schematic representation of **(a)** random, **(b)** alternating, **(c)** block, and **(d)** graft copolymers. The different monomers are represented by the black and grey circles (Callister, 1997, p. 454).

2.1.3 Polymer synthesis

There are two main polymerisation mechanisms. These are traditionally called *condensation* and *addition* polymerisation, however, they are more correctly known as *step-* and *chain-reaction* polymerisation (Morrison & Boyd, 1992 p.1078). There is a third category of polymerisation, known as *ring-opening polymerisation* (Challa, 1993 p. 20). Examples of these are given in Figure 2.4.

At the beginning of step-reaction polymerisation, the whole system gradually transforms from a mixture of short chains to longer chains as the monomers are consumed. In chain-reaction polymerisation, a small number of very long chains form through a series of reactions, each of which consumes a reactive particle, and produces another. The reactive particle can be a free radical, cation or anion, and its role is to provide a site at which the next monomer may react. Ring-opening polymerisation is viewed as a special case where monomeric rings are opened and then added to the polymer chain. It is possible to make the same polymer by different polymerisation mechanisms (Challa, 1993 p. 20).

The polymerisation of silicic acid proceeds by step-reaction polymerisation as shown in Figure 2.5. Between a pH of 8 and 10.5, the reaction proceeds by the reaction of singly ionised silicate ions and neutral silicic and polysilicic acid molecules. The average molecular weight of the polymer formed will depend on the pH of the solution. At high pH, no reaction takes place, as the solution consists of nearly all silicic acid ions, which would repel each other.

When two or more chemical sites on the monomers are active, then the outcome is a network polymer. One of the oldest types of network polymerisation is the reaction between phenols and formaldehyde (*Bakelite*). In this polymerisation reaction, shown in Figure 2.6, when phenol is treated with formaldehyde in the presence of an acid or alkali, the phenol groups link with CH_2 groups to form a phenol-formaldehyde resin.

Another example of a network polymer is the silane-imine polymer formed from silicon tetrachloride. The network in this polymer relies on the crosslinking provided by both Si and N, as is shown in Figure 2.7.

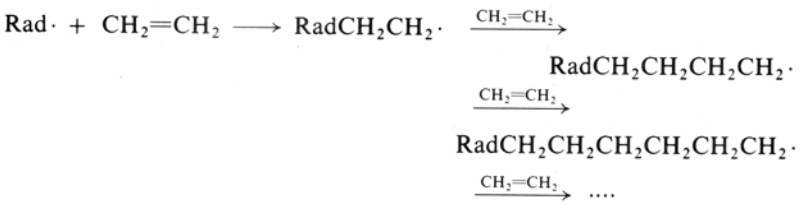

(a)

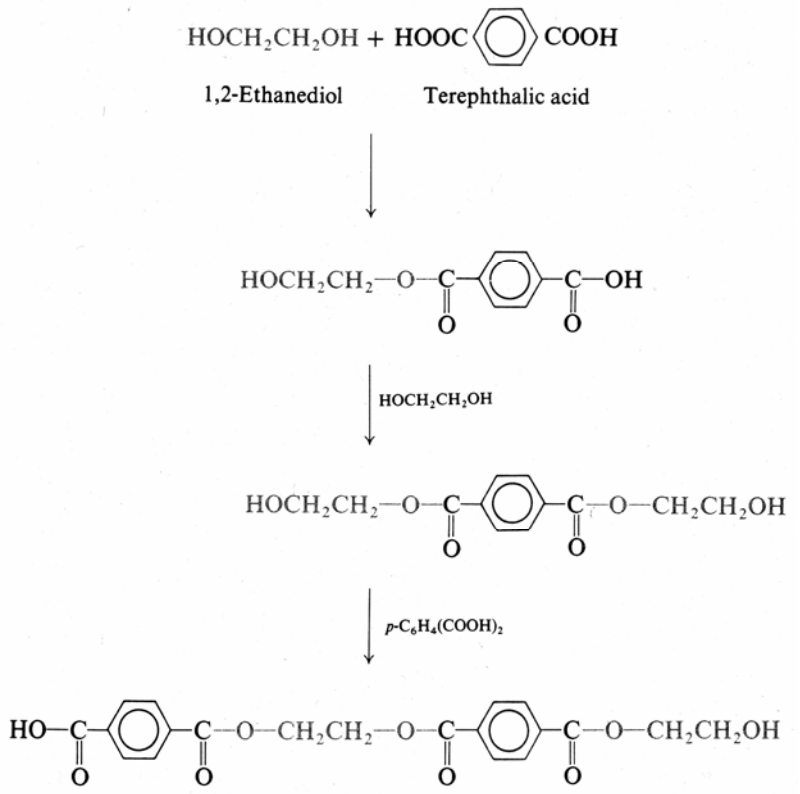

(b)

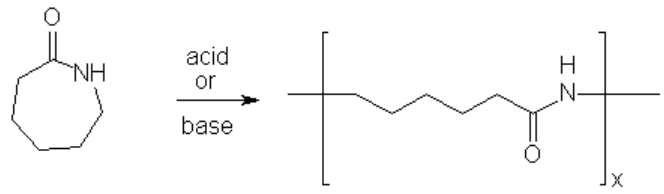

(c)

Figure 2.4: Schematic representations of the three types of polymerisation reaction. **(a)** Chain-reaction polymerisation showing the formation of polyethylene (Morrison & Boyd, 1992 p. 1078), **(b)** Step-reaction polymerisation showing the formation of a polyester (Morrison & Boyd, 1992 p. 1079), and **(c)** ring opening polymerisation showing the formation of nylon (Robello, 2002).

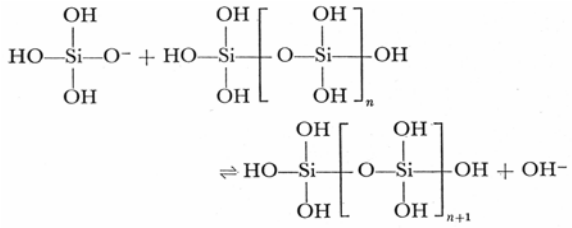

Figure 2.5: Formation of polysilicic acid (Gimblett, 1963, p. 170).

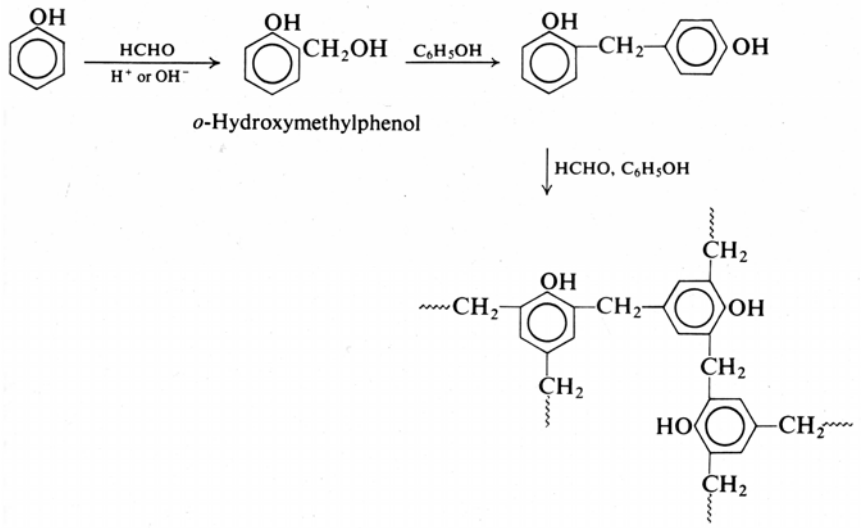

Figure 2.6: Formation of a phenol-formaldehyde resin, a network polymer, by step-reaction polymerisation (Morrison & Boyd, 1992 p.1078)**.**

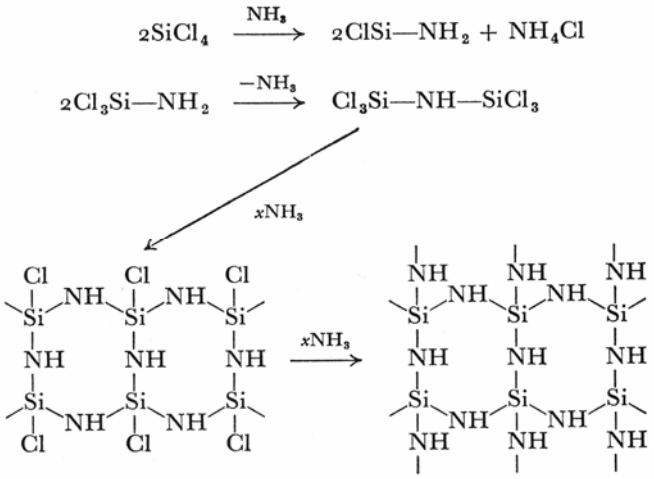

Figure 2.7: Proposed formation mechanism of polysilianimine (Hunter, 1963 p. 47)

2.2 Aluminosilicate inorganic polymers

Aluminosilicate inorganic polymers (AIPs), also known as geopolymers (Davidovits, 1989), form a small subset of all possible inorganic polymers. AIPs are network heteropolymers, with the alternating monomers being SiO_4 and AlO_4 tetrahedra joined by a shared oxygen.

2.2.1 Structure

Davidovits (1989) proposed use of the term *poly(sialate)* for describing the polymer structure of AIPs. The "sialate" monomer represents SiO_4 and AlO_4 tetrahedra joined by an oxygen bridge. Polysialates are represented by the empirical formula

$$M_n\,[-(SiO_2)_z\text{-}(AlO_2)\text{-}]_n$$

where *z* ranges between approximately 1-3, *M* is a monovalent cation such a sodium, and *n* is the degree of polymerisation. For z=1, 2 or 3, the nomenclature proposed by Davidovits for naming the AIPs formed are termed poly(sialate), poly(sialate-siloxo) and poly(sialate-disiloxo), respectively. Although Davidovits limits his nomenclature to integer values of *z*, the formation of polymers with non-integer values of *z* is possible. The *siloxo* term represents the additional SiO_4 tetrahedra added to the polymer chain in order to increase the silicon content. The cation must be present in order to balance the negative charge introduced by having Al^{3+} present in four-fold coordination. The cation can be any one of the alkali metals or alkaline earth metals available, such as Na^+, K^+, Ca^{2+} or Mg^{2+}. Figure 2.8 shows how the polymer chain grows with additional siloxo groups.

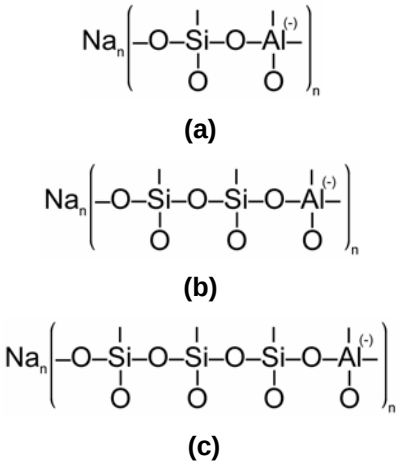

Figure 2.8: Schematic representation of the **(a)** polysialate, **(b)** poly(sialate-siloxo) and **(c)** poly(sialate-disiloxo) polymer chains (after Davidovits, 1991).

AIPs are x-ray amorphous, and as such, characterisation utilising nuclear magnetic resonance (NMR) and fourier transform infra-red (FTIR)

has been carried out in many cases (Barbosa, MacKenzie & Thaumaturgo, 2000; Palomo & de la Fuente, 2003; Hos, McCormick & Byrne, 2002). *Radial distribution function analysis* (RDF) is an additional prospective method for analysing the diffraction patterns of amorphous materials (Wagner, 1978). Radial distribution analysis has been used in the analysis of aluminosilicate glasses, and is able to provide coordination, as well as structural information (Petkov *et al.*, 2000). The analysis of materials with NMR and RDFs is reviewed in Chapter 3.

NMR studies have shown that the silicon and aluminium present in the AIP are tetrahedrally coordinated to oxygen. Barbosa, MacKenzie & Thaumaturgo (2000) used NMR and FTIR to study the polymerisation and structure of AIPs synthesised by the sodium silicate activation of metakaolinite. ^{27}Al magic-angle spinning (MAS) NMR of the metakaolinite showed broad resonances that were attributed to Al in the 4-, 5- and 6-fold coordinate state with oxygen. It was found that all of the Al changes to the 4-coordinate state when the metakaolinite is activated with the alkaline solution, irrespective of the final strength of the material. They found that the intensities of the ^{27}Al MAS NMR spectra changed significantly, with the strongest sample having an integrated intensity ~10 times greater than that of the weakest. Samples with compressive strengths between 0 and 30 MPa showed similar intensities. The ^{29}Si MAS NMR spectrum of metakaolinite showed a single resonance attributed to Q^4(1Al). After activation, the (still broad) peak shifted to a position characteristic of Q^4(2Al) and Q^4(3Al)[1]. They found that the shape and position of the peak did not depend on the composition or curing regime indicating that the Si environment did not change significantly with compositional or curing changes. However, intensity variations were seen between samples. ^{23}Na MAS NMR spectra of the AIPs gave a single peak that did not change with composition or curing regime. The position of the Na peak is postulated by Barbosa, MacKenzie & Thaumaturgo (2000) to be due to hydrated Na^+ present in the AIP structure

[1] The Q notation refers to Si bonded to 4 oxygens with 1, 2 or 3 Al-O tetrahedra bonded through shared oxygens. For a full explanation, see §3.1.5.

Structural models

Barbosa, MacKenzie & Thaumaturgo (2000) proposed a structure for the AIP where SiO_4 and AlO_4 tetrahedra are joined by an oxygen bridge with hydrated Na^+ present in framework cavities. The structure, presented in Figure 2.9, is proposed from their NMR results as indicating the presence of hydrated Na^+ in the framework cavities, and the presence of both Q^4(3Al) and Q^4(2Al) is designated by the '⊗' and '✶', respectively. The cages would be enclosed by the extension of the structure in three dimensions. The proposed structure shows a variety of bond lengths and angles to indicate a lack of long range order, but the structure has been created primarily to be consistent with the NMR results.

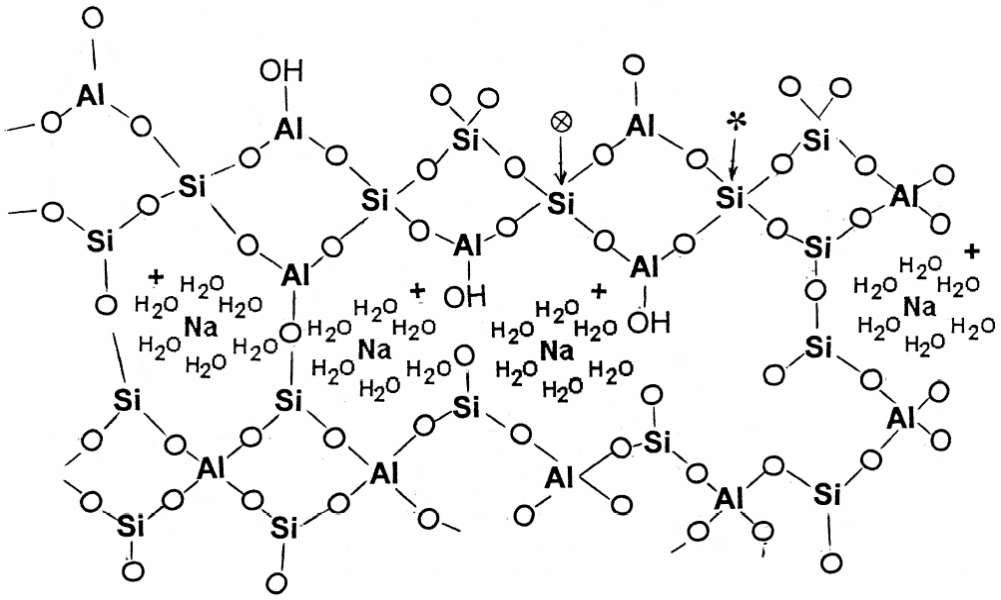

Figure 2.9: Proposed structure for a Na-polysialate polymer (after Barbosa, MacKenzie & Thaumaturgo, 2000). Q^4(3Al) and Q^4(2Al) silicon sites are indicated by the '⊗' and '✶'

Davidovits (1994b) has proposed an alternative AIP bonding network model (Figure 2.10) for K-poly(sialate-siloxo), in which K, analogous to Na, is associated with the aluminate tetrahedra. Davidovits' model is similar to that proposed by Li, Ding & Zhang (2004) (Figure 2.11), who simulated a statistical structure that was consistent with their NMR spectra. These structures appear to be more ordered than the diffraction patterns would suggest (Barbosa, MacKenzie & Thaumaturgo, 2000). It appears that these structures were produced to give the correct distribution of Q^4(*m*Al) sites,

without regard for bond length and angle distributions. Also, no note is made of the presence of water in the structure, as is suggested by the ^{23}Na MAS NMR of Barbosa, MacKenzie & Thaumaturgo (2000)

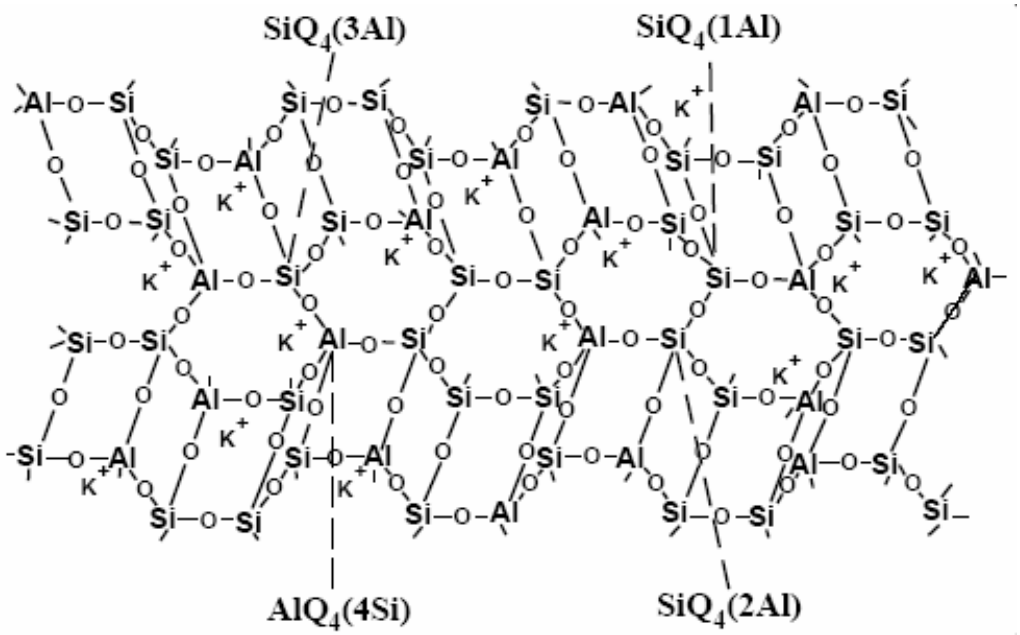

Figure 2.10: Proposed structural model for K-poly(sialate-siloxo). In this model, the K is analogous to Na (Davidovits, 1994b).

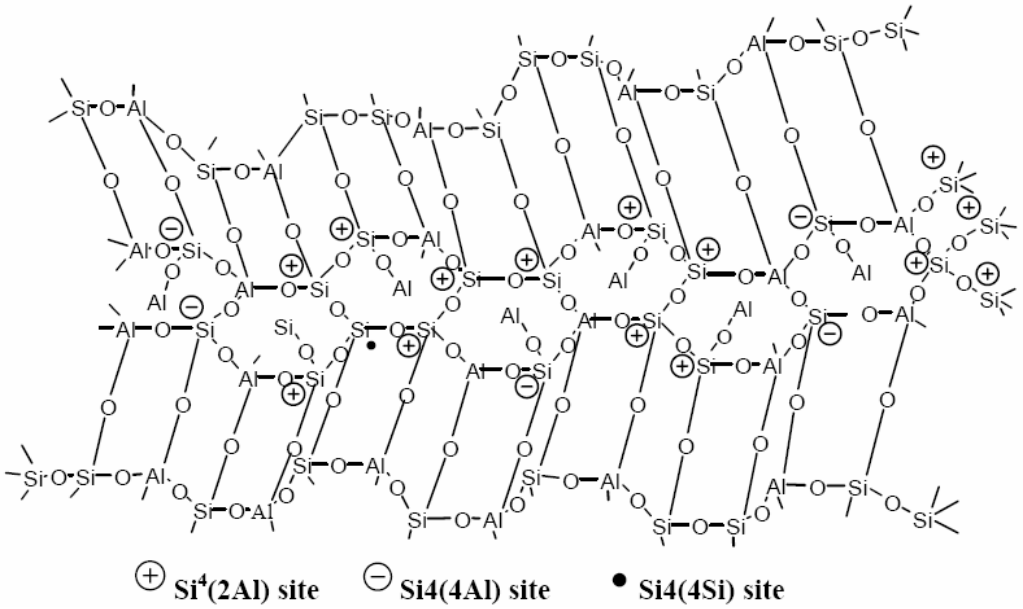

Figure 2.11: Statistical structure of K-polysialate (Li, Ding & Zhang, 2004). Li, Ding & Zhang state that K is present in the framework cavities to counter the negative charge of the AlO_4 tetrahedra.

2.2.2 Synthesis

AIPs can be synthesised by various means, using diverse precursor materials. The most common ways are outlined in the following sections.

Aluminosilicate inorganic polymer precursors

Several precursor materials have been used as a basis for forming AIPs. These include: metakaolinite, kaolinite and other aluminosilicate minerals, flyash and blast furnace slag, as well as mixtures of all of these. The rate at which the activation process proceeds depends on the reactivity of the precursor. For example, the dissolution rate of metakaolinite is much faster than kaolinite due to the higher reactivity in alkaline solutions of amorphous aluminosilicates (Granizo, Blanco-Varela & Palomo, 2000).

Use of mineral sources of aluminosilicate precursors (Barbosa, MacKenzie & Thaumaturgo, 2000; Granizo & Blanco, 1998; Palomo *et al.*, 1999; Rahier *et al.*, 1996; Xu & van Deventer, 2000) has an advantage over other precursors inasmuch as they usually contain fewer impurities. The incorporation of impurities such as Fe and Ti into the AIP matrix has an unknown effect on the materials properties. The bulk of the literature reports the use of metakaolinite as the aluminosilicate precursor, which is manufactured by dehydroxylating kaolinite (nominal composition of $Al_2O_3.2SiO_2.2H_2O$). The dehydroxylation process removes the water from the aluminosilicate and results in a material with a disordered crystal structure showing a wide range of coordination states for both silicon and aluminium. The process is carried out by heating the kaolinite to 550 – 900 °C, with temperatures between 700 and 900 °C creating almost “pure” metakaolinite (Rahier, Wullaert & van Mele, 2000). The dehydroxylation process has been reported to be between 1 and 24 hours in duration.

Fly ash (Palomo, Grutzeck & Blanco, 1999; Swanepoel & Strydom, 2002; van Jaarsveld, van Deventer & Schwartzman, 1999) and blast furnace slag (Bakharev, Sanjayan & Cheng, 1999; Brough & Atkinson, 2002; Fernández-Jiménez, Palomo & Puertas, 1999) have been extensively studied as a source of material for AIP production. Fly ash is a by-product of coal

combustion, and is an aluminosilicate with significant amounts of Fe_2O_3 and CaO also present. Fly ash is categorised into two classes, F and C, based on its chemical composition (ASTM, 2002). The criteria for these categories are given in Table 2.1. F class fly ash is normally produced from the burning of anthracitic or bituminous coal, and C class fly ash from the burning of lignite or sub-bituminous coal. Class F and C fly ash are also known as low- and high-calcium fly ash, respectively.

Table 2.1: Compositions for the classification of fly ash (ASTM, 2002).

	Fly ash class	
	F	**C**
$SiO_2 + Al_2O_3 + Fe_2O_3$, min wt%	70.0	50.0
SO_3, max wt%	5.0	5.0
Moisture content, max wt%	3.0	3.0
LOI, max wt%	6.0	6.0

Blast furnace slag is a by-product of the metallurgical industry and consists mainly of calcium magnesium aluminosilicates. The major drawback to the use of these materials as precursors is that the properties of the materials synthesised from them are affected by variations in the composition and morphology of the precursor. In particular, the amounts of Fe, Mg and Ca are highly variable. This variation in composition means that one set of experimental conditions cannot be imposed directly onto a material made from a material of a different composition; a new procedure must be established to make the most of the new material (Bakharev, Sanjayan & Cheng, 1999).

Various mixtures of minerals, fly ash and blast slag have also been studied for their ability to form AIPs (Allahverdi & Skvára, 2001a; Puertas *et al.*, 2000; van Jaarsveld, van Deventer & Lukey, 2002). These studies show that it is possible to design a material mix to give the desired chemical composition, however, the majority of the work seems to report mixtures created without regard for the final composition. Another way of producing tailored chemical compositions was reported by Hos, McCormick & Byrne (2002). This method involved melt-quenching of a mixture of alumina

and silica, which resulted in an amorphous aluminosilicate with traces of mullite and aluminium silicate hydroxide.

Alkaline activation

AIPs can be formed by alkaline activation of the aluminosilicate precursor. The activation process is initiated by the addition of an alkali metal hydroxide. The addition of the hydroxide starts a polycondensation reaction which leads to a cementitious material (Granizo & Blanco, 1998). The activation process creates a network polymer consisting of SiO_4 and AlO_4 tetrahedra joined by an oxygen bridge (Davidovits, 1989). In this configuration, the AlO_4 tetrahedron introduces a negative charge, which the alkali metal balances.

Theoretically, almost any positive ion could be used to act as the charge balancing ion; however, in practice, only a small number of ions are used. These activators include solutions of: sodium hydroxide & silicate (Palomo *et al.*, 1999), potassium hydroxide & silicate (Barbosa & MacKenzie, 2003) and calcium hydroxide (Alonso & Palomo, 2001). Mixtures of these activating solutions have also been used to initiate the polymerisation reaction.

Manipulation of the composition of the AIP can be carried out with the activating solution. There are many publications that show that the AIP properties change when the relative amounts of Si and alkali are changed (Rahier *et al.*, 1996; Barbosa, MacKenzie & Thaumaturgo, 2000; van Jaarsveld, van Deventer & Schwartzman, 1999). The most common way of representing the composition of an AIP is with the use of the Si:Al and Na:Al molar ratios. According to Davidovits (1991), AIPs are best formed with a Si:Al molar ratio of between 1 and 3. Rahier *et al.* (1996) claim that the ideal Na:Al molar ratio for the formation of AIPs is 1, which gives a stoichiometric amount of Na; the negative charge introduced by the AlO_4 tetrahedra is countered exactly by the positive charge of the Na^+.

Polymer curing and aging

The aluminosilicate precursor and the activating solution are mixed to form a viscous inorganic polymer resin. The viscosity of the resin depends on the water content, chemical composition and the age of the resin.

The polymerisation reaction is exothermic and can be carried out at temperatures between room temperature and ~150 °C (Davidovits, 1989; Granizo & Blanco, 1998). Typically, temperatures less than 100 °C are employed to avoid the use of pressure vessels. During the curing process, the loss of water from the reaction vessels is unwanted, and the vessels are sealed to prevent this loss.

The post-cure treatments of AIPs depend on the application for which they are being produced. For example, AIP matrix fibre composite materials require drying to increase their strength and water resistance (Lyon *et al.*, 1997), whereas AIPs used as cements are most often left in their own post-cured state.

Cements made from ordinary Portland cement (OPC) exhibit an aging effect which results in the compressive strength of the material increasing as the material becomes older due to formation of Calcium Silicate Hydrate (CSH) crystals. The aging process continues to reinforce the concrete as the crystals develop.

The aging effect is not supposed to affect concretes made with AIPs, as the polymerisation process is believed to be complete after the initial curing process. Davidovits has claimed that once the polymerisation reaction has completed, ie during the curing process, then the compressive strength of the material is at its maximum (per. comm., 2002). This observation has been supported by Hardjito, Wallah & Rangan (2002) in their study on the engineering properties of flyash based geopolymer concrete which showed that the compressive strength of their optimum mix did not vary significantly over a period of 60 days. However, Subaer (2004) found that the compressive strength increased over a period of 14 days, after which it

remained constant. This later result could reflect incomplete curing, or the influence of different precursor materials on the strength development of AIPs.

Sol-gel processing

The sol-gel process involves the hydrolysis of a solution containing precursor molecules to obtain a suspension of colloidal particles (sol), which then ages to produce a dense aggregate (gel) (Brinker & Scherer, 1990 p. 2). This technique allows the manufacture of inorganic materials from organic precursors.

The sol-gel process allows for the production of very pure aluminosilicate precursors with a range of aluminium and silicon coordination and concentrations (May *et al.*, 1997; Jaymes *et al.*, 1995; Sinkó & Mezei, 1998).

There are several different ways to produce aluminosilicates by sol-gel processing. One reaction pathway is the reaction of tetraethoxysilane (TEOS) with aluminium triisopropoxide in the presence of water, which proceeds as shown (Léonard *et al.*, 1964).

$$m\mathrm{Al(OCH(CH_3)_2)_3} + n\mathrm{Si(OC_2H_5)_4} \rightarrow (\mathrm{Al_2O_3})_m(\mathrm{SiO_2})_n.x\mathrm{H_2O} + 3m\mathrm{(CH_3)_2CHOH} + 4n\mathrm{C_2H_2OH}$$

Another preparation route is through the use of TEOS and aluminium nitrate nonahydrate in propanol. The final composition of the aluminosilicate can be altered by changing the starting materials and mixing method.

Sinkó & Mezei (1998) found that gels made with several Si:Al molar ratios had varying amounts of aluminium chemically incorporated into the aluminosilicate network, dependent on the water content of the sol-gel, and on the amount of prehydrolysis carried out on the aluminium nitrate nonahydrate. May *et al.* (1997) prepared many aluminosilicates with the same composition by reacting TEOS with different aluminium alkoxides, and demonstrated that the coordination of the silicon and aluminium was also dependent on the hydrolysis water concentration.

The main role of sol-gel processing in the production of AIPs is in the manufacturing of high purity precursors. Sol-gel has the advantage of being able to tailor the composition and the coordination of the Si and Al present in the precursor to allow the effects of both to be studied. The major disadvantage to the sol-gel route is the large cost associated with the production of the aluminosilicates. The cost of the reactants can run into the hundreds of dollars per gram, but must be set against the high purity of the final product. A final cost-benefit scheme must be introduced to calculate if the cost of the sol-gel route is worth the additional purity.

Co-formation of zeolites in aluminosilicate inorganic polymer production

Zeolites are macromolecular crystalline aluminosilicates made up of SiO_4 and AlO_4 tetrahedra joined by an oxygen bridge. The conditions and materials by which zeolites are manufactured are similar to those in which AIPs are made, which is highlighted by the observation of zeolite formation during the production and use of AIPs (Palomo *et al.*, 1999; Brough *et al.*, 2001). Palomo *et al.* (1999) found that following approximately 56 days of submersion in a Na_2SO_4 solution, faujasite zeolites had formed in the AIP samples. Brough *et al*. (2001) observed the formation of several types of zeolite in a cement made of a mixture of flyash and OPC. The zeolites observed were hydroxysodalite ($Na_6Si_6Al_6O_{24}.2NaOH.nH_2O$) and zeolite Na-P1 ($Na_6Al_6Si_{10}O_{32}.15H_2O$). The formation of zeolites and other crystalline aluminosilicates in the AIP could affect the strength of the material. The magnitude of the change would be dependent on the amount of material produced, and its distribution.

The formation of zeolites using AIP production methods means that it is possible to adapt what is known about the synthesis of zeolites to the establishment of the AIP polymer structure. The main difference between zeolite synthesis and AIP synthesis is the amount of water used and the curing temperature. The curing process for AIPs is carried out below 100 °C, whereas zeolites are normally synthesised at temperatures ranging from 100 to 300 °C. The amount of water used in the production of AIPs is typically enough to allow for adequate mixing of the components. Zeolite production

can use up to 670 mL of water per 100 g of solids (Basaldella, Kikot & Tara, 1997; Murayama, Yamamoto & Shibata, 2002). This large amount of water is necessary to allow for the distribution of ions through the solution. With lower water content, the solution is more viscous, and the transport of ions would be more difficult and the growth of the zeolites would be affected.

Zeolites are used in many different applications. They are used as ion exchange resins, due to their need to have cations in the structure to act as charge balancers. They are also used as molecular sieves due to the tailorability of the pores sizes in their structure. The presence of zeolites in AIPs could be used in waste immobilisation applications, as the zeolite cages could be constructed in order to contain the waste elements. The use of zeolites in OPC concretes for the immobilisation of toxic waste has been investigated previously (Atkins, Glasser & Jack, 1995).

2.2.3 Reaction chemistry

Davidovits (1989) states that AIPs are formed by the polycondensation of hypothetical intermediary monomers, the *orthosialate* ions. In this proposed reaction pathway, the aluminosilicate precursor is transformed into the orthosialate ion in the presence of water and alkali, and this ion then polycondenses into the final AIP product. Davidovits supposes that the syntheses are carried out through oligomers which provide the structural units of the network polymer. The reaction proposed is given in Figure 2.12.

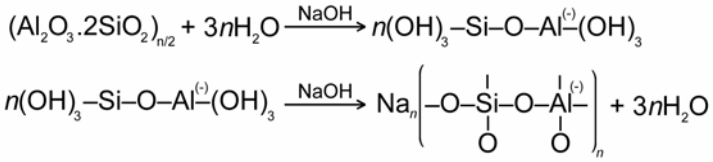

Figure 2.12: Reaction pathway showing the polymerisation of the orthosialate ions (after Davidovits, 1991)

It is reasonable to assume that the polymerisation process is initiated by the alkali-catalysed dissolution of the aluminosilicate precursor in the AIP resin. This assumption is supported by reaction pathways in zeolite synthesis (Murayama, Yamamoto & Shibata, 2002), the chemistry of which is very similar to that of AIPs.

In the reaction given above, the resultant AIP is of the polysialate variety. In order to produce polymers with higher silicon content, the poly(sialate-siloxo) and poly(sialate-disiloxo) type AIPs, additional silicon is added in the first step, resulting in longer Si-O chains in the final AIP. These have been previously outlined in §2.2.1.

Alkali aluminosilicates are highly insoluble in aqueous solution (Iler, 1986), and as such, the polymerisation process most likely occurs as the concurrent dissolution and polycondensation of the aluminosilicate. These two steps continue until the aluminosilicate is consumed, or the dissolution kinetics are halted due to the highly viscous/solid AIP not allowing the ions to move freely to polymerise.

Aluminosilicate dissolution

The first step in the polymerisation process is the dissolution of the aluminosilicate precursor. In an alkaline solution, aluminium and silicon dissolve to form the aluminate ion and monosilicic acid; $Al(OH)_4^-$ and $Si(OH)_4$. The dissolution formulae for SiO_2 and Al_2O_3 are given below (Iler, 1986).

$$SiO_2 + 2H_2O \Leftrightarrow Si(OH)_4$$
$$Si(OH)_4 + Na^+ + OH^- \Leftrightarrow OSi(OH)_3^- + H_2O + Na^+$$

$$Al_2O_3 + 3H_2O + 2Na^+ + 2OH^- \Leftrightarrow 2\left(Al(OH)_4^- + Na^+\right)$$
$$\left(Al(OH)_4^- + Na^+\right) + Na^+ + OH^- \Leftrightarrow NaOAl(OH)_3^- + H_2O + Na^+$$

These species are tetrahedrally coordinated due to the highly alkaline conditions (Iler, 1986), and copolymerise in all proportions, limited by the Loewenstein Avoidance Principle (Loewenstein, 1954). The kinetics of the dissolution process depend on the aluminosilicate used and on the pH and temperature.

A study on the formation of zeolite P from fly ash (Murayama, Yamamoto & Shibata, 2002) showed that the dissolution of the flyash was dependent on the OH^- concentration, and that dissolution can be greatly enhanced by adding only a small amount of OH^-.

Aluminosilicate inorganic polymer polycondensation

NMR is an excellent technique for determining the presence and structure of dissolved silicate, aluminate and aluminosilicate anions. However, characterisation of the intermediate species involved in the polymerisation reaction by NMR is very difficult, and can be attributed to two effects. The first is that the linewidth of the NMR peaks increases as the viscosity of the solution increases, as a result of solid-state effects (Engelhardt & Michel, 1987). These effects are due to the non-random orientation of the magnetic moments on the nuclei. An explanation of this effect is given in §3.1. The second is that the contribution to the signal from two ionic species will be broadened beyond recognition if the reaction between those species is faster than the NMR signal collection time (Engelhardt & Michel, 1987). In relation to the second point, North & Swaddle (2000) found that silicate-aluminate exchange reactions could be followed by NMR only when the temperature of the system was below 5 °C.

North & Swaddle (2000) studied the formation of alkaline aluminosilicates by the addition of both silicate and aluminate solutions in order to avoid the viscosity problem. Low temperatures were also employed to further aid the detection of intermediate species. Analysis of the ^{27}Al NMR spectra show that there was no significant concentration of $Al(OH)_4^-$ in solution, which implies that the main Al-O-Si species present contains an Al centre with either one or two –OSi links.

The rate of the silicon exchange reaction in aluminosilicates is at least 4 orders of magnitude faster than that in silicate systems. North & Swaddle (2000) suggest that the reason that the aluminosilicate process is so fast is that the Al centres are able to expand their coordination with respect to oxygen beyond 4, allowing for transient 5- and 6-coordinate species to be formed during ion exchange. The formation of the aluminosilicate polymer can be modelled on a single reaction as outlined by North & Swaddle (2000).

$$(^-O)_3SiOH + HOAl(OH)_2OSiO_3^{3-} \leftrightarrow (^-O)_3SiOAl(OH)_2OSiO_3^{3-} + H_2O$$

In light of the work by North & Swaddle (2000), a likely model of AIP formation would involve the immediate consumption of $Si(OH)_4$ in the liquid phase by the constant dissolution of $Al(OH)_4^-$, as outlined in the above equation. As the concentration of the aluminosilicate anions increases, they will coalesce to form an aluminosilicate gel which grows as the aluminosilicate precursor is consumed, and hardens to form the AIP.

2.2.4 Uses and relevant environmental influences

AIPs of the type investigated in the current study have a wide range of applications, with a particular emphasis on engineering applications.

Cements and concretes

One of the main foci of research in this area has been on the use of AIPs as a replacement for OPC for two reasons. First, the production of OPC produces large amounts of CO_2; each tonne of cement produced generates a tonne of CO_2 (Davidovits, 1991). In this age of increased awareness of greenhouse gas emissions, all ways of decreasing the production of these gases should be investigated. Second, waste materials such as fly ash and blast slag are produced in large quantities by industry, the vast majority of which is used as landfill (Jahanian & Rostami, 2001). The development of cementitious materials based on these waste materials would consume millions of tonnes of waste material that would have had to have been disposed of by other means.

In order to allow the comparison of OPC properties to be made with those of AIP cements and concretes, the resistance of AIP cements and concretes to extremes of temperature and chemical attack has been the focus of much study.

Palomo *et al.* (1999) report an investigation into the stability of AIPs based on metakaolinite when exposed to fluids such as deionised water, sea water, sodium sulphate and sulphuric acid. It was found that these solutions had little negative effect on the strength and microstructure of the materials, with all materials showing an increase in their flexural strength after 90 days of exposure. X-ray diffraction (XRD) analysis showed that some of the

originally amorphous AIP had transformed into a zeolitic material belonging to the faujasite family of zeolites. The faujasite family consists of zeolites that are composed of SiO_4 and AlO_4 tetrahedra arranged in truncated octahedra.

The alteration of the AIP structure has also been reported by Allahverdi & Skvára (2001a; 2001b). They show that AIPs formed from blast slag and fly ash, when exposed to nitric acid, leach Na^+ and Ca^{2+} ions from the surface of the material, where they are replaced by H^+ ions from solution resulting in an electrophilic attack on the Si-O-Al bonds. The attack leads to the ejection of the tetrahedral Al from the aluminosilicate network, resulting in the formation of a siliceous framework with octahedral Al accumulating in the framework spaces. Allahverdi & Skvára hypothesised that a reduction in the amount of soluble content, namely sodium and calcium, will result in a more acid resistant AIP.

Shi & Stegemann (2000) reported a comparison between the nitric and acetic acid resistance of OPC, activated blast slag and an activated lime-flyash mixture. They found that OPC pastes corroded faster than both the slag and flyash based pastes, and that the porosity of the pastes did not correlate to their acid resistance. From this, they concluded that the nature of the corrosion product controlled the rate of corrosion. In all cases, the corrosion layer was reported as being an $SiO_2.nH_2O$ gel.

A comprehensive study on the effect of silica fume, metakaolinite and low calcium fly ash on the chemical resistance of OPC mortar was reported by Roy, Arjunan & Silsbee (2001). The samples tested in their study were made as OPC mixtures, and no supplementary alkali activator was added. A wide variety of acids were used, and it was found that the substitution of OPC for silica fume, flyash or metakaolinite increased the chemical resistance of the mortars.

Toxic waste management

AIPs have also been investigated as potential sources of toxic waste management. The main thrust behind this research is that AIPs can

potentially offer physical encapsulation of waste (which OPC is able to do) as well as chemical encapsulation, where the toxic material is incorporated into the AIP matrix.

Several studies have reported work on the immobilisation of boron (Palomo & de la Fuente, 2003), chromium & lead (Palomo & Palacios, 2003; Rha, Kang & Kim, 2000), copper & lead (van Jaarsveld & van Deventer, 1999a; van Jaarsveld, van Deventer & Schwartzman, 1999; van Jaarsveld, van Deventer & Lorenzen, 1998) and caesium & strontium (Perera *et al.*, 2003; Perera *et al.*, 2004a)

The presence of these contaminants in the AIP has the potential to alter the way in which the AIP forms, and in most cases, the response of the AIP to the contaminant was found to be opposite to that of the response of OPC. It was found that whilst the activation process of fly ash is not affected by boron, OPC hydration is significantly affected, and the final compressive strength of OPC+B can be up to 10 times less than the compressive strength of OPC. In addition to the large change in strength, the leaching rate of boron in OPC is up to 100 times greater than the leach rates in flyash (Palomo & de la Fuente, 2003).

Studies into the encapsulation of chromium (Palomo & Palacios, 2003; Rha, Kang & Kim, 2000) report seemingly contradictory results. Palomo & Palacios (2003) found that the addition of chromium in the form of CrO_3 affected the activation of the flyash to the extent that no polymer network formed. Chromium was easily leached, as it was taken up as a soluble sodium chromate. Rha, Kang & Kim (2000) found that whilst the effect of the alkali activator was reduced by the addition of chromium, an AIP was still formed that was able to hold the chromium in its structure. Upon closer inspection, it appears that the difference between these two studies was the amount of calcium in the precursor materials. Palomo & Palacios (2003) also studied the effect of Cr on OPC, and found that the Cr was incorporated as Ca_2CrO_4, which increased the strength of the OPC. It is possible that this was also the case in the results reported by Rha, Kang & Kim (2000), which

shows that the presence of secondary/minor elements in the precursors can have large impacts on the final AIP.

AIPs have been found to encapsulate lead very effectively (van Jaarsveld & van Deventer, 1999a; Palomo & Palacios, 2003). Palomo & Palacios (2003) found that the addition of lead at concentrations up to 3.125% did not significantly affect the properties of the AIP matrix. They found that FTIR did not show any bands that could be assigned to a lead compound, while x-ray diffraction (XRD) showed a trace phase of Pb_3SiO_5, which has a very low solubility. Palomo & Palacios do not state the method of incorporation of lead into the AIP, whereas van Jaarsveld & van Deventer (1999a) state that their FTIR and transmission electron microscopy (TEM) results support the assertion that lead is both physically and chemically bonded in the AIP network.

Fibre reinforced composites

AIPs have been investigated as the matrix material for fibre reinforced composite materials. As AIP resins are easily moulded and have minimal shrinkage upon setting, they mimic the behaviour of organic thermosetting polymers traditionally used in fibre reinforced composite materials. The main difference between the organic and AIP resins is that AIP based composites offer both fire and ultraviolet resistance.

Lyon *et al.* (1997) reported the fire resistance of glass and carbon fibre composites made with AIP and a variety of organic polymers. They found that the AIP matrix composite did not burn, support combustion or produce smoke in irradiance testing. The AIP composite had a much higher maximum operating temperature of ~800 °C, as opposed to 200 °C for the organic matrix composites and 500 °C for structural steel. Also, the strength retention after exposure to fire of the AIP based composites was greater than both organic matrix composites and structural steel. Overall, AIPs appear to be a superior material for composite applications requiring fire-proof properties.

Kriven, Bell & Gordon (2003) have reported the properties of AIPs reinforced with basalt fibres. They found that with the inclusion of the fibres, the bending strength of the AIPs was increased from an average of 2.8 MPa to 10.3 MPa. The compressive strength of the material was decreased following the addition of fibres. Neat AIP paste had a compressive strength of ~60 MPa, which was reduced to 20-30 MPa upon the addition of 1 vol% fibres. The addition of fibres also changed the fracture properties of the material, with samples chipping or splintering prior to catastrophic failure.

3.0 BONDING CHARACTERISATION SCIENCE

This chapter gives a detailed review of the bonding characterisation sciences that were considered for use in the course of the current study. The descriptions are designed to give the reader a background in the relevant mathematics and physical reasons for the experimental methods used.

3.1 Solid-state nuclear magnetic resonance

This section details the use of solid-state NMR (SSNMR) in the study of materials that exhibit little, or no crystallinity. Information can be gleaned from these spectra that is difficult to find any other way. For example, ranges of bond angles in glassy materials have been studied by correlations between chemical shifts and bond angles (Duer, 2002).

3.1.1 Theory

An NMR experiment uses nuclear spin systems as the probe of a material. For simple spin systems (nuclear spin = ½), it is sufficient to consider the classical vector model. However, once the spins of nuclei begin to interact with each other, such as via dipolar and quadrupolar coupling, then a full quantum mechanical model must be used to describe the effects. As this section is intended solely as an overview, only the simple case will be considered.

In simple, spin-½ systems, the net magnetisation of the system is the vectorial sum of the individual magnetic moments associated with the nuclei present, as illustrated in Figure 3.1.

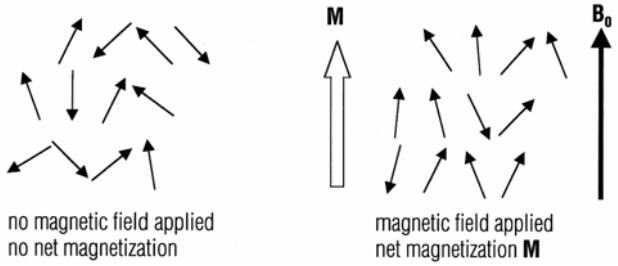

Figure 3.1: Classical model of the formation of a net magnetisation vector in a material under an applied field (Duer, 2002 p. 4).

The nuclear magnetic moment is related to the nuclear spin of the nucleus by

$$\mu_i = \gamma \mathbf{I}_i \qquad \textbf{Equation 3.1}$$

where γ, the magnetogyric ratio, is a constant for any given nucleus. From this, it follows that the net magnetisation of the sample can be written as

$$\mathbf{M} = \gamma \mathbf{J} \qquad \textbf{Equation 3.2}$$

where **J** is the net spin angular momentum of the sample giving rise to the magnetisation **M**. In a zero applied field, the net magnetisation is zero. However, if the nuclei are placed in a magnetic field **B**, then a torque **T** is applied to the magnetisation vector to induce a net magnetisation:

$$\mathbf{T} = \frac{\mathrm{d}}{\mathrm{d}t}\mathbf{J} \qquad \textbf{Equation 3.3}$$

The motion of the magnetisation vector in the applied field is described by

$$\frac{\mathrm{d}\mathbf{M}}{\mathrm{d}t} = \gamma \mathbf{M} \times \mathbf{B} \qquad \textbf{Equation 3.4}$$

This equation predicts that the magnetisation vectors will precess about the applied field vector. If the applied field is assumed to be in the *z* direction, then the frequency with which the magnetisation precesses about the applied field is defined as ω_0, the *Larmor frequency.*

$$\omega_0 = \gamma B_0 \qquad \textbf{Equation 3.5}$$

The Larmor frequency is a constant for a particular nucleus. It is this difference in frequencies between nuclei that allows for the selectivity of an NMR experiment.

The application of an external static field is the first part of the NMR experiment. The second part of the experiment consists of introducing an alternating magnetic field to perturb the magnetisation vectors.

The second applied field is a radiofrequency (rf) pulse arranged such that the alternating magnetic field is perpendicular to the static field ($\mathbf{B}_0$). This field can be written as the sum of two components rotating about $\mathbf{B}_0$ in opposite directions with frequencies of $\pm\omega_{rf}$. The only component of the field that interacts with the magnetisation vector of the nuclei is that which is in the same direction as the precession. This magnetic field is called $\mathbf{B}_1$.

If the frame of reference is now changed to one that rotates about $\mathbf{B}_0$ with a frequency ω_{rf}, then $\mathbf{B}_1$ appears stationary. If $\omega_{rf} = \omega_0$, then the magnetisation vector also appears stationary. If the precession frequency is zero, then the applied field has been removed from the reference frame. The result of the removal of applied field is that the magnetisation vector now precesses about $\mathbf{B}_1$ with a frequency $\gamma B_1 = \omega_1$.

The effect of the rf pulse is to “flip” the magnetisation. The flip angle of an on-resonance pulse is the angle that $\mathbf{B}_1$ turns the magnetisation during time t.

$$\theta_{rf} = \omega_1 t \qquad \textbf{Equation 3.6}$$

A 90° pulse is one that has a pulse length long enough to flip the magnetisation by 90°. After the pulse is switched off, the magnetisation acts only on the magnetic field remaining. If the effective field is zero, then the magnetisation is stationary in the rotating frame.

The third part of the NMR experiment consists of recording the *free induction decay* (FID, G(*t*)) in the receiver coil. The FID registers the sample’s response to the perturbation, which is a measure of the magnetisation vectors returning to their equilibrium position. The fourier transform of the FID yields the NMR spectrum. The initial amplitude of the

FID is proportional to the equilibrium magnetisation (the number of observed nuclear spins) (Engelhardt & Michel, 1987). An example of a FID and its corresponding NMR spectrum is given in Figure 3.2.

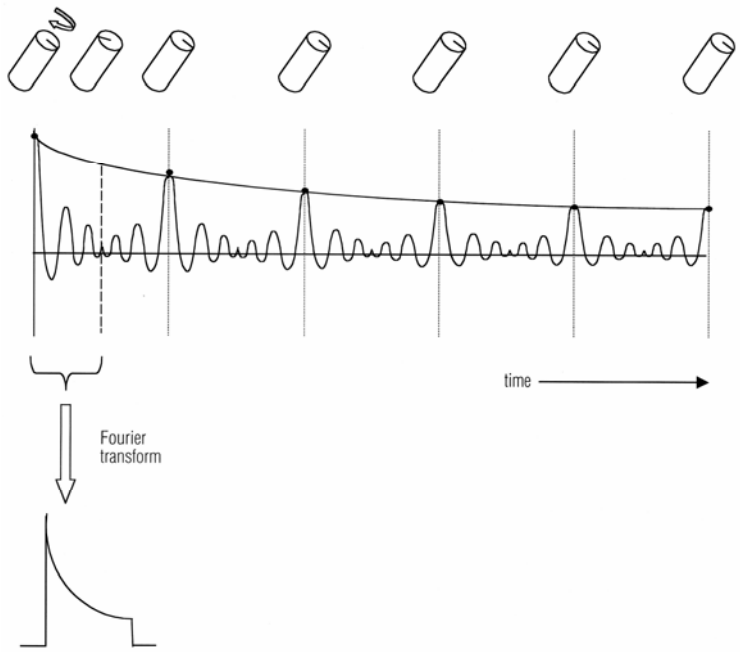

Figure 3.2: The FID shown is formed under MAS conditions. The Fourier transform of one half of a rotor cycle (as shown) gives a powder pattern that would be collected in the absence of MAS conditions. The Fourier transform of the FID maxima would result in a single line at the isotropic chemical shift. The Fourier transform of the entire FID results in a line at the isotropic chemical shift flanked by spinning sidebands (Duer, 2002 p.80).

3.1.2 Practice

In solid state NMR, the samples are presented as powders. As all possible orientations of the powder are possible, the resultant NMR spectra are very broad, as the magnetic field/nuclear spin interactions depend on the orientation of the nuclei, known as *chemical shift anisotropy*. Because of this broadness, any detail that may have been contained in the spectra will be lost and it becomes necessary to employ a variety of techniques to increase the resolution of the recorded spectra.

Magic angle spinning

Magic angle spinning (MAS) is an essential part of SSNMR. It is used to remove the effects of chemical shift anisotropy, narrow lines from quadrupolar nuclei and to remove hetero- and homonuclear dipolar-coupling effects.

In a liquid, molecular motion eliminates any chemical shift anisotropy as the molecular orientation is averaged with respect to the applied field **B**. To mimic molecular motion with solids, MAS is used. Figure 3.3 shows an experimental MAS setup.

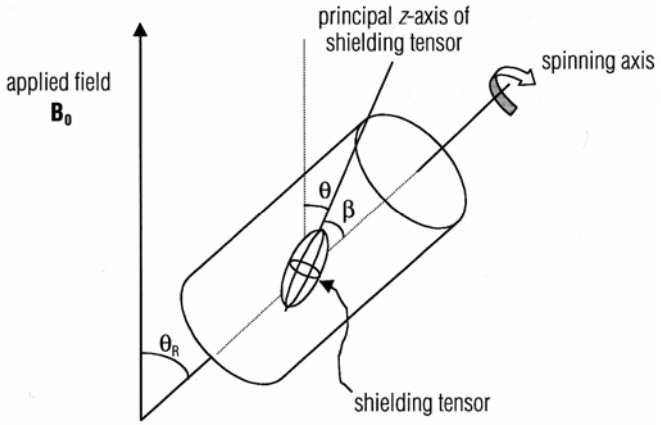

Figure 3.3: The magic-angle spinning experiment. The sample is spun about a spinning axis oriented at 54.74° to the applied field (Duer, 2002 p. 74)

If the sample is spun about an axis inclined to the applied field, θ_R, then the angle describing the orientation of the interaction tensor of the sample varies as the sample rotates. The average of the tensor orientation ($3\cos^2\theta$ - 1) can be expressed as follows

$$\left\langle 3\cos^2\theta - 1 \right\rangle = \frac{1}{2}\left(3\cos^2\theta_R - 1\right)\left(3\cos^2\beta - 1\right) \qquad \textbf{Equation 3.7}$$

The values of θ and β are fixed for any given rigid solid, but in a powder sample, they are able to take on all orientations. The angle θ_R is under the control of the experimenter. If the sample is spun at an angle of 54.74°, then the average of ($3\cos^2\theta$ – 1) will be zero. Therefore, if the rate of spin is fast enough such that the motion of the sample mimics that of molecular motion in liquids, then the chemical shift anisotropy will be averaged out.

One disadvantage of MAS is the presence of spinning side-bands (SSs). The SSs are sharp lines that appear in the spectrum at distances from the central peak according to the spinning speed. When the spectrum is represented in the frequency domain, the SSs appear at distances away from

the central peak set by the spinning speed. SSs can be used to determine details of the anisotropic interactions that are being averaged out, but can also obscure other signals that may be present in the spectrum. The SSs can be removed simply by spinning the sample faster. If this is not possible, one method of suppressing SSs is to collect data from the FID in time with the rotation of the sample. This technique is not used often, as it restricts the spectral width of the data collected.

Cross polarisation

Cross polarisation (CP) is utilised in SSNMR to perform "spectral editing" to obtain information on spins that are close together in space. In a cross polarisation experiment, the nucleus X derives its magnetisation from an abundant network of nearby spins, assumed to be ^{1}H in this instance. Two rf pulses are used to excite both types of nuclei. The amplitudes of these pulses must be set to the Hartmann-Hahn matching condition (Duer, 2002)

$$\gamma_{\mathrm{H}} B_1\left(^{1}\mathrm{H}\right) = \gamma_{\mathrm{X}} B_1\left(\mathrm{X}\right) \qquad \textbf{Equation 3.8}$$

The matching condition sets the energy gaps between the spin states of ^{1}H and X to be equal, and allows and energy input for a ^{1}H transition to also induce an opposite transition in X.

Data representation

Data are collected from the FID in the time domain and averaged over many cycles to increase the accuracy of the data. The final data set is then fourier transformed to the frequency domain and the frequencies of lines measured in the unknowns are compared relative to a specific line in a standard, as absolute frequency units are not used when reporting the results of an NMR experiment. The line positions are quoted as "parts per million chemical shifts with respect to (substance)". Commonly used standards are sodium chloride for sodium, aluminium nitrate for aluminium and tetramethylsilane (TMS) for silicon. This method ensures comparability between results from different laboratories.

3.1.3 Spectral details

In the interpretation of NMR spectra, the chemical shift, line height and width are the all-important factors.

Chemical shift

The electrons surrounding the nuclei also react to $\mathbf{B}_0$ by producing a secondary field, which also contributes to the total field experienced by the nucleus and has the potential to shift the nuclei's resonant frequency. The interaction of the secondary field produced by the electrons is called the *shielding interaction*. The frequency shift caused by the shielding interaction in an NMR spectrum is called the *chemical shift* (Duer, 2002).

The chemical shift (δ) is measured relative to a specific line in a reference spectrum, and is reported as the "chemical shift with respect to that reference". Values of chemical shift are given in parts per million shift from the reference. These shifts are generally indicative of a particular type of chemical environment surrounding the nuclei in question. Figure 3.4 shows the chemical shifts exhibited by silicon in an aluminosilicate environment.

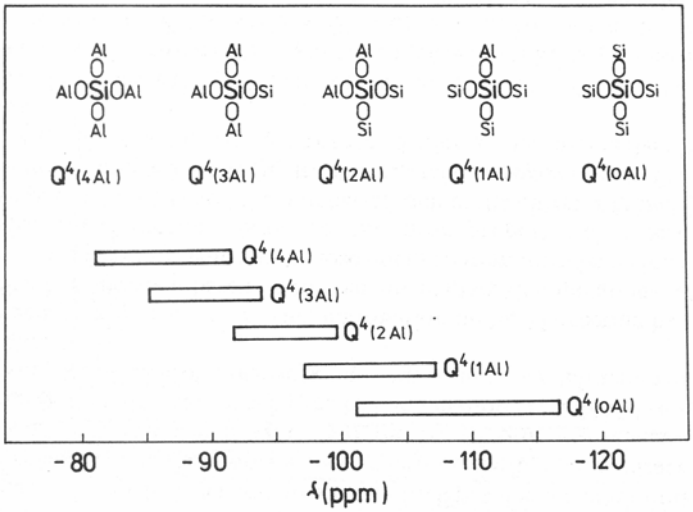

Figure 3.4: Depiction of the range of chemical shifts observed due to the Si chemical environment in aluminosilicates (Engelhardt & Michel, 1987 p. 149).

Line intensity

In general, the intensities of peaks in an NMR spectrum are directly related to the concentration of that particular atomic species in the sample. Relative concentrations of the same nuclei in different chemical states can be

calculated by comparing the relative peak intensities. However, to calculate absolute concentrations requires the use of a standard sample for intensity comparison.

Linewidth

The primary cause of line broadening is a distribution of chemical shifts due to a large number of structurally different environments surrounding chemically similar nuclei. These different environments are created by distortion of bond lengths and angles, and also by variations in the local distribution of second-nearest and further neighbours. It follows that amorphous materials will have very wide linewidths, whilst crystalline materials will exhibit very narrow peaks.

3.1.4 Use of solid state nuclear magnetic resonance

SSNMR has been used to study a wide range of materials and to answer a large number of questions. These applications include such diverse areas as molecular motion in solids, determination of protein structures, structure studies of glasses and studies of polymer dynamics (Duer, 2002).

A study by Schneider, Cincotto and Panepucci (2001) looked at ^{29}Si and ^{27}Al NMR of cement materials made using blast-furnace slag. The main constituents in the slag were CaO (43 wt%), SiO_2 (34 wt%) and Al_2O_3 (13 wt%). The material was mixed with different activating solutions, including sodium and calcium silicate, and sodium hydroxide. Both ^{29}Si and ^{27}Al NMR show that there is a definite structural change upon activation, and that the change depends on the activation regime. In particular, ^{27}Al-^{1}H CPMAS NMR shows the presence of OH or water surrounding octahedrally coordinated Al.

Stebbins *et al.* (2000) used ^{27}Al NMR to study the presence of five- and six-coordinated Al in aluminosilicate glasses. The existence of five- and six-coordinated Al has implications for the liquid-state viscosity of the glass; the current assumption is that the Al in the glass is 100% Al^{IV}. The use of magnetic fields of up to 18.8 T enabled Stebbins *et al.* to resolve Al^{V} concentrations as low as 1%.

An extensive study of the structure of calcium aluminosilicate glasses was carried out by Engelhardt *et al.* (Engelhardt *et al.*, 1985). In this study, 54 glasses were investigated with ^{29}Si and ^{27}Al NMR. Analysis of the ^{29}Si NMR spectra shows that the chemical shifts and linewidths vary systematically across the compositional range. This indicates a characteristic change in the structural environment of the SiO_4 tetrahedra.

Engelhardt & Michel (1987 pp. 355-365) report on the use of ^{1}H NMR in the study of zeolites. H can be present in aluminosilicates as bridging hydroxyl groups [Si(OH)Al], terminal hydroxides (SiOH and AlOH) and H can also be associated with the charge balancing cations present in the framework. Each of these different types of H environments results in a unique chemical shift, as shown in Figure 3.5. The lineshapes associated with ^{1}H spectra are broad, and are usually measured under fast MAS conditions, or using Combined Rotation and Multiple-Pulse Spectroscopy (CRAMPS) (Engelhardt & Michel, 1987 p. 43). Use of these techniques narrows the lines and enables detailed analyses of the collected spectra.

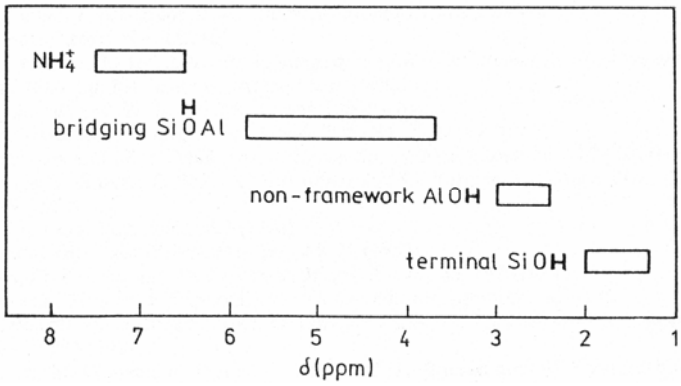

Figure 3.5: ^{1}H chemical shift ranges of protons in zeolites (Engelhardt & Michel, 1987 p. 365)

3.1.5 Q notation for the description of silicate and aluminate groups

In the description of silicate groups, the Q^n notation is adopted. In this notation, Q represents an SiO_4 tetrahedron. The superscript *n* denotes the connectivity, or the number of other Q units linked to the group. For the description of aluminate groups, the same convention is adopted, but using

q^n notation. A subscript attached to the Q denotes the number of equal Q^n species in the group in question. For aluminosilicates, the number of AlO_4 tetrahedra bound to the Q^n group is given in parentheses. $Q^n(m\text{Al})$ means an SiO_4 tetrahedron connected via oxygen bridges to *m* Al and *n-m* other Si atoms, where *n* = 0-4 and $m \leq n$ (Engelhardt & Michel, 1987). Schematic representations of the Q notations are shown in Figure 3.6.

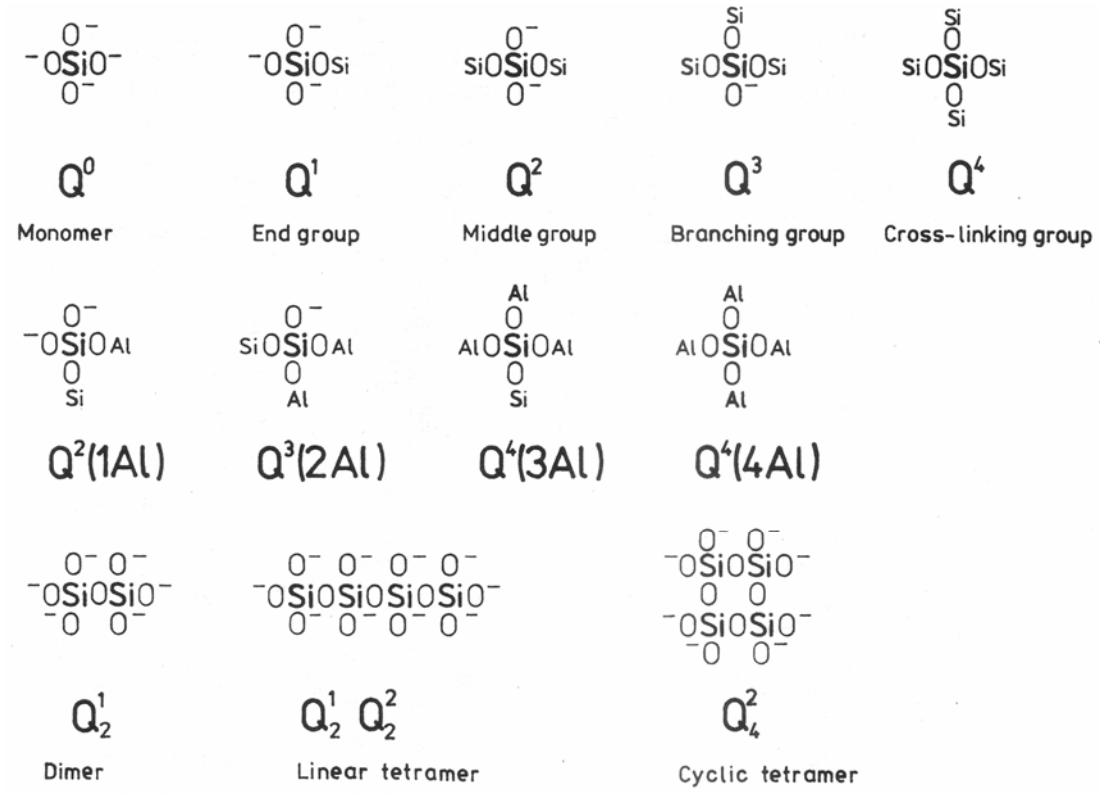

Figure 3.6: Notation for building units and silicate anions. Top line are Q^n units of silicates; centre $Q^n(m\text{Al})$ units of aluminosilicates; bottom examples of silicate anions (Engelhardt & Michel, 1987 p. 76).

3.2 Radial distribution studies

This section details the potential for the use of x-ray diffraction to be used to analyse materials that show little or no crystallinity. There is no hard and fast distinction between non-crystalline and crystalline materials, there being only a trend from one to the other as the size of the ordered domain increases. Klug and Alexander (1974 p. 791) define a crystalline material arbitrarily as a material that has three-dimensional periodicity over at least 6 unit cell translations.

James (1962 p. 526) derived a formula (Equation 3.9) which represents the average intensity distribution corresponding to a random orientation of parallelepipedal crystallites.

$$\bar{I}_0(r) = \sum_p \sum_{q}^{N-1} \sum_{-(N-1)} \sum_s (N_1 - |p|)(N_2 - |q|)(N_3 - |s|) \frac{\sin(2\pi r l_{pqs})}{2\pi r l_{pqs}} \qquad \textbf{Equation 3.9}$$

where $N_{1,2,3}$ represents the number of scattering points (atom equivalents) in the *a*, *b* and *c* directions; *p*, *q* and *s* represent the integers over which the summation is to be taken; l_{pqs} is the distance from the origin to the point (*p,q,s*) in the crystal lattice; and $r = 2\sin\theta/\lambda$. The lattice planes in the crystallite are equivalent to the (*pqs*) planes.

As the number of scattering points increases, the apparent crystallinity of the calculated diffraction pattern also increases, showing that the size of a crystallite affects the apparent crystallinity, even though the points within the crystal are constrained to a lattice. This is an example of why a crystal lattice is important in the distinction of crystalline and amorphous materials. Small crystals lack periodicity, but possess a crystal lattice, whereas amorphous materials lack both periodicity and a lattice. In Figure 3.7, the diffracted intensities from crystallites with 8, 27 and 1000 scattering points, corresponding to cubes with 2, 3 and 10 repeating units on each side, are given.

The arrangement of atoms in non-crystalline materials may show little long-range correlation, but their relative positions in space are not random. Distances of closest approach are limited by the physical size of atoms in atomic materials and correlations between atoms are formed due to interatomic potentials. These influences ensure that there is at least nearest neighbour correlation, and as such, these distances can be investigated by radial distribution studies.

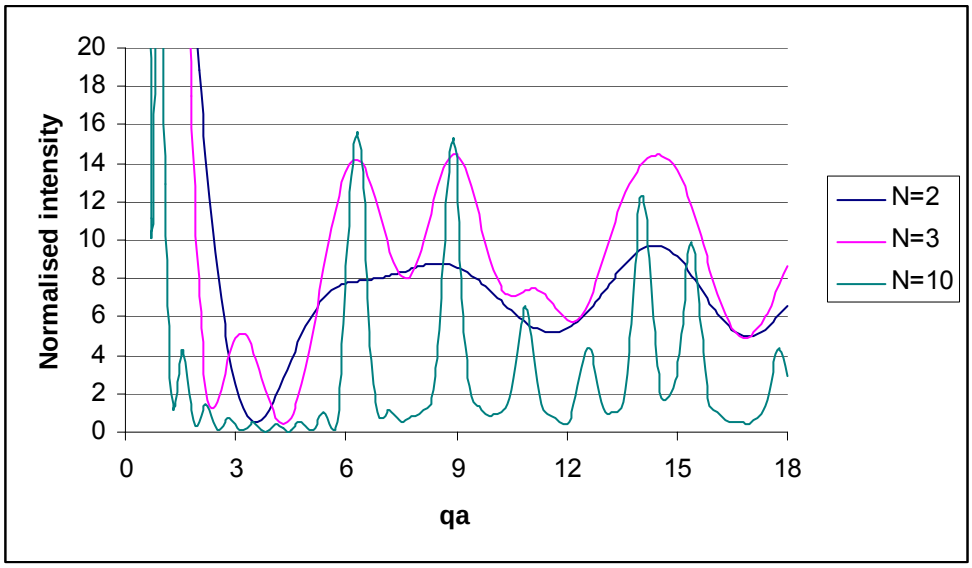

Figure 3.7: Calculated diffraction patterns for parallelepipedal crystallites as described in Equation 3.9. The diffraction patterns show that the apparent crystallinity of the crystallites increases as the number of scattering points increases, even though the patterns are calculated assuming a perfect lattice. The increase in apparent crystallinity shows that it is possible to obtain an "amorphous" diffraction pattern from a perfect crystal.

Radial distribution studies consider the distribution of bond lengths present in a material through the Fourier analysis of diffraction patterns. The features of the Radial Distribution Function (RDF) show the electron density (in the case of x-rays), and reveal the extent of ordering in the material. In glassy materials, such as vitreous silica, this ordering is negligible beyond ~7 Å. In crystalline materials, this ordering extends into the 10s of ångstroms range, and is shown in Figure 3.8. The RDF not only shows bond lengths and bond length distributions, but also allows for an estimation of long-range order and estimation of coordination numbers.

Traditionally, RDF analysis has been used for the study of non-crystalline materials, as this analysis does not require any *a priori* assumptions as to the structure of the material. Recently, there has been a trend towards analysing crystalline materials by this method. The aim in most RDF analyses is to look for alterations in the short-range order of materials that exhibit the classic sign of non-crystallinity, the "amorphous hump", in an otherwise crystalline diffraction pattern.

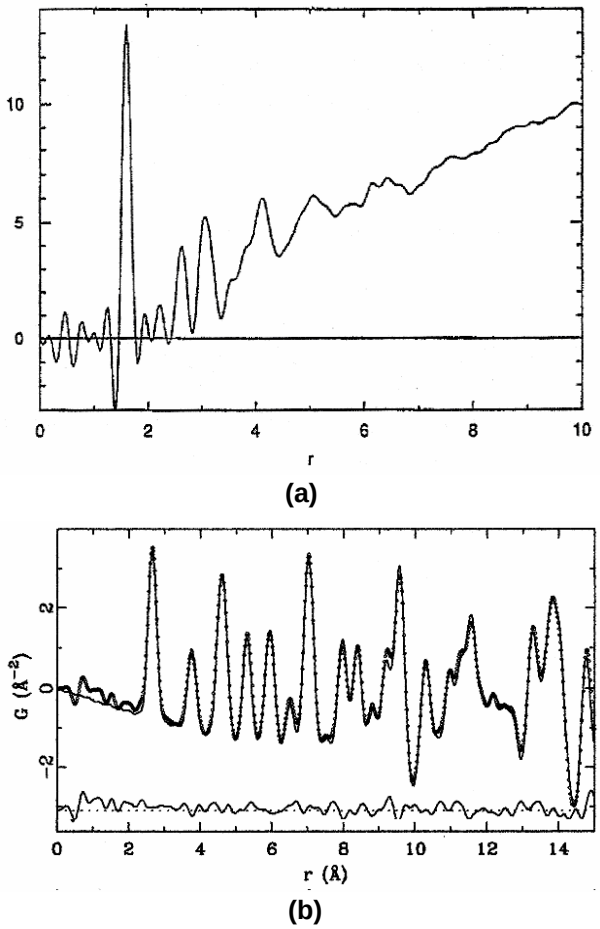

Figure 3.8: Examples of RDFs from amorphous and crystalline materials. **(a)** amorphous silica (Poulsen *et al.*, 1995). **(b)** crystalline Cu_3Au (Proffen *et al.*, 2002).

Although this section details the use of x-rays as a materials probe, neutrons and electrons can also be used in this capacity.

Neutron diffraction (ND) has a great advantage over XRD inasmuch as neutrons are able to penetrate through much thicker materials, enabling a much better sampling of the specimen than is normally possible with an x-ray beam. Coupled with their penetration power is the fact that the neutron scattering factors of the elements do not change proportionally with their atomic weights. The non-linearity of this change allows low atomic number elements, and elements that are close together in the periodic table, to be distinguished by the use of ND. One main disadvantage with the use of neutrons is the large scattering factor of H. This requires that the samples used for ND do not have any water present, as water will contribute significantly to the measured background.

Electron diffraction (ED) has the advantage that is can be used to probe the local structure of a material, whereas the usual application of x-ray diffraction only gives an average structure. The disadvantage of this technique is that most ED is carried out in a TEM, which requires the sample to be electron transparent. The production of such samples is a difficult process and can introduce artefacts into the sample.

In an ideal scattering experiment, x-rays, neutrons and electrons would be used, as they all give different information about the same system, allowing for a superior determination of the sample structure.

3.2.1 Theory

The theoretical basis for RDF, and diffraction analysis in general, was described by Debye, who showed that the coherent scattered intensity at angle θ, in electron units, from a noncrystalline array of atoms is given by

$$I = \sum_m \sum_n f_m f_n \frac{\sin(qr_{mn})}{qr_{mn}} \qquad \textbf{Equation 3.10}$$

where f_m and f_n are the atomic scattering factors of the m^{th} and n^{th} atoms, and r_{mn} is the magnitude of the vector separating the two atoms. q is given by $4\pi \sin(\theta)/\lambda$. θ is defined as the angle between the incident beam and the sample surface. The double summation is taken over all atoms in the array. RDFs can be calculated from this intensity distribution by comparison with computed models. However, to obtain an RDF without any *a priori* assumptions as to the structure of the material, the experimental intensity function is inverted by use of the *Fourier integral theorem*. In the case of a monatomic array, Equation 3.10 becomes

$$I = Nf^2 \sum_m \frac{\sin(qr_{mn})}{qr_{mn}} \qquad \textbf{Equation 3.11}$$

When the summation in Equation 3.11 is carried out, there are N terms with the value of 1 in the summation due to the interaction of the origin atom

with itself. As the value of each of these “self-interactions” is unity, Equation 3.11 can be rewritten as

$$I = Nf^2\left(1+\sum_{m`}\frac{\sin(qr_{mn})}{qr_{mn}}\right) \qquad \textbf{Equation 3.12}$$

where the summation excludes the origin atom. The summation now forms a continuous function due to the exclusion of the $\sin 0/0$ term, and can be replaced by an integral

$$I = Nf^2\left[1+\int_0^\infty 4\pi r^2\rho(r)\frac{\sin(qr)}{qr}dr\right] \qquad \textbf{Equation 3.13}$$

In Equation 3.13, $\rho(r)$ is the radially-averaged electron density at a distance r from the reference atom, and $4\pi r^2\rho(r)\,dr$ is the number of electrons contained in a spherical shell of radius r and thickness dr. In the RDF literature, $\rho(r)$ is designated the *atomic density*. Equation 3.13 can be simplified by introducing ρ_0, the *average electron density* in the sample.

$$I = Nf^2\left[1+\int_0^\infty 4\pi r^2[\rho(r)-\rho_0]\frac{\sin(qr)}{qr}dr+\int_0^\infty 4\pi r^2\rho_0\frac{\sin(qr)}{qr}dr\right] \qquad \textbf{Equation 3.14}$$

The last integral corresponds to the *central scattering*, which represents scattering that is not able to be resolved from the direct beam, and so can be ignored in the analysis. Application of the Fourier integral theorem to the simplified equation yields the *total RDF*

$$T(r) = 4\pi r^2\rho(r) = 4\pi r^2\rho_0+\frac{2r}{\pi}\int_0^\infty qi(q)\sin(rq)dq \qquad \textbf{Equation 3.15}$$

where

$$i(q) = \frac{I}{Nf^2}-1$$

The total RDF shows the variation in the *atomic density of the material* under investigation. The *reduced RDF* (RRDF), as shown in Equation 3.16, is used much more often than the total RDF.

$$g(r) = r[\rho(r) - \rho_0] = \frac{1}{2\pi^2}\int_0^\infty qi(q)\sin(rq)dq \qquad \textbf{Equation 3.16}$$

The RRDF shows only deviations of atomic density from the macroscopic average, and as such, the structural differences presented by the RRDF are much more immediately visible when viewed in this form. The difference between the two RDF representations is illustrated in Figure 3.9.

The introduction of heteroatomic materials introduces problems in the calculation of the interference function, $i(q)$. An average scattering factor for the sample, f_e, was introduced (James, 1962 p. 505) to circumvent the problem.

$$f_e = \sum f_i / \sum Z_i \qquad \textbf{Equation 3.17}$$

where f_i is the scattering factor of atom type i, and Z_i is the atomic number of atom i, and the sums are taken over a "molecular unit" or the "group of atoms under consideration" (Pings & Waser, 1968). Use of this method to calculate the scattering factors introduces errors into the RDFs, as Equation 3.17 is based on the assumption that the scattering factor of an atom can be expressed as a multiple of an "average" scattering factor. Pings & Waser (1968) described a method that permits an exact determination of the interference function for a system of n atoms.

$$i(q) = \left[\frac{I}{N} - \sum_{i=1}^{n} x_i f_i^{\,2}\right] \Big/ \left[\sum_{i=1}^{n} x_i f_i\right]^2 \qquad \textbf{Equation 3.18}$$

where the x_i are the molar fractions of the components.

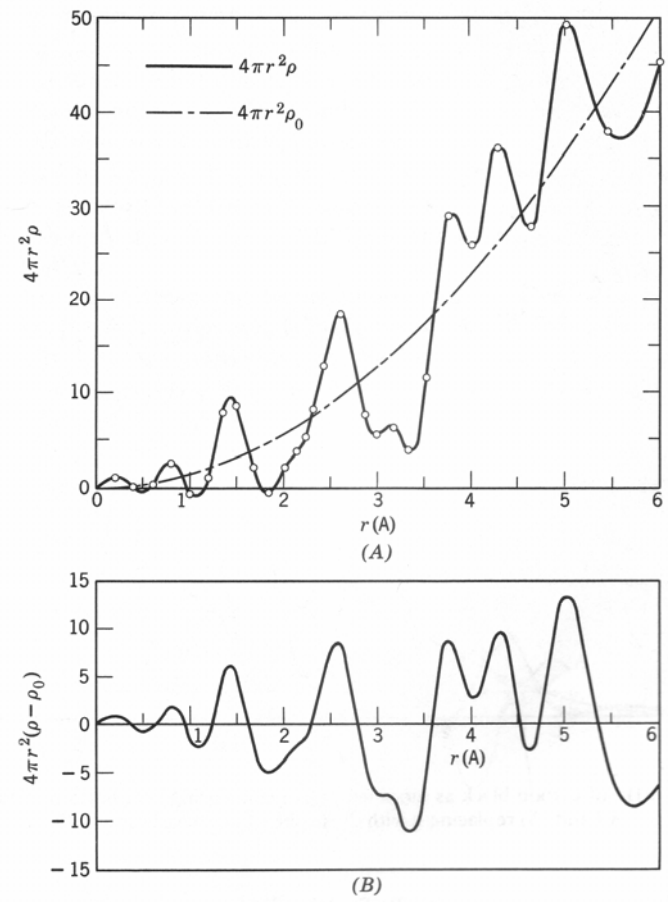

Figure 3.9: Radial distribution functions for carbon black **(a)** Total RDF. **(b)** Reduced RDF. (Klug & Alexander, 1974 p. 815).

The introduction of multiple atom types allows for the production of an RDF for each pair interaction in the material. These RDFs are known as *partial RDFs* (PRDFs). For example, in SiO_2, there are three PRDFs, $g_{Si\text{-}Si}(r)$, $g_{Si\text{-}O}(r)$ and $g_{O\text{-}O}(r)$. These PRDFs show only the atomic density variations corresponding to differences due to the two atoms involved. The examples of PRDFs given in Figure 3.10 clearly show the contribution of each atom pair to the final RDF. Peaks from the total RDF are traced through the component PRDFs, and their origins are shown.

Local structural information can be obtained by analysing the *pair distribution function* (PDF). The PDF is represented by

$$g(r) = \frac{\rho(r)}{\rho_0} \qquad \textbf{Equation 3.19}$$

and can be calculated from the RDF. The PDF, see the example in Figure 3.11, shows the deviation of the atomic density normalised to the average atomic density, whereas the RDF just shows the variation in the atomic density. As a result of the mathematical formalism, PDFs tend to 1 for large *r*, whereas RDFs tend to 0.

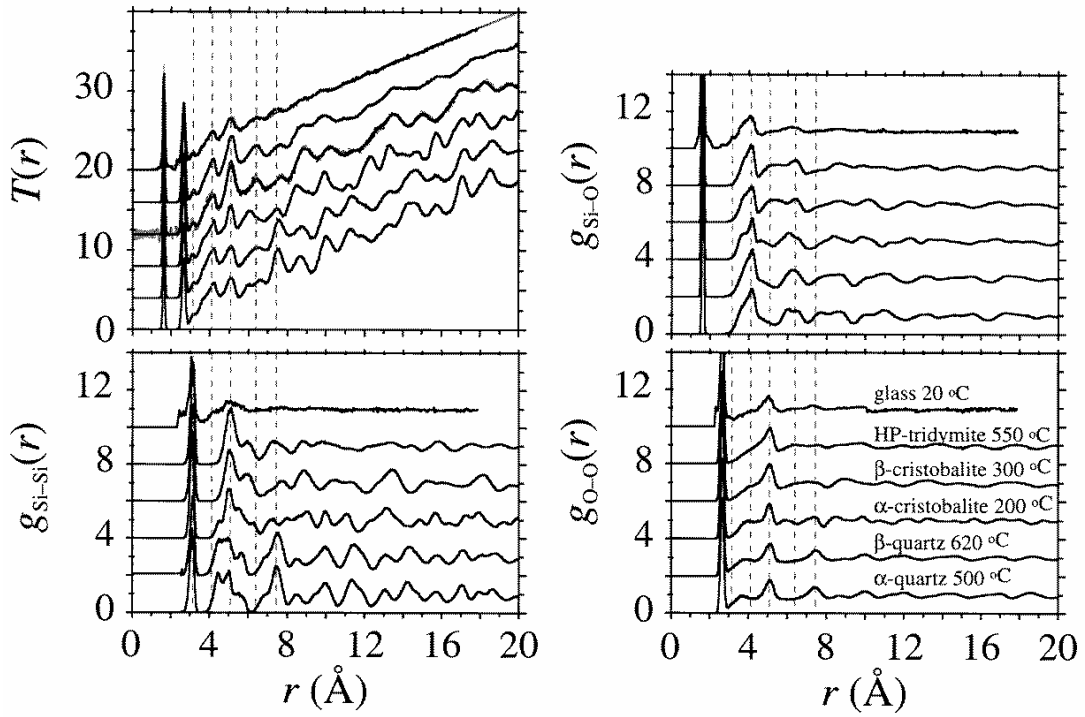

Figure 3.10: Total and partial RDFs obtained from various forms of SiO_2 by reverse monte carlo modelling (Keen & Dove, 1999).

PDFs are more useful for peak deconvolution, in order to find out the contributions of various atom pairs, as the contribution of each pair to the atomic density is additive, not differential, as in the RDFs

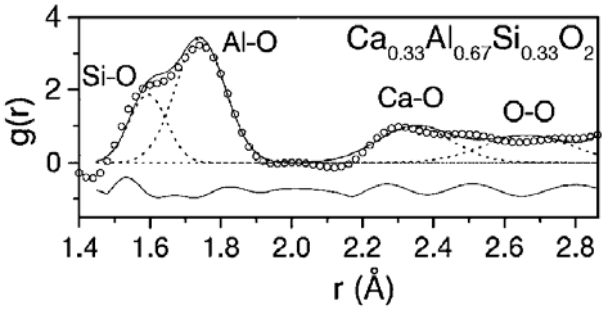

Figure 3.11: Example of a PDF. Note that the PDF tends to 1 for large *r.* RDFs tend to 0 (Petkov *et al.*, 2000).

3.2.2 Practice

The x-ray intensity scattered by an amorphous sample, $I_s(2\theta,E)$, can be represented as follows:

$$I_s(2\theta,E) = I_p(2\theta,E)\{A(2\theta,E)P(2\theta,E)[I_a(q) + I_{ms}^{elas}(q)]\} + I_p(2\theta,E')\{A(2\theta,E')P(2\theta,E')[I_{ine}(q') + I_{ms}^{ine}(q')]\} \quad \textbf{Equation 3.20}$$

where $I_p(2\theta,E)$ is the intensity of the primary beam; $A(2\theta,E)$ is the absorption; $P(2\theta,E)$ is the polarisation factor; $I_a(q)$ is the elastic scattering per atom; $I_{ine}(q')$ is the inelastic scattering per atom; $I^{elas}{}_{ms}(q)$ and $I^{ine}{}_{ms}(q')$ represent the multiple scattering of elastic and inelastic radiation per atom (Wagner, 1978).

The measured intensity must be corrected for absorption and polarisation, depending on the experimental configuration. The measured intensity must also be corrected for Compton scattering as photons that have lost energy in the scattering process do not carry information regarding the structure of the material. The Compton corrections can be done experimentally by the use of monochromators or energy-sensitive detectors in the diffracted beam, or they can be done computationally from inelastic scattering tables. Multiple scattering must also be removed, as any multiple scattering destroys the information that was carried by the diffracted beam. In most situations, it is sufficient to consider only double scattering (Wagner, 1978).

The last step in the correction process is to normalise the measured intensity from arbitrary units to the intensity scattered by one atom and expressed in electron units, known as *independent scattering*, and is shown in Figure 3.12. Independent scattering is defined as the hypothetical scattered intensity from a group of atoms when each atom scatters independently of the others, so that no interference effects are produced. The independent scattering curve is the curve that is fitted to the experimental intensity in order to give the correct normalisation constant.

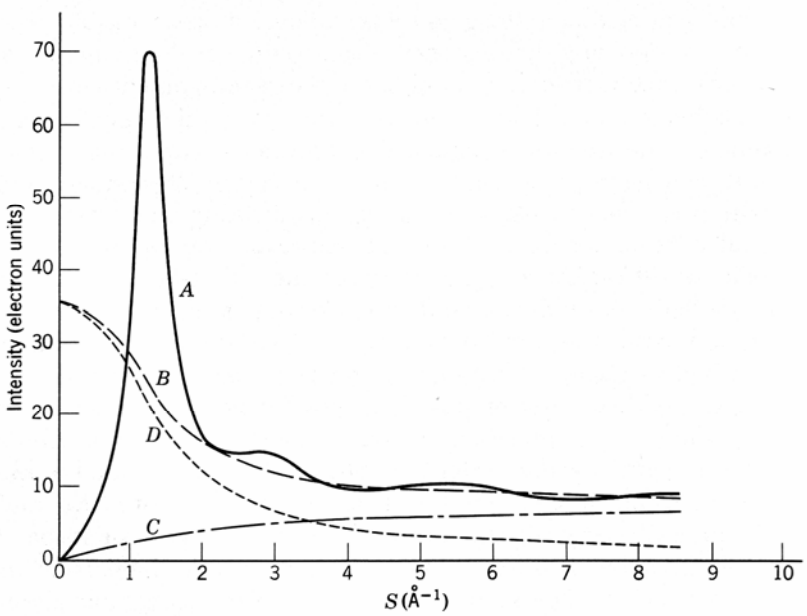

Figure 3.12: Experimental and independent scattering curves for synthetic polyisoprene. **(a)** Experimental scattering, **(b)** Total independent scattering, **(c)** Incoherent scattering, and **(d)** Independent coherent scattering. (b=c+d) (note: S≡q) (Klug & Alexander, 1974 p. 798).

The normalisation constant can be calculated directly from the scattering pattern, as the intensity of the scattered radiation tends to the average of the square of the scattering factor ($I_a(q) \rightarrow \langle f^2 \rangle$) for large q. Thus, I_s measured at high q will exhibit small oscillations about I_p. Setting $I_a(q) = \langle f^2 \rangle$ enables the calculation of a normalisation constant to convert the intensity measured in arbitrary units into an intensity expressed in electron units, scattering by one electron. The high-angle normalisation constant is given by

$$\beta = \int_{q_{min}}^{q_{max}} \left[\left\langle f^2(q) \right\rangle + I_{ine}(q) + I_{ms}(q) \right] dq \Big/ \int_{q_{min}}^{q_{max}} I_s(q) dq \left[A(2\theta) P(2\theta) \right]^{-1} \qquad \textbf{Equation 3.21}$$

where q_{min} and q_{max} are the values of q between which data were collected (Wagner, 1978). This corrected intensity is then Fourier transformed to calculate the RDF. When the RDF is calculated, various errors due to incorrect normalisation and scattering factors and termination effects will manifest themselves. The manner of their manifestation is discussed by Kaplow *et al.* (1965) and outlined in the following discussion.

Scattering factors

The scattering factors used in the calculation of the RDF are all-important. A scattering factor (*f*) is a measure of the amplitude scattered by an atom when radiation of a given amplitude falls upon it (James, 1962 p. 93). For incident radiation of a frequency that is large compared to the atomic absorption frequencies, the scattering factor approaches *Z*, the total number of electrons in the atom, for small angles of scattering.

The scattering factor for an atom depends on the radial charge-density distribution, U(*r*), inside that atom. U(*r*) can be calculated by classical, quantum or numerical means. Once U(*r*) is known, the scattering factor can be determined by the evaluation of the integral

$$f = \int_0^\infty U(r)\frac{\sin(qr)}{qr}dr \qquad \textbf{Equation 3.22}$$

provided that the $\sin\theta/\lambda$ dependence of the scattering factor is not taken outside the validity range of theory under which it was developed.

The scattering factors for most elements are well known for small values of *q* (Cromer & Mann, 1968; Waasmaier & Kirfel, 1995), however, RDF analysis requires diffraction information collected to large values of *q*, typically 20-50 $Å^{-1}$. These high values mean that care must be taken to choose scattering factors developed with theories that are able to reliably calculate the factors to high *q* values.

Compton scattering

Compton scattering, also known as inelastic, incoherent or modified scattering, occurs when the electron with which the x-ray is interacting, recoils and absorbs some of the energy of the x-ray (Klug & Alexander, 1974 p. 99). The change in the energy of the x-ray destroys any structural information that it may have otherwise contained. The energy shift of the x-ray is well defined according to

$$\Delta\lambda = \frac{h}{mc}\left(1-\cos 2\theta\right)$$ **Equation 3.23**

where *h* is Planck's constant, *c* is the speed of light and *m* is the mass of an electron. The intensity of the Compton radiation increases with increasing angle, as stated in Equation 3.24, which can swamp the elastic signal completely, and must be taken into account in any data analysis. Values for the intensity of the Compton scattering can be taken from tables (e.g. MacGillavary & Rieck, 1968 pp. 250-251), which are usually calculated from first principles (e.g. Cromer & Mann, 1967), or the intensities can be calculated from by semi-empirical means (e.g. Thijsse, 1984). The semi-empirical means are based on first-principles calculations, but allow for a much faster determination of the Compton intensity. The empirical formula proposed by Thijsse (1984), based on the work of Cromer & Mann (1967), gives the Compton scattered intensity per atom as follows

$$I_a^{compt}(q) = \left(\frac{\lambda}{\lambda'}\right)^2 \sum_{j=1}^{n} c_j Z_j \frac{\left(b_j q\right)^{a_j}}{1+\left(b_j q\right)^{a_j}}$$ **Equation 3.24**

where *n* is the number of atomic species, Z_j the atomic weight of species *j*, and a_j and b_j being semi-empirical expressions given by

$$a_j = \frac{2.6917}{Z_j} + 1.2450$$

$$b_j = \frac{1.1870}{Z_j} + 0.1075 + 0.00436 Z_j - \left(0.01543 Z_j\right)^2 + \left(0.01422 Z_j\right)^3$$

The corrections for Compton scattering can be reduced by excluding Compton scattering experimentally by using either an energy sensitive detector, or a monochromator in the diffracted beam. Depending on the detector resolution, Compton scatter at high angles should be completely discriminated. However, Compton scatter in the mid-range will only be partially discriminated, necessitating the calculation of a band-pass function

that denotes the fraction of Compton scatter passed by the medium. The method most commonly used is the Ruland method (Ruland, 1964). The band-pass of the medium is calculated, in the first instance, by a comparison of the intensities collected both with, and without the medium. This first estimate can be then further refined to decrease any errors being propagated through the RDF calculations.

Multiple scattering

When x-rays are scattered by a material, the majority of the scattered intensity is due to single scattering of the primary beam. There is also a contribution to the scattered intensity arising from the scattered beam being scattered a second time. As well as this double scattering, higher orders of scattering also occur, however, double scattering represents the majority of multiple scattering, and for most cases, correcting only for double scattering is sufficient (Warren & Mozzi, 1966; Wagner, 1978).

The double scattering ratio (Dwiggins Jr. & Park, 1971; Warren & Mozzi, 1966), the ratio of double scattered intensity to single scattered intensity, is given by

$$\frac{I_{ds}}{I_{ss}} = \frac{B^2 Q_M\left(2\theta, a, b, \mu t\right)}{J\left(2\theta\right)\sum_{i=1}^{n} A_i \mu_i\left(m\right)} \qquad \textbf{Equation 3.25}$$

where $B = \sum_i Z_i^2$ and A_i, $\mu_i(m)$ are the atomic weights and mass absorption coefficients of the atoms. $J(2\theta)$ is an approximate representation of independent scattering according to Equation 3.26

$$J\left(2\theta\right) = B\left(a + \frac{1-a}{1+b\sin^2\left(\theta\right)}\right) \qquad \textbf{Equation 3.26}$$

where a and b are parameters that can be obtained by fitting $J(2\theta)$ to $\sum_i f_i^2$. Q_M is a function depending on the scattering angle, μt, a and b, and the

experimental geometry. The details of these formulae can be found in Dwiggins & Park (1971).

Background corrections

Air scatter can contribute significantly to the measured background. Other background contributions come from sample fluorescence and detector noise. Air scatter corrections can be done computationally, but may also be accomplished easily by experimental means. When collecting diffraction information under ambient conditions, air scatter will form a small, but significant, part of the measured intensity at mid to high angles, whereas air scatter at low angles contributes to the majority of the scattered intensity. The contribution of air scatter to the measured intensity can be reduced by collecting the diffraction information in a vacuum, or in a helium (for example) atmosphere. In experiments conducted for the current study, enclosing approximately 5 cm of diffracted beam path length resulted in a complete loss in air scatter above 4° 2θ.

The contribution of sample fluorescence to the background intensity can be minimised by selecting an incident wavelength that is away from the absorption edges of the elements contained in the sample. Unlike air scatter, fluorescence contributes noise evenly across all scattering angles.

RDF calculation errors

The errors that can produce significant changes in a calculated RDF are normalisation errors, scattering factor errors and termination errors. A study of these errors was carried out by Kaplow *et al.* (1965). The influences of each error were investigated by comparing differences in the RDFs after altering the interference function. The general forms of these errors are shown in Figure 3.13.

It was found that for a given error in the normalisation constant β, the corresponding error in $i(q)$ is of the form:

$$\Delta i(q) = \frac{\Delta\beta}{\beta} q i(q) + \frac{\Delta\beta}{\beta} q \qquad \textbf{Equation 3.27}$$

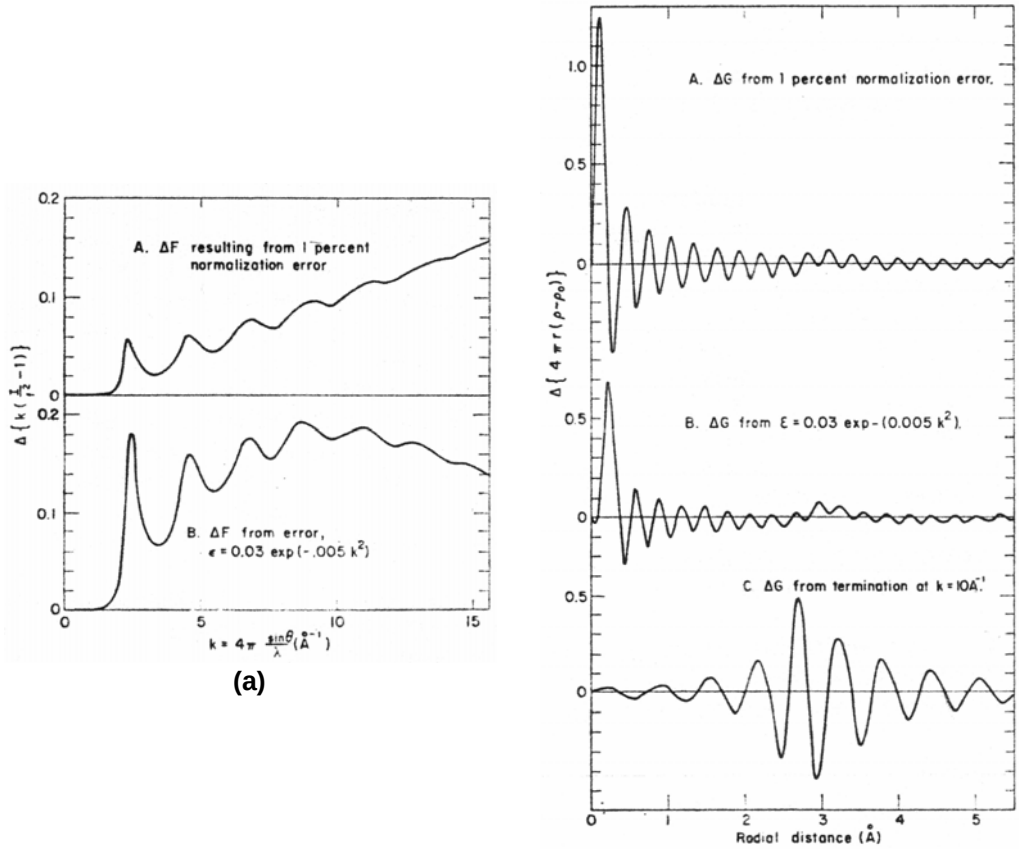

Figure 3.13: Variations resulting from induced errors in the RDF calculation process. **(a)** Variations induced in the interference function by errors in (A) normalisation and (B) scattering factors. **(b)** Variations induced in the RDF by errors in (A) normalisation, (B) scattering factors and (C) termination effects (Kaplow, Strong & Averbach, 1965).

The RDF resulting from an incorrect normalisation constant has a sinusoid with large amplitude at small *r*, and decreasing quickly as *r* increases superimposed on the "correct" RDF. The error in the RDF can be expressed as follows:

$$\Delta G = \frac{\Delta\beta}{\beta}\left[\frac{\sin(q_{\max} r)}{r^2} - \frac{q_{\max}\cos(q_{\max} r)}{r}\right] \qquad \textbf{Equation 3.28}$$

where $q_{\max}$ is the maximum value of q used in the transform. This superposition can mask structural details, and can suggest detail that is spurious.

Kaplow *et al.* found it probable that the errors in the scattering factors have the form $\Delta\left(I/f^2\right)=\left(I/f^2\right)\varepsilon$ where ε is a function of q. The corresponding error in $i(q)$ can be expressed as:

$$\Delta i(q) = \varepsilon q\, i(q) + \varepsilon q \qquad \textbf{Equation 3.29}$$

The form of the error in the calculated RDF is of a similar form to that of the normalisation error. This error is also characterised by large peaks at small r. This error can be differentiated from a normalisation error by inspection of the interference function. In the case of a scattering factor error, the interference function exhibits a large hump in the mid-q range.

Termination errors, or ripples, arise from the finite nature of the diffraction information, as the Fourier analysis used in calculating the RDF ideally requires data from $q = 0\ldots\infty$. Diffraction information below q_{min} can be extrapolated to zero (Petkov, 1989), however, there isn't a simple method to "add" data above q_{max}. The form the termination error takes is an oscillation with an approximate period of $2\pi/q_{\max}$ constrained by a smooth envelope with a maximum amplitude in the vicinity of the first peak. The influence of the termination ripples can be minimised by the inclusion of an exponential smoothing term in the calculation of the RDF.

$$g(r) = \frac{1}{2\pi^2}\int_{q_{\min}}^{q_{\max}} q i(q)\sin(qr)\exp\left(-bq^2\right)dq \qquad \textbf{Equation 3.30}$$

Care must be taken in the choice of b, as an overly large value will remove real information from the RDF.

RDF resolution

Due to the discrete nature of the information contained in the scattering patterns, the resolution of the RDF derived from that pattern is dependent on the q_{max} value of the data. The resolution limit of the RDF arises from the finite nature of the scattering data, and is given by

$$\Delta r = 2\pi / q_{\max}$$ **Equation 3.31**

where Δr denotes the smallest distance able to be resolved in the RDF and q_{max} is the maximum value of q used in the transformation (Cartwright, 1990 pp. 205-206).

3.2.3 Structural models

The calculation of an RDF relies on Fourier transforms, converting diffraction information in reciprocal space to atom correlations, or bond lengths, in real space. The information presented in an RDF is a one-dimensional representation of the three-dimensional structure in the material being analysed. This reduction of information contained in the RDF makes it difficult to obtain pertinent structural models by diffraction methods alone.

To calculate structural models, an RDF is required for each atom pair in the material (McGreevy & Pusztai, 1988). In effect, the model is constructed of several PRDFs. For a monatomic solid, liquid or gas, this requirement is met by default, as there is only one type of atom present in the material. For a diatomic material, 3 different diffraction patterns are required to produce three PRDFs, as there are three different atom pairs present (eg SiO_2 → Si-Si, Si-O and O-O). Three atomic species necessitate 6 diffraction experiments, whilst four require 10. This large increase in the required number of independent diffraction patterns makes it unreasonable to rely upon diffraction information alone when trying to determine a structural model. Additional information can be obtained from alternative techniques such as NMR and XPS, which give information on local coordination, and can therefore be used as constraints on the choice of structural model.

Reverse Monte Carlo (RMC) modelling (McGreevy & Pusztai, 1988) is a method that is utilised for the calculation of structural models. In this method, an array of N points is generated, and periodic boundary conditions are applied and an RDF is generated. The periodic boundary conditions act as “mirrors”, reflecting the initial array to form a superarray of a much larger size, with little increase in the use of computing power. The array of points

may be a random array, or may be arranged in a lattice. The RDF is then compared with the experimentally determined RDF. A point in the array is then moved, and the new RDF calculated and compared using a standard chi-squared test. If the correlation is increased, then the move is accepted. If the correlation is decreased, then the move is either accepted or rejected with a probability that follows a normal distribution. The new array then becomes the start array and the process is repeated until the value of chi-squared decreases to an equilibrium value.

The RMC method of structural modelling produces a structure that is consistent with the experimentally measured data; however, it is not necessarily a unique solution. The validity of the calculated structures can be increased by the use of additional experimental data such as coordination and bond lengths. The coordination of the atoms can be constrained, so that any moves that alter the coordination are rejected. Also, unreasonable bond lengths can also be excluded from the model. Even though the calculated structure may not be unique, insight into the structure of a material can be gained by comparison of different, but consistent, structural solutions to diffraction information.

RMC modelling has been used to examine the structures of several amorphous materials. These include silica (Dove *et al.*, 1997) and cation clustering in potassium silicates (McGreevy & Zetterström, 2001) and show that RMC can be useful in the study of amorphous materials. One study on cation clustering in potassium silicates (McGreevy & Zetterström, 2001) showed that the K ions tend to cluster in the silicate structure, and, in doing so, provide independent confirmation of conduction pathways in K silicates.

3.2.4 Utilising radial distribution functions

RDFs have been used to study a large range of materials. Some examples of the systems that have been studied include vitreous selenium and silica (Kaplow, Rowe & Averbach, 1968; Mozzi & Warren, 1969); calcium and samarium aluminosilicates (Petkov *et al.*, 2000; Jin *et al.*, 2000); InGaAs semiconductors (Jeong *et al.*, 2000) and intermetallics such as

Cu_3Au and RE_3Al_4 (Proffen *et al.*, 2002; Petkov, Apostolov & Skumryev, 1989).

The presence of non-bridging oxygens (NBOs) in calcium aluminosilicate ($Ca_{x/2}Al_xSi_{1-x}O_2$) glasses has been studied using RDFs (Petkov *et al.*, 2000). The presence of NBOs affects the thermodynamics of the glass and other properties, such as melt viscosity. The study by Petkov *et al.* used high energy x-rays (80.6 keV) to produce RDFs that resolved the Si-O and Al-O bonds lengths of 1.60 and 1.75 Å respectively, and allowed the study of the Si-O and Al-O coordination. The results from this study show that at small Ca concentrations (x=0, 0.25), the network consists of 4-coordinate Si and Al. As the Ca level increases to 0.67, the number of NBOs increases, making the average Si-O coordination number as low as 3.2. Concurrent with this decrease in Si coordination, the Al-O coordination remains steady at 4, which suggests that the tetrahedral network breaks down as a result of the formation of Si-O-Ca bonds.

The use of RDFs is not limited to amorphous materials. RDFs have been used to help differentiate structural models for technologically important materials such as InGaAs semiconductors (Jeong *et al.*, 2000). Previous tests of structural models have relied on x-ray absorption fine structure (XAFS), which can only give information on nearest- and next nearest-neighbour distances, whereas RDFs can give this information, plus far-neighbour distances and bond length distributions. From the structural information gained from the RDFs, a supercell model based on the Kirkwood potential was constructed and probability distributions were constructed for the constituent atoms. These distributions showed that As atom displacements are highly directional, and can be described as a combination of <100> and <110> displacements, in contrast to the In and Ga distributions, which are much more isotropic.

An RDF study of rare-earth (RE) intermetallics (Petkov, Apostolov & Skumryev, 1989) obtained RE-RE distances and proposed a structural model for four (Pr, Gd, Tb, Dy) RE metallic glasses. The model proposed was a

non-crystalline structure based on random dense hard-sphere packing with a high degree of tetrahedrality. This structure suggests that RE_4Al_3 glasses are an assembly of tetrahedral units.

3.3 Other techniques

This section briefly reviews other techniques that can be used to study bonding configurations in materials

3.3.1 X-ray absorption spectroscopy

X-ray absorption spectroscopy (XAS) measures how x-rays are absorbed by an atom at energies near and above the core-level binding energies of that atom. XAS spectra are especially sensitive to the formal oxidation state, coordination chemistry, and the distances, coordination number and species of the atoms immediately surrounding the selected element. XAS is divided into two broad disciplines, x-ray absorption near-edge spectroscopy (XANES) and extended x-ray absorption fine-structure spectroscopy (EXAFS). XANES and EXAFS have the same physical origin; this distinction is applied to allow for differences in interpretation. XANES is strongly sensitive to formal oxidation state and coordination chemistry of the absorbing atom, while EXAFS is used to determine the bond distances, coordination number, and species of the neighbours of the absorbing atom.

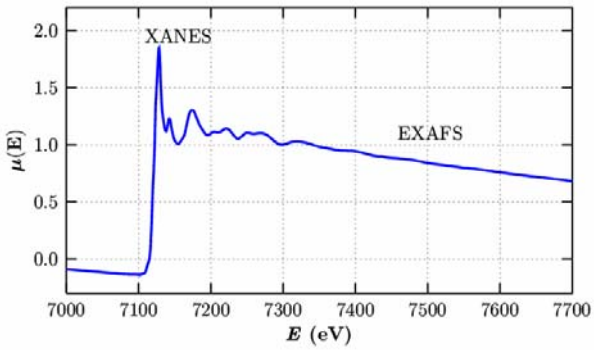

Figure 3.14: XAS measurement of FeO with the XANES and EXAFS regions marked (Newville, 2004).

In an XAS experiment, a tuneable source of x-rays is required. The x-rays are sent through the sample and the intensity measured as a function of wavelength. As the energy of the incident photons crosses the absorption

edge of the element under scrutiny, the transmitted intensity changes drastically. Superimposed on this large change are small aberrations that are dependent on the coordination, oxidation state and nearest neighbours. XANES deals with the modulations near the absorption edge, whilst EXAFS looks at the change in the absorption well past the edge (>30 eV). An example of an XAFS spectrum is given in Figure 3.14.

XAS would be useful in the measurement of AIP, as it would help determine the location of the charge balancing cations. Also, microXAS would be able to be used to study the variation in the coordination states of the constituent elements between the different phases present in the sample. Where NMR gives an average of the coordination of the elements, microXAS could give spatial information with regards to the different coordination states of the elements present.

3.3.2 X-ray photoelectron spectroscopy

X-ray photoelectron spectroscopy (XPS) is the study of electrons that are ejected from the surface of a material under x-ray bombardment. This is a surface-sensitive technique that allows for the determination of the elemental species and their binding states.

In this technique, a focussed monochromatic beam of soft x-rays is made incident on the surface of the sample under analysis. This technique is carried out under a high vacuum. The x-ray energies used are typically 0.2-2 keV. As the energy of the ejected photoelectrons is so low, this technique is restricted to surface analysis due to the limited mean free path of the electrons. The x-ray photons knock out electrons from the inner shells of the atoms in the sample. The kinetic energy of the ejected photoelectrons is given by

$$E_K = E_p - E_b$$

where E_p is the photon energy and E_b is the binding energy of the electron. This energy is dependent on the elemental species and oxidation state.

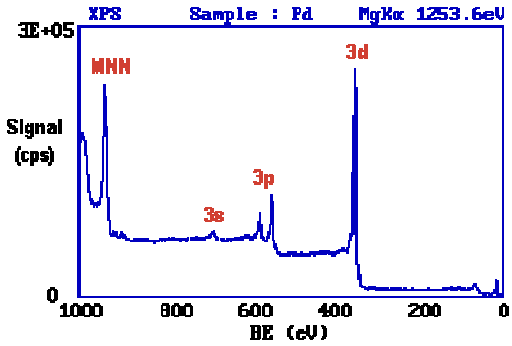

Figure 3.15: XPS spectrum of palladium metal. The abscissa is the binding energy of the photoelectrons. Emissions relating to the 3s, p and d orbitals are labelled at 673, 534/561 and 335 eV. The peak labelled "MNN" is an Auger emission (Nix, 1996).

For each element, there will be a characteristic binding energy associated with each core atomic orbital. This gives rise to a characteristic set of peaks in the photoelectron spectrum at kinetic energies determined by the photon energy and the respective binding energies. The presence of peaks at particular energies indicates the presence of a specific element in the sample under study. In addition to this, the intensity of the peaks is related to the concentration of the element within the sampled region. An example of an XPS spectrum is given in Figure 3.15. The position of the peaks is shifted due to chemical interactions. A change in the oxidation state of the atom alters the coulombic interaction with the electron shells and the photoelectron, which affects the energy of the ejected electron and is detected as a chemical shift, shown in Figure 3.16. This is a particularly sensitive technique, and is fairly easy to interpret, as it is a one-electron process.

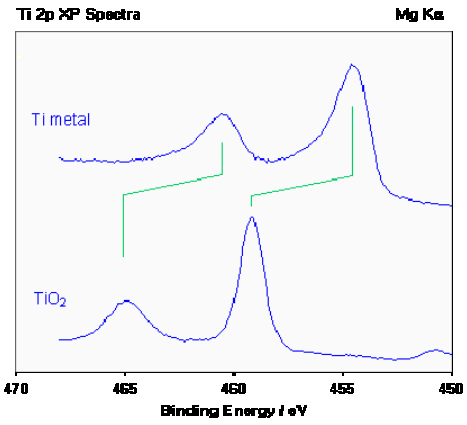

Figure 3.16: Ti XPS spectra of Ti in different oxidation states. This figure shows the difference in the peak position due to chemical shift (Nix, 1996).

Use of this technique in the analysis of AIPs would help to find the location of any hydroxide or other groups, such as Na^+, bonding to the polymer network. XPS would enable the determination of the role of hydroxides and bonding and non-bonding oxygens on the formation of the polymer network.

3.3.3 Electron energy-loss spectroscopy

Electron energy loss spectroscopy (EELS) refers to the energy loss of an incident electron beam onto a sample. An example of the spectra collected is given in Figure 3.17. When an electron beam is incident on a sample, some of the electrons in the transmitted beam will be inelastically scattered by the atoms in the sample. By studying the intensity of the electron beam as a function of energy loss, the elemental composition and atomic bonding state can be determined. EELS has an advantage over other techniques inasmuch as the volume from which the signal is generated is very small which allows for the investigation of composition and bonding state in the sample on a local scale. EELS is also able to distinguish between different allotropes due to changes in the fine structure of the spectrum.

Scanning TEM has allowed this technique to be used for elemental phase mapping. The energy loss of the incident electron beam is overlaid on an image of the sample, and the different elements or phases present in the sample are shown. This gives a spatial layout of the elements present in the sample.

EELS requires electron-transparent samples, as this is a transmission technique. In addition to this, the samples must also be able to withstand the high vacuum environment required for electron imaging.

Use of this technique in the analysis of AIPs would help to determine to valency state of the elements in the AIP, which would help in the identification of the role of Na in the formation of the polymer network.

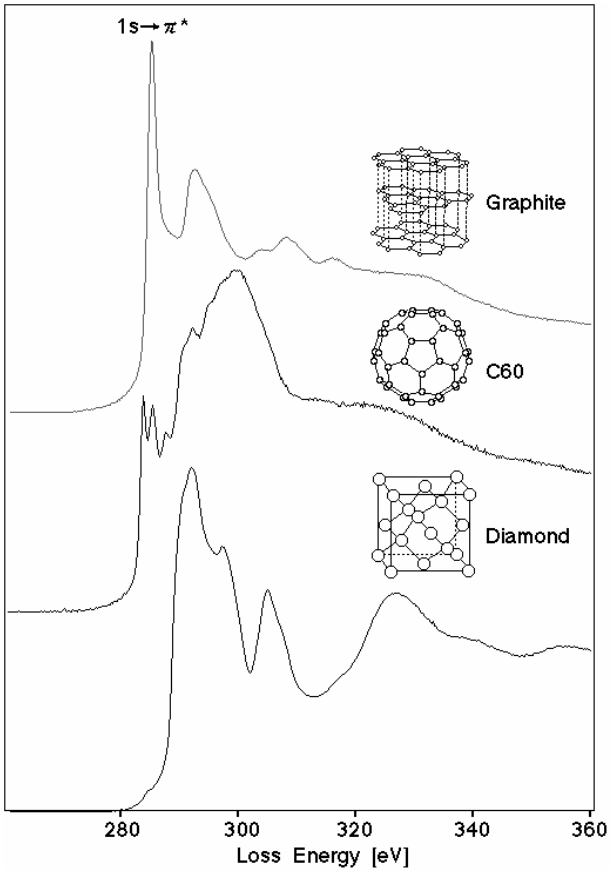

Figure 3.17: Examples of EELS spectra from different allotropes of carbon (Institute for Chemical Research).

3.4 Experimental technique overview with reference to aluminosilicate inorganic polymer bonding characterisation

All of the techniques reviewed in this chapter are able to reveal information about the bonding character of AIPs.

RDF analysis will give the bond distances present in the AIPs directly, and allows coordination and bond angles to be calculated, given sufficient RDF resolution. NMR can give the coordination states of the atoms present in the AIPs, and also allows for the calculation of bond distances and angles. The RDF technique is an averaging technique, and as such, 3D information is lost in the process. NMR can only be used on atomic species that have a nuclear spin. For AIPs, isotopes of Si, Al, Na and O all have nuclear spins. The isotopes and their abundances are ^{29}Si (4.7%), ^{27}Al (100%), ^{23}Na (100%) and ^{17}O (0.038%). X-ray analysis is isotope independent. NMR can also be used to elucidate the role of non-structural atoms, such as H. Use of ^{1}H NMR

is able to show how H, OH or other species containing H, interact with the AIP network.

XPS and EELS are both high vacuum experiments. They both require extremely clean samples, and EELS needs electron transparent samples. Both of these techniques will give information as to the elemental composition of the AIPs and the oxidation states in which the constituent elements are. The elemental composition and coordination chemistry of the AIPs can also be shown by XAS techniques.

All of these techniques are very capable in revealing elemental and atomic information relevant to the determination of the structural properties of AIPs. The use of any one of these techniques is governed by the fine detail that can be exposed in a better way by a particular method. As is always the case, it is much better to utilise multiple techniques than to rely on just a single method.

4.0 EXPERIMENTAL DETAILS

This chapter gives a detailed account of the experimental procedures used in the course of the current study. The descriptions are designed to give the reader the opportunity to recreate the work carried out in the course of the project.

4.1 Experimental design

The experiments were designed to meet the objectives given in §1.2. The principal aspects of the experimental design were:

1) Selection of AIP production method,
2) Choice of composition range of AIPs to be studied,
3) Use of mechanical testing for macro property testing,
4) Use of microscopy for the investigation of microstructure, and
5) Use of nuclear magnetic resonance and x-ray scattering for nanoscale investigation.

4.1.1 Aluminosilicate inorganic polymer production method

The preparation of AIP precursor materials by various methods was considered, notably sol-gel (Sinkó & Mezei, 1998), melt-quench (Hos, McCormick & Byrne, 2002) and the use of natural minerals (Rahier *et al.*, 1996). Sol-gel allows for the synthesis of relatively pure aluminosilicate precursor materials, but this production method has large material costs and a specialised working environment is required. Melt-quench allows for a tailoring of precursor composition with much less cost than sol-gel, but this method requires high temperatures to melt the powders and requires special care during preparation to ensure sample homogeneity. The use of natural minerals has the benefit of having a source of cheap, homogenous material available. The disadvantages of using minerals are the presence of impurities, and fixed chemical composition.

Natural minerals were chosen as the source of the aluminosilicate precursor material due to the industrial relevance of these inorganic polymers. As one potential use for these materials is as a Portland cement replacement, industry would require a large amount of freely available

material with which to make the cement substitute which would not be available for either the sol-gel or melt-quench method.

The choice of activation method was carried out in conjunction with the choice of precursor material. Various alkali hydroxides have been reported in the literature (Palomo *et al.*, 1999; Barbosa & MacKenzie, 2003; Alonso & Palomo, 2001), as have Group II sulphates and ammonia. The activation solution acts to dissolve the precursor material to allow it to reform as an inorganic polymer material, and can also be used to alter the composition of the final inorganic polymer by adding Al or Si to the system. The cations present in the activating solution neutralise the equivalent negative charge of the 4-coordinate Al atom in the AIP structure. Sodium hydroxide was chosen as the activation compound in this project due to its cost and ready availability.

The Si:Al molar ratio in the AIP was controlled by the addition of amorphous silica fume to the activating solution. Amorphous silica was chosen as it readily dissolves in alkaline solutions, making available Si ions for incorporation into the polymer network.

4.1.2 Composition range

The range of Si:Al molar ratios was chosen after considering a paper by Davidovits (1991), in which it is stated that geopolymers are best formed with Si:Al molar ratio values between 1 and 3. Following those guidelines, a mineral source of aluminosilicate precursor was chosen to give an initial Si:Al molar ratio as close to 1 as possible, which enabled higher Si:Al molar ratios to be achieved by adding Si via the activating solution.

Initial experiments involved changing the Na:Al molar ratio used in the activating solutions up to a value of 3. The activating solutions proved to be dangerous to work with owing to the heat produced when the silica fume was added to the solution. Following this initial work, the range of Na:Al molar ratios was constrained between 0.5 and 2. The stoichiometric value, according to Davidovits (1989), is 1.

The total span of Si:Al and Na:Al molar ratios were divided into five Si:Na molar ratio ranges of 0.75, 1.0, 1.5, 2.0 and 2.5 in order to evenly distribute samples across the possible range of compositions.

Unless otherwise stated, ratios regarding the chemical composition of the polymers are molar ratios.

4.1.3 Macro-property testing

A number of different physical property tests, including compressive strength, tensile strength and hardness, were considered to enable the determination of a macro property of the AIPs to allow for comparison between different compositions. Of these tests, compressive strength was chosen due to its ease of application and ready availability of experimental apparatus.

4.1.4 Microscale analysis

Scanning electron microscopy (SEM) was selected as the preferred method for assessing the microstructure of the AIPs, as this method is also able to provide local compositional information through energy dispersive spectroscopy (EDS).

4.1.5 Nanoscale investigation

X-ray scattering (XRS) and nuclear magnetic resonance (NMR) were chosen as the tools of choice for investigating the properties of the AIPs on the nanometre scale. These methods were chosen due to the direct way in which the relevant information could be extracted from the data; bond length information from XRS and coordination information from NMR. A description of these techniques is given in Chapter 3. Neutron diffraction was considered, however, time restraints precluded its use. Other experimental methods considered for this section of the project included X-ray Photoelectron Spectroscopy (XPS), Electron Energy-Loss Spectroscopy (EELS) and X-ray Absorption Spectroscopy (XAS). Investigation by XPS and EELS were discounted due to sample preparation problems. XRS and NMR were used in place of XAS to try and obtain a structural, as well as bonding, picture of the AIPs.

4.2 Aluminosilicate inorganic polymer production

The procedure used to synthesise the AIP material was based on a series of papers published by Rahier *et al.* (1996; 1996; 1997) describing the use of kaolinite as the precursor material. In this method, crystalline kaolinite is dehydroxylated to form amorphous metakaolinite, which is then combined with silica fume and sodium hydroxide, in various quantities in solution, to form the AIP. The mixture is then placed in an oven at an elevated temperature (less than 100 °C) to cure.

4.2.1 Characterisation of the precursor materials

A crystalline kaolinite (Kingwhite 65, Unimin Australia Ltd.) was chosen as it enabled the synthesis of AIPs with an Si:Al ratio (with no additional Si) of approximately 1. The kaolinite was dehydroxylated to form metakaolinite (MK) by heating in air to 750 °C for 24 h. The kaolinite was spread on alumina trays, not more than ~15 mm thick, and the surface of the powder was broken to ensure that the water produced during the dehydroxylation process was able to escape the bulk powder. The chemical composition of the metakaolinite was approximately $Al_2O_3 \cdot 2.16SiO_2$. The results of XRF analyses are given in Table 4.1.

Table 4.1: Chemical composition of the precursor materials (wt%) determined by XRF analysis. Nominal composition values are given in the right hand column. LOI: Loss on ignition.

	Metakaolinite		Silica Fume	
SiO_2	54.2	54.10	94.2	100.00
Al_2O_3	42.1	45.90	0.15	
Fe_2O_3	1.29		0.49	
MgO	0.19		0.05	
CaO	0.13		<0.01	
Na_2O	0.14		0.04	
K_2O	0.20		0.01	
TiO_2	1.15		0.03	
ZrO_2	0.04		3.69	
LOI	0.84	0.00	0.86	0.00
Total	100.28	100.00	99.52	100.00

SEM micrographs of the kaolinite and metakaolinite powders are given in Figure 4.1. As can be seen from the micrographs, the MK particles range

in size from ~2 μm to ~40 μm. The morphology of the particles is not affected by the dehydroxylation process. The large spread in the particle size has an effect on the microstructure of the AIPs, as is discussed in Chapter 6.

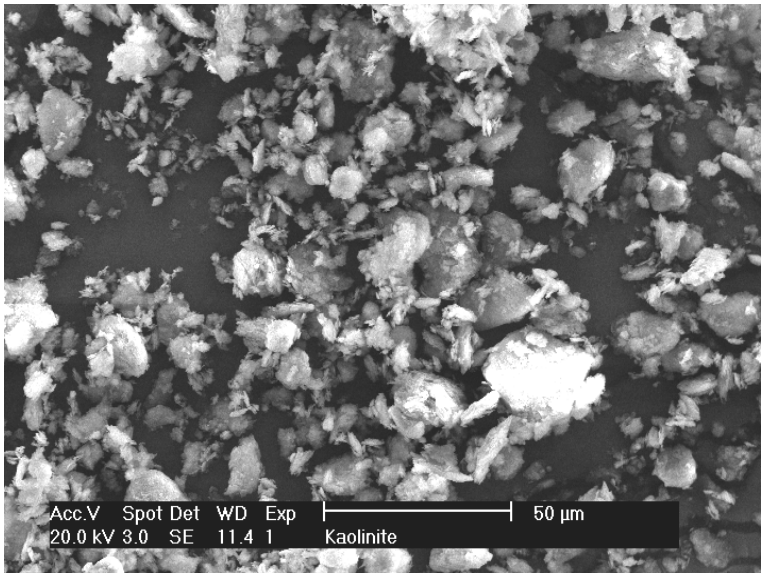

(a)

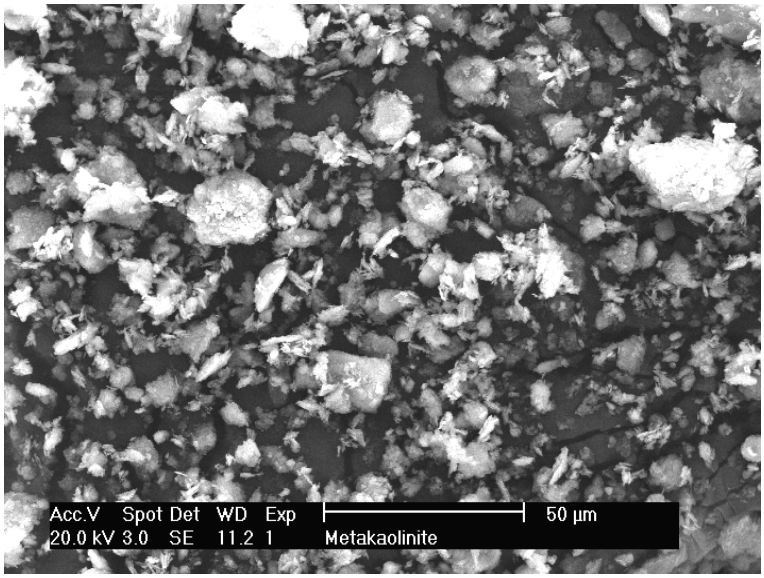

(b)

Figure 4.1: Micrographs of **(a)** kaolinite, and the **(b)** metakaolinite derived from it.

An amorphous silica fume (SF; Australian Fused Materials Pty Ltd.) was used to alter the Si:Al ratio in the final polymer. The chemical composition of the silica fume is given in Table 4.1. The alkali used in all investigations was sodium hydroxide (AR grade, Sigma Chemicals). Other alkalis, such as potassium and calcium hydroxides, were considered, but

were not used as they would greatly increase the number of variables present in the current study.

The precursor powders were analysed by XRD to test for the presence of any crystalline impurities. Figure 4.2 shows that MK was found to contain quartz and anatase. SF was found to contain zirconia. The quartz and anatase impurities in the MK carried through the AIP production process into the final AIP material, whereas the zirconia in the SF was excluded from the AIP synthesis as it is insoluble in alkaline solutions.

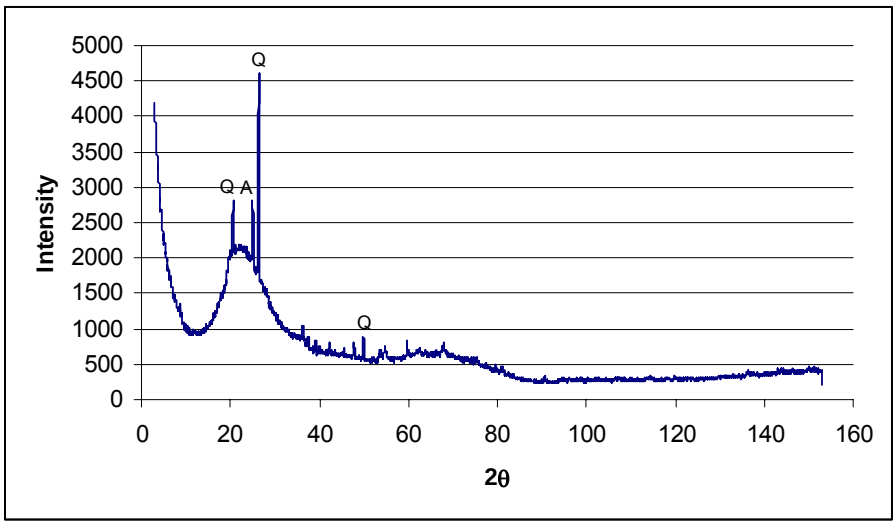

(a)

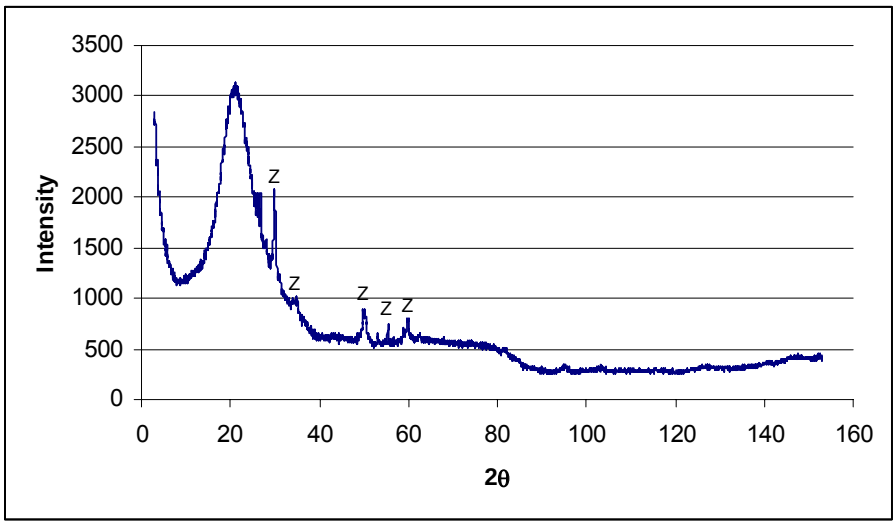

(b)

Figure 4.2: XRD patterns of the precursor powers. The major peaks from the impurity phases are marked. **(a)** Metakaolinite, showing crystalline impurities of quartz (Q) and anatase (A). **(b)** Silica fume, showing crystalline impurities of zirconia (Z).

4.2.2 Production of aluminosilicate inorganic polymers

In order to make the AIP, an activating solution was first prepared. Nineteen samples were prepared with final Si:Al ratios ranging between 1.08–3.0, and with Na:Al ratios between 0.51–2.0. These ranges equate to sample suites with Si:Na ratios of 0.75, 1.0, 1.5, 2.0 and 2.5.

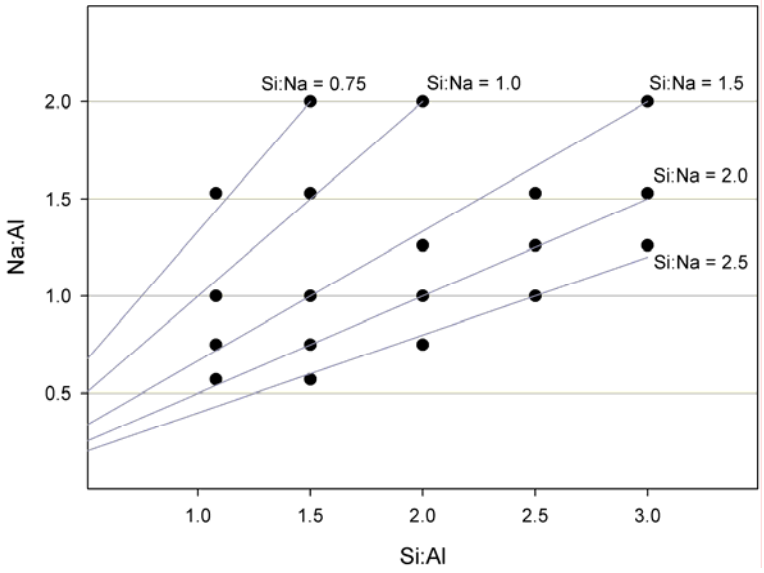

Figure 4.3: Composition of the activating solutions. Solid lines show composition as set by the Si:Na ratio, whilst the solid dots show the actual composition of the prepared solutions. The ratios given are molar ratios.

To prepare polymers with the required Si:Al and Na:Al ratios, the amounts of SF and NaOH added to the solution were varied as shown in Table 4.2. The sodium content of the activating solutions was varied from the design values suggested by the molar ratios of the composition. These small deviations, as shown in Figure 4.3, allow comparisons to be made between samples of differing molar ratios, by only having to take into account the variation of a single ratio into any differences in the material property.

The solutions were prepared in three stages. In stage one, NaOH pellets were weighed and added to deionised water. The amount of water used to make the solutions equated to an H_2O:SiO_2 molar ratio of ~2.8, where the amount of SiO_2 was calculated from the final composition of the polymer. The addition of NaOH was carried out in a water bath to cool the water and minimise water loss to due to evaporation resulting from the exothermic dissolution.

Table 4.2: Amounts of materials needed to produce polymers of a desired composition when mixed with 100 g of metakaolinite. The sample designation is given in the first column. Note: For this calculation, 100 g of MK is assumed to contain 53.3 g of SiO_2 and 41.9 g of Al_2O_3. "additional H_2O" denotes water added to give equivalent consistencies to all mixtures. m(*X*) denotes the mass of *X* required in grams. The ratios given are molar ratios.

Sample code	Si:Na	Si:Al	Na:Al	m(NaOH)	m(H_2O)	m(SF)	additional m(H_2O)	total m(H_2O)
1.5/0.6	2.5	1.5	0.57	18.72	66.60	22.18	28.90	95.50
2.0/0.8	2.5	2.0	0.75	24.63	88.80	48.64	14.45	103.25
2.5/1.0	2.5	2.5	1.00	32.84	111.00	75.11	0.00	111.00
3.0/1.3	2.5	3.0	1.26	41.37	133.21	101.57	0.00	133.21
1.1/0.6	2.0	1.08	0.57	18.72	48.00	0.00	41.00	89.00
1.5/0.8	2.0	1.5	0.75	24.63	66.60	22.18	28.90	95.50
2.0/1.0	2.0	2.0	1.00	32.84	88.80	48.64	14.45	103.25
2.5/1.3	2.0	2.5	1.26	41.37	111.00	75.11	0.00	111.00
3.0/1.5	2.0	3.0	1.53	50.24	133.21	101.57	0.00	133.21
1.1/0.8	1.5	1.08	0.75	24.63	48.00	0.00	41.00	89.00
1.5/1.0	1.5	1.5	1.00	32.84	66.60	22.18	28.90	95.50
2.0/1.3	1.5	2.0	1.26	41.37	88.80	48.64	14.45	103.25
2.5/1.5	1.5	2.5	1.53	50.24	111.00	75.11	0.00	111.00
3.0/2.0	1.5	3.0	2.00	65.67	133.21	101.57	0.00	133.21
1.1/1.0	1.0	1.08	1.00	32.84	48.00	0.00	41.00	89.00
1.5/1.5	1.0	1.5	1.53	50.24	66.60	22.18	28.90	95.50
2.0/2.0	1.0	2.0	2.00	65.67	88.80	48.64	14.45	103.25
1.1/1.5	0.75	1.08	1.53	50.24	48.00	0.00	41.00	89.00
1.5/2.0	0.75	1.5	2.00	65.67	66.60	22.18	28.90	95.50

Stage two involved the addition of SF followed by heating the solution to 75 °C for approximately 8 hours in airtight polypropylene bottles (Nalgene). Periodic agitation was required during this time to negate the settling of the SF. The masses of the bottles were monitored during this process and any weight loss was corrected by the addition of water. Any significant loss of water would result in the activating solutions forming a very dense gel, which was very difficult to rehydrate, as some of the solutions were very close to their saturation point.

Stage three involved the settling and decantation of the solutions. The solutions were allowed to settle in the oven overnight, thus removing the insoluble zirconia and quartz from the bulk solution. The solutions were then

decanted and stored in the oven until used. Fresh solutions were prepared for each batch of polymer to be made.

To produce the AIP, the requisite amount of MK was mixed with the appropriate activating solution to give the required Si:Al:Na ratios. As some of the activating solution remains in the bottle after decanting, the required amount of MK was determined for each sample by calculating, from the masses of substances added to the activating solution, a theoretical composition of activating solution assuming 100% dissolution of the SF. It was assumed that the impurities present in the SF did not enter solution. From this mass, the dependence of the amount of sodium on the mass of solution was derived. After weighing the amount of solution decanted, the amount of sodium present was calculated. From this number, the amount of MK to added was calculated to give the required Na:Al ratio.

For some samples, additional water was added to enhance the workability of the mixture and to give equivalent consistencies to all samples. The mixture consistency used was constrained by the sample preparation method; all samples had to be prepared by hand as there were no machines available to be used in the preparation or casting of the AIPs. The mixture was then poured into screw-top polycarbonate tubes and sealed. These moulds were then cured in an oven at 75 °C for 24 h. Samples prepared for compressive strength testing were subject to vibration prior to curing in order to reduce sample porosity.

XRD analysis was carried out on the first samples prepared in the current study to confirm that the polymerisation reaction had occurred. Figure 4.4 shows that, contrary to some studies (e.g. Hos, McCormick & Byrne, 2002), the scattering patterns of these AIPs do differ from those of the precursor materials

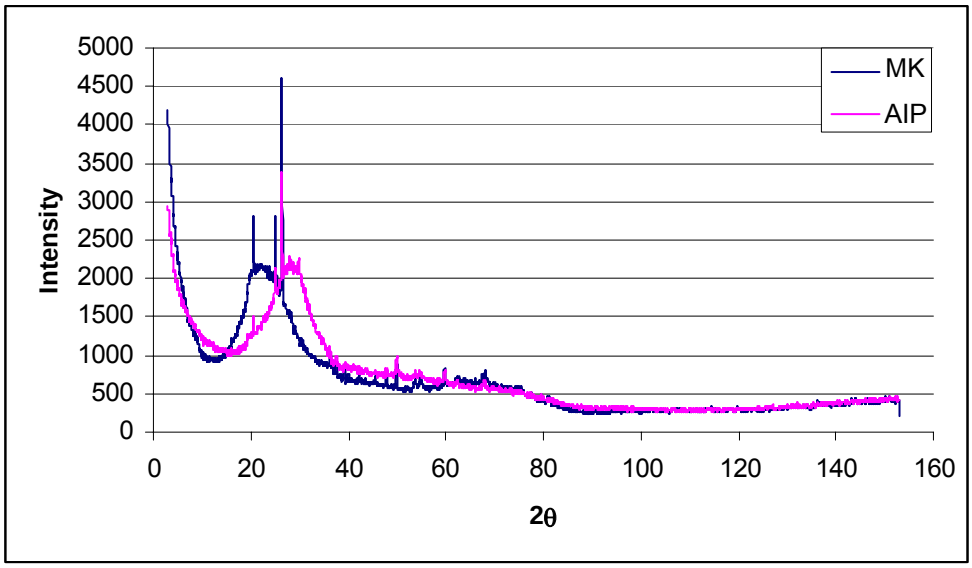

Figure 4.4: Comparison of the XRD patterns (Cu Kα) of MK and an AIP with a composition of Si:Al:Na = 2.0:1:1.4. It can be seen that the only crystalline material present in the AIP has its origin in the MK.

4.3 Compressive strength measurements

Samples prepared for compressive strength measurements were cast on a vibration table into moulds 25 mm in diameter and approximately 60 mm high. After the curing period, the samples were kept in their moulds for 7 days in ambient conditions before being cut with a diamond saw to a height of 50 mm, as required for mechanical testing.

Mechanical testing was performed in the Faculty of Engineering with a Wykeham Farrance 50 tonne compression machine with a loading rate of 0.33 mm·min^{-1}. Compressive tests were carried out following the principles outlined in ASTM C39-96 (1999) (sample length-to-diameter ratio of 2.0). Australian Standard 1012.9 (2001) was also consulted during the experimental planning. The ASTM and AS differ inasmuch as the ASTM gives guidelines as to the permissible ages of the samples at which they should be tested, and also outlines the possible failure modes that the samples may exhibit. Three samples were tested for each composition. The Australian Standard also specifies a sample length-to-diameter ratio of 2.0. The compressive strength was calculated from the applied load at the point of sample failure. The error in the measurement was calculated as the standard deviation of the mean compressive strength from three samples.

4.4 Scanning electron microscopy

Scanning electron microscopy (SEM) was carried out using a Philips XL30 SEM located in the Department of Applied Physics at Curtin University of Technology. An Oxford Instruments energy dispersive spectrometer (EDS) was used to carry out elemental analyses of the samples.

The samples for SEM were prepared by mounting the polymer in epoxy resin, grinding in water and polishing to 1 μm with diamond paste, as outlined in Table 4.3. Water was used, as a non-polar liquid was not available. After polishing, the samples were dried overnight in the oven at ~40 °C. The drying process sometimes introduced shrinkage cracks. The samples were then carbon coated and introduced into the SEM.

Table 4.3: Sample polishing regime.

	Diamond size (μm)	Revolution speed (rpm)	Load (N)	Time (min)
Grinding	20	200	25	0.5
Polishing	9	200	20	5
	6	200	20	5
	3	200	20	5
	1	200	15	10

The system conditions of the SEM were standardised to allow for maximum repeatability between sample batches – see Table 4.4. Secondary electron imaging was used for routine imaging, with back scattered electron imaging being used to help identify high atomic number impurities.

Table 4.4: SEM conditions for imaging and EDS.

	Setting
Accelerating voltage	20 kV
Beam current	60 pA
Working distance	10.4 mm

EDS measurements were taken at various magnifications. 400x was used to give indications of the variation in chemical composition between areas of interest, whilst lower magnifications were used to give overall averages of composition over larger areas, looking for the possibility of large scale changes.

4.5 Bonding characterisation

This section deals with the experimental methods used in studying the nanoscale details of the AIPs. Only indirect methods were used in the part of the project.

4.5.1 Nuclear magnetic resonance

High resolution solid-state ^{29}Si, ^{27}Al and ^{23}Na magic-angle-spinning (MAS) NMR spectra were acquired at ambient temperatures using an MSL-400 NMR spectrometer (B_o = 9.4 T) operating at the ^{29}Si, ^{27}Al and ^{23}Na frequencies of 79.48 MHz, 104.23 MHz and 105.10 MHz, respectively. The use of ^{1}H MAS NMR was considered to elucidate any potential role of H containing species in the formation of the polymer network, but was decided against as it was considered to be beyond the scope of the current study – see discussion in §7.1 and 8.2.

^{27}Al and ^{23}Na experiments were conducted using a Bruker 4 mm double-air-bearing probe from which MAS frequencies of ~15-16 kHz were implemented for line-narrowing, and all such measurements utilised single pulse (Bloch decay) experiments without ^{1}H decoupling. The quadrupolar nature of the ^{27}Al (I = 5/2) and ^{23}Na (I = 3/2) nuclei necessitated that flip angles be close to the condition

$$(I + \tfrac{1}{2})\omega_{rf} t_p \leq \pi/6$$

for quantitative estimates of the central transition intensities to be made (Smith, 1993; MacKenzie & Smith, 2002; Lippmaa, Samoson & Mägi, 1986).

For ^{27}Al measurements, non-selective $\pi/2$ pulse times of 4 μs were calibrated on a 1M $Al(NO_3)_3$ solution from which selective pulse times of 0.6 μs were employed for data acquisition on all solid samples. For ^{23}Na measurements, non-selective pulse times of 3 μs were calibrated on a 1M NaCl solution from which non-selective pulse times of 0.6 μs were chosen for data acquisition. These 1M NaCl and 1M $Al(NO_3)_3$ solutions were also used

as ^{23}Na and ^{27}Al chemical shift references, respectively, with each resonance assigned to represent 0.0 ppm for their respective nuclei.

^{29}Si MAS NMR data were acquired using a Bruker 7 mm double-air-bearing probe with a single pulse (Bloch decay) method, which utilised high-power ^{1}H decoupling during data acquisition. The MAS frequencies implemented for these measurements were ~5 kHz. For the ^{29}Si MAS single pulse/high-power ^{1}H decoupling measurements, a single ^{29}Si $\pi/4$ pulse width of 2.5 μs was used in conjunction with recycle delays of 30 – 60 s for quantitative ^{29}Si measurements. All ^{29}Si MAS chemical shifts were externally referenced to tetramethylsilane (TMS) via a high purity sample of kaolinite.

4.5.2 X-ray scattering

Laboratory measurements

X-ray scattering (XRS) measurements were carried out using a laboratory Bragg-Brentano x-ray diffractometer. Measurements were taken at room temperature in reflection geometry using Cu Kα radiation. A schematic of the experiment is shown in Figure 4.5. The details are given in Table 4.5.

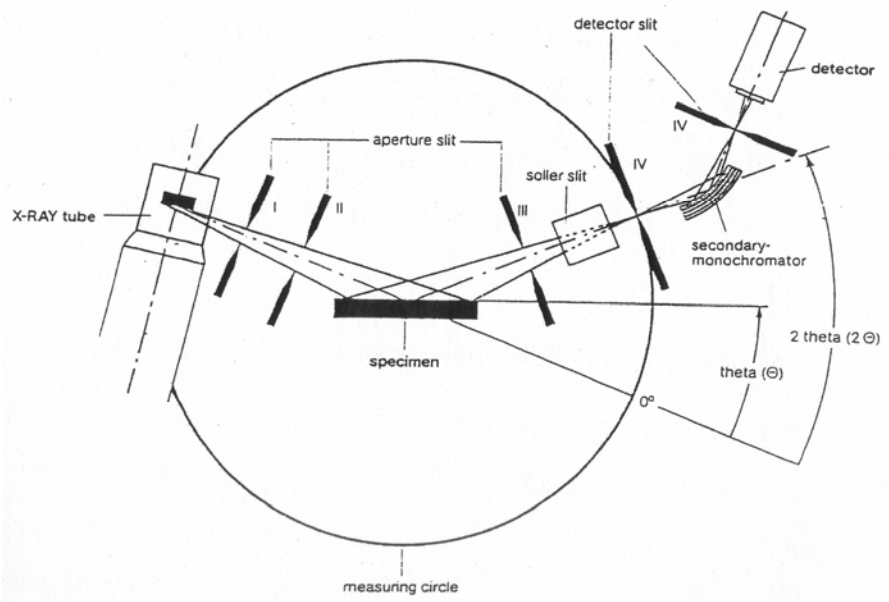

Figure 4.5: Schematic of a Bragg-Brentano diffractometer (Siemens, 1986).

Table 4.5: Experimental details for laboratory XRS pattern collection.

	Setting
Optics	Bragg-Brentano
Beam energy	8.048 keV (CuKα)
Incident slits	1 º
Scatter slits	1 º
Receiving slits	0.15 º
Angular collection range	0.5 – 160 °2θ
Scan size	0.05 °2θ
Scan time	10 sec
Temperature	~300 K

In order to expedite the collection of scattering patterns for sample comparisons, a large scan size was used, as the resolution provided by smaller scan sizes was not required. As the detector collected the scattered intensity in scan mode, rather than step mode, the use of a scan size greater than 0.05 °2θ would have smeared the measured intensity excessively.

Photon Factory (Tsukuba, Japan)

XRS measurements were carried out on powder samples contained in borosilicate capillaries. The monolithic AIP samples were crushed in a mortar and pestle and dried before being sealed in 0.5 mm borosilicate capillaries.

Scattering data were collected using BIGDIFF (O'Connor *et al.*, 1997) at the Australian National Beamline Facility (ANBF) at the Photon Factory (PF) at the High Energy Accelerator Research Organisation (KEK). A schematic of the experiment is shown in Figure 4.6. The details are given in Table 4.6. Measurements were taken at room temperature in capillary geometry using 20 keV photons, as the data collected were intended for RDF analysis which requires data covering a large *q* range. The samples were mounted in capillaries in order to allow for maximum sample throughput. The incident energy was limited to 20 keV, as the intensity of the incident beam drops substantially as the energy is increased beyond 20 keV. 400 mm x 200 mm image plates with 100 μm pixel size (Fuji Photo Film Co., Tokyo Japan) were used to collect the scattering data.

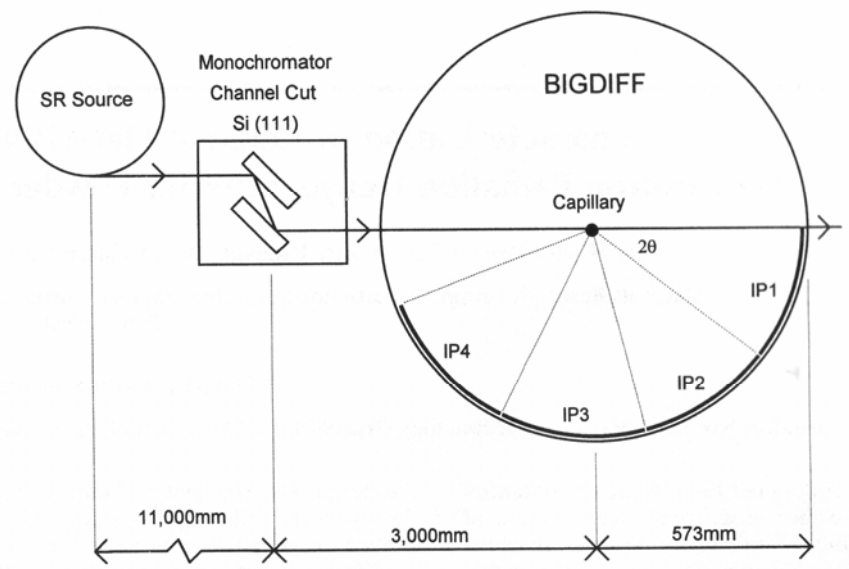

Figure 4.6: Schematic representation of a BIGDIFF diffraction experiment (O'Connor *et al.*, 1997).

Table 4.6: Experimental details for Photon Factory XRS pattern collection.

	Setting
Optics	Debye-Scherrer
Beam energy	20 keV
Beam size	2 x 1 mm
Angular collection range	0.5 – 160 °2θ (q = 0.09 – 20 Å^{-1})
Angular resolution	0.01 °2θ
Count time	30 min
Temperature	~300 K

A typical run would take approximately 330 min. The first 30 min were associated with sample mounting and alignment. A single sample suite consisted of 8 samples. The next 60 min was used in evacuating the sample chamber. Data collection required 240 min; 8 samples, each with a 30 minute exposure. After the scattering data were collected, the sample chamber was vented, the image plates replaced and the next sample suite was loaded. The image plates were downloaded whilst the chamber was in use for the next sample suite. The image plate data was converted into an XY scattering file using the program PPDA (Garrett *et al.*, 2000). Search/match identification was carried out using the program Jade (Materials Data Inc., 2004) and the Powder Diffraction File 2 (ICDD, 2001)

Advanced Photon Source (Chicago, USA)

Scattering patterns were also collected from the Advanced Photon Source (APS), as higher x-ray energies, and consequently a larger *q* range, were available than from the Photon Factory. X-ray scattering (XRS) measurements were carried out on pressed powder flat plate samples. As the flat plate samples prepared were self-supporting, they did not require any additional materials present, such as the capillaries used in the Photon Factory experiment, in order to present the sample to the x-ray beam

The AIP samples were crushed in a mortar & pestle and dried before being ground in a rotary mill (Rocklabs, Model 1A) for between 30 and 300 s. All samples were prepared as pressed powder flat plates in order to reduce any systematic errors in the scattering data resulting from different sample presentation formats and preparation methods.

The powders were pressed in a 20 mm diameter die, lightly lubricated with sodium stearate, to 70 MPa for 30 s. The pressure was then increased to 200 MPa for 5 s, before being slowly released. Samples of the desired final thickness of 2 mm were made by pressing 1 g of sample and back-calculating the required mass of powder necessary to make a 2 mm thick sample. A sample thickness of 2 mm was used as this was as thin as the samples could be made, and still allow the samples to consistently support their own weight. Thicker samples would be ideal for increased scattering intensity, but would introduce additional multiple scattering and decrease the resolution of the scattering pattern. The calculated μt of the samples for the energy used was ~0.07.

Scattering data were collected using beamline 1-ID at the Advanced Photon Source (APS) at the Argonne National Laboratories. A schematic of the experiment is shown in Figure 4.7. The details of the setup are given in Table 4.7. Measurements were taken at low temperature in transmission mode using 81.6 keV photons (q_{max} = 40 Å^{-1}). Data collected over this q-range would enable the calculation of RDFs that can resolve Si-O and Al-O bonds at 1.6 and 1.75 Å respectively. A germanium energy sensitive detector

was used to allow discrimination of Compton and elastic scattering in the diffracted beam for data analysis.

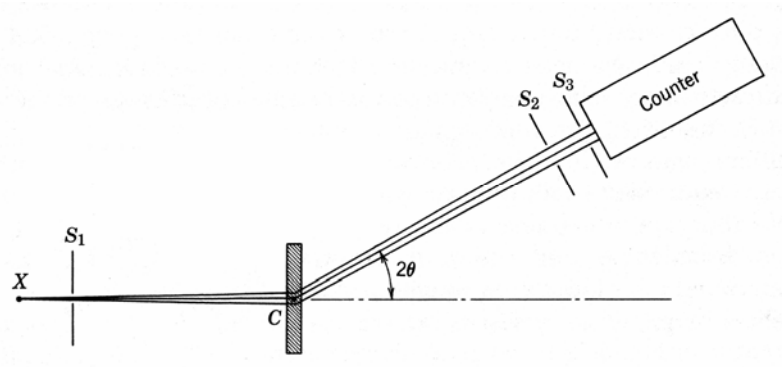

Figure 4.7: Schematic representation of normal-beam transmission optics. The sources is represented by *X*. S_1, S_2 and S_3 are the beam, scattering and receiving slits,, respectively (after Klug & Alexander, 1974).

Table 4.7: Experimental details for Advanced Photon Source XRS pattern collection.

	Setting
Optics	Normal-beam transmission
Beam energy	81.6 keV
Beam size	2 x 1 mm
Receiving slits	3 x 0.5 mm
Scatter slits	5 x 4 mm
Angular collection range	0.5 – 60 °2θ (q = 0.4 – 41 Å^{-1})
Step size	0.028 °2θ
Count time	5 s
Temperature	8 – 15 K

The sample was held in a brass ring fitted to a copper cold finger. The sample was enclosed in a beryllium can and the sample chamber was evacuated. At this point, the sample was cooled to 8 – 15 K in order to minimise the contribution of thermal vibration to the scattered intensity, which would serve to degrade the resolution of the resultant RDF.

The transmissions of the samples were measured at both room and low temperature. The absorption (μt) for the samples was calculated by the following procedure. The intensity of the through-beam was measured using a gas proportional counter for both the sample in the Be can and for an empty Be can. These intensities were then normalised using the monitor counts. The transmission measured for the samples included a component

from the Be can which was removed by calculating the ratio of the normalised transmissions of the sample and can. The value of μt for the samples was then calculated by finding the negative natural logarithm of $\left(T_{sample} / T_{can}\right)$.

An intrinsic Ge energy sensitive detector with multi-channel analyser (MCA) was used to collect, and bin, the scattered intensity according to energy to allow for experimental, rather than theoretical, determination of Compton scattering. The experimental determination of Compton scattering is preferred as it can compensate for any bias in the recorded energies of the scattered beam, and does not rely on accurate knowledge of the chemical composition of the sample. During the collection of the XRS patterns, the counts being recorded were stored in 3 bins. Bin 1 was the total counts across the entire spectrum. Bin 2 was set to bracket both the elastic and inelastic peaks (67.85 – 81.62 keV). Bin 3 was set to collect the elastic peak (79.69 – 81.45 keV). A series of spectra covering the full energy range of the MCA were collected for each sample every 5 $Å^{-1}$ from 5 – 40 $Å^{-1}$ to facilitate the calculation of the intensity correction factor to allow only elastic counts to be factored into the RDF calculations. Figure 4.8 shows an MCA spectrum collected at 40 $Å^{-1}$.

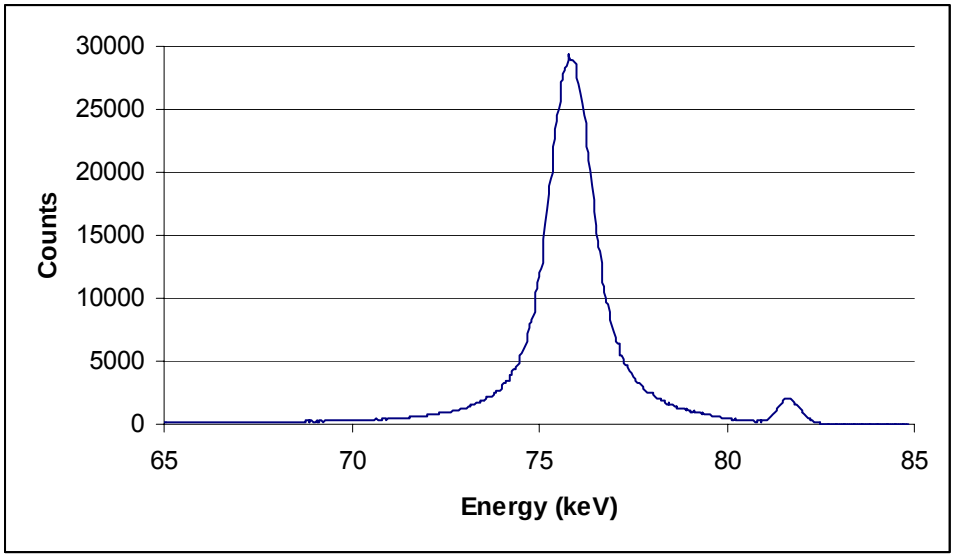

Figure 4.8: MCA spectrum collected at q = 40 $Å^{-1}$. The larger peak is due to inelastic scattering, whilst the smaller is elastic scattering.

Due to the presence of Bragg peaks at low angles, and the need to protect the detector from high count-rates to preserve deadtime linearity, data were collected in two sets for each sample. The two data sets were split between 0.5 – 13 °2θ and 13 – 60 °2θ. At high count-rates (>120 kHz), the deadtime response of the detector becomes non-linear, making the deadtime corrections to be carried out more difficult. Copper filters of varying thickness were used to attenuate the beam in the low angle region. Once this region was passed, these filters were removed to provide maximum intensity, which allowed for a highest amount of collected counts without altering the collection time.

A typical run would take approximately 380 min. The first 10 min were associated will sample mounting and alignment. The next 80 min was used in cooling the sample. The initial room temperature transmission measurements were taken in the initial stages of this phase. The first data set took approximately 50 minutes to collect. This was followed by a 30 min period to collect the MCA spectra. The second data set took 160 min. The final phase consisted of a 50 min warming period, after which the next sample was loaded.

4.5.3 Data analysis

Nuclear magnetic resonance analysis

The chemical shift and linewidths of the measured MAS NMR spectra were calculated using the WINFIT profile fitting program (Krumm, 1997). ^{29}Si spectra were fitted using gaussian curves, whereas ^{27}Al and ^{23}Na spectra were fitted using lorentzian curves as necessitated by the quadrupolar nature of the ^{27}Al and ^{23}Na nuclei. Each spectrum was fitted five times, and the average of these fits was reported as the values for chemical shift and linewidth.

X-ray scattering analysis

The scattered intensities were corrected for background scattering, absorption and multiple scattering (Petkov, 1989). Compton scattering was excluded from the measured intensity through theoretical calculations. The

measured Compton intensity was unable to be removed experimentally as a sufficiently accurate band pass function (Ruland, 1964) was not able to be constructed. Experimental structure functions were then derived from the corrected scattering data using the program RAD (Petkov, 1989), which were then used to calculate the reduced radial distribution functions (RRDFs) and pair distribution functions (PDFs). All elements with an abundance above 0.5 wt% (as oxides, by XRF) were included in the data analysis.

The normalisation constants (N) for the RRDFs were first calculated using the high angle normalisation method (Wagner, 1978). These values were then adjusted through the successive calculation of RRDFs and the subsequent alteration of N in order to keep the oscillations at low r to a minimum as discussed in §3.2.2. The RRDFs were calculated with an r step size of 0.005 Å and a damping factor of 0.003 (see Equation 3.30).

Peak deconvolution of the PDFs was carried out be approximating each atomic pair by one or two symmetric Gaussian functions. Multiple Gaussians were used if the peak to be fitted showed significant asymmetry. Available codes, such as PDFFIT (Proffen & Billinge, 1999), were considered for the peak deconvolution, however, these programs required the input of cell parameters and atom positions, which were no available for this amorphous material.

5.0 INFLUENCE OF CHEMICAL COMPOSITION ON COMPRESSIVE STRENGTH

Chapter 5 presents the experimental results on the study into the influence of the chemical composition on the compressive strength of AIPs synthesised by the sodium silicate alkaline activation of metakaolinite.

The chapter is the first of three results chapters in this thesis, and gives the outcomes of the experiments into the macro-properties of the AIPs. The results presented in this chapter set the scene for the further results chapters, which delve into the micro and nanoscale character of the AIPs, and provide a framework for discussion of the consequences of the work.

The principal questions that the chapter seeks to answer are:

1) How does the macroscale character of the AIPs change with composition? and
2) Is it possible to optimise the compressive strength of the AIPs?

5.1 Results

The results section is divided into two parts. The first details the numerical results of the compressive strength and discusses trends present in the data; the second details the failure mechanisms observed and compares these results with those for conventional cements

5.1.1 Trends in compressive strength

The results are given in Figure 5.1 and Table 5.1. The compressive strengths of the AIPs show that the material strength depends markedly on the chemical composition of the AIP. Trends in the compressive strength versus composition are clearly visible in the graphical representation of the data in Figure 5.1. The maximum compressive strength measured was 62 ± 3 MPa for Sample 2.5/1.3.

The chemical composition for the highest compressive strength sample corresponds to Si:Al:Na = 2.5:1:1.29, which indicates the network formula $Na_n[-(SiO_2)_{2.5}-(AlO_2)-]_n$, if the presence of undissolved grains is

ignored – see §6.2 for a discussion on the matrix composition. The level of Na used to prepare the material exceeds the amount required for charge balancing by approximately 30%. The results also indicate that the Si:Al ratios of the samples for which relatively high compressive strengths (> 45 MPa) were obtained ranged from approximately 1.8 to 2.7.

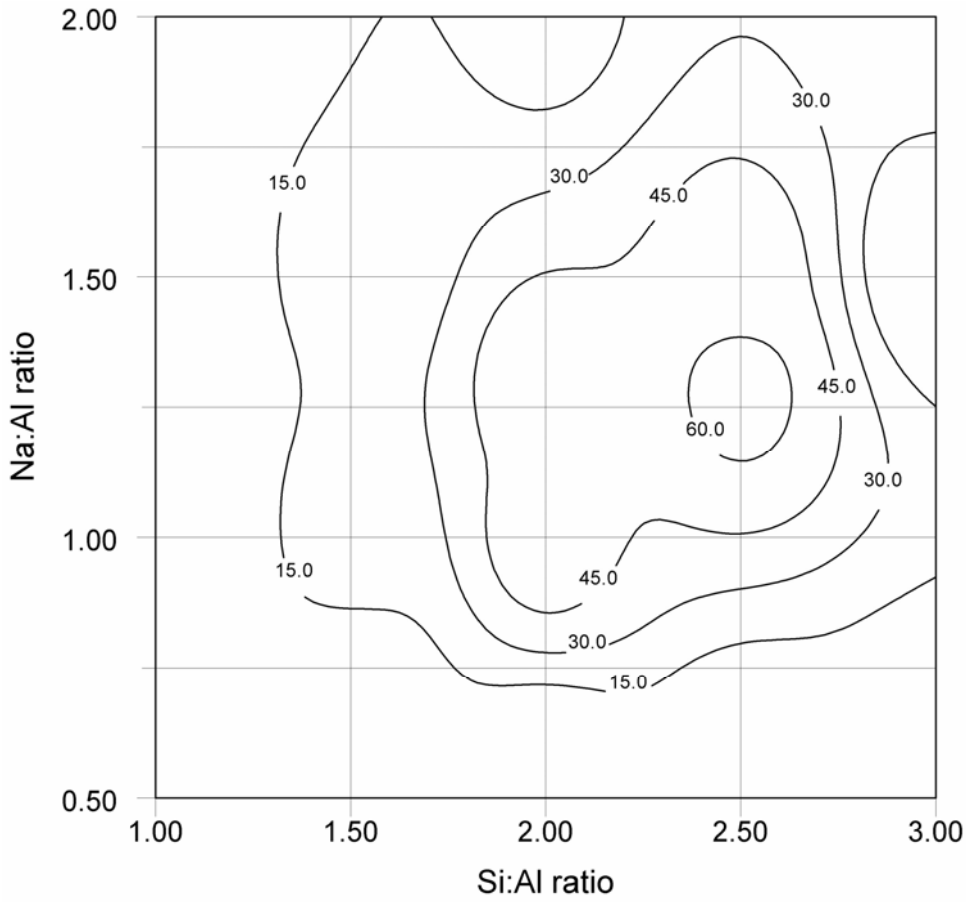

Figure 5.1: Compressive strength contours for the aluminosilicate polymers. The first contour is 15 MPa and the contour interval is 15 MPa. The compressive strength of Si:Al and Na:Al ratios equal to 1.0 and 0.5 respectively have been set to zero for contouring purposes. The contour lines in Figure 5.1 were created in SigmaPlot (SPSS, 2001). The ratios given in this figure are molar ratios.

Table 5.1: Compressive strengths of AIPs in MPa. Errors are one standard deviation calculated from three samples, as shown in parentheses for the least significant figure. Samples corresponding to the entries marked with dashes were not prepared. Molar ratios are quoted.

Si:Al	Na:Al					
	0.51	0.72	1.0	1.29	1.53	2.0
1.08	0.40(2)	2.2(3)	4.4(7)	-	-	-
1.5	-	6.2(5)	23.4(2)	-	19.8(8)	-
2.0	-	-	51.3(13)	53.1(10)	-	11.8(16)
2.5	-	-	-	64(3)	49(3)	-
3.0	-	-	-	-	2.6(2)	19.9(7)

Figure 5.2 shows that the compressive strengths of the AIPs form a lopsided cone around the highest strength sample, Sample 2.5/1.3. The vertical edges, as defined by the Si:Al ratio, show that the change in compressive strength due to changes in Si:Al ratios are generally independent of the Na:Al ratio. For example, for a Si:Al ratio of ~1.75, the compressive strength is essentially constant for Na:Al ratios between 0.8 and 1.5. When changing the Si:Al ratio of the sample from the Si:Al ratio of the maximum compressive strength sample, the change required in the ratio in order to produce the same change in the compressive strength is dependent on whether the Si:Al ratio is being increased or decreased. Increasing the Si:Al ratio from 2.5 to 2.75 (a 10% increase) would result in a drop in compressive strength from 64 MPa to ~30 MPa, whereas decreasing the Si:Al ratio to 1.75 from 2.5 (a 30% decrease) results in the same decrease in strength. The dependence on the direction of Si:Al ratio change on the change in compressive strength suggests that there is a critical Si level, beyond which the preparation regime used in the current study is no longer effective.

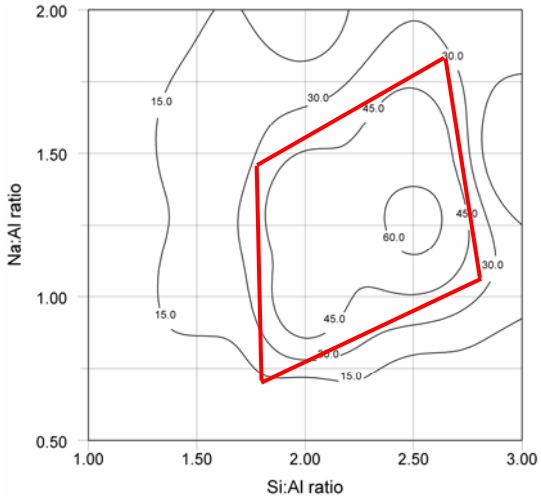

Figure 5.2: Compressive strength contours for the aluminosilicate polymers showing the edges of the cone. The vertical edges, show that the change in compressive strength due to changes in Si:Al molar ratios are generally independent of the Na:Al molar ratio.

Compressive strength variations are also seen when considering Na:Al ratios. Decreasing the Na:Al ratio below the stoichiometric ratio of one, results in reduced compressive strengths, regardless of the Si:Al ratio, as there is then insufficient Na^{+} to act as a charge balancer for Al^{3+}. This

decrease in strength has been widely reported in other AIPs (Rahier *et al.*, 1997; van Jaarsveld & van Deventer, 1999b). A reduction in the amount of Na^+ available to act as a charge balancer for Al^{3+} should result in AlO_4 tetrahedra forming AlO_n entities (AlO_5, AlO_6…), as Al adjusts its coordination to account for the lack of Na. However, NMR results, as presented in Chapter 7, show that Al is present almost exclusively in 4-fold coordination. The formation of AlO_n entities due to the lack of Na is not believed to have occurred, due to the low level of 5- and 6-coordinate Al observed.

The change in compressive strength with an increase in the Na:Al ratio is dependent on the Si:Al ratio. Increasing the Na:Al ratio above 0.75 had no effect on the compressive strength of the AIP up to an Si:Al ratio of ~1.75. Inspection of the microstructure of these samples shows that the structure of the Si:Al = 1.08 samples is invariant with changes in the Na:Al ratio. Samples corresponding to Si:Al = 1.5 do change with an increasing Na:Al ratio, however the potential increase in strength due to a more homogenous microstructure is offset by the presence of excess Na, which weakens the structure. For Si:Al ratios between ~1.75 and 2.5 the Na:Al ratio must increase in order to keep the compressive strength constant, as indicated by the horizontal lines in Figure 5.2. The increase in the Na:Al ratio required to keep a constant compressive strength is considered to be due to a more concentrated NaOH solution being required to dissolve the SF added to the mixture. For Si:Al ratios greater than 2.5, the compressive strength decreases, regardless of the Na:Al ratio, mirroring the strength behaviour for Si:Al ratios less than 1.75.

The nature of these trends in compressive strength suggests that the strength is determined largely by the Si:Al ratio, with the Na:Al ratio acting as the means by which the maximum strength possible at a particular Si:Al ratio is achieved.

The relationship between the Si:Al and Na:Al ratios is most likely linked with the kinetics of the curing process; altering these conditions would alter the composition-strength relationship. The linking of the curing process with

the composition-strength relationship is supported by empirical evidence gathered during the current study which showed that samples cured at room temperature required a longer period of time to cure, and resulted in lower compressive strengths. The elucidation of the relationships between the curing process and the composition of the AIP relies on the determination of the polymer formation mechanisms. Failure to determine the formation mechanisms will not allow the use of these materials to be developed fully.

5.1.2 Modes of failure

The samples tested had a variety of failure types. The types of failure are described in ASTM C 39 (ASTM, 1999) and outlined in Figure 5.3.

The failure type predominately observed in this experiment was of the *cone & split* variety. A variant on this failure type is the *cone & multiple split*, which was seen in several samples. Other samples failed in *shear*, *cone* and *cone & shear* modes. These samples split into between 4 and 10 pieces upon failure. No samples failed solely in *columnar* form. Other modes of failure observed were *catastrophic fracture*, in which the sample disintegrated on failure and *irreversible plastic deformation* (IPD), in which the sample would continue to be compressed, with material being squeezed out of the sides.

There is a correlation between compressive strength and the type of failure exhibited by the sample. Samples with a compressive strength above 50 MPa failed by catastrophic fracture. These samples were visibly “normal” when being loaded, with a slight bulging at the centre, until failure, when they shattered. This failure type is indicative of brittle fracture, emphasising the ceramic nature of this particular compositional subset of the material. In the samples that shattered, no pieces were larger than approximately 5 mm on any side, with the original samples being 25 mm in diameter and 50 mm high.

Samples with compressive strengths below 5 MPa did not fail in a manner as outlined in Figure 5.3. These samples would continue be compressed, with the AIP being squeezed out of the sides of the sample.

The point of failure was taken as the load at which the IPD mode of failure was apparent. This mode showed that the local bonding may have been strong, but the bonding, as measured over the extent of the sample, was not. The strength of these samples may have been improved with the addition of aggregate, but, as the aim of this experiment was to investigate the nature of neat AIP paste, aggregate addition was not carried out.

The samples that didn't fail catastrophically, or by IPD, would fail by standard ASTM modes as outlined in Figure 5.3, with the addition of Figure 5.3(f). All types of failure were observed, except for columnar. The types of failure for each sample are given in Table 5.2

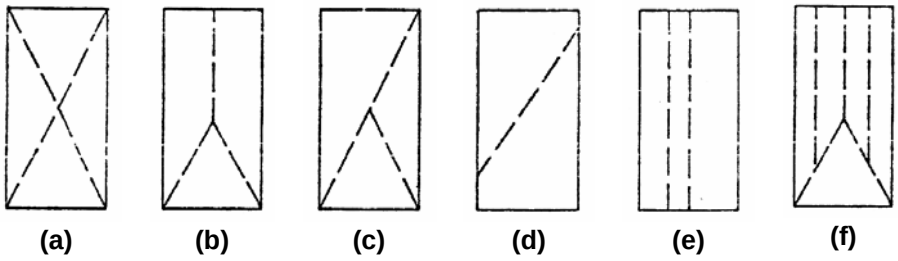

Figure 5.3: Schematic representation of types of fracture (after ASTM, 1999). **(a)** Cone, **(b)** Cone and split, **(c)** Cone and shear, **(d)** Shear, **(e)** Columnar, and **(f)** Cone and multiple split.

Table 5.2: Types of failure observed in compressive strength testing. "C" denotes catastrophic failure. "I" denotes irreversible plastic deformation; see text for details. Ratios stated are molar ratios.

Si:Al	Na:Al					
	0.51	0.72	1.0	1.29	1.53	2.0
1.08	III	III				
1.5						
2.0			CCC	CC		
2.5				CCC		
3.0					III	

5.2 Possible AIP formation mechanisms

As stated in §5.1.1, the sample strength is dependent on both the Si:Al and Na:Al ratios of the material. As zeolites have been produced using the synthesis route for AIPs (see §2.2.2 and §6.3), it can be argued that

information regarding the formation of zeolites can be used to help elucidate a theory of AIP development, and explain the measured compressive strengths.

Murayama, Yamamoto & Shibata (2002) proposed that the OH^- ion in alkaline solution helps to facilitate the dissolution step of Si^{4+} and Al^{3+} from flyash, whilst the Na^+ ion, in its role as a charge balancing ion, contributes to the crystallisation of zeolite P [$Na_2O.(2.0\text{-}2.66)SiO_2{:}Al_2O_3.yH_2O$]. In the production of the AIP, the amounts of OH^- and Na^+ are coupled, as the only source of these ions is the NaOH present in the activating solution. The amounts of Al and Si available from the powder are fixed, whilst the amount of Si in the activating solution is variable.

In samples with low sodium content, there would be both insufficient OH^- to completely dissolve Si^{4+} and Al^{3+} from the MK, and insufficient Na^+ to permit complete polymerisation of the network. Both incomplete dissolution and incomplete polycondensation result in unreacted MK and, therefore, a lower strength material. MK retains the morphology of the original kaolinite, namely a platey structure, and it is conjectured that this platey structure is a cause of the weakening in the AIP. Any stress applied to a MK particle in the AIP matrix would result in the particle shearing across the plates, instead of deflecting the crack. Therefore, the cracking could continue unabated and lead to sample failure. Kriven, Bell & Gordon (2003) conjecture that the presence of residual MK would lead to higher compressive strengths, due to the MK acting as a "filler" phase. Their conjecture is based on the observation of samples of the same composition, made from a different kaolinite, which showed less "filler" phase, and had a lower compressive strength (83 vs. 48 MPa). Work by Subaer (2004), and discussed in §5.3.1 showed that the addition of quartz sand did not result in any increase in the compressive strength of the sample. Examination of Figure 5.1 shows that for lower Na:Al ratios (~0.75) the compressive strength is independent of the Si:Al ratio, suggesting that the limiting factor in the compressive strength is the availability of Na^+ to act as a charge balancer for Al^{3+} in the AIP network.

For a more detailed discussion on the microstructural implications of the composition of the AIPs, see §6.2.

In samples with high sodium content, there would be excess OH^-, allowing for complete dissolution of Si^{4+} and Al^{3+} from the MK. However, excess sodium would be left in the sample, weakening the structure. A study of calcium aluminosilicate glasses (Petkov *et al.*, 2000) show that the calcium bonds to the polymer network as Si-O-Ca. At higher Ca levels, some of the oxygens in the SiO_4 tetrahedra become non-bonding oxygens (NBOs), that is, they no longer form part of the aluminosilicate network. These NBOs then bond with Ca, effectively lowering the average Si-O coordination number, which indicates that the connectivity of the calcium aluminosilicate changes considerably at high Al and Ca levels.

In the current study, sodium carries out the role of calcium as a charge balancer, and as such, it is possible that sodium will bond to the polymer network in the same way. If this is the case, then the polymer chain is terminated, and no more atoms can join that chain. At high sodium levels ($Na:Al \gg 1$), the silicon network connectivity is disrupted, resulting in a weaker material. Inspection of Figure 5.1 shows that the effects of high levels of NaOH are compensated by increasing the Si concentration, supporting the network connectivity proposition. The effect of the Si-O-Na bonds on the polymer network will decrease as the Si:Na ratio increases. Lower compressive strengths at both high and low sodium levels have been previously reported (Rahier *et al.*, 1997). The role of Na in the formation of the polymer network is discussed further in §7.3.

The reduced compressive strengths associated with lower Si content are thought to be due to the Loewenstein Avoidance Principle (Loewenstein, 1954), which states that whenever a single O bridge links two tetrahedra, Al can occupy the centre of only one of the tetrahedra (i.e. Al-O-Al bonds are impossible). It is thought that the lower Si content polymers cannot form polymer networks of sufficient extent to have high structural integrity, whereas the polymer networks constructed by the high Si content AIPs are

much more extensive. The decrease in compressive strength with higher Si content can be explained by there being insufficient OH^- to fully dissolve the Al^{3+} ions which, in turn, would leave residual MK, thus weakening the material

5.3 Comparison of results with the literature

5.3.1 Inorganic polymer cements and concretes

Investigation of a Synthetic Aluminosilicate Inorganic Polymer (Hos, McCormick & Byrne, 2002)

An investigation into the compressive strength of AIPs was reported by Hos, McCormick & Byrne (2002). The reported trend in the measured compressive strength is in disagreement with the observations made in the current study. The reported maximum compressive strength by Hos, McCormick & Byrne is *ca.* 6 times that observed in the current study and additionally, the maximum occurs at Na:Al = 0.36, which is significantly lower than the value of 1.29 reported in the current study.

The preparation method of Hos, McCormick & Byrne involved the melt-quenching of a previously prepared sintered $Al_2O_3.2SiO_2$ pellet. The melt-quenched material was then milled, and mixed with a sodium silicate solution and cured at 60 °C for 18 hours. XRD analysis of the melt-quenched material showed a large amorphous hump, with minor reflections corresponding to mullite and aluminium silicate hydroxide. The amount of crystalline material present was not reported. The only such material present in the MK used in the current study was quartz and anatase, both at ~1% levels.

Compressive strength measurements were carried out by Hos, McCormick & Byrne on samples that had a length to diameter ratio ‘‘exceeding one’’, whereas the present project used a length to diameter ratio of 2, in keeping with the ASTM standard (ASTM, 1999). In both cases, however, the sample size was much less than the ASTM recommended 150 mm diameter. Hos, McCormick & Byrne reported that the compressive strength of their AIP increased as the Na:Al ratio was reduced. They ascribed

the increase in compressive strength to particle reinforcement resulting from unreacted precursor aluminosilicate.

The results presented by Hos, McCormick & Byrne differ from those given in this thesis in two ways: in the absolute compressive strength values and in the trend in the compressive strength over the composition range. The difference in the absolute values of the compressive strength can be explained by the size effect (Bazant, 1984), although the trend should be independent of the sample size. The size effect, as outlined by Bazant, states that in the absence of flaws, the strength of the sample increases as the size of a sample is decreased.

The disparity in the strength-composition trends in the two studies could be explained by the different synthesis methods. The XRD pattern of the cured AIPs, as prepared by Hos, McCormick & Byrne, showed no change from the XRD pattern of the precursor aluminosilicate. The lack of change in the XRD patterns suggests that either there is a different synthesis mechanism involved in the formation of the AIP, or that the manufacturing of the precursor material results in a material that has a similar structure to the resultant AIP.

Effect of the Alkali Metal Activator on the Properties of Fly Ash-Based Geopolymers (van Jaarsveld & van Deventer, 1999b)

Van Jaarsveld and van Deventer (1999b) studied the effect of the alkali metal activators on the compressive strength of fly-ash based geopolymers. In particular, they looked at the effect of both K and Na on the compressive strength. The samples were prepared with flyash, kaolinite, Na- or K-silicate and NaOH or KOH, allowed to set at 30 °C for 24 h, and tested after aging for 14 days.

XRD analysis of the materials showed that no additional crystalline phases were formed during the curing process; however, there was an increase in the intensity of the amorphous hump present in the diffraction patterns. The current study also did not detect additional crystalline phases

being formed in the majority of samples. However, upon curing, the amorphous hump shifted to higher 2θ and retained the same intensity.

Samples for compressive strength testing were prepared as 50 mm diameter cylinders in accordance with Australian Standard 1012.9 (2001). Samples for the current study were prepared as 25 mm diameter cylinders. For materials made with both Na and K, Van Jaarsveld and van Deventer found that the optimum M_2O:SiO_2 molar ratio for maximum compressive strength was approximately equal to one. The compressive strengths of the materials made with Na and K differed substantially. The compressive strength of a material containing K was usually higher than a material of the same composition where Na has been substituted for K. The highest compressive strength reported was 36.7 MPa for a flyash/kaolinite sample.

The influence of K on the compressive strength of the material was studied by varying the moles of NaOH and KOH added to the material while keeping the total moles of (NaOH+KOH) constant. At a KOH/SiO_2 molar ratio of 0.49 and a NaOH/SiO_2 molar ratio of 0.84, the compressive strength was 2.1 MPa. When the KOH/SiO_2 molar ratio was increased to 0.71, the compressive strength increased to 10.1 MPa, indicating that the materials containing K may have a different structure to those containing only Na, possibly due to the larger K ions distorting the arrangement of the SiO_4 and AlO_4 tetrahedra compared to Na. The “pockets” of distortion could reinforce the polymer network.

The work reported by van Jaarsveld and van Deventer graphically demonstrates the difference that altering the alkali metal has on the compressive strength. However, they do not appear to take into account the chemical composition of the precursors and of the activating solution. The precursor materials may have been added in a methodical manner, but with little regard to the final chemistry of the final product. There is no doubt that there is a dramatic effect on the compressive strength due to K, but a more methodical study of the chemistry of the materials may reveal more as to the mechanisms of compressive strength enhancement.

Geopolymers Made Using New Zealand Flyash (Perera et al., 2004b)

An investigation into the material properties of inorganic polymers made with fly ash was reported by Perera *et al*. (2004b). The compressive strength of the neat geopolymer paste was measured over a period of 28 days. The testing showed that the geopolymers had a compressive strength of 85 MPa in the first week, but had decreased to 47 MPa after 28 days. This decrease in strength over time was also observed in geopolymer concretes, with a peak strength of 68 MPa, decreasing to 60 MPa. This strength trend is opposite to that observed in Portland cement concretes, where the strength increases with time (Hardjito, Wallah & Rangan, 2002).

The samples were made by mixing Class C flyash, NaOH, sodium silicate and water, followed by curing at 80-90 °C for 18 hours. The starting materials differ from those used in the current study with respect to the composition and type of the aluminosilicate precursor. The flyash contained 22 wt% CaO, which would act as a charge balancer for the AlO_4 tetrahedra, diminishing the need for Na to be added to the mixture. The exact composition of the geopolymer is not stated, making it impossible to make accurate comparisons with the results reported in this thesis.

The samples tested for compressive strength by Perera *et al*. (2004b) were cast in 100 x 50 mm cylinders, the same length:diameter ratio as used in the current study. XRD analysis of the flyash showed the presence of quartz, calcite and mullite. Analyses of a 1 day and a 2 year old sample showed the presence of similar amounts of quartz, calcite, mullite and a calcium silicate. The calcium silicate formed during the curing process was most probably due to the excessive amount of Ca present in the flyash. In the current study, no crystalline phases were formed in the curing process apart from zeolites, as reported in §6.3.

SEM analysis of a 6 month old sample carried out by Perera *et al*. showed that the flyash had not fully dissolved in the activation process. As shown in Chapter 6, there can be large amounts of undissolved material

present in metakaolinite derived AIPs. The presence of undissolved material is thought to be indicative of a curing process that is not fully optimised.

The results presented by Perera *et al.* are for only one sample composition, and as such, it is impossible to draw any conclusions based on the composition of the material. However, the compressive strength results suggest that the geopolymer undergoes further reactions with time, possibly resulting in the connectivity of the polymer network increasing.

Study on Engineering Properties of Fly Ash-Based Geopolymer Concrete (Hardjito, Wallah & Rangan, 2002)

Hardjito, Wallah & Rangan (2002) studied the effect of composition, age and curing temperature & time on the compressive strength of inorganic polymer concrete made with Class F fly ash. The maximum strength reported was 67.6 MPa for a concrete cured at 60 °C for 24 h.

The fly ash used was low in Ca (CaO - 1.34 wt%), but high in Fe (Fe_2O_3 - 10.86 wt%). Samples corresponding to four compositions were prepared with varying amounts of NaOH and sodium silicate. The samples were cured between 30 and 90 °C for 4 or 24 hours. From the information reported, it is impossible to calculate Si:Al ratios for the material. The sample preparation process was similar to that used in the current study, inasmuch as the curing time and temperature are similar.

The optimum curing temperature was found to be 60 °C, with any increase resulting only in a minor change in the final compressive strength, which may be attributed to the exothermic nature of the reaction process. The curing temperature used in the current study fell into the range identified by Hardjito, Wallah & Rangan as only influencing the compressive strength slightly. The heat of reaction, coupled with the curing temperature may have exceeded 100 °C and resulted in water being lost from the material. All samples showed a substantial increase in compressive strength upon lengthening the curing times from 4 to 24 hours. For all of the curing temperatures studied, the order of the samples, when ranked by compressive strength, was the same, regardless of the curing conditions.

The evolution of the compressive strength with respect to time was measured for one sample composition, curing time and temperature. The compressive strength was measured over an age range of 3-56 days, and did not vary substantially from ~60 MPa over the time span.

Hardjito, Wallah & Rangan showed that the sample composition plays an important role in determining the compressive strength of the concrete, as was also demonstrated in the current study. Curing temperature was a secondary effect, with an increase in temperature only increasing the overall compressive strength; a temperature increase did not serve to promote one sample composition over another. Increasing the curing time allowed for the full polymerisation reaction to occur, and affected all samples.

Influence of aggregate on the microstructure of geopolymer (Subaer, 2004)

An investigation into the influence of aggregate on the microstructure of AIPs was reported by Subaer (2004). As a part of the study, the compressive strength of AIPs with different compositions, both with and without aggregate, was determined. The maximum compressive strength reported for a sample without aggregate was 86 ± 16 MPa with the composition of Si:Al:Na = 1.5:1:0.6. Subaer also reported on the effect of aggregate addition in the form of quartz grains. The addition of up to 30 wt% quartz did not increase the compressive strength of the AIP, and levels above 30 wt% decreased the strength.

The samples used were made under similar conditions to those used in the current study. The required amounts of MK (prepared from the same kaolinite used in the current study), NaOH, sodium silicate (Sigma Chemicals, Ltd Australia) and water were mixed together and cured in an oven at 70 ºC for 2 h. Samples produced in the current study did not use a commercially available activating solution. The samples tested for compressive strength were cast in 25 mm diameter moulds and cut to 50 mm height for testing.

For the 3 samples prepared with Si:Al = 1.5, the compressive strength increased with decrease in the Na:Al ratio. This trend was also seen by Hos, McCormick & Byrne (2002), and previously reviewed in this section. It is thought that this trend may be due to the nature of the activating solution. In both the Subaer (2004) and Hos, McCormick & Byrne (2002) work, commercially available sodium silicate solutions were used. These solutions may have a different Si and Na speciation in solution compared to the silicate solutions prepared for the current study. A difference in speciation may change the availability of the elements to participate in the polymerisation reaction, and hence change the behaviour of the materials prepared by its use.

The work by Subaer (2004) showed that the final compressive strength of a material can be determined solely by the *type* of activation solution used. In almost all other aspects, the samples used were the same as those used in the current study.

Microstructure and Microchemistry of Fully-Reacted Geopolymers and Geopolymer Matrix Composites (Kriven, Bell & Gordon, 2003)

Kriven, Bell & Gordon (2003) reported on the microstructure and microchemisty of both AIPs, and AIP matrix composites. As a part of the study, the compressive strengths of their materials were determined. The maximum reported compressive strength was 83 MPa for a non-reinforced sample with a composition of Si:Al:Na = 1.65:1:1.0. Following addition of 1 vol% basalt fibres, the compressive strength was lowered to 32 MPa.

The samples prepared by Kriven, Bell & Gordon followed a similar synthesis route to that in the current study. Silica fume was added to a NaOH solution in order to prepare the activating solution. Metakaolinite, derived from kaolinite calcined at 700 ºC, was then added. When applicable, fibre reinforcement was added to the mixture before curing. Samples for compressive strength testing were 25 x 6 mm cylinders. The major difference between the synthesis routes for Kriven, Bell & Gordon and the current study is in the curing process. Kriven, Bell & Gordon used pressureless curing

(similar to that used in the current study) coupled with vacuum treatment to remove trapped air bubbles at 40 – 60 ºC, warm pressing at 80 ºC & ~18 MPa for 2 h and warm isostatic pressing (WIP) at 80 ºC & 20 MPa for 24 h.

The use of the different curing methods did affect the final compressive strength of the AIPs. Normal pressureless curing, analogous to that used in the current study, produced samples with a maximum compressive strength of 58 MPa, whereas including vacuum treatment to remove trapped porosity increased the compressive strength to 83 MPa. The work by Kriven, Bell & Gordon (2003) shows that treatment of the sample during the curing process can significantly affect the final compressive strength.

5.3.2 Portland cement pastes

When AIPs are compared to ordinary Portland cement (OPC), the measured compressive strengths show that AIPs can exhibit superior properties. A literature survey revealed only one paper that reported compressive strengths of neat OPC pastes (i.e. containing no aggregate). Escalante-García & Sharp (2001) reported the compressive strengths of OPC pastes hydrated at various temperatures. For conditions similar to those used in the current study (time ~ 7 days, temperature ~ 60 °C), the highest strength reported for a cement paste was 42 MPa.

The samples prepared by Escalante-García & Sharp were markedly different (10 mm cubes) from those used in the current study, which does not allow for a direct comparison of results. However, a basic interpretation of size effect theory (Bazant, 1984) is that as sample size decreases, the strength increases (see p. 92), giving the samples used in the current study a higher compressive strength, thus further increasing the difference in strength between the samples used by Escalante-García & Sharp and those used in the current study.

Nevertheless, allowing for these differences, the high strength composition from the current study shows that when the composition of the AIP is optimised, the resultant compressive strengths exceed those for Portland cement pastes.

5.4 Concluding comments

5.4.1 Summary of results

In the current study, it was found that:

1) The compressive strength of the AIP is directly affected by the sample's chemical composition. Change in the Si:Al ratio from the optimum value (2.5) by only 15% could result in a 50% decrease in compressive strength,
2) The maximum compressive strength was 64 ± 3 MPa for Sample 2.5/1.3, corresponding to Si:Al:Na = 2.5:1:1.3 and a network formula of $Na_n[-(SiO_2)_{2.5}-(AlO_2)-]_n$, if the presence of residual grains is ignored. The Na:Al ratio of 1.29 for this sample indicates that approximately 30% of the Na is not taken up into the network. The minimum compressive strength was 0.40 ± 2 MPa for Sample 1.1/0.6,
3) The compositions producing AIPs with compressive strengths above ~45 MPa may be represented by $Na_n[-(SiO_2)_{1.8\text{-}2.7}-(AlO_2)-]_n$,
4) The sample material producing the highest compressive strength corresponds to the combination of 100 g MK, 75.1 g SF, 42.4 g NaOH and 111 g H_2O,
5) The sample failure mode changed with the compressive strength. Compressive strengths above 50 MPa resulted in catastrophic failure, whereas strengths below 5 MPa resulted in irreversible plastic deformation, and samples between these two extremes failed primarily by cone & split failure. These different failure mechanisms show that the highest strength AIPs exhibit almost ceramic like behaviour in their failure, whilst the medium strength AIPs act as cement paste analogues, and
6) The trends in the compressive strength with composition can be explained with reference to zeolite formation chemistry, namely

the effect of OH^- on the dissolution of Si^{4+} and Al^{3+} and of Na^+ on the polycondensation of the AIP. The use of zeolite chemistry to explain the trends may allow some insight into the formation mechanisms of the AIP.

The variations in compressive strength with the relative concentrations of the precursor materials show that the optimum strength (64 MPa) occurs for Si:Al:Na = 2.5:1:1.3, with the Na level exceeding the requirement for charge balance by ~30%.

While the reason for the optimisation of compressive strength for this Si:Al ratio in unclear from the Chapter 5 results, it is obvious that the maximisation of the compressive strength at a given Si:Al ratio requires the optimum amount of Na. An excess or deficit of Na weakens the material. The reason for the optimisation of compressive strength at Si:Al = 2.5 are explored further in Chapters 6 and 7.

From the results discussed in §5.3, it is hypothesised that the composition of the AIP must be such that it allows for a full dissolution of the precursor materials, and the curing time and temperature must be selected to enable the full dissolution to occur.

This hypothesis is supported by the current study inasmuch as a single curing time and temperature regime produced a single strongest sample, and this sample had the minimum amount of residual MK, as determined by NMR – see §7.1.1. XRD results from van Jaarsveld & van Deventer (1999b) show that there is residual precursor material present in their final AIPs, and the SEM results from Perera *et al.* (2004b) also show that there is substantial residual precursor. Furthermore, the decrease in strength observed by Perera *et al.* is attributed to “on-going reactions” taking place. It is suggested that if the initial conditions used by Perera *et al.* were altered, this decline in strength might not be seen. Optimisation of the curing conditions was undertaken by Hardjito, Wallah & Rangan (2002), which resulted in samples that did not show any change in their compressive strength with time.

The maximum compressive strengths of the samples measured in the studies reviewed in §5.3 are summarised in Table 5.3. These results show that the chemical composition of the AIP and the origin of the precursor materials influences the maximum compressive strength. The results also show that the precursor material type and the activation and curing regimes all interact to determine the compressive strength of the material. The way in which this happens is worthy of further research. As can be seen in Table 5.3, AIPs synthesised from the same type of material can differ significantly in compressive strength.

Table 5.3: Maximum compressive strengths reported for inorganic polymer pastes and concretes, as well as a Portland cement paste. See §5.3.2 for a detailed discussion. Where errors are given, they are cited as the variation in the last significant digit. Ratios stated are molar ratios.

Author	Material[a]	Si:Al:Na composition[b]	Maximum compressive strength (MPa)
The current study	MK	2.5:1:1.26	64(3)
Hos, McCormick & Byrne (2002)	MQ	1:1:0.36	375[c]
van Jaarsveld & van Deventer (1999b)	FA	NC	36.7
Perera *et al.* (2004b)	FA	NC	85(9)
		NC	68[d]
Hardjito, Wallah & Rangan (2002)	FA	NC	67.6[d]
Subaer (2004)	MK	1.5:1:0.6	86(16)
Kriven, Bell & Gordon (2003)	MK	1.65:1:1.0	83
Escalante-García & Sharp (2001)	OPC	NA	42

[a] The abbreviations used are: metakaolinite (MK), melt-quench (MQ), fly ash (FA) and ordinary Portland cement (OPC).

[b] NC – Not able to be calculated. NA – Not applicable.

[c] There is a significant difference in the sample format that could account for this large disparity.

[d] These samples are inorganic polymer concrete samples, as opposed to plain pastes.

6.0 INFLUENCE OF CHEMICAL COMPOSITION ON THE MICROSTRUCTURE

This chapter, the second of three results chapters, presents the experimental results of the study into the influence of the chemical composition on the microstructure of AIPs synthesised by sodium silicate alkaline activation of metakaolinite. The chapter describes the microstructural nature of the AIPs as determined by SEM and EDS analysis, with particular reference to the compressive strength results presented in Chapter 5. Thus, the purpose of this chapter is to examine the way in which chemical composition influences the microstructure, and in turn, the compressive strength. The chapter therefore provides valuable information on the optimisation of the processing conditions to achieve maximum compressive strength.

The principal questions that the chapter seeks to answer are:

1) How does dissolution proceed according to the chemical composition of the feed materials?
2) Is dissolution complete when maximum compressive strength is obtained? and
3) To what extent can the compressive strength optimisation be attributed to microstructural changes?

Also presented are the results of XRD characterisation showing the presence of zeolites in some of the AIPs. The observation of zeolites co-forming with AIPs is of consequence as it shows that the differences in the structures of zeolites and AIPs relate only to long range order. The co-formation of zeolites and AIPs suggests that the formation models for zeolites can be modified to describe the formation of AIPs.

6.1 Microstructural analysis

The AIPs prepared for the current study have a wide range of compressive strengths, as discussed in Chapter 5. In addition to the wide range of compressive strengths, the samples also exhibit large differences

microstructure as shown in Figure 6.1. An expanded version of Figure 6.1 is presented in Appendix IV. In order to discuss both the overall trends in the microstructure and to allow sample specific discussion, this section is split into two subsections. The first deals with the broad trends, and common features found in all the AIPs. The second considers in detail the microstructures of each of the AIPs synthesised in the current study.

6.1.1 Overall results and discussion

An overview of the microstructures of all AIPs investigated is given in Figure 6.1. The following discussion of the broad trends in the microstructure refers to this figure.

In general, low strength AIPs showed a distinct “grainy” structure. As can be seen for Sample 1.1/0.6, the AIP is predominantly a “two-phase” material comprising the inorganic polymer matrix and undissolved grains. The grain phase is suggestive of the MK precursor material, which is attributed to incomplete dissolution of the MK during the polymerisation process. The AIPs exhibiting the grainy microstructure had a low compressive strength, which is thought to arise from the incomplete dissolution of the MK.

In contrast to the grainy structure of the low strength materials, the high strength AIPs had a more uniform microstructure. In these materials, the grain structure was still apparent, but the inorganic polymer matrix material is much more pervasive. Sample 2.5/1.3 gives an example. AIPs that had higher strengths showed the more uniform microstructure to varying degrees. It is thought that the higher strength stems from the greater amount of inorganic polymer formed, and that the material strength is determined primarily by the chemical composition. The presence of MK alters the composition of the inorganic polymer, and hence the compressive strength.

Samples 1.5/1.5, 1.5/2.0 and 2.0/2.0 were low strength AIPs that did not display the grainy microstructure. The microstructures for these samples

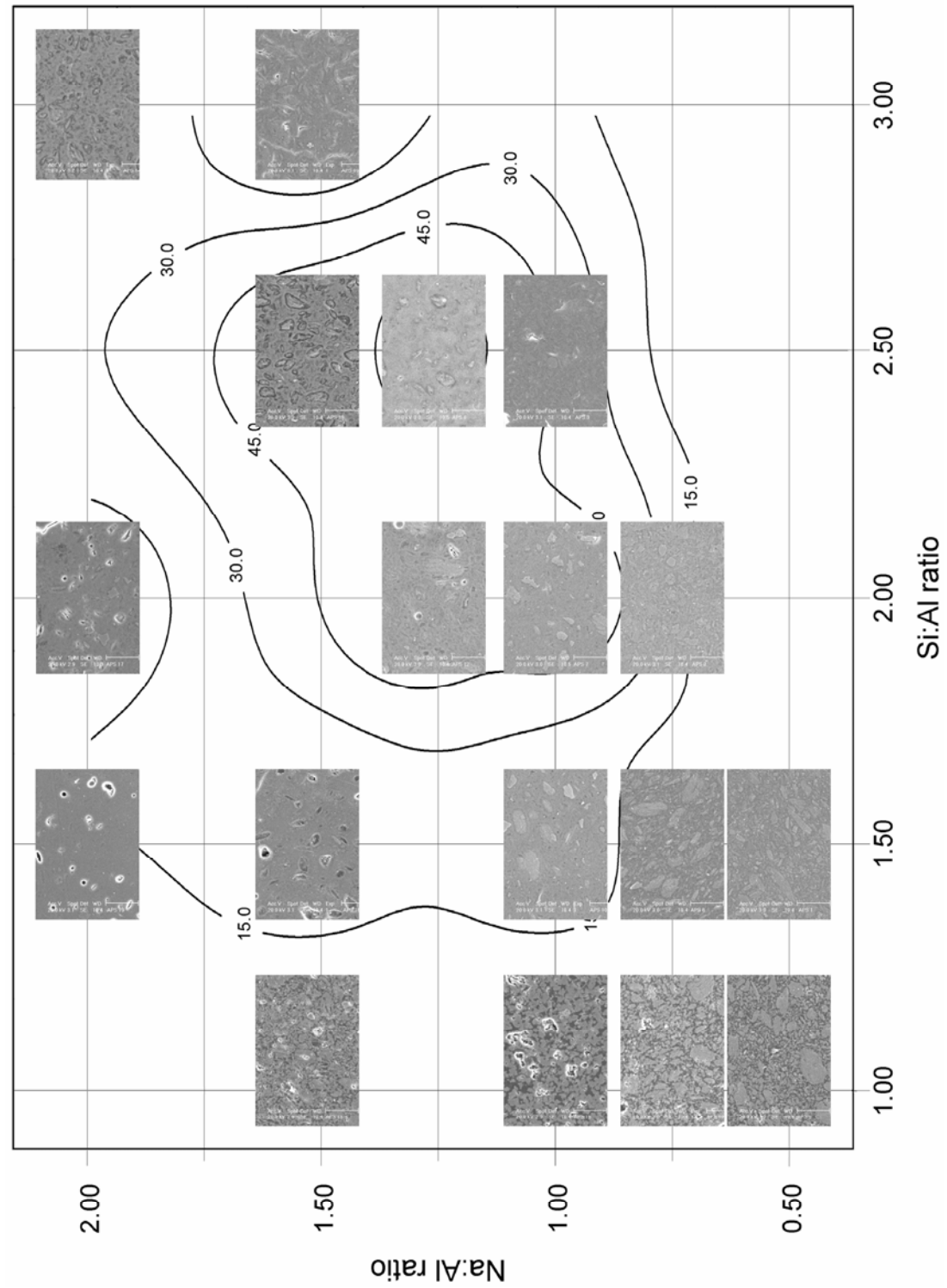

Figure 6.1: Compilation figure of the microstructures of the entire sample suite investigated in the current study. The cropped micrographs are presented on the compressive strength diagram. The position of the sample micrographs on the compressive strength diagram corresponds approximately to the centre of each image. For full images see §6.1.2. An expanded version of the figure is reproduced in Appendix IV.

are similar to those observed for the high strength samples. All have signs of grain pullout. During the sample polishing procedure, grains were removed from the surface of the samples, which is indicative of poor bonding between

the grain and matrix. The interface between the two phases acts as a “crack deflector”, enhancing the strength of the material by absorbing energy from any fractures that propagate through the sample. However, the sample composition and vol% of grains also play a role in determining the sample’s compressive strength. If the material has a composition that is inherently weak, then particle reinforcement will not help. Also, if there are too many particles present, the intervening matrix will not have enough structural integrity to retain its shape under an applied load, and will fail. In the case of Samples 1.5/1.5, 1.5/2.0 and 2.0/2.0, the composition of the AIPs is thought to be the dominant factor in determining the compressive strength.

Micropores were observed in most samples. An example of the pores observed in the samples is given in Figure 6.2. The pores were typically circular in shape and between 1 and 10 μm in diameter. The porosity of the samples was very dependent on the manner in which the sample was prepared. Samples synthesised in the early stages of the current study could have greater than 50% porosity. The porosity of the samples was minimised through the use of sample vibration as a part of the curing process.

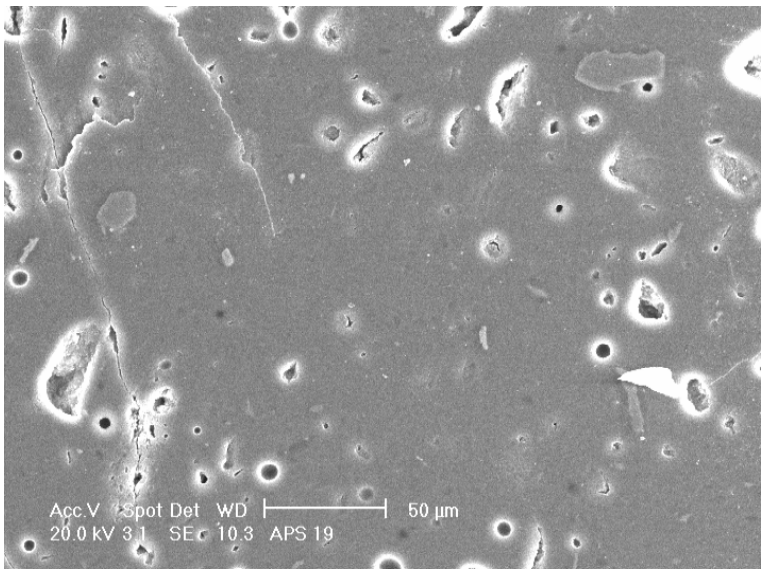

Figure 6.2: A micrograph of Sample 1.5/2.0 showing the presence of micropores.

Samples 1.1/0.6-1.5, 1.5/1.5-2.0 and 2.5/2.0 formed zeolites in conjunction with the AIP during the curing process, see §6.3. No microstructural characteristics were observed in the micrographs of the

samples which could be attributed to zeolites. The appearance of both the grain and matrix phases in the samples which contained zeolites was not significantly different from the samples which did not contain zeolites

Samples 1.1/1.5, 1.5/1.5, 1.5/2.0 and 2.0/2.0 formed Na_2CO_3 crystals on the surface, as shown in Figure 6.3. The formation of Na_2CO_3 was limited to those AIPs with both high Na:Al and low Si:Al ratios, indicating that these samples had unreacted Na present in the microstructure. *Furthermore, the Na_2CO_3 crystals grew only from the matrix, showing that the source of the Na was from the fully formed inorganic polymer*. The presence of Na_2CO_3 has been previously reported (Barbosa, MacKenzie & Thaumaturgo, 2000). The formation of Na_2CO_3 was put down to the reaction of atmospheric CO_2 with unreacted Na, which then migrates to the surface and forms long, thin white crystals. To lessen Na_2CO_3 formation, samples prepared for SEM analysis were stored under vacuum until needed.

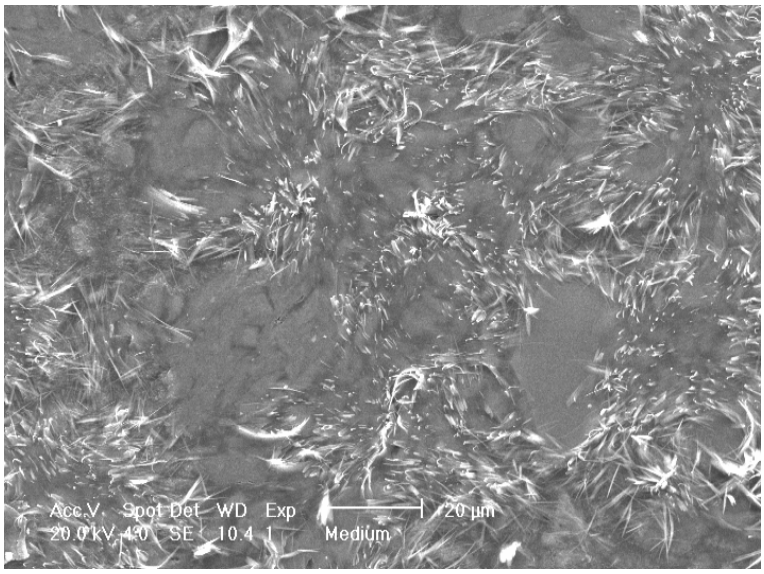

Figure 6.3: Micrograph of Sample 1.5/1.5 showing the formation of Na_2CO_3 on the surface. See also Figure 6.5(b).

The presence of grains in the AIPs can be attributed to the incomplete dissolution of MK. To form a single phase material would entail an optimisation of the either the curing regime or of the particle size of the MK. Optimisation of the curing regime would create an environment in which all of the MK is able to dissolve, whereas selecting the particle size would entail

observing the maximum particle size that is able to fully dissolve under the curing conditions used.

6.1.2 Sample specific discussion

Focussing the discussion of the results grouped by their composition allows for specific comments to be made on the microstructure of each sample with particular reference to the Si:Al ratio.

Si:Al = 1.08

Samples 1.1/0.6, 1.1/0.8, 1.1/1.0 and 1.1/1.5, all have similar “grainy” structures, as seen in Figure 6.4, indicating the grain structure reminiscent of the original MK.

The topological relief shown in the samples, notably 1.1/0.5 and 1.1/0.8, suggests that the matrix phase is softer than the grain phase, which could also contribute to the lower compressive strength of these materials. Sample 1.1/1.0 is relatively flat, compared with the other samples, which is most probably attributable to the epoxy in which the samples are mounted. This sample had a higher uptake of epoxy during the sample preparation process, which would have resulted in a flatter finish due to the epoxy level.

Si:Al = 1.5

The microstructure of Samples 1.5/0.6, 1.5/0.8, 1.5/1.0, 1.5/1.5 and 1.5/2.0 change from a grainy to a uniform microstructure as the Na:Al ratio increases. All samples, as seen in Figure 6.5, show the grain structure reminiscent of the original MK, with the amount of intervening matrix material increasing with an increasing Na:Al ratio.

Samples 1.5/0.6 and 1.5/0.8 have similar microstructures to the Si:Al = 1.08 samples, and their compressive strength is approximately the same as the Si:Al = 1.08 samples (~5 MPa). Again, topological relief as a result of the sample preparation process suggests that the inorganic polymer is softer than the grain phase. In these two samples, the amount of matrix material present increases with an increasing Na:Al ratio. The higher strength

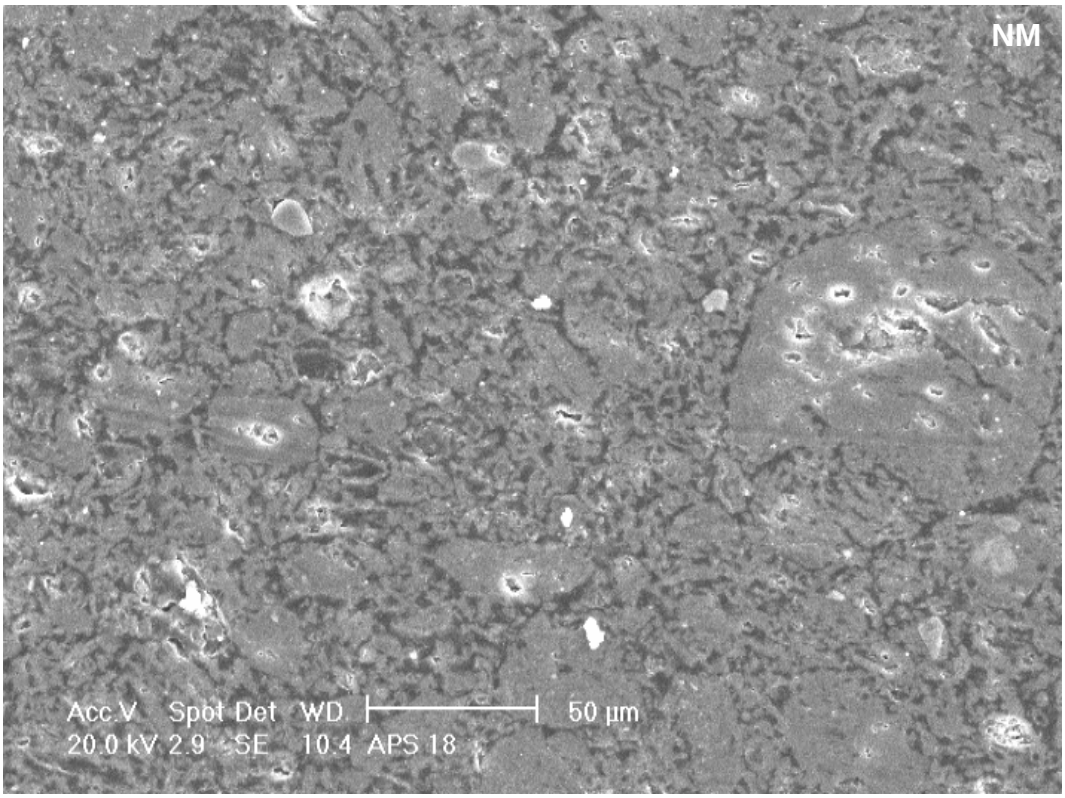

(a)

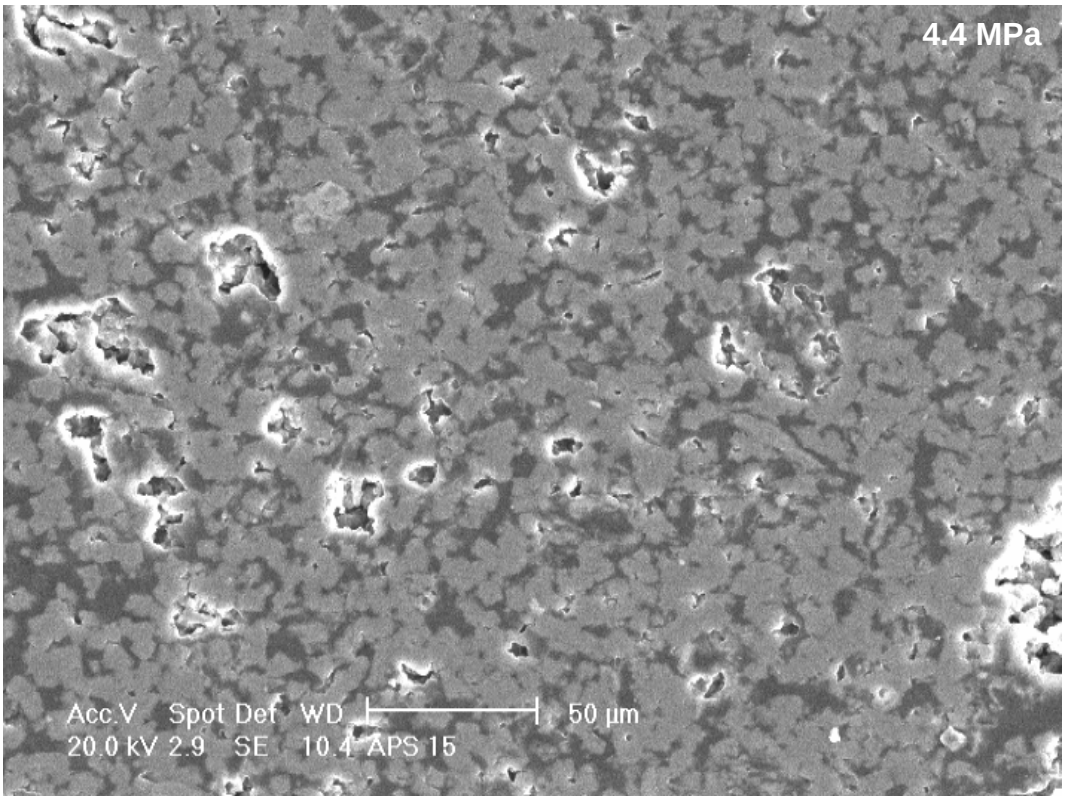

(b)

Figure 6.4: Samples corresponding to Si:Al = 1.08. The compressive strength of the samples, where measured, is given in the top right corner of the image – NM indicates "not measured". Samples: **(a)** 1.1/1.5, **(b)** 1.1/1.0, **(c)** 1.1/0.8 and **(d)** 1.1/0.6.

.

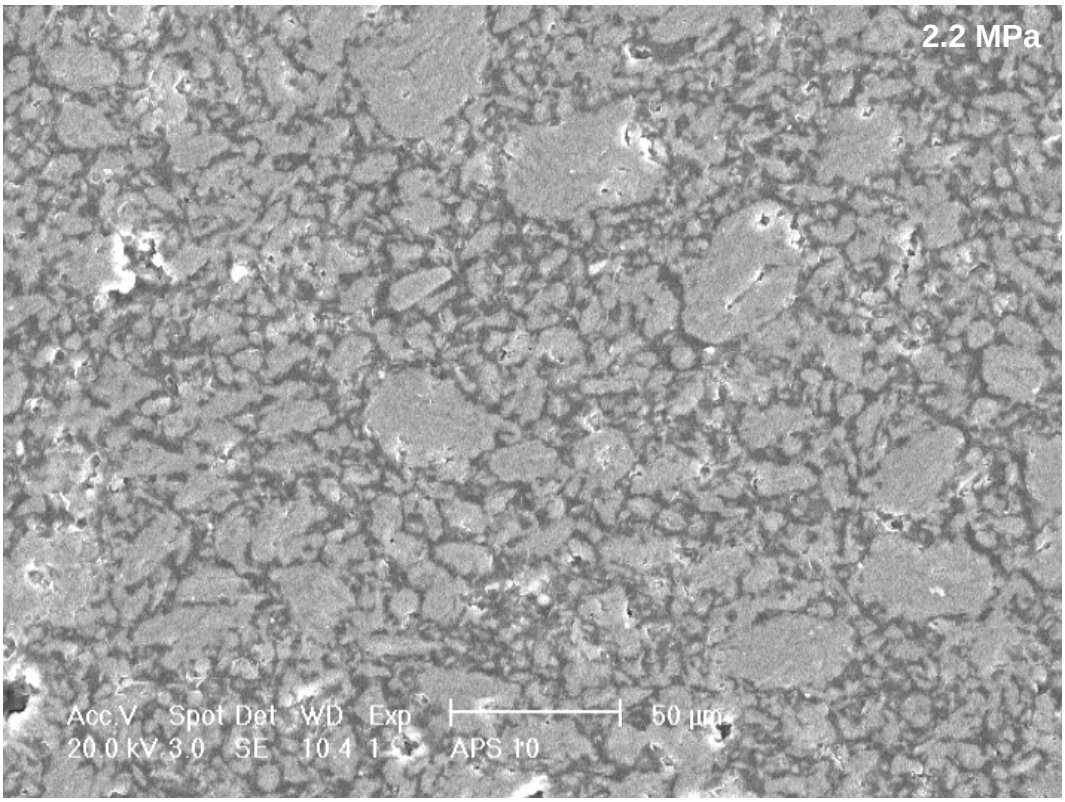

(c)

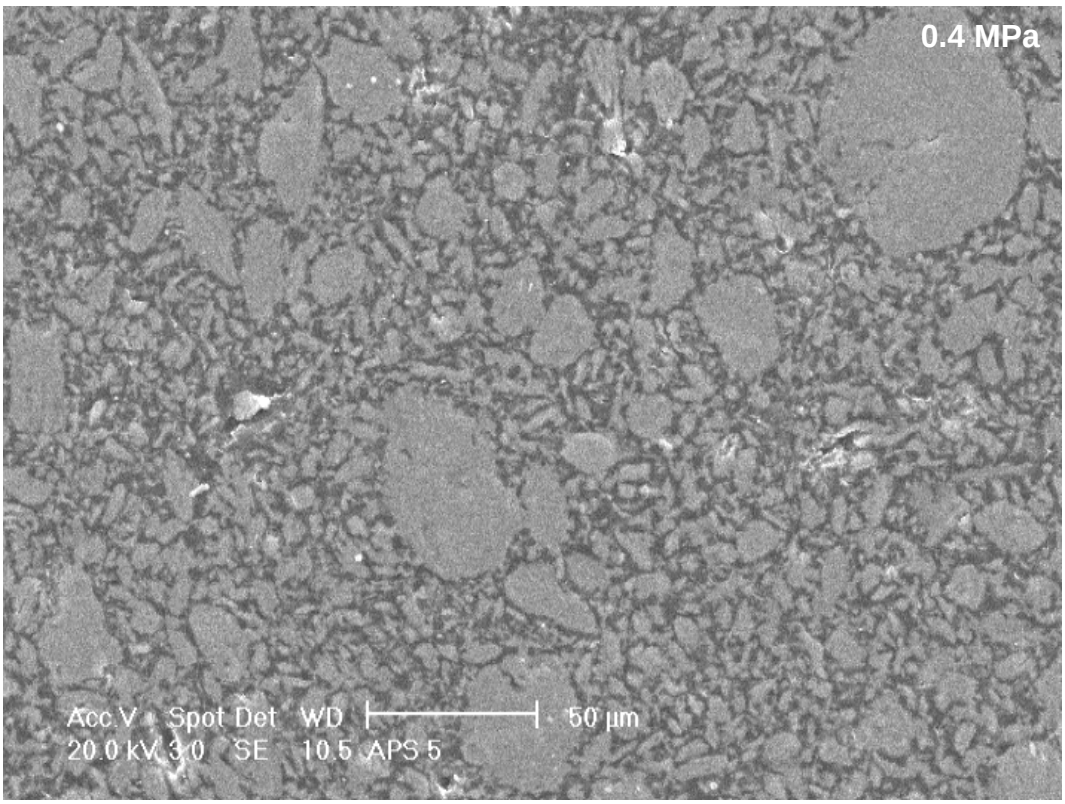

(d)

Figure 6.4 cont'd: Samples corresponding to Si:Al = 1.08. The compressive strength of the samples, where measured, is given in the top right corner of the image – NM indicates "not measured". Samples: **(c)** 1.1/0.8, 2.2 MPa and **(d)** 1.1/0.6, 0.4 MPa.

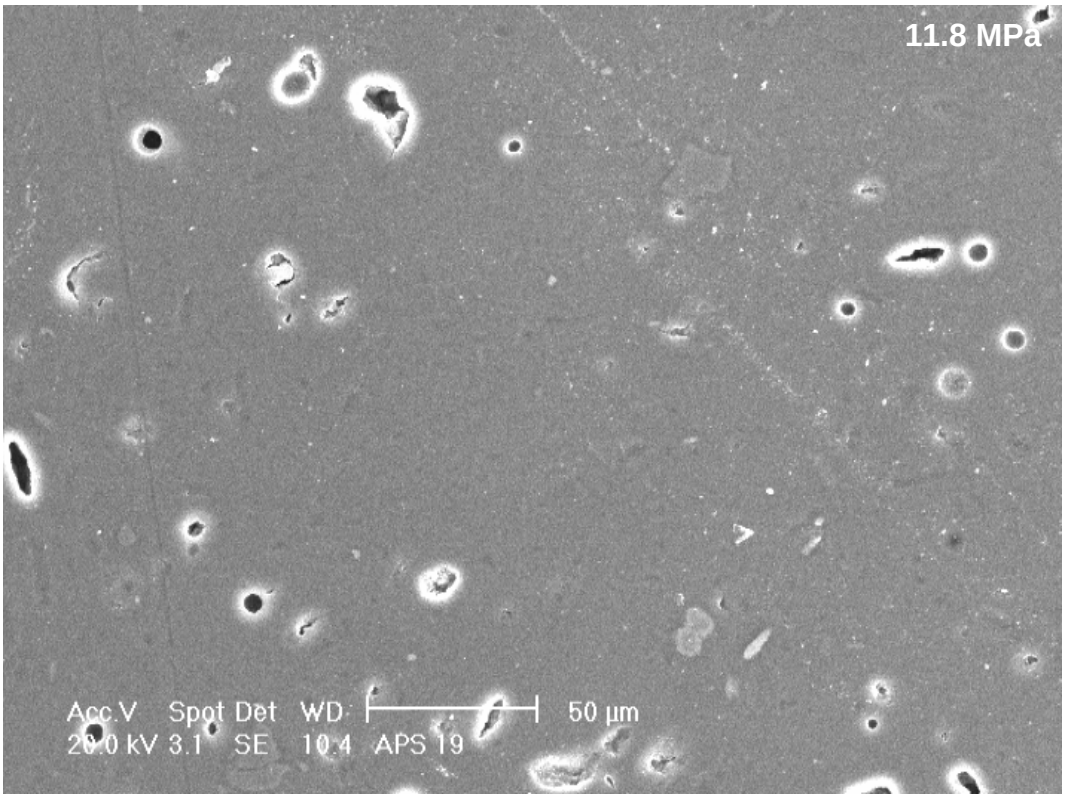

(a)

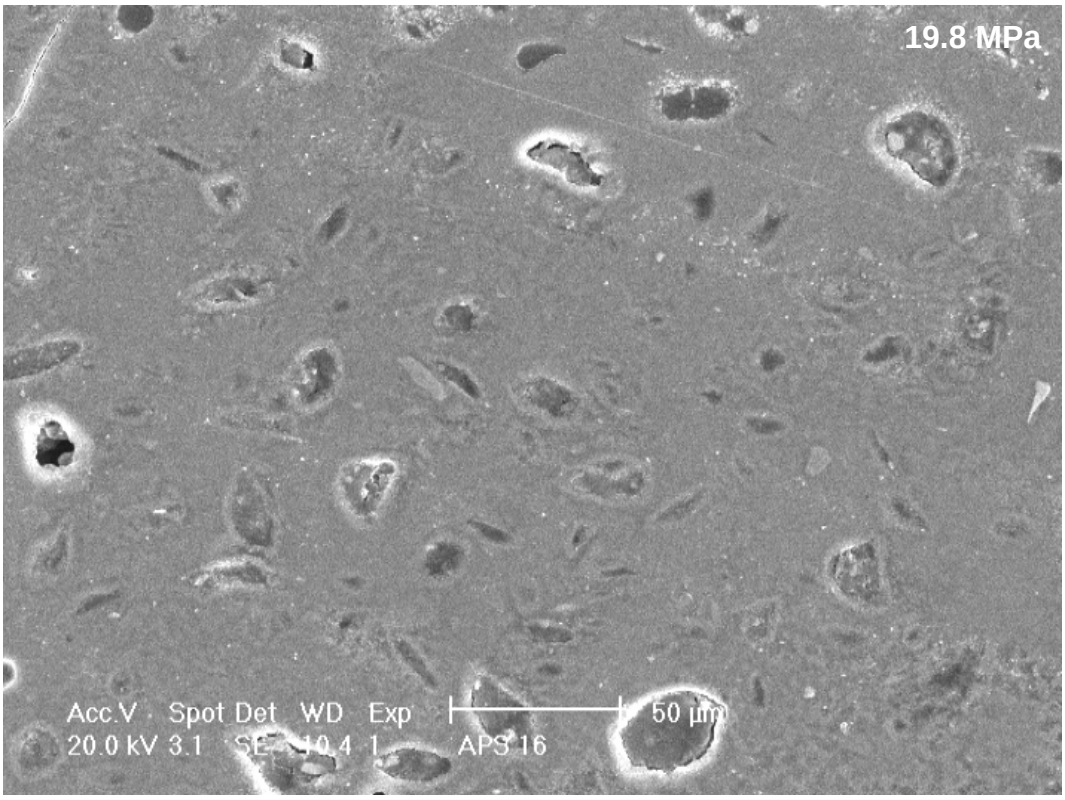

(b)

Figure 6.5: Samples corresponding to Si:Al = 1.5. The compressive strength of the samples, where measured, is given in the top right corner of the image – NM indicates "not measured". Samples: **(a)** 1.5/2.0, **(b)** 1.5/1.5, **(c)** 1.5/1.0, **(d)** 1.5/0.8 and **(e)** 1.5/0.6.

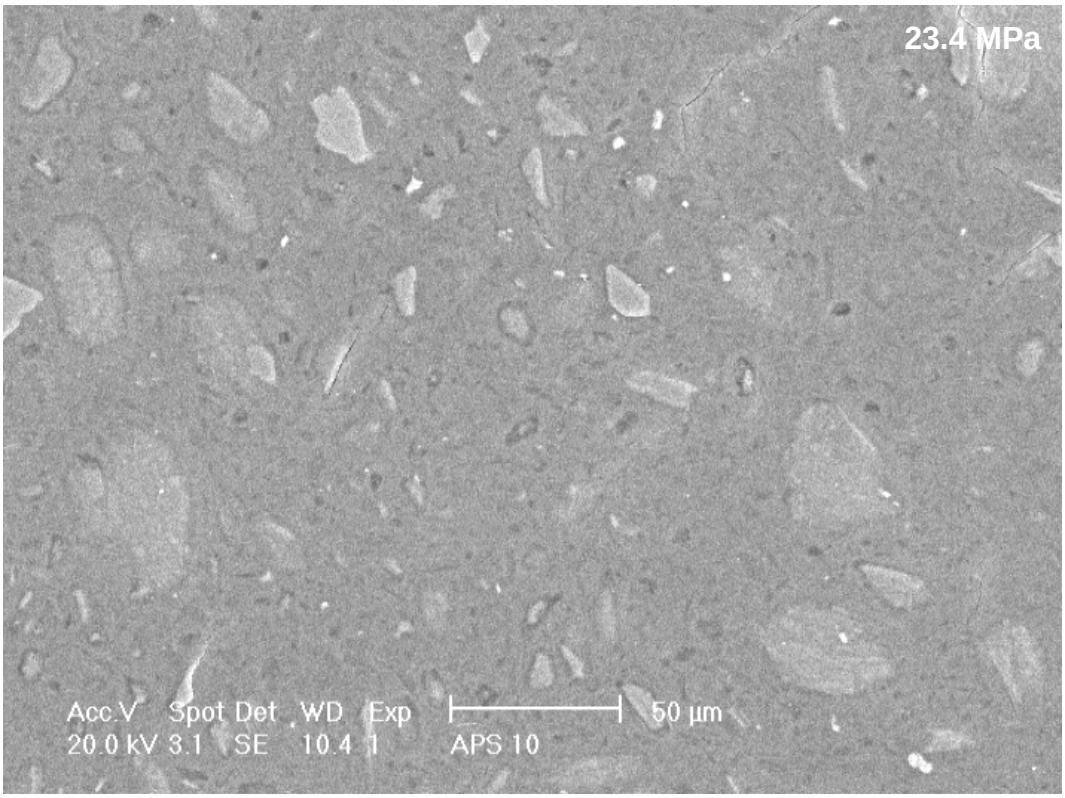

(c)

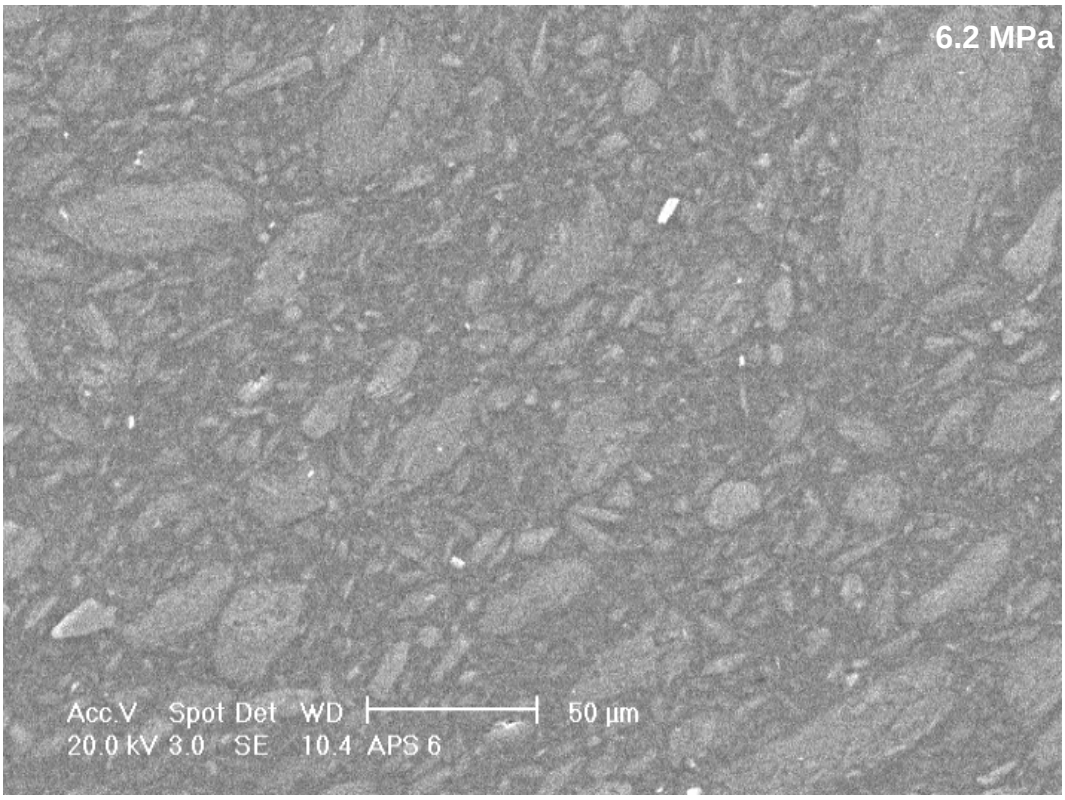

(d)

Figure 6.5 cont'd: Samples corresponding to Si:Al = 1.5. The compressive strength of the samples, where measured, is given in the top right corner of the image – NM indicates "not measured". Samples: **(c)** 1.5/1.0 and **(d)** 1.5/0.8.

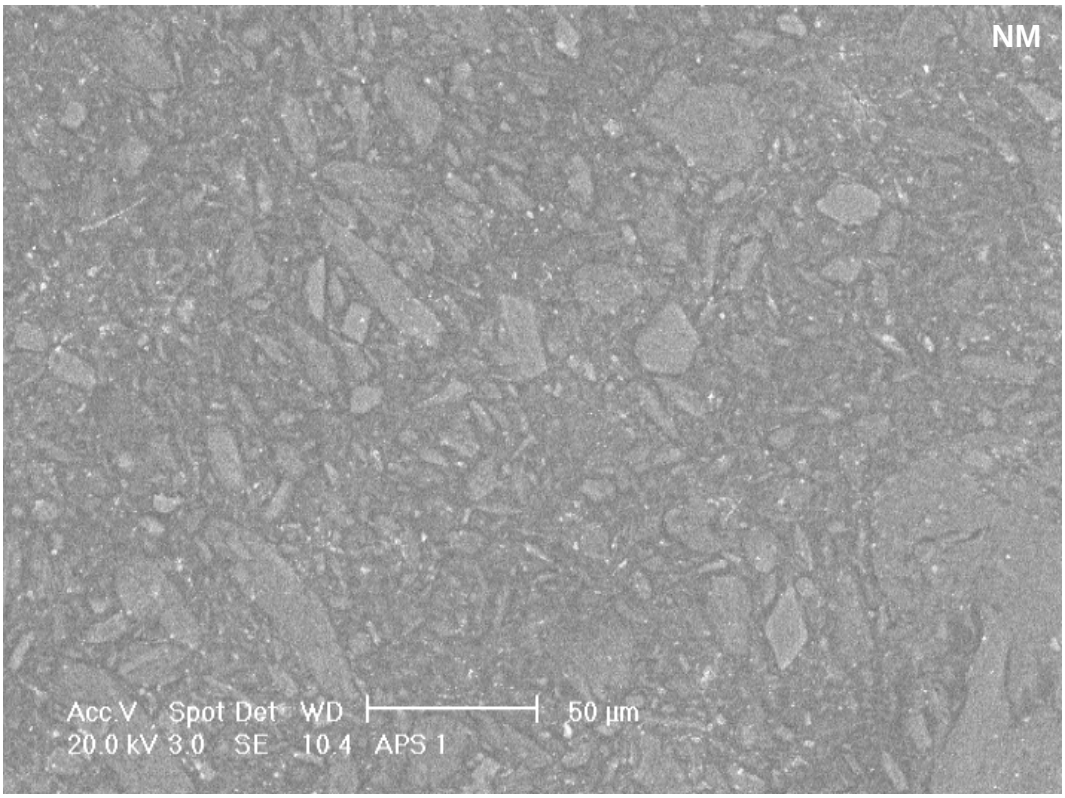

(e)

Figure 6.5 cont'd: Samples corresponding to Si:Al = 1.5. The compressive strength of the samples, where measured, is given in the top right corner of the image – NM indicates "not measured". **(e)** 1.5/0.6.

microstructure is shown by Sample 1.5/1.0. In this material, there is much more of the matrix, and its hardness is approximately the same as the grains, as shown by the lack of surface relief between the two phases.

In the upper central part of Sample 1.5/1.0, quartz grains can be seen distinctly in the AIP matrix. The quartz grains also show relief due to the sample preparation process. Samples 1.5/1.5 and 1.5/2.0 display a homogenous microstructure with some evidence of grain pullout which demonstrates that the bonding between the two phases in this sample is relatively weak. Comparison of the surface relief of the samples due to polishing indicates that the matrix phase is increasing in hardness relative to the grains with an increasing Na:Al ratio. The increase in hardness follows the increase in the compressive strength of the samples.

Si:Al = 2.0

As the Na:Al ratio of Samples 2.0/0.8, 2.0/1.0, 2.0/1.3 and 2.0/2.0 increases, the microstructure changes from grainy to uniform. Most samples, as seen in Figure 6.6, show the grain structure reminiscent of the original MK, with the relative amount of matrix phase increasing with an increasing Na:Al ratio.

Sample 2.0/0.8 shows the same low strength microstructure as the Si:Al = 1.08 samples, whereas Samples 2.0/1.0 and 2.0/1.3 show the high strength microstructure with the relative amount of matrix phase present increasing with an increasing Na:Al ratio. Samples 2.0/1.0 and 2.0/1.3 exhibit a similar surface finish from the polishing process between both the grain and matrix phases. Sample 2.0/1.3 shows some signs of grain pullout. Sample 2.0/2.0 shows a homogenous microstructure with some evidence of grain pullout. The compressive strength of Samples 2.0/1.0 and 2.0/1.3 is quite high (~50 MPa), with Samples 2.0/0.8 and 2.0/1.5 having compressive strengths of ~10 MPa. The difference in the compressive strengths is reflected in the change of the microstructure.

Si:Al = 2.5

Samples 2.5/1.0, 2.5/1.3 and 2.5/1.5, show only uniform microstructures. All samples, as seen in Figure 6.6, show a grain structure reminiscent of the original MK, with the amount of intervening matrix material changing with different Na:Al ratios.

Sample 2.5/1.0 shows a uniform microstructure with some evidence of cracking, which could be due to the preparation of the samples for SEM. Sample 2.5/1.3, which had the highest compressive strength, and Sample 2.5/1.5 exhibit a grainy microstructure, however, the surface relief due to polishing of these samples is reversed to that previously seen. In these two cases, the hardness of the matrix is greater than that of the grains. The increase in hardness could account for the increase in compressive strength.

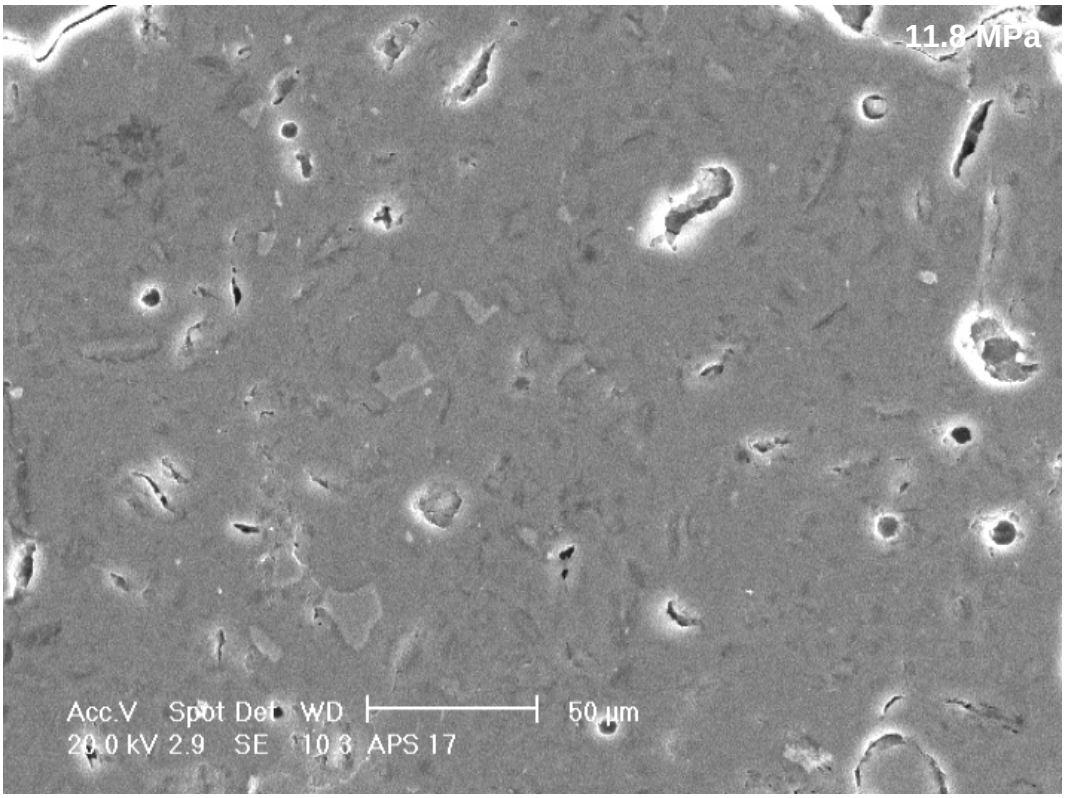

(a)

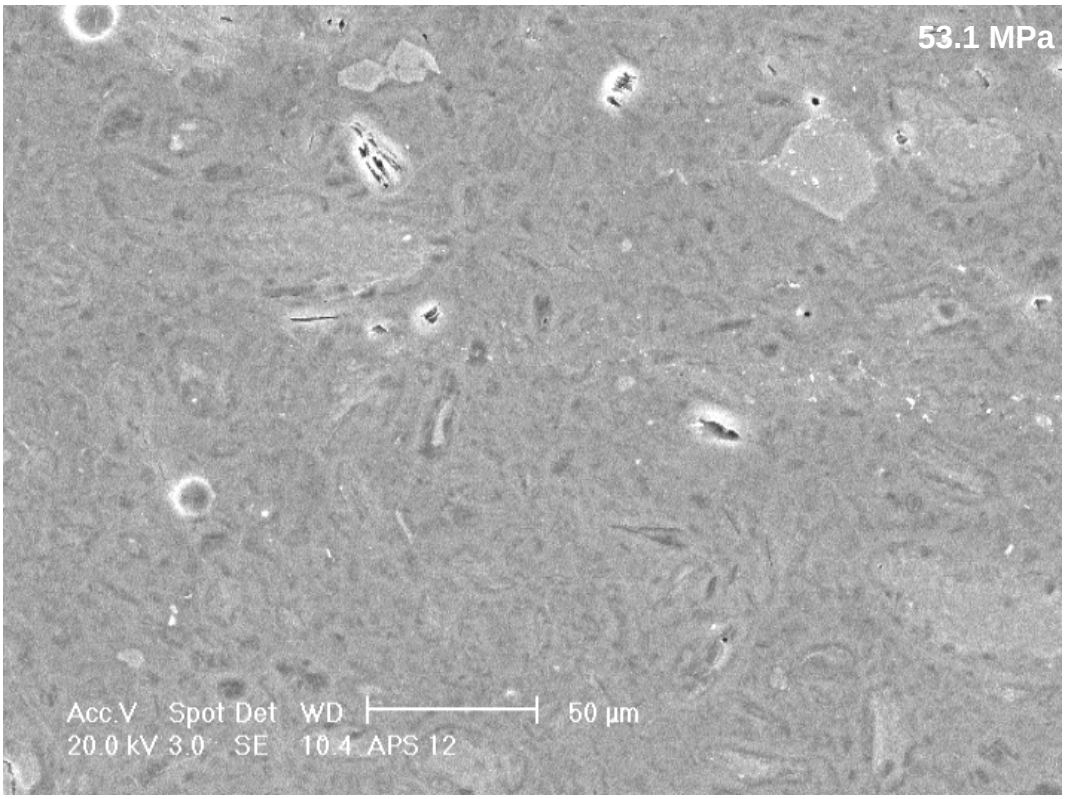

(b)

Figure 6.6: Samples corresponding to Si:Al = 2.0. The compressive strength of the samples, where measured, is given in the top right corner of the image – NM indicates "not measured". Samples: **(a)** 2.0/2.0, **(b)** 2.0/1.3, **(c)** 2.0/1.0 and **(d)** 2.0/0.8.

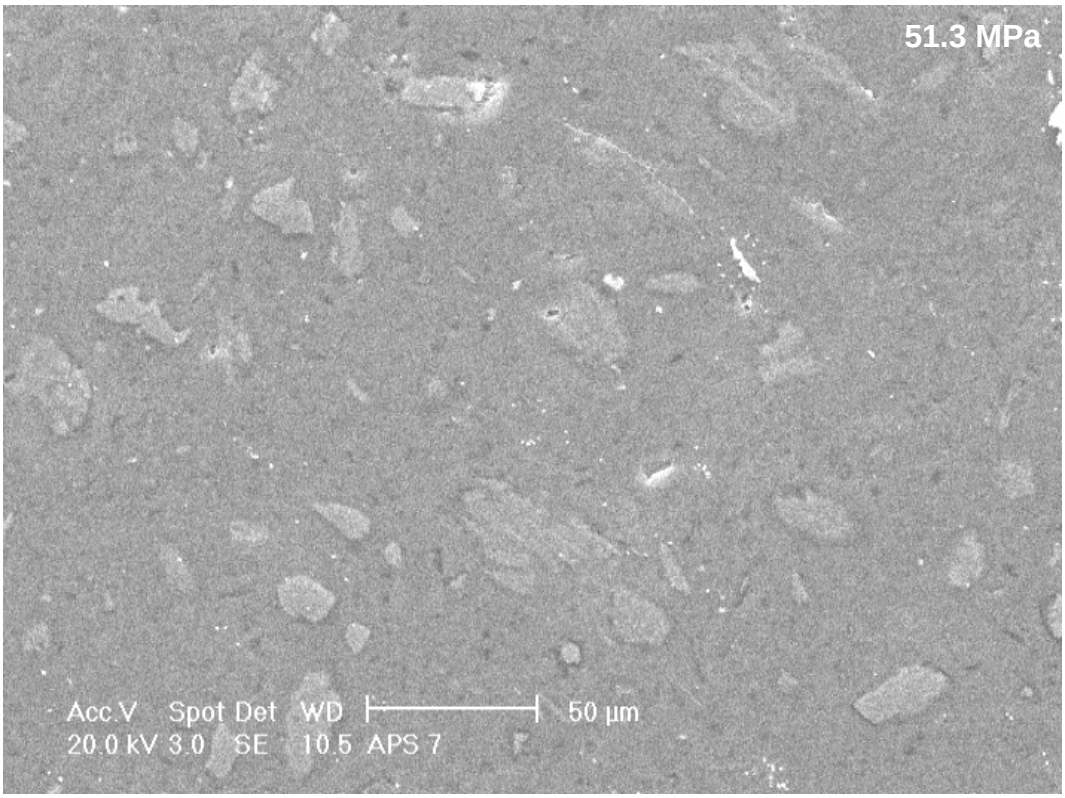

(c)

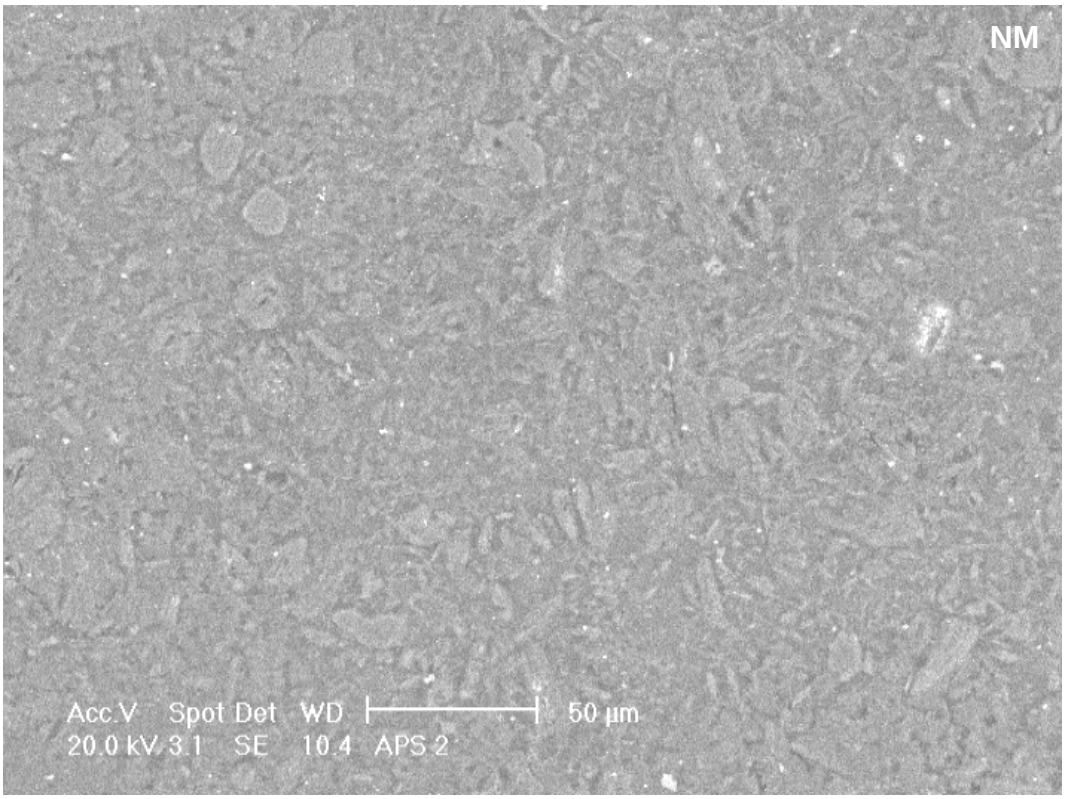

(d)

Figure 6.6 cont'd: Samples corresponding to Si:Al = 2.0. The compressive strength of the samples, where measured, is given in the top right corner of the image – NM indicates "not measured". Samples: **(c)** 2.0/1.0 and **(d)** 2.0/0.8.

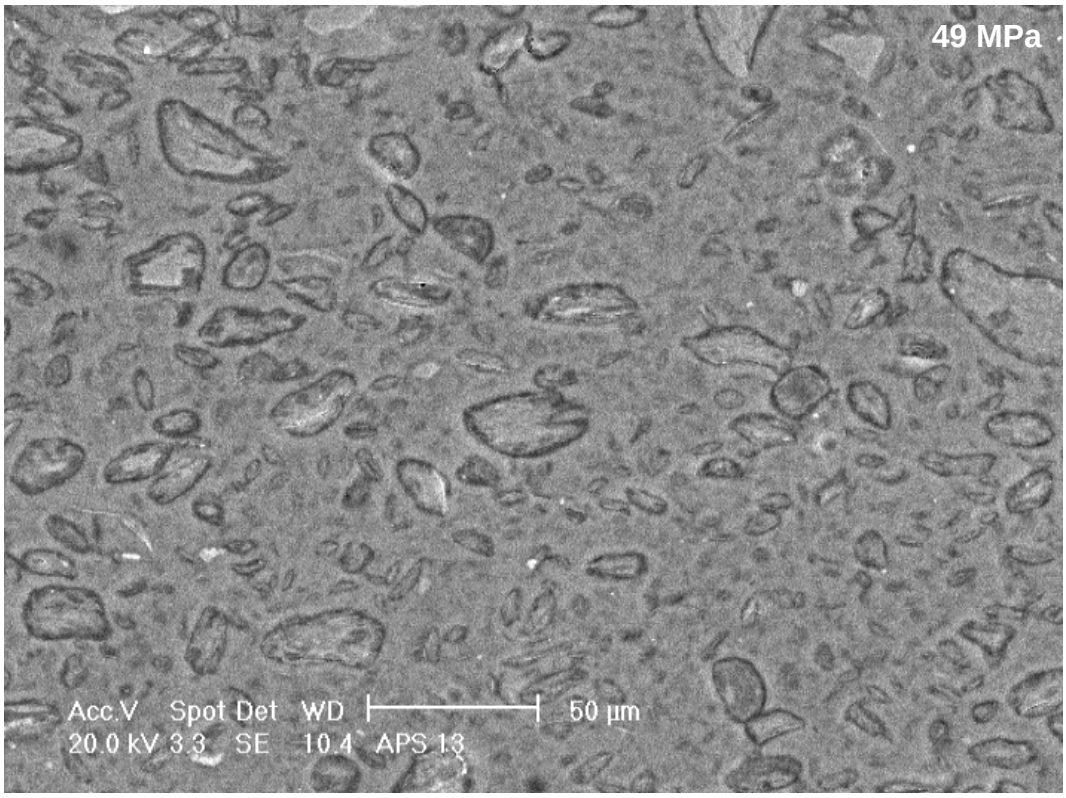

(a)

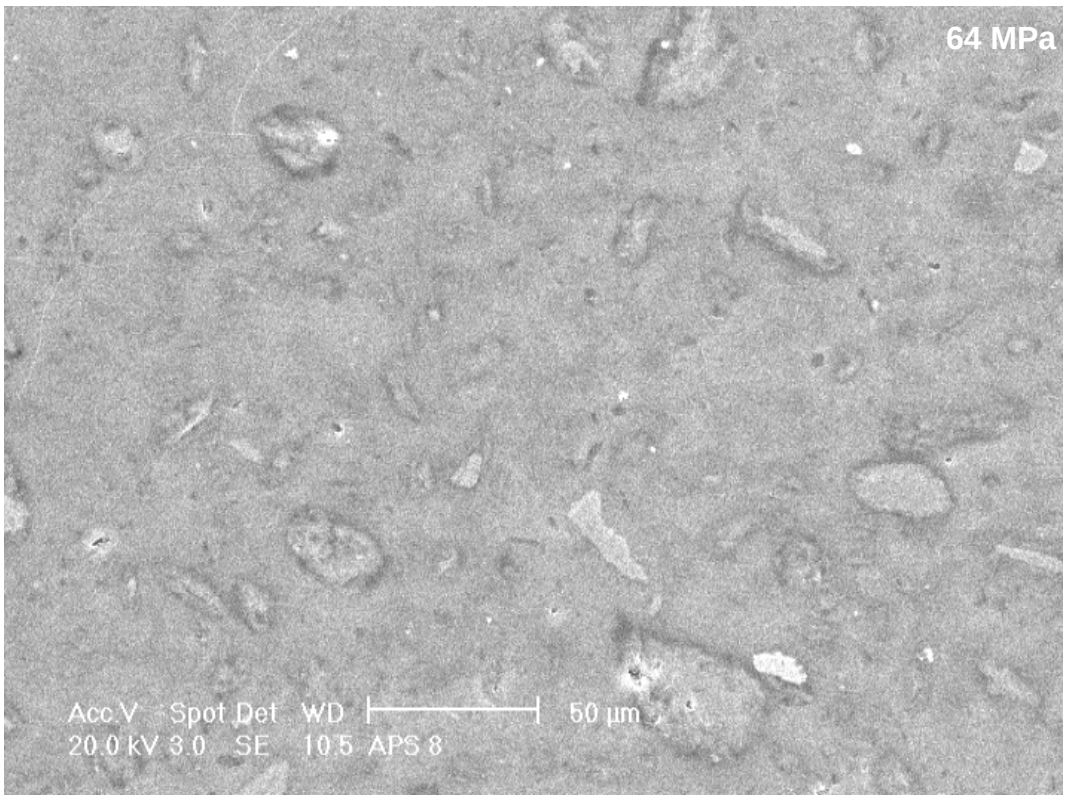

(b)

Figure 6.7: Samples corresponding to Si:Al = 2.5. The compressive strength of the samples, where measured, is given in the top right corner of the image – NM indicates "not measured". Samples: **(a)** 2.5/1.5, **(b)** 2.5/1.3 and **(c)** 2.5/1.0.

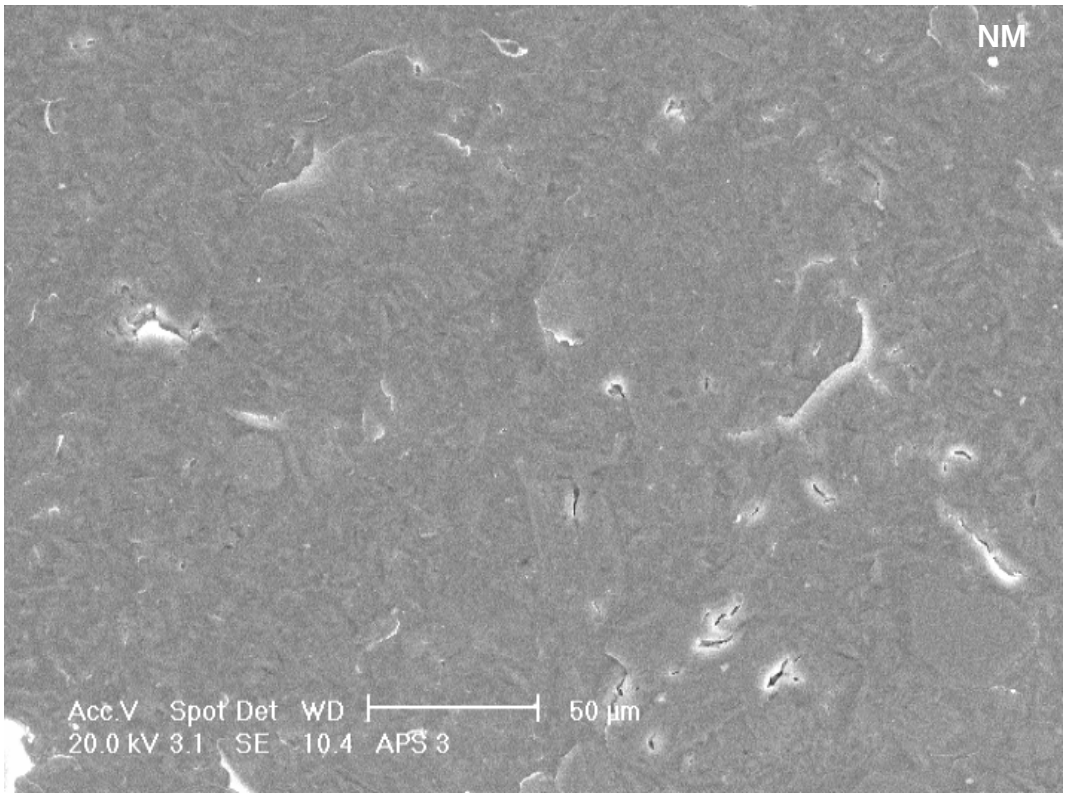

(c)

Figure 6.7 cont'd: Samples corresponding to Si:Al = 2.5. The compressive strength of the samples, where measured, is given in the top right corner of the image – NM indicates "not measured". Sample: **(c)** 2.5/1.0.

Si:Al = 3.0

Samples 3.0/1.5 and 3.0/2.0 show only uniform microstructures, with compressive strengths of 2.6 and 19.9 MPa, respectively. All samples, as seen in Figure 6.8, show the grain structure reminiscent of the original MK, with the amount of intervening matrix material changing.

Sample 3.0/1.5 shows extensive cracking. It is not known if this is due to the sample preparation process, but it could explain the dramatic decrease in the strength of this sample. No polishing relief was seen in this sample. Sample 3.0/2.0 shows polishing relief, indicating the relative hardness of the grains is lower. No cracking was observed in this sample, perhaps accounting for its higher strength compared to Sample 3.0/1.5.

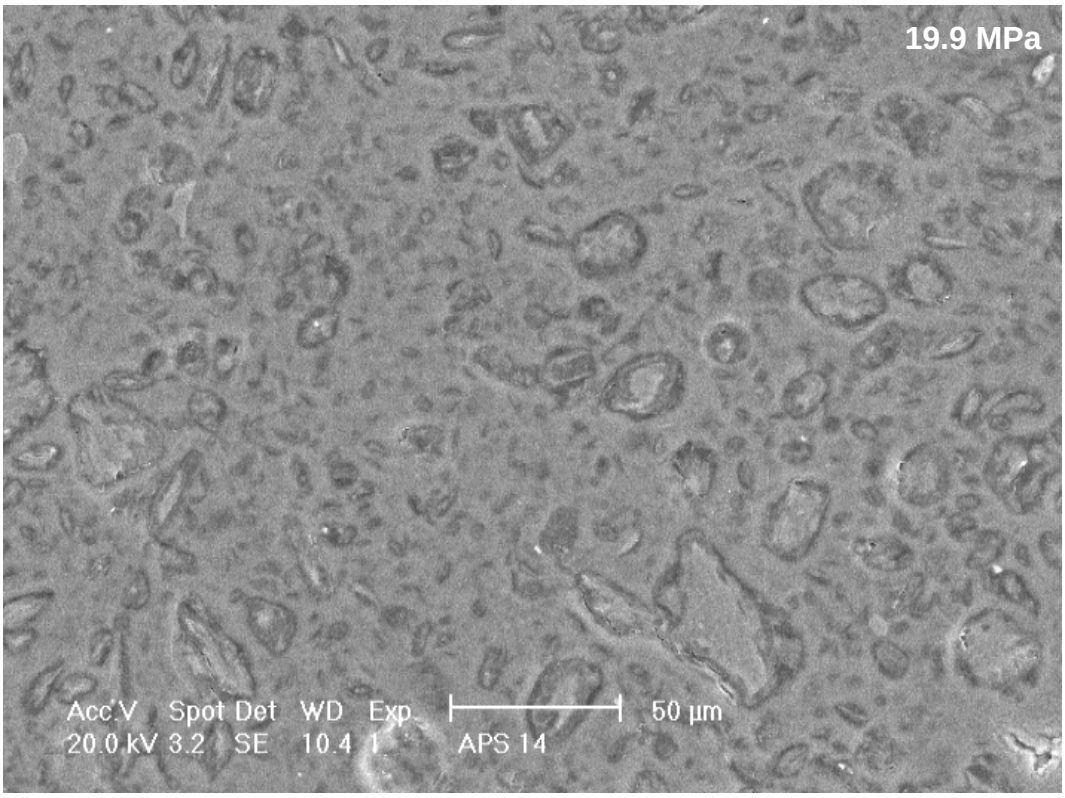

(a)

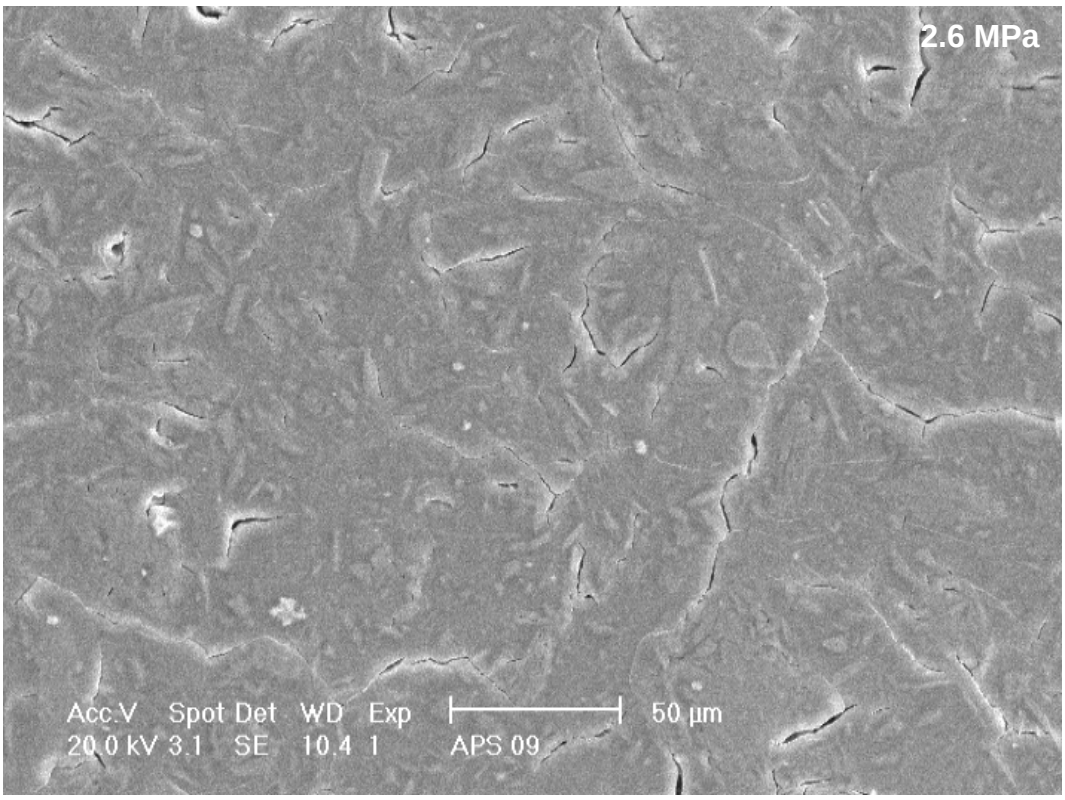

(b)

Figure 6.8: Samples corresponding to Si:Al = 3.0. The compressive strength of the samples, where measured, is given in the top right corner of the image. Samples: **(a)** 3.0/2.0 and **(b)** 3.0/1.5.

6.1.3 Microstructure analysis summary

Analysis of the SEM images taken of the AIPs show that, as a general rule, the low strength AIPs exhibit a “grainy” microstructure, where the major phase consists of grains reminiscent of the MK precursor. High strength AIPs showed a more uniform microstructure, with the matrix phase being dominant. The grains present in the high strength samples showed a preferential loss of material at the grain boundaries as a result of the sample preparation process, demonstrating that the grain phase is softer than the surrounding matrix.

Samples 1.5/1.5, 1.5/2.0 and 2.0/2.0 had a uniform microstructure, yet their strength was lower than could be expected for a uniform material. The uniform microstructure and the low compressive strength are both thought to be due to the high Na content of these AIPs, showing that knowledge of both the chemistry and microstructure is required to draw any conclusions with regards to the properties of the material on the macroscale.

The variation in the compressive strength of the AIPs cannot be attributed solely to changes in the microstructure as it can be shown that the chemical composition of the AIP also causes changes in the compressive strength. This point is highlighted by the comparison of Samples 1.5/1.0 & 2.0/1.0 (Figure 6.5(c) & Figure 6.6(c)) and Samples 2.5/1.5 & 3.0/2.0 (Figure 6.7(a) & Figure 6.8(a)). The microstructures of these two sets of samples is similar, however there is a 100% difference in the compressive strengths of the samples of each set.

No features were identified in the micrographs as being sufficiently different as to be attributed to the presence of zeolites, suggesting that the zeolites were distributed throughout the AIPs rather than as localised crystals. Samples 1.1/1.5, 1.5/1.5, 1.5/2.0 and 2.0/2.0 formed Na_2CO_3 crystals on the sample surface due to atmospheric CO_2 interacting with excess Na present in the material. Small particles consisting of Ti and Fe were sometimes seen on the surface of the samples. Silica grains were also observed on the sample surface.

6.2 Elemental analysis

As shown in §6.1 the microstructure of the AIPs varies substantially with composition. This variation is also seen in the distribution of the elements within the AIPs. In order to discuss both the overall trends in the chemistry and to allow sample specific discussion, this section is split into two subsections. The first deals with the broad trends, and common features found in all AIPs. The second briefly discusses each of the AIPs made in the current study.

6.2.1 Results and discussion

For each sample, micrographs of 5 sites of interest were collected of approximately 300 x 200 μm. On each of these sites of interest, an EDS spectrum was collected of the entire area, for 5 points on grains and for 5 points within the matrix. The local composition results showed that there was a significant difference between the composition of the grains and that of the matrix for almost all of the samples. All of the images representing the sites of interest used in EDS analysis are reproduced in Appendix I. The average compositions for each of the set of results from the samples are given in Table 6.1. Graphical representations of the results are given in Figure 6.9 and Figure 6.10. A table of results detailing the individual compositions of all the analysed spots is given in Appendix II. A graphical representation of the results follows in Appendix III.

The presence of a two-phase microstructure means that the composition of the matrix and grains is different, as discussed in the following sections. Generally, the matrix phase has an Si:Al ratio higher than the nominal ratio for the sample, whereas the grain phase has a lower Si:Al ratio. For both the matrix and grain phases, the measured Na:Al ratio was lower than the nominal composition, indicating that Na had been lost from the sample due to the SEM sample preparation process, or by migration away from the electron beam. Regardless of the absolute Na:Al ratios, the Na:Al ratio of the matrix phase always exceeded that of the grain phase. The observation that Na was leached in the sample preparation process shows

Table 6.1: Sample molar ratio compositions by EDS and x-ray fluorescence (XRF), listed by sample number. "N" denotes the nominal sample composition, "X" denotes the sample composition as determined by XRF[a], "A" denotes the area composition, "G" denotes the grain composition and "M" denotes the matrix composition. Errors given are 2σ, derived from approximately 25 observations from each sample.

		Si:Al			Na:Al		
1.1/0.6	N	1.08			0.51		
	X	1.10			0.51		
	A	0.90	±	0.10	0.46	±	0.05
	G	1.03	±	0.06	0.33	±	0.05
	M	0.83	±	0.09	0.42	±	0.05
1.1/0.8	N	1.08			0.75		
	X	-			-		
	A	1.26	±	0.11	0.97	±	0.13
	G	1.18	±	0.05	0.56	±	0.07
	M	1.4	±	0.4	0.8	±	0.2
1.1/1.0	N	1.08			1.00		
	X	-					
	A	1.22	±	0.12	0.92	±	0.17
	G	1.15	±	0.05	0.74	±	0.06
	M	1.3	±	0.2	1.1	±	0.3
1.1/1.5	N	1.08			1.53		
	X	-			-		
	A	1.18	±	0.10	1.76	±	0.13
	G	1.17	±	0.07	1.37	±	0.12
	M	1.22	±	0.11	1.78	±	0.16
1.5/0.6	N	1.50			0.51		
	X	-			-		
	A	1.8	±	0.3	0.8	±	0.3
	G	1.32	±	0.07	0.23	±	0.06
	M	2.0	±	0.2	1.2	±	0.2
1.5/0.8	N	1.50			0.75		
	X	1.49			0.70		
	A	1.6	±	0.3	1.2	±	0.2
	G	1.41	±	0.09	0.43	±	0.09
	M	1.8	±	0.2	1.5	±	0.2
1.5/1.0	N	1.50			1.00		
	X	1.52			0.92		
	A	1.75	±	0.12	0.71	±	0.08
	G	1.40	±	0.07	0.37	±	0.07
	M	1.74	±	0.10	0.69	±	0.05
1.5/1.5	N	1.50			1.53		
	X	-			-		
	A	1.73	±	0.10	1.23	±	0.11
	G	1.9	±	0.2	1.3	±	0.3
	M	1.67	±	0.07	1.02	±	0.06
1.5/2.0	N	1.50			2.00		
	X	-			-		
	A	1.73	±	0.15	1.22	±	0.14
	G	1.75	±	0.18	1.12	±	0.11
	M	1.73	±	0.10	1.11	±	0.07
2.0/0.8	N	2.00			0.75		
	X	-			-		
	A	2.4	±	0.3	1.1	±	0.2
	G	1.56	±	0.11	0.27	±	0.08
	M	3.9	±	0.5	2.1	±	0.4
2.0/1.0	N	2.00			1.00		
	X	2.00			0.95		
	A	2.22	±	0.17	0.88	±	0.09
	G	1.55	±	0.10	0.26	±	0.05
	M	2.38	±	0.14	0.94	±	0.07
2.0/1.3	N	2.00			1.26		
	X	1.94			1.09		
	A	2.29	±	0.17	0.84	±	0.10
	G	1.65	±	0.15	0.39	±	0.07
	M	2.32	±	0.11	0.73	±	0.06
2.0/2.0	N	2.00			2.00		
	X	1.98			1.80		
	A	2.19	±	0.11	1.26	±	0.11
	G	2.06	±	0.16	1.04	±	0.15
	M	2.13	±	0.06	1.08	±	0.04
2.5/1.0	N	2.50			1.00		
	X	-			-		
	A	2.81	±	0.19	0.53	±	0.11
	G	1.9	±	0.3	0.26	±	0.09
	M	3.2	±	0.5	0.59	±	0.15
2.5/1.3	N	2.50			1.26		
	X	2.42			1.15		
	A	3.04	±	0.19	1.37	±	0.14
	G	1.7	±	0.2	0.35	±	0.09
	M	3.24	±	0.19	1.36	±	0.11
2.5/1.5	N	2.50			1.53		
	X	-			-		
	A	2.9	±	0.2	1.03	±	0.09
	G	1.66	±	0.15	0.31	±	0.06
	M	3.15	±	0.15	1.11	±	0.06
3.0/1.5	N	3.00			1.53		
	X	3.03			1.49		
	A	3.2	±	0.3	0.56	±	0.11
	G	2.2	±	0.4	0.29	±	0.10
	M	3.7	±	0.7	0.60	±	0.14
3.0/2.0	N	3.00			2.00		
	X	-			-		
	A	3.5	±	0.3	1.8	±	0.3
	G	1.64	±	0.16	0.32	±	0.08
	M	3.65	±	0.19	1.55	±	0.11

[a] Compositions were determined by XRF only for those samples to be analysed by the RDF technique.

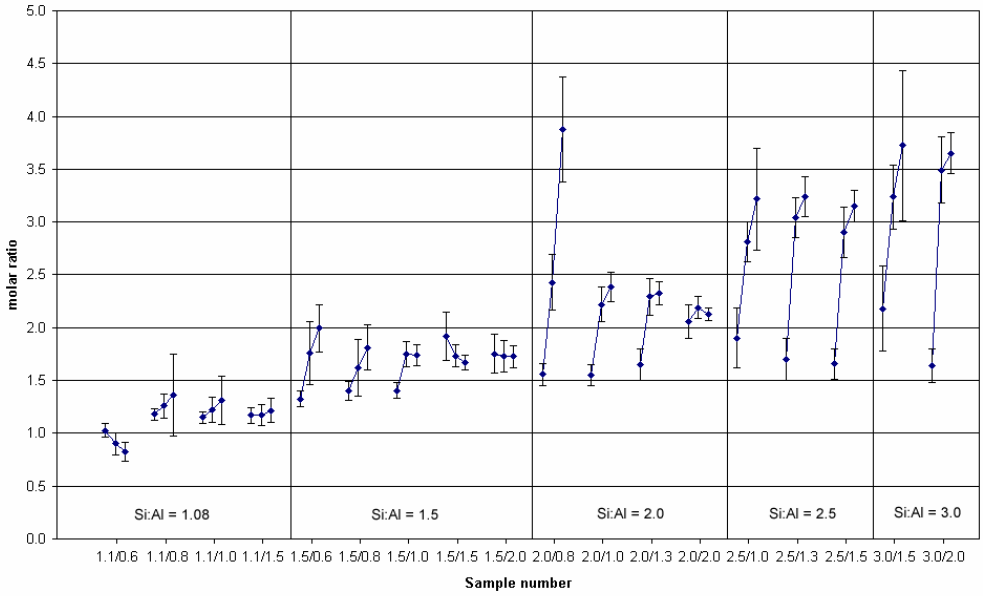

Figure 6.9: Graphical representation of the Si:Al ratios in the AlPs studied, grouped according to Si:Al ratio, with the Na:Al ratio increasing from left to right in each group. The first data point for each sample refers to the grain composition, the second is the area composition, whilst the last data point denotes the matrix composition. Errors denote 2σ.

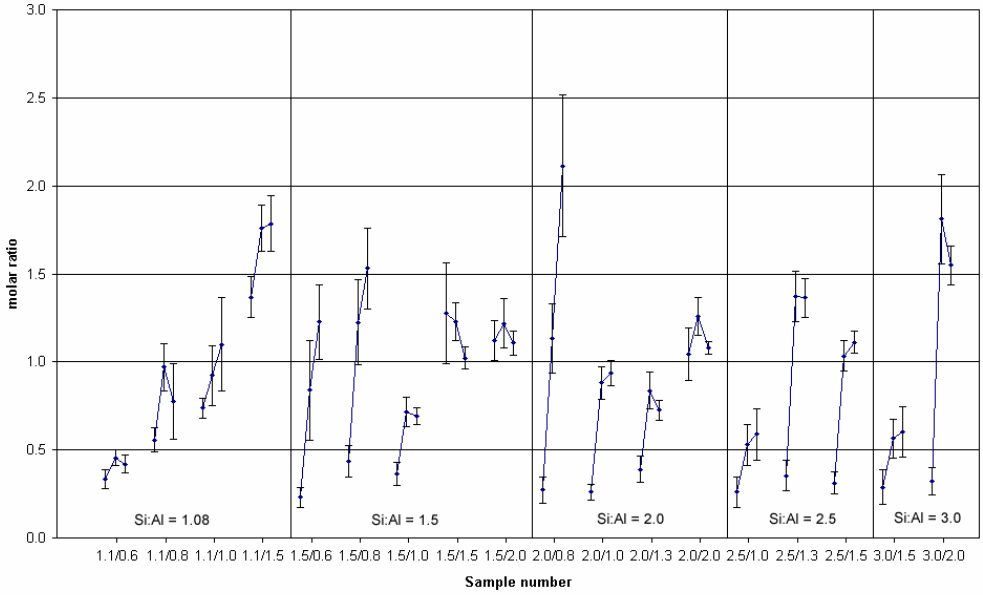

Figure 6.10: Graphical representation of the Na:Al ratios in the AlPs studied, grouped according to Si:Al ratio, with the Na:Al ratio increasing from left to right in each group. The first data point for each sample refers to the grain composition, the second is the area composition, whilst the last data point denotes the matrix composition. Errors denote 2σ.

that not all of the Na is strongly bonded to the polymer network. It may also indicate that not all of the Na present in the sample is involved in the formation of the polymer network. EDS results from Sample 3.0/1.5 are used

to illustrate the differences between the composition of the two phases. Sample 3.0/1.5 has a nominal composition of Si:Al:Na = 3.0:1:1.53. The overall composition of the sample by XRF was found to be Si:Al:Na = 3.03:1:1.49. From Table 6.1 it can be seen that the composition of the matrix phase is Si:Al:Na = 3.7:1:0.68, whilst the composition of the grain phase is Si:Al:Na = 2.2:1:0.29. The matrix network formula for the highest strength sample is $Na_n[-(SiO_2)_{3.2}-(AlO_2)-]_n$.

Matrix compositional trends

The discussion in this section aims to provide information on how the dissolution of MK proceeds according to the overall chemical composition of the AIP with particular reference to the Si:Al and Na:Al ratios of the matrix phase.

The Si:Al ratio of the matrix increases with increasing Si:Al ratio, as shown in Figure 6.11, indicating that the matrix phase consists of dissolved and reformed aluminosilicate. As Al is present only in the MK precursor, this shows that the matrix phase is the 'true' inorganic polymer.

Inspection of Figure 6.9 indicates that within groups of samples with constant nominal Si:Al ratios, the Si:Al ratio of the matrix of each sample decreases with an increasing Na:Al ratio, showing that the Al content of the matrix is increasing as more MK is being dissolved. Examination of the SEM images shows that the relative amount of the matrix increases with an increasing Na:Al ratio, showing that more Al is being incorporated into the AIP through the dissolution of MK, which results in the high strength microstructure.

If an average Si:Al ratio of the matrix is calculated for samples with the same Si:Al ratio, then it is seen that the average matrix Si:Al ratio for the Si:Al = 1.5 and 2.0 samples is greater than the nominal Si:Al by 0.3. The average matrix Si:Al ratio for the Si:Al = 2.5 and 3.0 samples is greater than the nominal Si:Al ratio by 0.7. The increase in the matrix Si:Al ratio over the nominal Si:Al

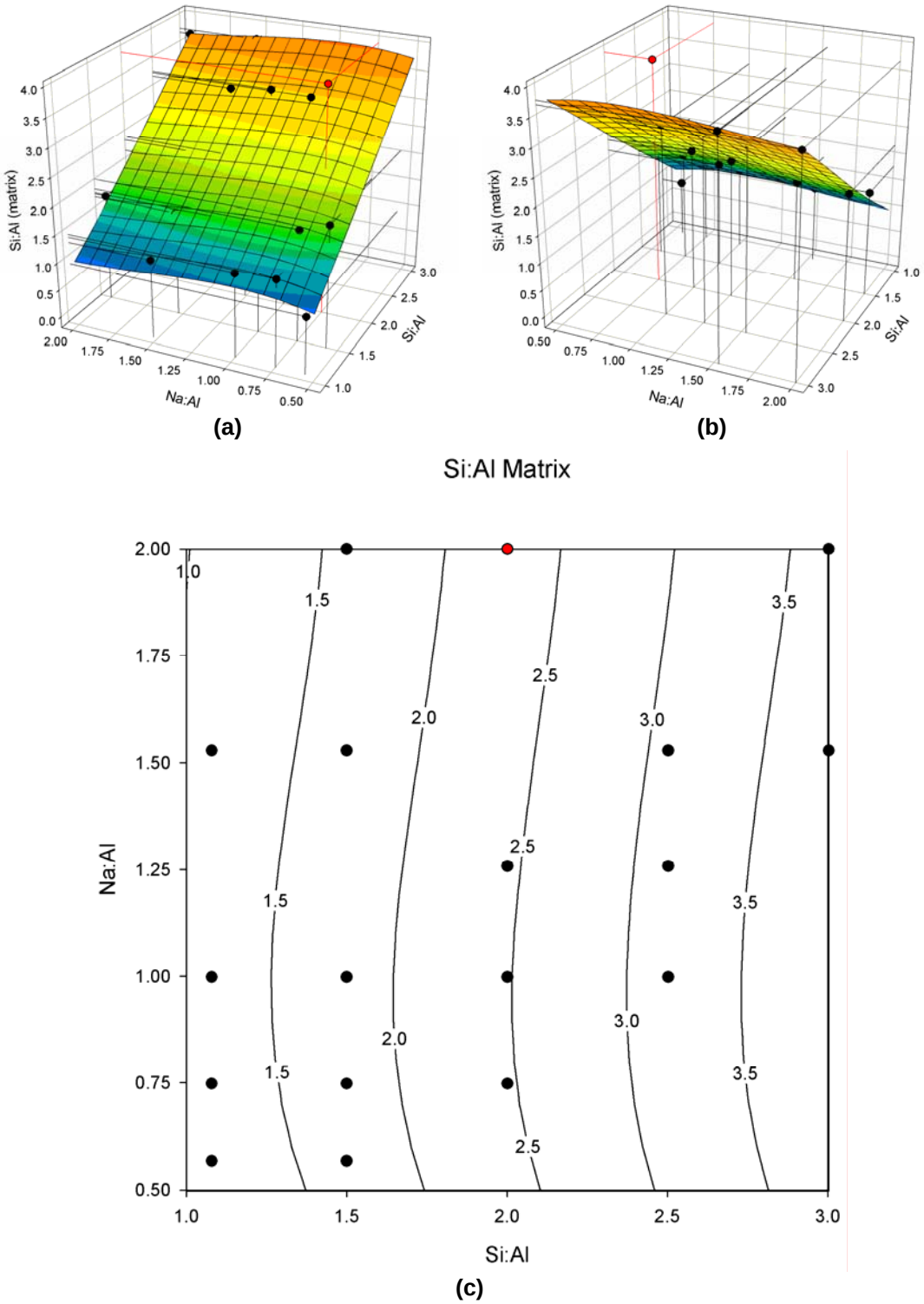

Figure 6.11: Representation of the Si:Al molar ratios in the matrix of the AIPs. The Si:Al/Na:Al axes represent the nominal composition of the AIP. The vertical axis gives the Si:Al molar ratio measured in the matrix. The red data point shows the sample that was excluded in the calculation of the contours. This data point represents Sample 2.0/2.0, which adversely affected the fit of the contours. **(a)** 3D representation of the contour plot with the data points shown to provide an indication of the scatter in the data. **(b)** A second representation of (a) with the Si:Al/Na:Al axes reversed. **(c)** Contour projection of the 3D plot. Contour values represent the Si:Al molar ratios in the grains of the AIPs, with an interval of 0.5.

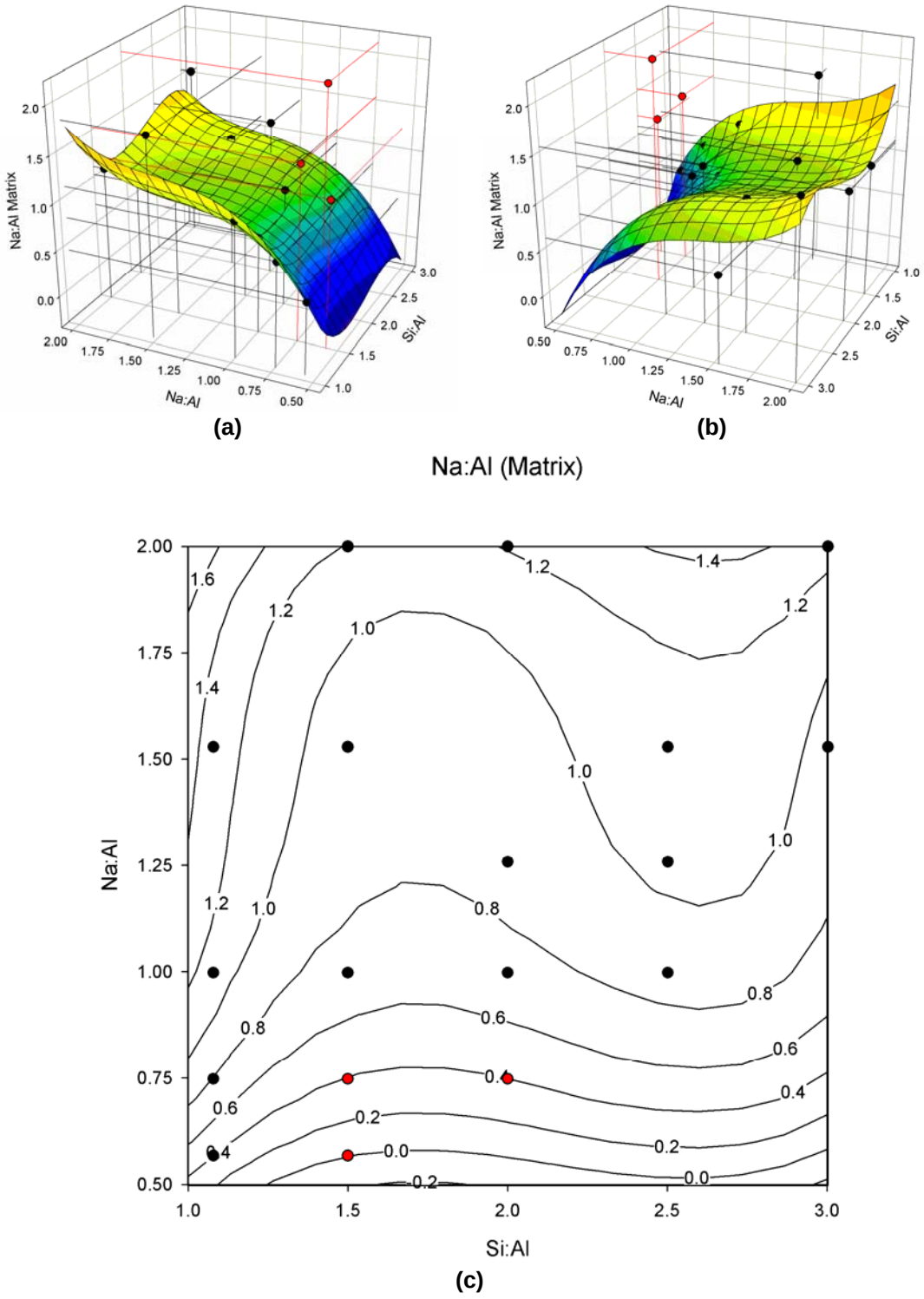

Figure 6.12: Representation of the Na:Al molar ratios in the matrix of the AIPs. The Si:Al/Na:Al axes represent the nominal composition of the AIP. The vertical axis gives the Na:Al molar ratio measured in the matrix. The red data points show the samples that were excluded in the calculation of the contours. These data points represent Samples 1.5/0.6, 1.5/0.8 and 2.0/0.8, which adversely affected the fit of the contours. **(a)** 3D representation of the contour plot with the data points shown to provide an indication of the scatter in the data. **(b)** A second representation of (a) with the Si:Al/Na:Al axes reversed. **(c)** Contour projection of the 3D plot. Contour values represent the Na:Al molar ratios in the grains of the AIPs, with an interval of 0.2**.**

ratio shows that for these samples, the grains in the sample do not take up as much Si as the other samples. The additional Si, therefore, must be taken up in the matrix phase.

The Na:Al ratio of the matrix in the samples corresponding to Si:Al = 1.08, shown in Figure 6.10, increases in step with the increasing nominal Na:Al ratio of the sample, with the Na:Al ratio of the matrix approximately the same, or greater than the nominal composition of the AIP. This smooth trend is unique among the AIPs studied. For all other samples, the Na:Al ratio of the matrix follows a general increasing trend with increasing Na content that is largely independent of the Si:Al ratio. There is a larger degree of scatter in these results, seen in Figure 6.12, but the general increasing trend can be observed. The soluble nature of Na may account for the degree of scatter, as any unreacted Na present may have been leached out during the sample preparation process. Na may also have been lost due to migration away from the electron beam. Figure 6.12 shows that the Na:Al ratio of the matrix is always less than the nominal Na:Al ratio of the samples. The Na:Al ratio of the AIPs increases quickly to ~0.8, after which the Na:Al ratio plateaus to a value of ~1 – 1.2, corresponding to samples with nominal Na:Al ratios of greater than 1.25. The plateau behaviour of the Na:Al ratio indicates that Na is only incorporated into the polymer network up to a ratio of ~1.0, after which, additional Na is not used in the polymer network formation.

The chemical composition of the matrix for the sample with the highest compressive strength corresponds to a network formula of $Na_n[-(SiO_2)_{3.24}-(AlO_2)-]_n$, according to EDS analysis. The relative concentration of Na corresponds to an excess of 40% above the amount required for charge balance.

Grain compositional trends

The discussion in this section aims to provide information on how the formation of the AIP proceeds according to the overall chemical composition, with particular reference to the Si:Al and Na:Al ratios of the grain phase.

A common trend across the samples is that when Si is added in the form of the activating solution, the Si:Al ratio of the grains increases, depending on the overall Si content of the AIP, with minimal dependence on the Na content. The dependence is shown in Figure 6.13, which indicates that the Si content of the grains is set by the Si content of the AIP. The initial Si:Al ratio of the MK was 1.08. The Si content of the grains is not affected by the amount of Na present in the AIP. Note that Samples 1.5/1.5, 2.0/2.0 and 1.5/2.0 suffered from grain pullout problems in sample preparation, and as a result, their grain compositions are not representative.

The increase in the Si:Al ratio of the grains can be explained by the preferential dissolution of Al from the MK precursor. As discussed in §5.2, the OH^- content controls the dissolution of the aluminosilicate and may show that the dissolution is dependent on the concentration of the hydroxide species. An increase in the Na content of the polymer results in more of the grains dissolving, but the increase in the Na content may not affect the rate at which Al may be preferentially dissolved from the MK.

The Si:Al ratio of the grains increases through the Si:Al = 1.08/1.5 samples to a value of approximately 1.6 for the Si:Al = 2.0 – 3.0 samples, indicating that the grains have reached a “saturation point” and are unable to support any additional Si in their structure. It is conjectured that grains at this point would start to dissolve. The grains observed did not dissolve, as the movement of ions required, for the formation of the polymer, was halted due to an increase in viscosity of the AIP as a result of the curing process.

A common trend across all samples is the appearance of Na in the grains. As Na is soluble, it is possible that it was transported to the grains during sample preparation; however, the trend correlation with composition is high enough to discount this possibility. As illustrated in Figure 6.14, the Na:Al ratio of the grains is less than 0.4, and approximately constant across all sample compositions.

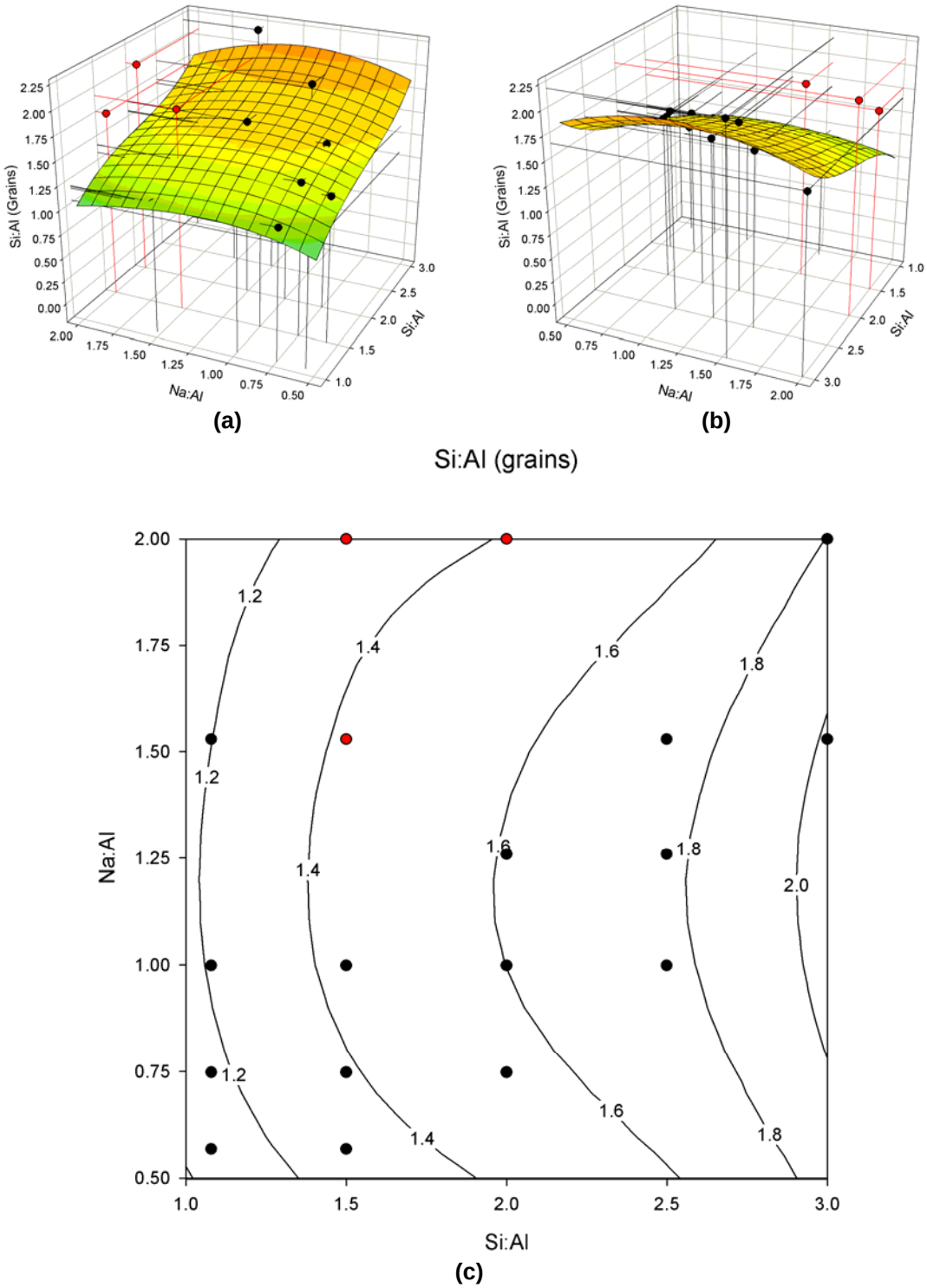

Figure 6.13: Representation of the Si:Al molar ratios in the grains of the AIPs. The Si:Al/Na:Al axes represent the nominal molar ratio composition of the AIP. The vertical axis gives the Si:Al molar ratio measured in the grains. The red data points show samples that were excluded in the calculation of the contours. These data points represent Samples 1.5/1.5, 1.5/2.0 and 2.0/2.0, which suffered from grain pullout, and as such, do not provide a representative grain measurement. **(a)** 3D representation of the contour plot with the data points shown to provide an indication of the scatter in the data. **(b)** A second representation of (a) with the Si:Al/Na:Al axes reversed. **(c)** Contour projection of the 3D plot. Contour values represent the Si:Al molar ratios in the grains of the AIPs, with an interval of 0.2.

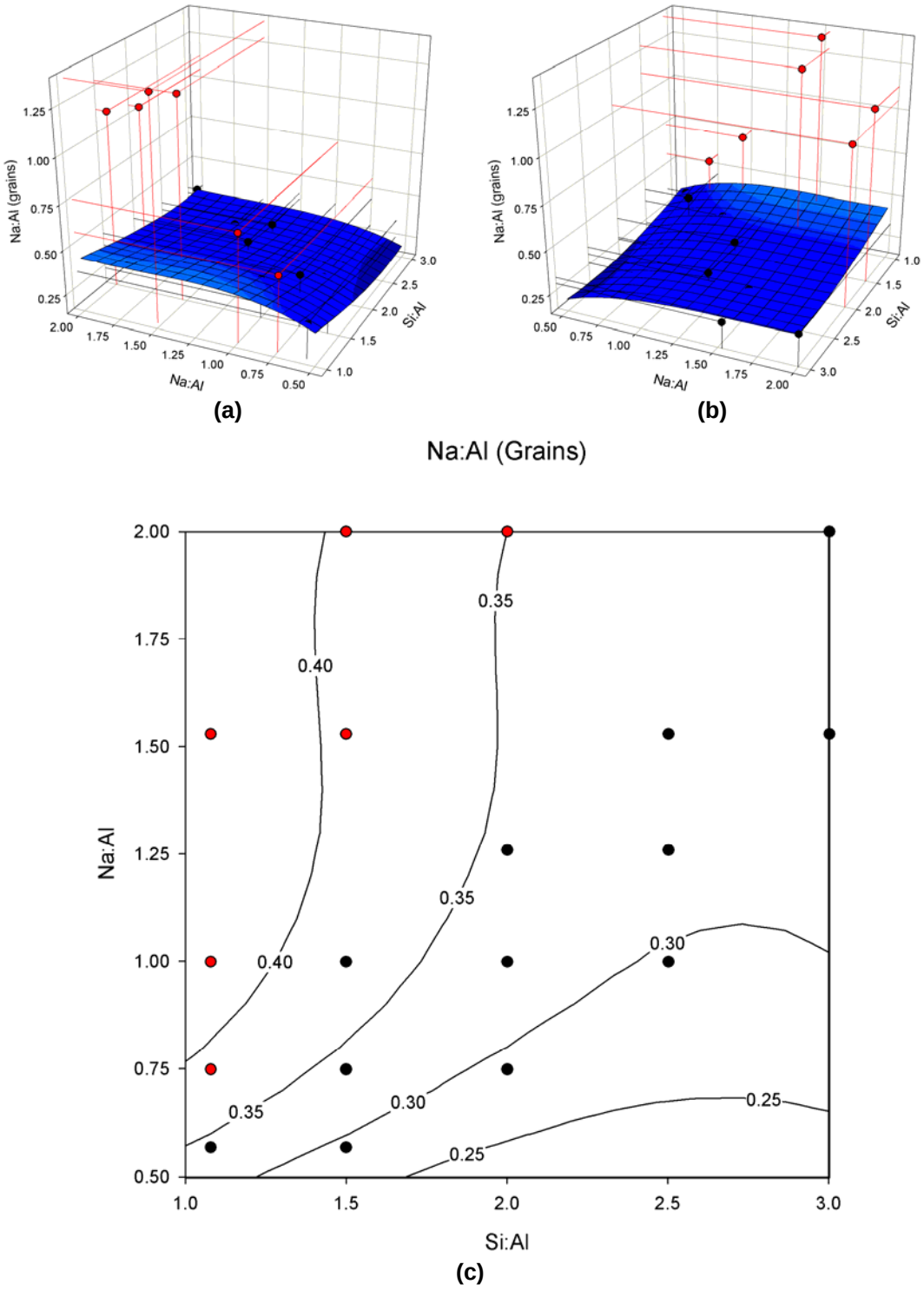

Figure 6.14: Representation of the Na:Al molar ratios in the grains of the AIPs. The Si:Al/Na:Al axes represent the nominal composition of the AIP. The vertical axis gives the Na:Al molar ratio measured in the grains. The red data points show samples that were excluded in the calculation of the contours. These data points represent Samples 1.5/1.5, 1.5/2.0 and 2.0/2.0, which suffered from grain pullout, and as such, do not provide a representative grain measurement. Also included in the grains excluded are those for Si:Al = 1.08. These grains adversely affected the contour fit. **(a)** 3D representation of the contour plot with the data points shown to provide an indication of the scatter in the data. **(b)** A second representation of (a) with the Si:Al/Na:Al axes reversed. **(c)** Contour projection of the 3D plot. Contour values represent the Na:Al molar ratios in the grains of the AIPs, with an interval of 0.5.

The grains in the samples corresponding to Si:Al = 1.08 are a notable exception to the trend shown in Figure 6.14. In these samples, the Na content of the grains increases with increasing Na:Al ratio, as shown in Figure 6.10. In the activating solution for these samples, there was no Si present. The increased uptake of Na in these grains may be due to the increased availability of Na in the solutions that did not contain Si.

Impurity elements

When analysing the EDS results, presented in Table 6.2, attention was also paid to the location of Ca, Mg, Ti, Fe and Zr, as these were the main impurities in the precursor materials. The key difference between these elements is that Ca and Mg are soluble in solution and are able to take part in the AIP formation reaction, whereas Ti, Fe and Zr are insoluble.

Analysis of the location of these impurities revealed that Ca and Mg are more likely to be found in the matrix phase, whereas Ti and Fe were more likely to be found in the grain phase. This shows that during the dissolution/polycondensation phase of the reaction, Ca and Mg leach out of the grains and are incorporated into the matrix. Ti and Fe are not involved in the activation process, and remain in the grains. Zr was not detected.

Table 6.2: Showing the number of EDS spectra in which Ca, Mg, Ti or Fe was found in the AIPs. The % confidence interval given is the level of confidence that the element is more likely to be associated with the matrix (for Ca and Mg) or with the grains (for Ti and Fe).

	Grain	Matrix	%CI
Mg	36	64	99.4
Ca	90	158	99.9997
Ti	16	8	92.2
Fe	8	1	98.4
n	425	444	

6.2.2 Elemental analysis summary

1) The composition of the matrix of the highest strength sample is corresponds to a network formula of $Na_n[-(SiO_2)_{3.24}-(AlO_2)-]_n$.
2) The Si:Al ratio of the matrix is higher than the nominal composition of the AIP, and is dependent on the Na:Al ratio,

3) The presence of Al in the matrix phase indicates that this phase has resulted from the dissolution of MK, as MK is the sole source of Al,

4) The Na:Al ratio of the matrix is variable, but generally increases with increasing nominal Na:Al ratio. In all cases, the Na:Al ratio of the matrix is less than the nominal composition of the AIP indicating that Na has been lost from the AIP, most probably during the sample preparation process,

5) The Si:Al ratio of the grains is increased from that of MK, and may indicate that Al is being preferentially dissolved from the grains,

6) The Na:Al ratio of the grains depends on both the Na:Al and Si:Al ratios. For the Si:Al = 1.08 samples, the Na content of the grains is only slightly less than the nominal Na:Al ratio of the AIP. For the remainder of the samples, the Na:Al ratio is approximately constant, and

7) It is conjectured that the grains start to dissolve as they reach 'saturation' point, in terms of Si content. The grains observed in the micrographs did not dissolve, as the curing process halted the movement of ions, stopping further formation of the polymer.

6.3 X-ray diffraction

Synchrotron XRD (SRD) results from the Photon Factory show that the majority of AIPs synthesised consist of solely amorphous components. A small proportion of the AIPs formed crystalline phases in conjunction with the formation of the AIP. SRD patterns for some of the zeolites formed in the AIP synthesis are shown in Figure 6.15. Table 6.3 details the zeolites found in the AIPs.

The crystalline phases formed in the synthesis process were determined to be zeolites A, X & Y and sodalite by search/match analysis of the diffraction patterns according to the PDF-2 Release 2002 database (ICDD, 2001). By the Database of Zeolite Structures (IZA Structure

Commission, 2004) the framework of both zeolites A and X are described by type LTA zeolites. Zeolite Y's framework is described by type FAU zeolites.

Table 6.3: Zeolites formed in the AIP formation process.

Sample	Zeolite[a]		PDF no.
1.1/0.6	A	LTA	38-0241
1.1/0.8	A	LTA	38-0241
1.1/1.0	A	LTA	38-0241
1.1/1.5	S	SOD	41-0009
1.5/1.5	X, Y	LTA, FAU	38-0237, 43-0168
1.5/2.0	A, S	LTA, SOD	38-0241, 41-0009
2.0/2.0	X	LTA	38-0237

[a] A, X and Y represent Zeolites A, X and Y. S denotes sodalite.

The zeolites fall in a distinct 'formation region' corresponding to Si:Al:Na = 1.1:1:0.6-1.5, 1.5:1:1.5-2.0 and 2.0:1:2.0. This distribution is represented graphically in Figure 6.16. An expanded version of Figure 6.16 is given in Appendix IV. It is thought that zeolites develop only in this region as they need either low Si:Al ratios or high Na:Al ratios to form under the conditions that the AIPs are synthesised.

Zeolites are crystalline hydrated aluminosilicates with a cage structure with the cages being occupied by cations and water molecules. Zeolite A is represented by the formula $(NaAlSiO_4)_{12}$, zeolite X by $(NaAlSiO_4)_{96}$, zeolite Y by $(NaAlSi_{2.25}O_{6.5})_{59}$ and hydroxysodalite by $Na_8(AlSiO_4)_6(OH)_2{\cdot}4H_2O$. The compositions of these zeolites are consistent with the composition of the AIPs in which they were found. It is thought that zeolites A & X and sodalite formed predominately as the composition of these zeolites is similar to that of the AIPs in which they formed. That zeolites are not observed at higher Si:Al ratios may be due to the viscosity of the activating solution. The water used in the production of AIPs facilitates adequate mixing of the components. Zeolite production can use up to 670 mL of water per 100 g of solids (Basaldella, Kikot & Tara, 1997; Murayama, Yamamoto & Shibata, 2002) in order to allow for the transporting of ions through the solution to form structures with long range order. With lower water content, the solution is

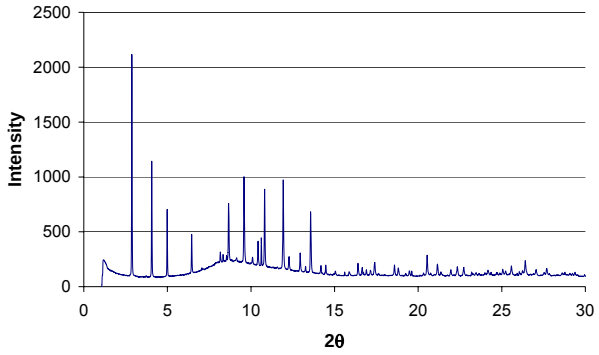

(a)

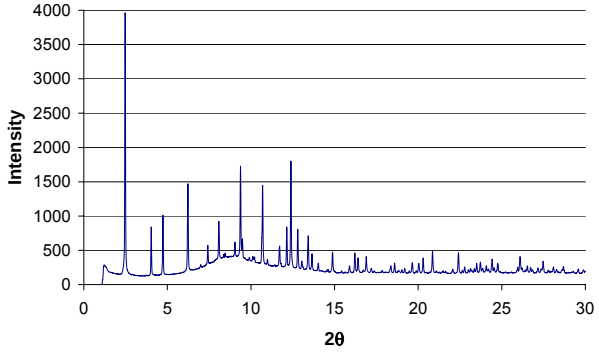

(b)

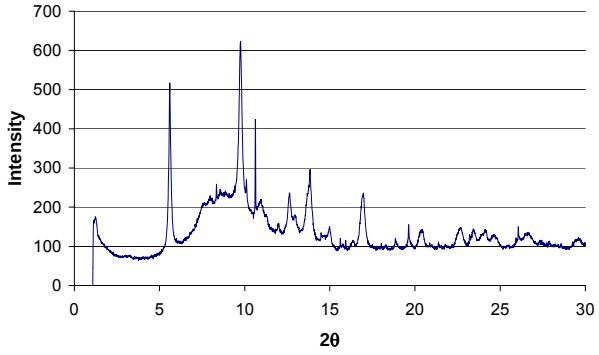

(c)

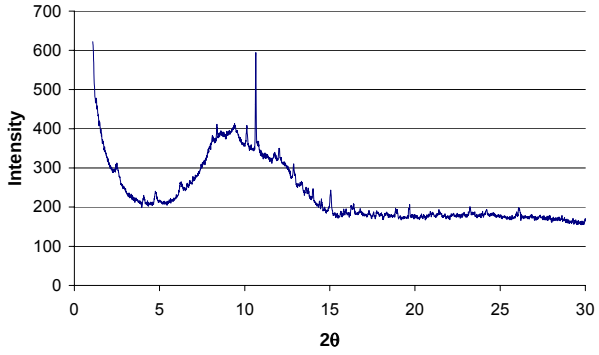

(d)

Figure 6.15: SRD patterns (λ = 0.62 Å) of zeolite formation during AIP synthesis. The peak at 10.7° 2θ is due to a quartz impurity. **(a)** Zeolite A, Sample 1.1/1.0 **(b)** Zeolite X and Y, Sample 1.5/1.5 **(c)** Sodalite, Sample 1.1/1.5 and **(d)** Zeolite X, 2.0/2.0.

Figure 6.16: Collection of SRD patterns (λ = 0.62 Å) showing the distribution of the zeolite formation region. The position of the diffraction patterns superimposed on the compressive strength diagrams corresponds to the composition of the sample from which they were measured. The ratios given are molar ratios. An expanded version of the figure is reproduced in Appendix IV.

more viscous, and the transport of ions would be more difficult and the growth of potential zeolites would be affected.

Sample 2.0/2.0 showed only the beginnings of zeolite formation. A possible explanation for this is that the sample composition lies on the edge of the composition range of the zeolites that were formed in the other AIPs, allowing only a minimum amount of zeolite to develop.

6.4 Concluding comments

6.4.1 Summary

SEM/EDS analysis of the AIPs shows that a wide variety of microstructures are present, and that they correlate with the compressive strength of the materials, indicating that the strength of the AIPs is controlled to an extent by the microstructure. The microstructure analysis also shows that the AIPs synthesised in the current study are essentially composite materials, consisting of an inorganic polymer matrix containing a grain phase. The morphology of the grain phase is reminiscent of MK, however, the chemical composition of the grains indicates that though the grains may have originated from MK, their current makeup is somewhat different. In order to study solely AIP using the existing processing conditions, it is most likely that the *particle size of the initial MK precursor would have to be reduced in order to allow for total dissolution*.

EDS showed that not all of the Na is necessarily used in the polymerisation reaction, and can be leached out. The matrix phase composition of the highest strength sample corresponded to a network formula of $Na_n[-(SiO_2)_{3.24}-(AlO_2)-]_n$. The distribution of impurity elements was shown to be affected by the polymerisation process. Soluble elements (Mg and Ca) were found predominately in the matrix, whereas insoluble elements (Ti and Fe) were found mainly in the grains. Zr was not detected.

SRD analysis showed that the AIP formed was entirely amorphous, with deviations from non-crystallinity being due to the formation of zeolites and the presence of crystalline impurities. The observation of zeolites using an AIP synthesis route means that it may be possible to adapt what is known about the formation of zeolites to the formation of the AIP polymer structure, as was done in Chapter 5, to explain the trends present in the compressive

strength of the AIPs. The adaptation of zeolite synthesis models to the synthesis of AIPs may help in providing structural models for AIPs. The provision of structural models would allow for more efficient synthesis techniques to be developed. These models would be of great help to the use of AIPs as a waste encapsulation material, as the models could account for the influence of the waste elements. They could also be of use for AIPs made from precursors with high levels of impurities. Knowing how the AIP forms would allow for synthesis techniques to be developed without the need for extensive experimentation.

The dissolution of the MK is dependent predominantly on the Na content of the activating solution. For all samples with an Si:Al ratio ≥ 1.5, as the Na:Al ratio increases, the relative amount of matrix material also increases. For the Si:Al = 1.08 samples, there is little difference between the microstructures with changes in the Na:Al ratio, indicating the possibility that the presence of Si in the activating solution is required to initiate polymerisation.

For the highest strength material, dissolution of the grains is not complete, which gives some scope for the improvement of the compressive strength of these materials through the reduction in the size of the precursor particles, or through an optimisation of the synthesis process. The Si:Al ratio of the grains increases to a maximum of approximately 1.6 for samples corresponding to Si:Al = 2.0-3.0. It is conjectured that once the grains reached this composition, they would start to dissolve, having reached ‘saturation’ point in terms of Si content. The grains observed in the samples did not dissolve, as the curing process halted the movement of ions, stopping further formation of the polymer.

The changes in the AIP microstructure with composition reveal that residual MK is present, and reduces in level (see §7.1.1) to near negligible amounts when the compressive strength is at a maximum. The variation in the compressive strengths of the samples cannot be attributed solely to microstructural differences, as samples with similar microstructures exhibit

markedly different strengths, which is illustrated by Samples 1.5/1.0 (Figure 6.5(c)) and 2.0/1.0 (Figure 6.6(c)). These two samples have very similar microstructures, whereas Sample 2.0/1.0 has a compressive strength of ~x2 that of Sample 1.5/1.0.

6.4.2 Conclusions

1) The AIPs exhibit a two-phase microstructure, in which the relative levels of the grain and matrix phases vary with chemical composition,
2) The matrix phase has higher Si:Al and Na:Al ratios than the grain phases, indicating that the matrix was formed by the dissolution of MK. The matrix phase composition of the highest strength sample corresponded to a network formula of $Na_n[-(SiO_2)_{3.2}-(AlO_2)-]_n$,
3) The variation of the compressive strength cannot be attributed solely to microstructural changes, as samples with similar microstructures can exhibit markedly different strengths,
4) As the nominal Si:Al ratio of the sample increases, the Si:Al ratio of the grain phase is increased from the MK value of 1.08. It is conjectured that the grains start to dissolve as they reach 'saturation' point, in terms of Si content. The grains observed in the micrographs did not dissolve, as the curing process halted the movement of ions, stopping further formation of the polymer, and
5) Some of the AIPs synthesised co-formed zeolites during the curing process. The zeolites were observed for all samples with Si:Al = 1.08, regardless of the Na: level. AIPs with Si:Al = 1.5 and 2.0 also formed zeolites if the Na:Al ratio was sufficiently high. Visual evidence for these phases was not found in the microstructural investigation. The presence of zeolites has the potential to allow for the elucidation of formation mechanisms for the synthesis of AIPs.

7.0 INFLUENCE OF CHEMICAL COMPOSITION ON THE NANOSTRUCTURE

Chapter 7 presents the experimental results on the study into the influence of the chemical composition on the nanostructure of AIPs synthesised by sodium silicate alkaline activation of metakaolinite. The results are considered with particular reference to the bonding network structure within these amorphous materials.

This chapter, the last of three results chapters, details the changes in the bonding network structure of the AIPs as determined by NMR and SRD derived RDF analysis. The theoretical bases of these techniques are discussed in Chapter 3. The methodology used in the application of these techniques is presented in Chapter 4.

The purpose of this chapter is to examine the way in which the chemical composition influences the nanostructure of the AIP. This will provide valuable information on the combined influence of the micro and nanostructure on the AIPs compressive strength according to chemical composition.

The questions that this chapter seeks to answer by the combined use of NMR and RDF are:

1) How does the bonding network of the AIPs vary with changes in chemical composition? and
2) In what way does the nanostructure affect the microstructure of the AIPs?

7.1 Nuclear magnetic resonance

^{29}Si, ^{27}Al and ^{23}Na MAS NMR spectra were collected from 9 samples covering all Si:Al and Na:Al ratios - see Figure 7.1, enabling coordination information to be collected from the samples with the highest and lowest compressive strength, and also from the composition boundary of the samples investigated in the current study. The samples were further divided into 3 sample suites, as shown in Table 7.1.

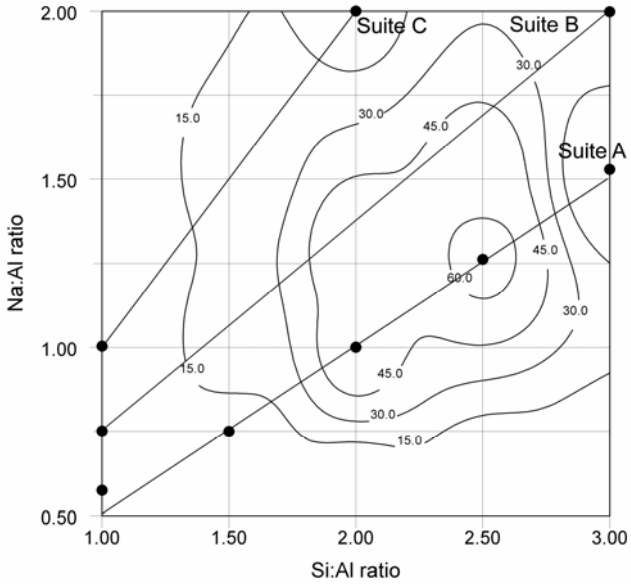

Figure 7.1: Sample compositions analysed, and their allocated Suite. The contours show the compressive strength of the AIPs in MPa.

Table 7.1: Sample designation[a] and their allocated suite.

Sample	Suite
K	-
MK	-
SF	-
1.1/0.6	A
1.5/0.8	A
2.0/1.0	A
2.5/1.3	A
3.0/1.5	A
1.1/0.8	B
3.0/2.0	B
1.1/1.0	C
2.0/2.0	C

[a] See Table 4.2 for the compositions of the samples.

Proton NMR was also considered as an NMR method for identifying proton sites and their distribution in framework aluminosilicates (Engelhardt & Michel, 1987 p. 365). Four types of protons can be easily distinguished by their chemical shift: *terminal SiOH*, *non-framework AlOH*, *bridging Si(OH)Al* and *ammonium ions*. The concentrations of the protons in these different sites can be calculated from their relative peak intensities. Difficulty arises in the collection of proton spectra from the necessity to use high magnetic fields and correspondingly high rotation speeds. These conditions necessitate the use of specialised NMR equipment. In this regard, the experiment was

considered to be beyond the scope of the current study – see discussion in §8.2.

7.1.1 ^{29}Silicon

The measured spectra are shown in Figure 7.2, and Table 7.2 gives the peak positions and linewidths. An example of the curve fitting used to calculate the peak positions and linewidths is given in Figure 7.3. The sharp peak in Samples 1.1/0.6, 1.1/0.8 and 1.1/1.0 is due to the presence of zeolites, which is consistent with the x-ray diffraction results presented in §6.3.

Spectra descriptions

Kaolinite shows a single sharp peak centred at -91.8 ppm indicating Si^{VI}, metakaolinite shows a broad peak centred on -104.8 ppm and silica fume gives a broad peak centred on -111.5 ppm. As the nearest-neighbour interactions dictate the chemical shift of a particular peak, the shift of the silicon peak in kaolinite to that of metakaolinite indicates that the silicon network, through the dehydroxylation process, is becoming 'detached' from the aluminium network; *i.e.*, the aluminium is exerting less influence on the chemical shifts and the silicon sub-lattice in metakaolinite is tending towards that observed for silica fume. The change in the average Si coordination is most likely due to the change in aluminium coordination from exclusively octahedral in K, to a mixture of tetra-, penta- and octahedral in MK.

The spectra for the AIPs show chemical shifts ranging between -85.5 and -94.0 ppm which correlate to a Si coordination number range of 3.7 - 2.2, representing the number of AlO_4 tetrahedra connected to a SiO_4 tetrahedron, as calculated from an interpolation of literature values (Lippmaa *et al.*, 1981; Nofz *et al.*, 1986).

The AIP ^{29}Si spectra have linewidths between 9.5 and 17 ppm, approximately x10 the widths for kaolinite, indicating that there is considerably less order in the AIPs than in kaolinite. The peak widths are distributed amongst two distinct groups. AIPs containing zeolites showed

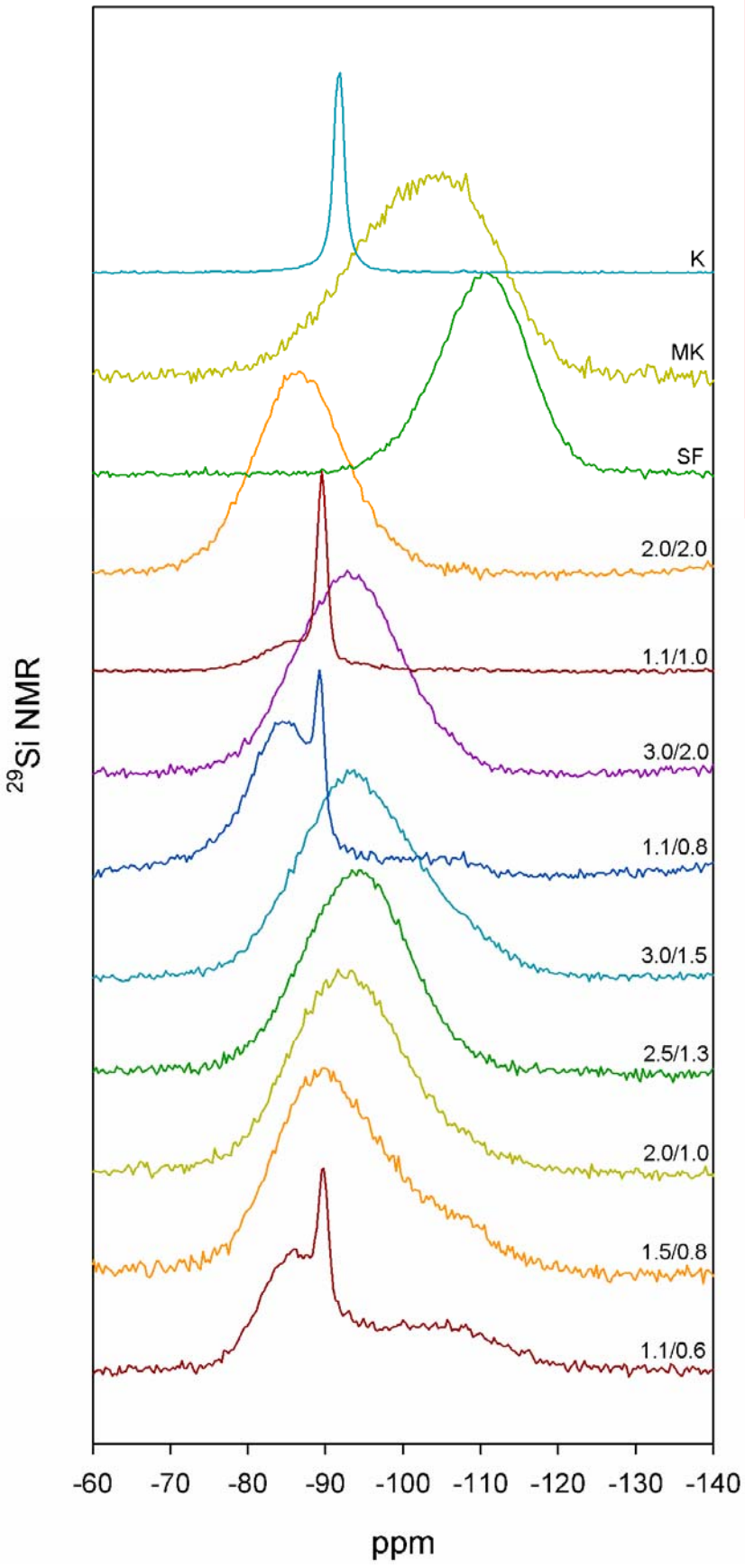

Figure 7.2: ^{29}Si MAS NMR spectra of the AIP samples.

Table 7.2: Peak positions and linewidths of the ^{29}Si spectra. Errors represent two standard deviations and refer to the uncertainty in the last digit. The estimated amount of MK present in each sample is shown in Figure 7.5.

Sample	Suite	^{29}Si Peak position (ppm)	^{29}Si Linewidth (ppm)
K	-	-91.721(4)	1.460(6)
MK	-	-104.80(4)	20.58(7)
SF	-	-111.43(5)	13.97(3)
1.1/0.6	A	-85.8(2) -89.73(4)	10.6(3) 1.33(4)
1.5/0.8	A	-88.87(3)	14.834(8)
2.0/1.0	A	-92.11(3)	15.85(4)
2.5/1.3	A	-94.03(4)	15.82(5)
3.0/1.5	A	-92.83(2)	16.57(13)
1.1/0.8	B	-84.39(4) -89.40(4)	9.846(8) 1.39(5)
3.0/2.0	B	-92.87(5)	16.0(3)
1.1/1.0	C	-86.47(6) -89.532	10.54(17) 1.452(4)
2.0/2.0	C	-85.942	14.656(8)

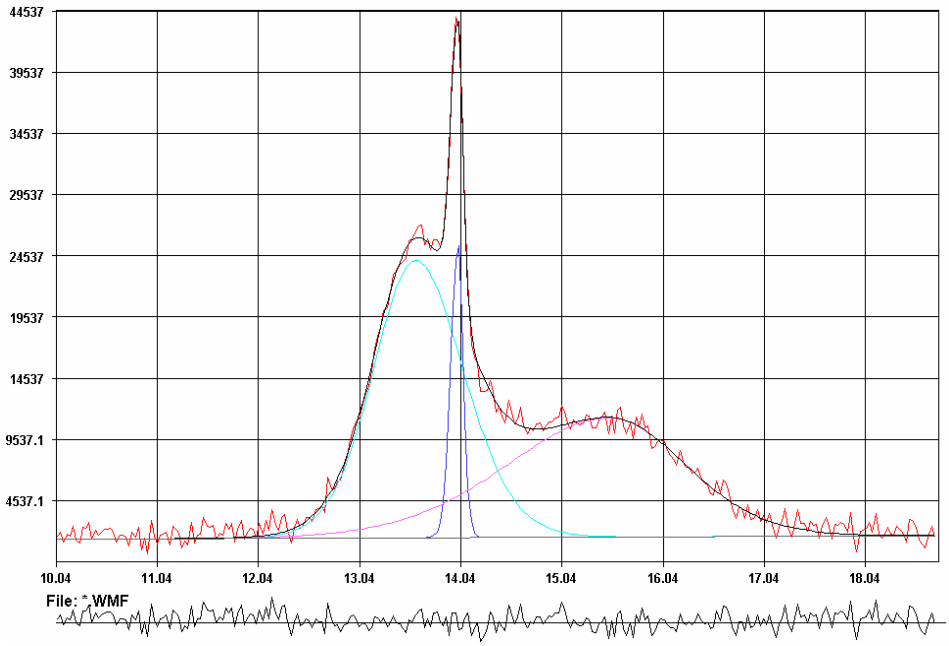

Figure 7.3: An example of the ^{29}Si curve fits used to calculate the peak positions, linewidths and peak areas. The difference pattern between the calculated peaks and measured data is also given. This figure shows Sample 1.1/0.6 with the contribution from the AIP in light blue, from the zeolite in dark blue and from the residual MK in pink.

linewidths between 9.5 and 10.6 ppm, whereas samples not containing zeolites had linewidths of between 14.5 and 17 ppm. The bimodal distribution suggests that the presence of zeolites in the material modifies the development of the AlP network, narrowing the distribution of bond lengths and angles.

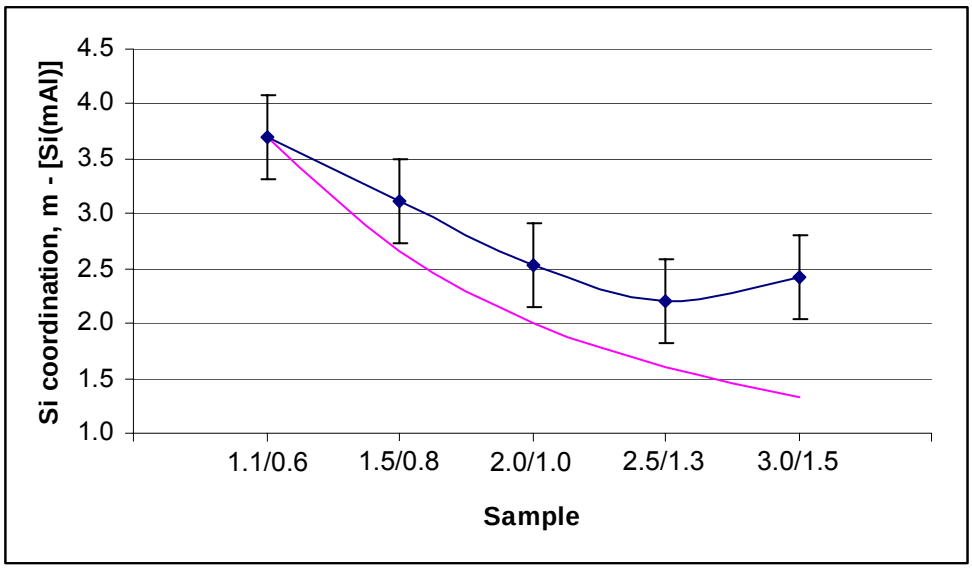

Figure 7.4: Plot of coordination number change of Si for sample suite A. The change in coordination represents a change in the Si(mAl). Errors represent 2σ. The blue plot shows the coordination numbers calculated from the measured peak shift. The pink plot shows the theoretical coordination number based on the sample composition assuming that the polymer network is made entirely of SiO_4 and AlO_4 tetrahedra.

A plot of the coordination numbers for sample suite A is shown in Figure 7.4. The errors in the coordination number were calculated as two standard deviations of the average of the chemical shift values given in the quoted references for sodium aluminosilicates. The peak shift of the spectra shows a steadily reducing average coordination from 3.7 to a value of 2.2 at Sample 2.5/1.3. As can be seen in Figure 7.4, the errors associated with the coordination numbers are considerable. These large errors arise from the spread of chemical shifts associated with each coordination number. The shift in the peak position, and hence the coordination, is mirrored in the physical properties of the material.

The Si coordination numbers derived from the chemical shifts differ from the theoretical coordination calculated from the overall sample Si:Al

ratio. The theoretical coordination numbers are derived from the chemical composition assuming that the polymer network is made entirely of SiO_4 and AlO_4 tetrahedra. The deviation in coordination number, shown in Figure 7.4, infers that the Al content of the AIP is higher than is possible according to the sample composition, and suggests that the Na content of the AIP alters the dependence of chemical shift on the calculated coordination number. One prospective mechanism is that the Na is being incorporated into the AIP network as Si-O-Na, so altering the number of SiO_4 tetrahedra bonded to the reference SiO_4 tetrahedron. The bonding of Na to the SiO_4 tetrahedra increases the apparent amount of Al present and can account for the change in coordination number.

Secondary phases

The tails on the AIP ^{29}Si spectra are due to residual MK. An example of the residual MK presence is given in Figure 7.3. The presence of residual MK in reacted AIPs has also been reported by Rahier *et al.* (1996). The strengths of these materials have been reported in Chapter 5. The ^{29}Si spectra corresponding to the highest strength material (see §5.1.1) does not show any indication of MK features. The residual MK content of the AIPs was compared to their compressive strength, and is shown in Figure 7.5. The amount of residual MK present in the materials was calculated by comparing the relative areas of the peaks fitted to the spectra (see Figure 7.3). *It was found that the amount of residual MK present in the sample correlates well with the compressive strength*, demonstrating that the residual MK, most likely present in the grains, is not acting as particle reinforcement, but may weaken the structure. It is thought that the primary cause of the change in compressive strength is the chemical composition. The presence of residual MK in the grains alters the composition of the matrix, and hence the compressive strength. The grains in the microstructure are an Al rich phase, whereas the matrix phase, the inorganic polymer, is Si rich. If all of the grains had dissolved, this would have affected the Si coordination of the inorganic polymer. The correlation between the coordination number of Si and the %MK present in the AIP is shown in Figure 7.6. For samples with a large amount of grain phase (e.g. Samples 1.1/0.8-1.5), the presence of the grains

may weaken the material due to there not being enough matrix phase to give sufficient structural integrity.

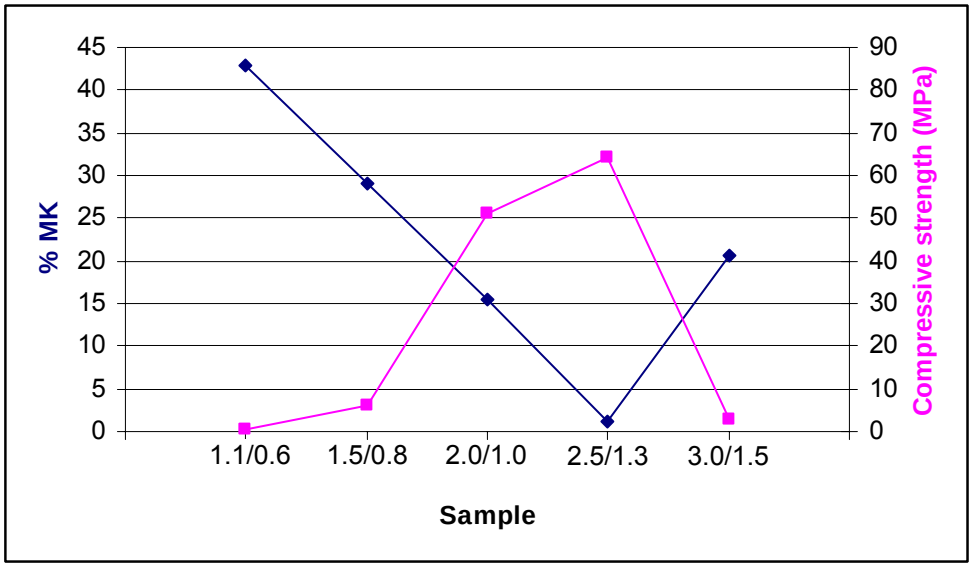

Figure 7.5: w/w concentration of residual metakaolinite present in the material as calculated from ^{29}Si spectra. The percentages given show the atomic percent of ^{29}Si corresponding to the MK signal. The compressive strength of the samples is given as an indication of the correlation between the two.

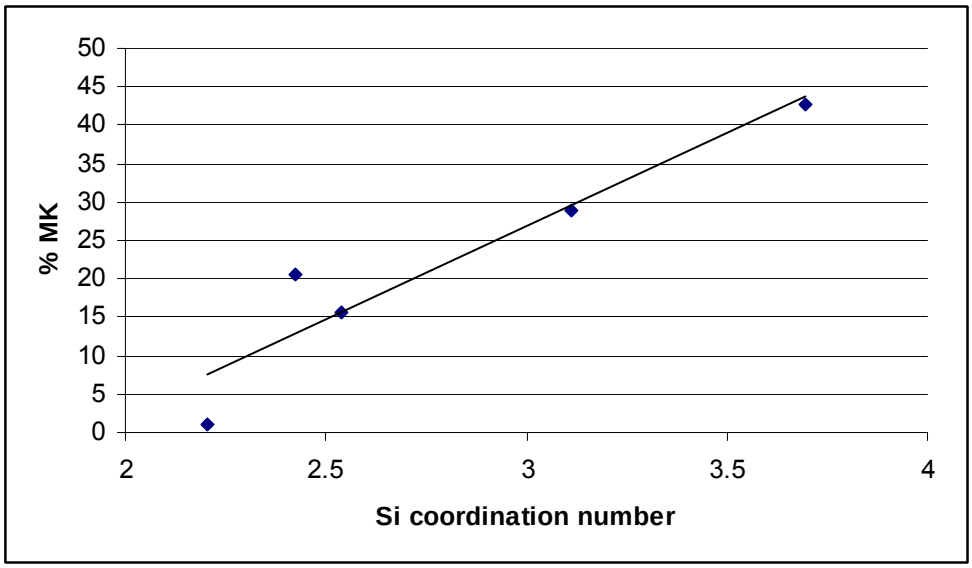

Figure 7.6: Correlation between the coordination number and %MK present of samples from suite A.

^{29}Si MAS NMR signals indicative of zeolites were found in Samples 1.1/0.6, 1.1/0.8 and 1.1/1.0. The presence of zeolites in the samples was also revealed by XRD analysis, as presented in §6.3. The levels of zeolite, estimated from the relative area of the deconvoluted NMR peaks, are

presented in Table 7.3. No NMR evidence was found for zeolite formation in Sample 2.0/2.0 as indicated by the XRD results, which may mean that the amount of zeolite formed was too small to be detected by NMR, or that no zeolites were produced due to the sample composition being at the extremities of the zeolite formation region.

Table 7.3: w/w concentration of zeolite present in the material as calculated from ^{29}Si spectra. The percentages given show the atomic percent of ^{29}Si corresponding to the zeolite signal. Errors represent 2σ.

Sample	% zeolite
1.1/0.6	6.8(2)
1.1/0.8	7.07(17)
1.1/1.0	44.7(5)
2.0/2.0	ND[a]

[a] Not detected

Comparison with previous work

Rahier *et al.* (1996) found that the ^{29}Si spectra were invariant with changes in the Si:Al ratio, and that samples synthesised with Na:Al ratios exceeding stoichiometric values (Na:Al = 1) showed silicate peaks in addition to the AIP peaks. In contrast to the Rahier study, the current study has shown that the Si spectra systematically change when the Si:Al ratio is altered, and that no silicate peaks were present in any of the AIPs. The samples prepared by Rahier *et al.* (1996) used a sodium silicate solution prepared in the same manner as in this experiment and metakaolinite, and were “cured in a closed mould at room temperature for at least two days” (Rahier *et al.*, 1996), whereas the samples in the current study were cured at 75 ºC. The invariant nature of the position of the Si peak for the AIPs prepared by Rahier *et al.* (1996), and the additional peaks due to residual Si from the silicate solution, are most likely due to the different curing method employed, showing that the production method can affect the properties exhibited by the materials.

Summary

The main outcomes from the ^{29}Si results were:

1) Si changes average coordination number continuously across all compositions from 3.7 for Sample 1.1/0.6 to 2.2 for Sample 2.5/1.3,
2) The level of residual MK present in the samples correlates with changes in the compressive strength, and
3) The presence and levels of zeolites in Samples 1.1/0.6, 1.1/0.8 and 1.1/1.0 is revealed by ^{29}Si NMR.

7.1.2 ^{27}Aluminium

The measured spectra are shown in Figure 7.7, and the peak positions and linewidths are given in Table 7.4. An example of the curve fits used to calculate the peak positions and linewidths is given in Figure 7.8.

Spectra descriptions

Kaolinite has a single peak centred at 0.4 ppm with a linewidth of 11.8 ppm showing Al^{VI} (MacKenzie *et al.*, 1985) This single sharp peak of high intensity shows that all of the Al in kaolinite is in the 6-coordinate state. The narrowness is indicative of a small range in bond lengths and angles.

Metakaolinite shows a broad peak centred on 25 ppm, with Al^{IV}, Al^{V} and Al^{VI} assigned to the fitted peaks (Rocha, 1999) at 55.2, 26.8 and 0.47 ppm respectively. The multiple coordination states of Al and the lack of long range order in MK, enhance the reactivity of the material, allowing the polymerisation reaction to take place (Granizo, Blanco-Varela & Palomo, 2000). The broad peaks assigned to the different coordination states are characteristic of an amorphous material, indicating that the aluminium environment does not show long range order. The estimated relative levels of Al in the three coordination states are given in Table 7.5 according to the relative areas of the Gaussian peaks fitted to the experimental profile.

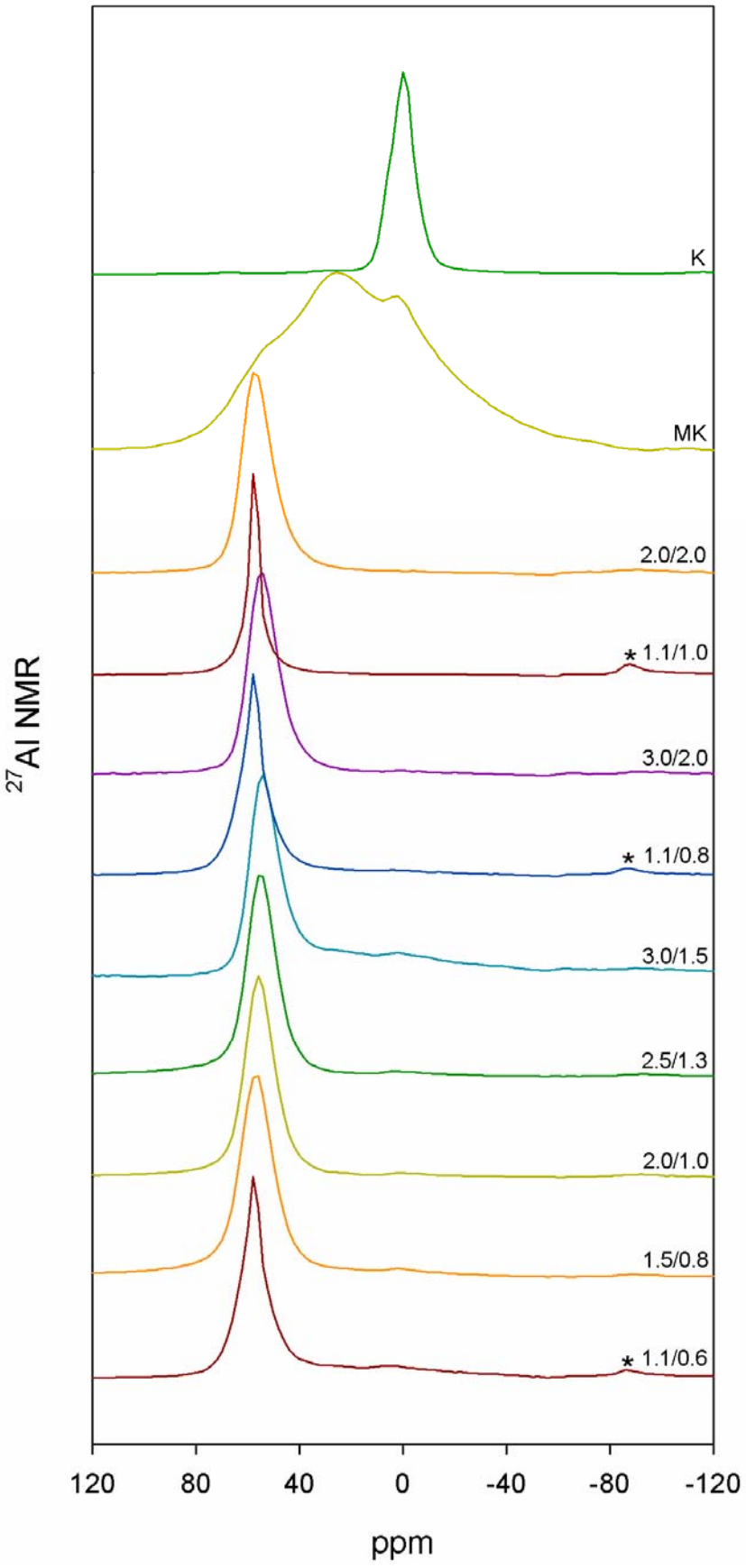

Figure 7.7: ^{27}Al MAS NMR spectra of the AIP samples. '*' denotes spinning side bands.

Table 7.4: Peak positions and linewidths of collected ^{27}Al spectra. Errors given are 2σ and refer to the uncertainty in the last digit. Only the Al^{IV} peak positions are given for the AlPs.

Sample	Suite	^{27}Al Peak position (ppm)	^{27}Al Linewidth (ppm)
K	-	-0.011	10.048
		1.6(2)	51.6(7)
MK	-	29.07(7)	34.1(9)
		53.58(14)	20.8(5)
1.1/0.6	A	58.30(5)	9.97(9)
1.5/0.8	A	56.51(4)	15.3(8)
2.0/1.0	A	55.30(2)	13.2(4)
2.5/1.3	A	54.64(3)	13.4(4)
3.0/1.5	A	56.212(4)	10.814(4)
1.1/0.8	B	58.17(2)	9.98(4)
3.0/2.0	B	55.516	10.212
1.1/1.0	C	57.439	5.301
2.0/2.0	C	58.003	10.773(3)

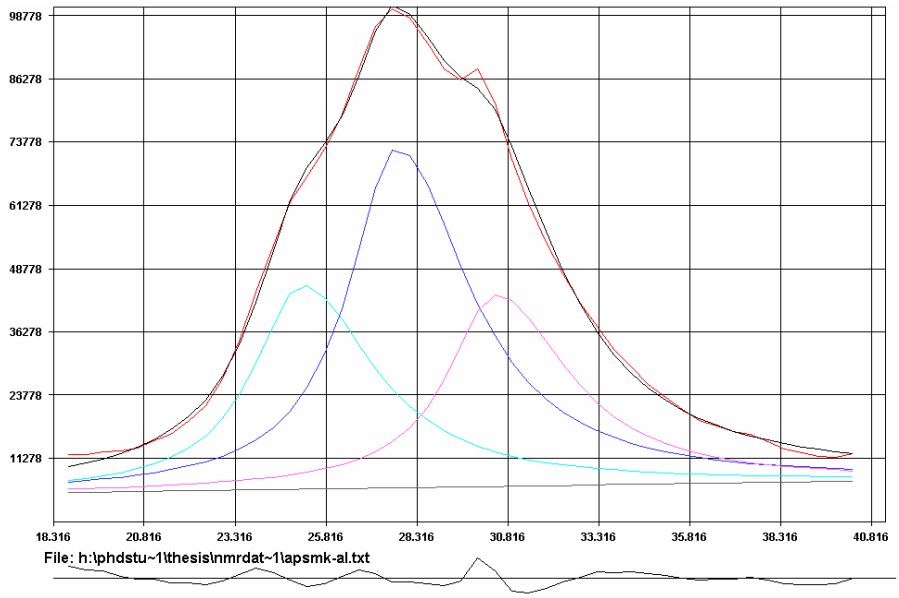

Figure 7.8: An example of the ^{27}Al curve fits used to calculate the peak positions, linewidths and peak areas. The difference pattern between the calculated peaks and measured data is also given. This figure shows MK with the contributions from the 4-, 5-, and 6-coordinate Al shown in light blue, dark blue and pink, respectively.

The AlPs all exhibit a single peak at 54.5-58.5 ppm. The change in peak position mirrors that of the Si shift, and is approximately the same when measured in ppm. However, the change in coordination, shown in Figure 7.9, associated with the peak shift is less than that displayed by Si, as extrapolation of the chemical shifts of the Al in MK show that the coordination change is only from 3.9 to 4.0. The errors associated with the coordination

numbers of the measured samples are much greater than the change in coordination, and as such, the change in the peak position does not correlate to a significant change in the coordination of Al. The positions of the 4-6 coordinate Al were taken from the Gaussian fits to the MK MAS NMR spectrum, and a linear regression was applied to extrapolate the coordination-chemical shift correlation. This calculation took into account the errors in the initial line positions, and may account for the large errors in the calculated coordination numbers.

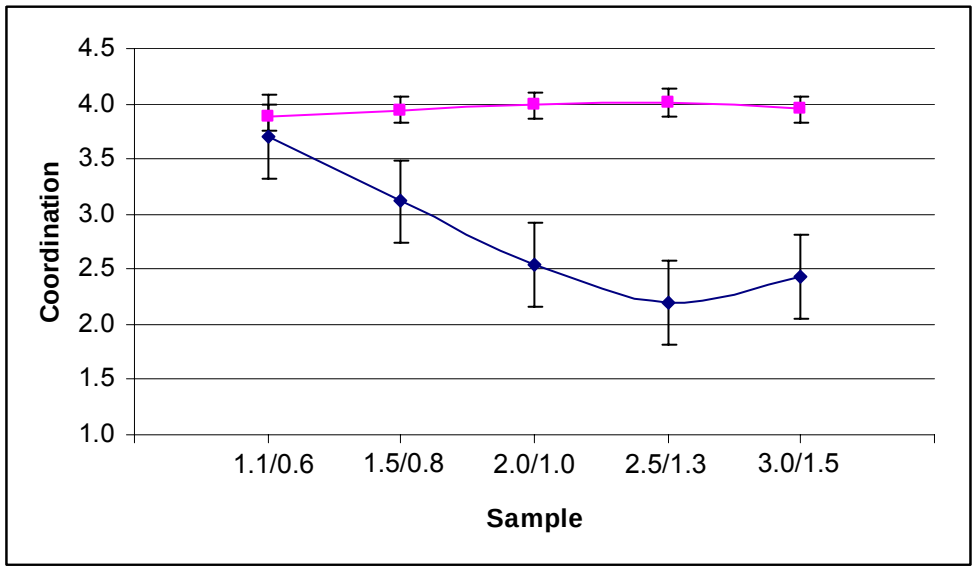

Figure 7.9: Plot of coordination number change of Al (pink) for sample suite A. In this plot, coordination represents the number of oxygen atoms bonded to the aluminium. The change in coordination number for Si has been included for comparison (blue; see Figure 7.4). Errors represent 2σ.

The AIP spectra have linewidths ranging from 10.0 to 10.8 ppm, similar to the linewidth of kaolinite (11.8 ppm), which suggests that the immediate structural environment of Al in both the AIPs and kaolinite is similar. This is a valid assumption, as the Loewenstein Avoidance Principle (Loewenstein, 1954) requires all AlO_4 tetrahedra to be surrounded by SiO_4 tetrahedra. The Si environment is not constrained by a similar condition.

Secondary phases

The tails on the AIP ^{27}Al spectra are consistent with Al^{V} and Al^{VI} being present in the form of residual MK – see Table 7.5 for the estimated levels of the different Al coordination states present in the samples. The amount of MK present in the AIPs cannot be calculated from these spectra as the relative

amounts of Al^{V} and Al^{VI} change as the AIPs form. The presence of MK is also revealed by ^{29}Si MAS NMR (see Figure 7.5).

Table 7.5: Estimated levels of Al present in samples according to coordination number. Errors represent 2σ and refer to the uncertainty in the last digit. Zero entries are due to the peak not being included in the area refinement in order to obtain a stable refinement.

Sample	% Al(IV)	% Al(V)	% Al(VI)
MK	10.39(11)	33.5(10)	56.1(11)
1.1/0.6	69(3)	6.2(11)	25(2)
1.5/0.8	95.1(3)	0.	4.9(3)
2.0/1.0	98.2(2)	0.	1.8(2)
2.5/1.3	98.22(16)	0.	1.78(16)
3.0/1.5	59(2)	12.0(11)	29(2)

The presence of zeolites is not revealed in the ^{27}Al spectra as the 4-coordinate Al signal of the zeolites would overlap with that of the AIP.

Summary

The main outcomes from the ^{27}Al MAS NMR measurements were:

1) MK contains Al in 4, 5- and 6-coordinate states,
2) Al is present the AIPs in exclusively 4-coordinate state, and
3) The presence of zeolites is not revealed by Al NMR.

7.1.3 ^{23}Sodium

^{23}Na MAS NMR gave broad spectra with both doublet and singlet peaks in different samples. The measured spectra are shown in Figure 7.10, and details of the peak positions and linewidths are given in Table 7.6. These spectra can then be deconvoluted to give between one and three peaks with chemical shifts of between 3.0 and -20.0 ppm, as shown in Figure 7.11.

Spectra descriptions

The Na peaks can be divided into four groups of similar chemical shift, indicating that similar Na environments are present in all AIP samples. These groups, according to ppm shifts are: (-20.2, -16.3), (-13.2, -8.2), (-5.9, -0.7) and (1.0, 2.6). Comparison of these groups with those presented by Koller *et al.* (1994) for various silicates, sodalites, phosphates and other inorganic

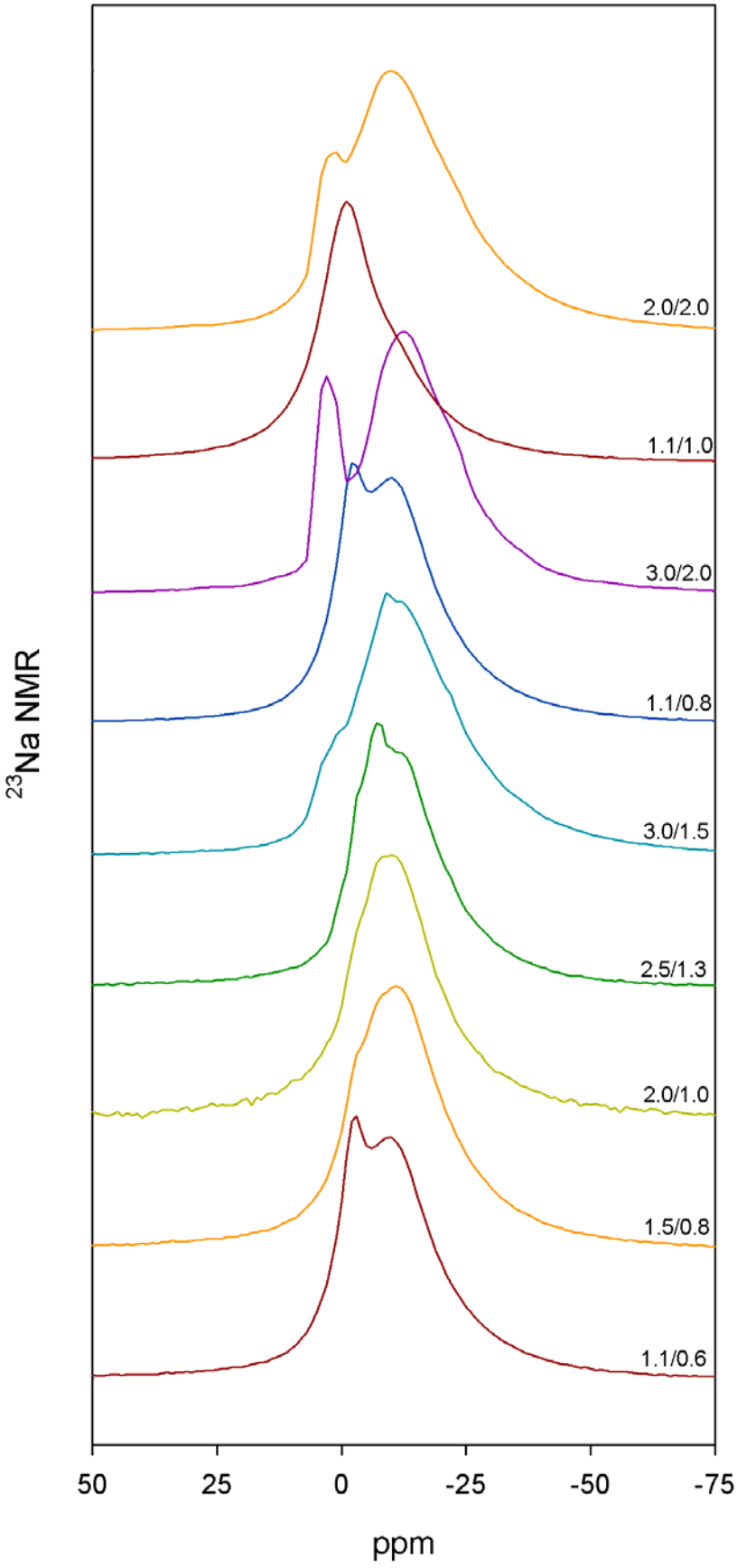

Figure 7.10: ^{23}Na MAS NMR spectra of the AlP samples.

Table 7.6: Peak positions, linewidths and shift parameters of the ^{23}Na spectra. The error in the shift parameter is derived from the regression fit to the data presented in Table 7.7.

Sample	Suite	Peak position (ppm)	^{23}Na Linewidth (ppm)	Shift Parameter (A)
1.1/0.6	A	-2.23	6.86	0.822(18)
		-10.04	12.42	0.87(3)
1.5/0.8	A	-4.43	8.77	0.84(2)
		-12.06	12.69	0.88(3)
2.0/1.0	A	-9.09	14.28	0.86(3)
2.5/1.3	A	-5.91	7.68	0.84(2)
		-13.05	9.80	0.89(3)
3.0/1.5	A	0.99	5.53	0.802(16)
		-8.15	8.36	0.86(3)
		-16.31	11.99	0.91(4)
1.1/0.8	B	-2.14	6.92	0.821(18)
		-10.97	11.49	0.88(3)
3.0/2.0	B	2.61	3.28	0.792(18)
1.1/1.0	C	-0.70	11.36	0.812(16)
		-12.12	13.12	0.88(3)
2.0/2.0	C	1.53	6.00	0.798(17)
		-10.04	11.72	0.87(3)
		-20.22	12.09	0.93(4)

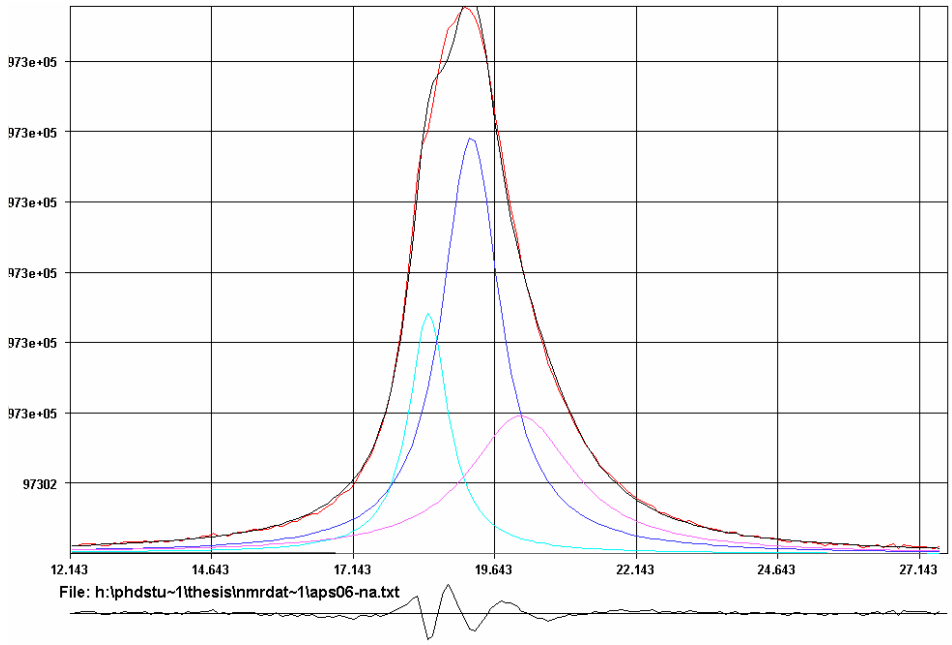

Figure 7.11: An example of the ^{23}Na curve fits used to calculate the peak positions, linewidths and peak areas. The difference pattern between the calculated peaks and measured data is also given. This figure shows a fit used on Sample 1.5/0.8 with the contributions from different Na sites shown in light blue, dark blue and pink.

compounds, show that the Na shifts observed for the AIPs are also found in hydrated silicates and aluminosilicates. Specific examples are given in Table 7.7.

Koller *et al.* (1994) have shown that the ^{23}Na chemical shifts correlate well with the total oxygen-cation bond valence and the Na-O bond distances of all oxygen atoms immediately surrounding the Na cation. The total oxygen-cation bond valence and the Na-O bond distances can be combined into a single parameter, the *shift parameter*, A. Comparison of the shift parameters can identify different silicates and aluminosilicates in which the Na has similar structural surrounds. The shift parameters given in Table 7.6 for the AIPs were calculated from the regression given by Koller *et al.* (1994). Calculation of the shift parameter from first principles requires knowledge of all oxygen bond lengths within 3.4 Å of Na atoms. The calculation could have been done using the bond lengths derived from the RDF work presented in §7.2, however, as the peak intensities for the Na-O bond did not follow the compositional trends, it was thought that these data were not of sufficient accuracy to allow calculation of the Na shift parameter.

Reports of ^{23}Na NMR in the literature do not refer to a Na NMR peak with a shift of 4 or -2 ppm, however, as these spectra are referenced to aqueous NaCl, peaks close to 0 ppm show that Na is in an aqueous environment. Peaks that were not close to 0 ppm have been assigned to specific sites in crystal lattices in the literature. Beyer *et al*. (1993) collected ^{23}Na MAS NMR spectra of faujasite-type zeolites. The Na signal at -9 ppm was attributed to Na cations at SIII sites in the large cavities, whereas the line at -13 ppm was assigned to sodium cations in truncated octahedra. A line seen at -55 pm was attributed to sodium cations in the SI site.

Table 7.7: Experimental ^{23}Na isotropic chemical shifts and calculated shift parameters for sodium silicates and aluminosilicates (after Koller *et al.*, 1994).

Compound *Na site*	δ (ppm)	A (calc)
$Na_2SiO_2(OH)_2.8H_2O$	-3.67	0.790
$Na_2SiO_2(OH)_2.7H_2O$ *Na1*	-0.94	0.800
$Na_2SiO_2(OH)_2.7H_2O$ *Na2*	-0.74	0.821
$Na_2SiO_2(OH)_2.5H_2O$ *Na1*	-1.50	0.843
$Na_2SiO_2(OH)_2.5H_2O$ *Na2*	-7.20	0.830
$Na_2SiO_2(OH)_2.4H_2O$ *Na1*	1.80	0.817
$Na_2SiO_2(OH)_2.4H_2O$ *Na2*	2.30	0.752
Na_2SiO_3	15.45	0.749
α-$Na_2Si_2O_5$	17.40	0.730
β-$Na_2Si_2O_5$ *Na1*	20.40	0.684
β-$Na_2Si_2O_5$ *Na2*	8.30	0.801
$Na_6(AlSiO_4)_6$	3.00	0.717
$Na_6(AlSiO_4)_6(OH)_2$	-4.00	-
$Na_6(AlSiO_4)_6(OH)_2.2H_2O$	-8.40	-

As the AIPs are amorphous, Na cannot be said to occupy specific crystallographic sites. However, cavities that mimic these crystallographic sites could be formed in the polymerisation process. Na could drift into these cavities and give the strong signal as seen in the spectra. These cavities have been suggested in the structural model of Barbosa, MacKenzie & Thaumaturgo (2000). Their model suggests that Na is present solely in its hydrated form, whereas the data presented from the current study show that there are ^{23}Na NMR signals indicating that Na may also be present in a non-hydrated form. The presence of these additional signals suggests that Na is active in forming and modifying the polymer network. The role of Na solely as a charge balancing cation is underestimating its contribution.

Summary

The main outcomes from ^{23}Na results were:

1) Hydrated Na is present in the AIP, most likely being constrained to framework cavities.
2) Na signals are detected from non-hydrated Na sites, which indicate that Na may be taking an active role in the formation of the polymer network, as opposed to being present solely as a charge balancing cation. Further work is recommended in §8.2 to clarify the role of Na in polymer formation.

7.2 X-ray scattering

Synchrotron x-ray scattering patterns of 8 AIPs, as well as MK and SF, were measured at a temperature of ~15 K. Data were collected from flat plate samples mounted in normal incidence transmission mode with an incident beam energy of 80.6 keV to a scattering angle of 60° 2θ, corresponding to q_{max} = 40 Å^{-1}. The scattered intensity was recorded with an intrinsic Ge energy sensitive detector. For additional details, refer to §4.5.1. Scattering data measured above q = 21 Å^{-1} were not able to be used in the calculation of the RDFs due to the scattered beam being partially obstructed by the receiving slits. Data were collected to q = 40 Å in order to allow for the resolution of the Si-O and Al-O bonds at 1.6 and 1.75 Å, respectively. The resolution of the RDF is given by $\Delta r = 2\pi/q_{max}$ – see §3.2.2. The reduction in the useable q_{max} resulted in the resolution of the RDFs being reduced to 0.3 Å, and as a consequence, the two bonds were not resolved.

7.2.1 Radial distribution analysis

The experimental structure functions, reduced radial distribution functions and pair distribution functions from the measured samples are presented in Figure 7.12, Figure 7.13 and Figure 7.14 respectively. As can be seen in Figure 7.12, the experimental structure functions exhibit oscillating behaviour up to the maximum q value of 20.5 Å^{-1}. The RDFs were calculated using the new q_{max} of 20.5 Å^{-1}, as data at higher q (20.5 – 40 Å^{-1}) had suppressed intensities consistent with the diffracted beam being cut off by receiver slits being set too close together. A correction routine, summarised in §7.2.2, was constructed to correct the data for q = 20.5-40 Å^{-1}, however, there was no qualitative change in the RRDFs due to inadequate counting statistics, and as a result, the correction routine was not used for further data processing.

The atomic densities of the AIPs were calculated from the RRDFs using the formula given by Wagner (1978); at low r, G(r) is approximated by a line with the slope $-4\pi\rho_0$ – see Figure 7.13. The determination of the atomic densities enabled the calculation of the PDFs.

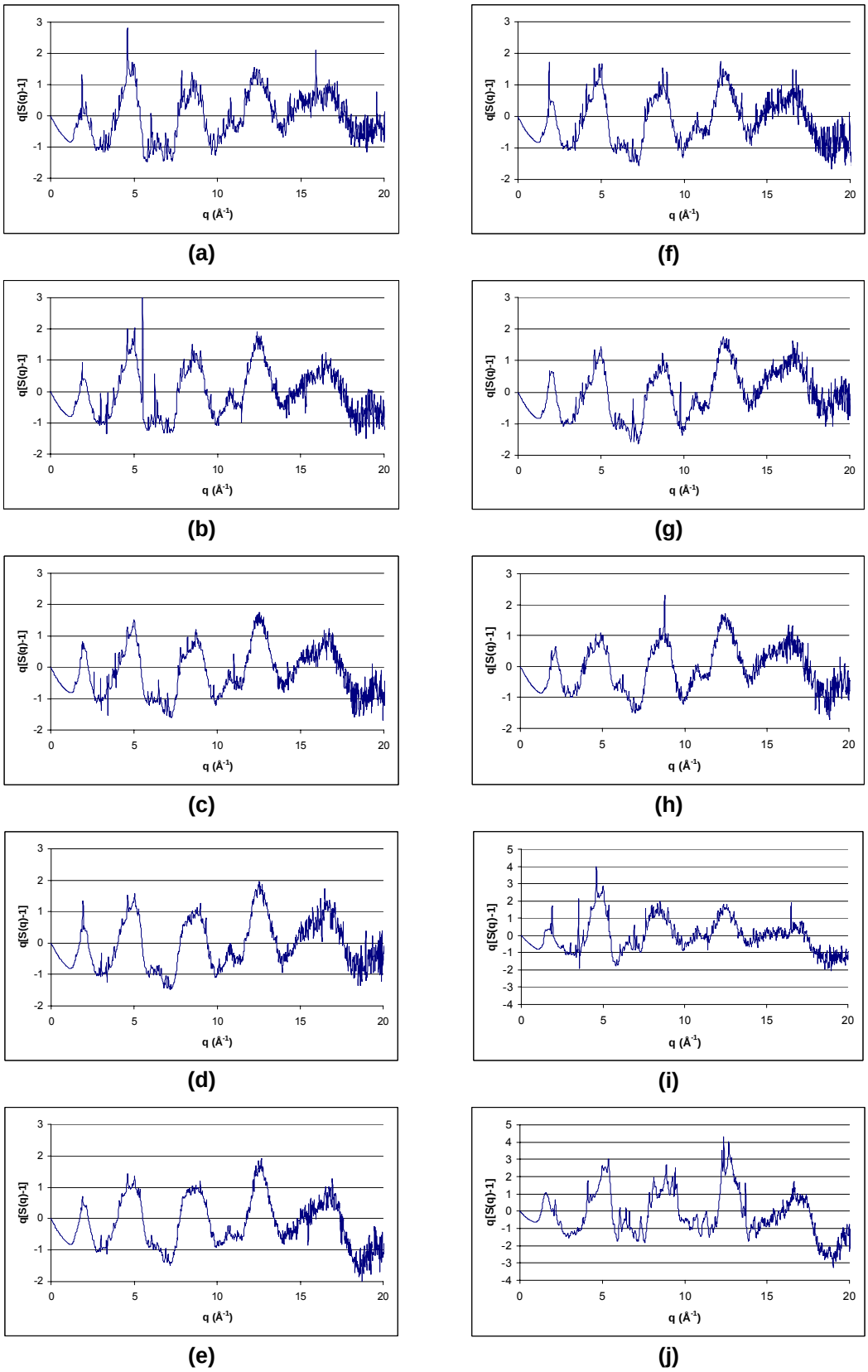

Figure 7.12: Experimental structure functions. Samples **(a)** 1.1/0.6, **(b)** 1.5/0.8, **(c)** 2.0/1.0, **(d)** 2.5/1.3, **(e)** 3.0/1.5, **(f)** 1.5/1.0, **(g)** 2.0/1.3, **(h)** 2.0/2.0, **(i)** MK and **(j)** SF.

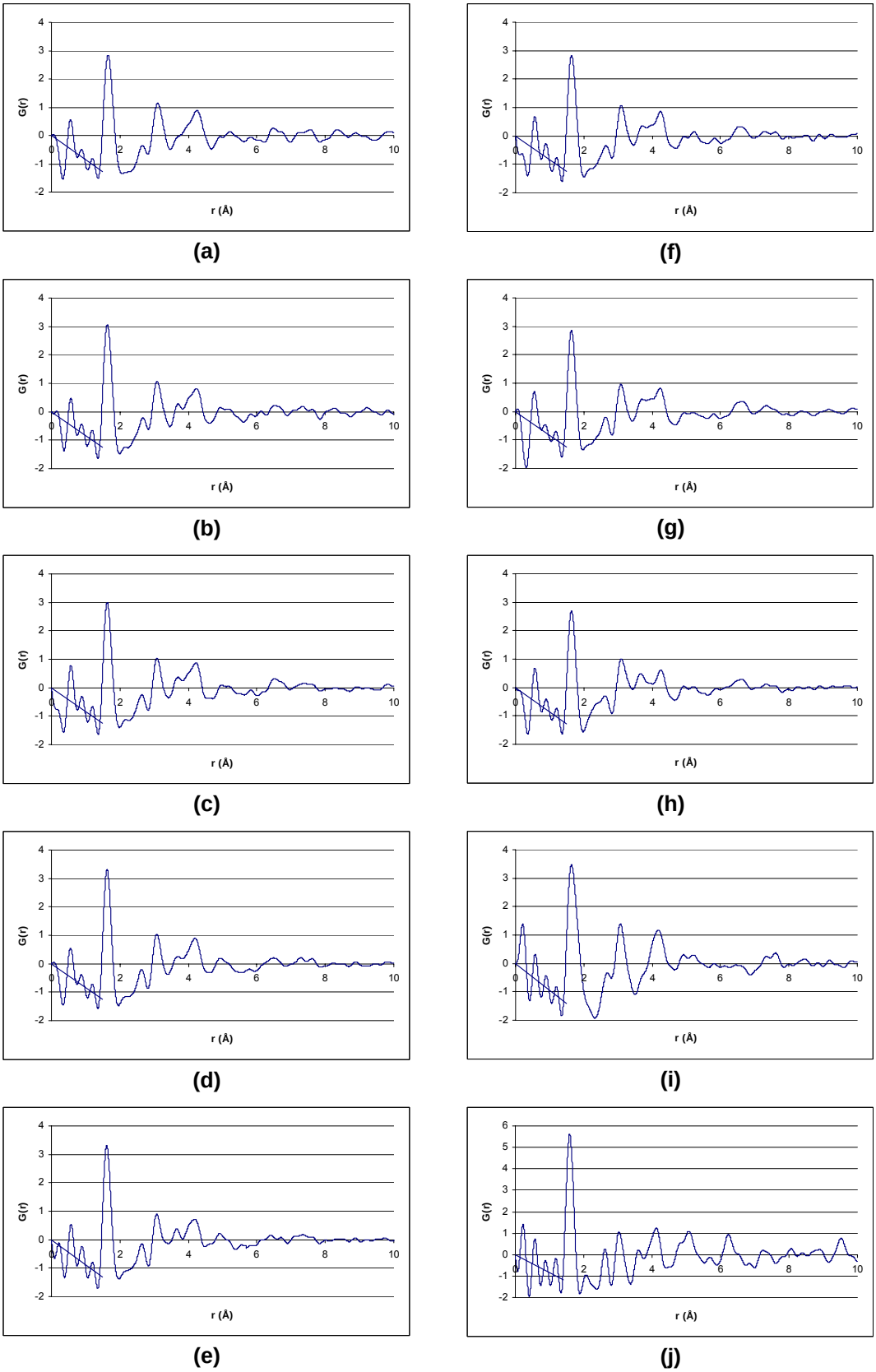

Figure 7.13: Reduced radial distribution functions. Samples **(a)** 1.1/0.6, **(b)** 1.5/0.8, **(c)** 2.0/1.0, **(d)** 2.5/1.3, **(e)** 3.0/1.5, **(f)** 1.5/1.0, **(g)** 2.0/1.3, **(h)** 2.0/2.0, **(i)** MK and **(j)** SF.

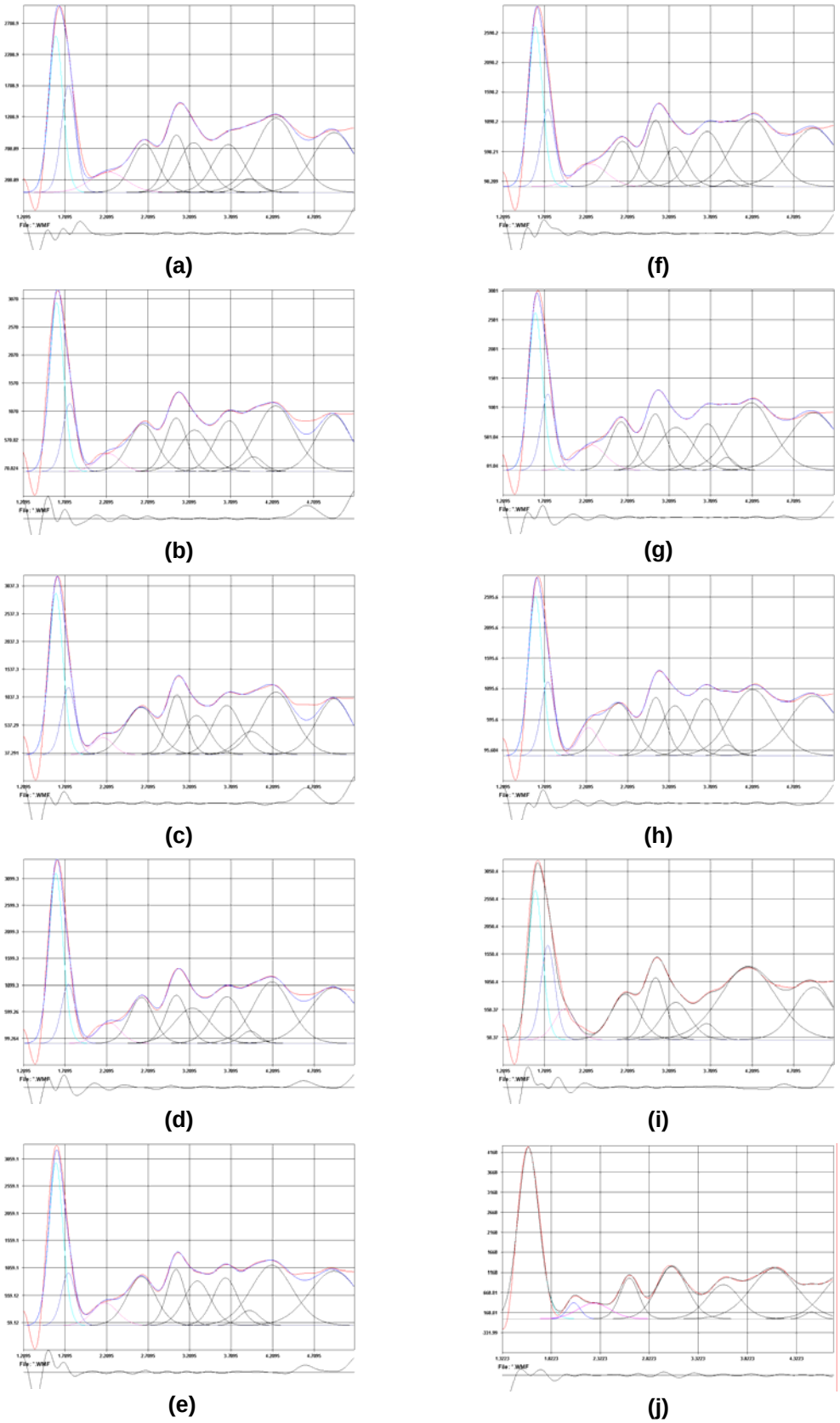

Figure 7.14: Pair distribution functions. Horizontal axis is radius (Å). Vertical axis is $g(r)=[\rho(r)/\rho_0]$ ($x10^{-3}$). Samples **(a)** 1.1/0.6, **(b)** 1.5/0.8, **(c)** 2.0/1.0, **(d)** 2.5/1.3, **(e)** 3.0/1.5, **(f)** 1.5/1.0, **(g)** 2.0/1.3, **(h)** 2.0/2.0, **(i)** MK and **(j)** SF.

The structural features present in the MK and SF RDFs are carried over to the AIP RDFS, as they correspond to Si-O/Si/Al and Al-O/Si/Al atom correlations. The additional features present in the AIP RDFs relate to Na-O/Si/Al/Na interactions. In order to quantify the changes between the different AIPs and precursor materials, PDFs were calculated to enable peak deconvolution to be carried out.

Table 7.8: Peak positions of the Gaussian curves used in the deconvolution process. The initial values correspond to those found in the literature and used in the initial curve fitting process, whereas the final values are those that were used to derive the final curve fit. Additional Gaussians were assigned to some atom pairs to allow for the fitting of asymmetric peaks.

Atom pair	Gaussian centre (Å)	
	Initial	Final
Si-O	1.6	1.6
Al^{IV}-O	1.75	1.75
Al^{VI}-O	1.9	1.9
Na-O	2.2	2.2
O-O	2.6	2.6
Si-Al	3.1	3.05
Si-Si		3.3
Al-Al		
Na-Si	3.9	3.7
Na-Al		3.9
Na-Na		
Si-O	4.2	4.2
Al-O		

Peak deconvolution was carried out by approximating each well-defined atomic pair by a symmetric Gaussian function, and fitting these curves to the experimental data. The Gaussian curves used in the first iteration of peak deconvolution are outlined in Table 7.8. The peak positions used were compiled from a series of sources (MacGillavary & Rieck, 1968 pp. 257-269; Palin, Trachenko & Dove, 2002; Keen & Dove, 1999; Ispas *et al.*, 2001; Gutiérrez, 2002). During the deconvolution process, it was found that there was significant asymmetry in some of the peaks. In order to account for the asymmetry, additional Gaussians, as given in Table 7.8, were assigned to the bonds that showed the most asymmetry. The results of these deconvolutions are presented in Figure 7.14 and Table 7.9.

Table 7.9: Peak parameters from the Gaussian fits to the PDFs shown in Figure 7.2. Peak position and FWHM are given in Å. The peak area has been increased by a factor of 1000 from the actual value. The bonds given are those most likely to occur at those peaks. The densities, ρ, are given in atoms/Å^3.

Sample	Peak	Area	FWHM	Bond
1.1/0.6	1.600	544	0.200	Si-O
	1.750	370	0.200	Al-O
ρ	2.229	182	0.508	Na-O
0.06922	2.668	319	0.380	O-O
	3.052	300	0.300	Si-Al
	3.259	364	0.420	Si-Si Al-Al
	3.678	367	0.440	Na-Si
	3.936	72	0.300	Na-Al Na-Na
	4.252	770	0.600	Si-O Al-O
	4.950	626	0.600	
1.5/0.8	1.600	652	0.200	Si-O
	1.750	261	0.200	Al-O
ρ	2.238	119	0.340	Na-O
0.06762	2.650	369	0.404	O-O
	3.053	314	0.302	Si-Al
	3.274	342	0.426	Si-Si Al-Al
	3.692	402	0.408	Na-Si
	3.986	80	0.280	Na-Al Na-Na
	4.250	706	0.560	Si-O Al-O
	4.950	544	0.500	
2.0/1.0	1.600	631	0.200	Si-O
	1.750	261	0.200	Al-O
ρ	2.166	98	0.290	Na-O
0.06634	2.625	429	0.460	O-O
	3.058	316	0.272	Si-Al
	3.292	287	0.374	Si-Si Al-Al
	3.657	384	0.398	Na-Si
	3.950	182	0.400	Na-Al Na-Na
	4.250	658	0.540	Si-O Al-O
	4.950	544	0.500	
2.5/1.3	1.600	696	0.200	Si-O
	1.750	239	0.200	Al-O
ρ	2.236	140	0.326	Na-O
0.06634	2.631	320	0.340	O-O
	3.052	300	0.304	Si-Al
	3.244	362	0.500	Si-Si Al-Al
	3.661	397	0.416	Na-Si
	3.940	64	0.256	Na-Al Na-Na
	4.202	675	0.540	Si-O Al-O
	4.950	799	0.700	
3.0/1.5	1.600	649	0.200	Si-O
	1.750	210	0.200	Al-O
ρ	2.192	163	0.362	Na-O
0.07087	2.630	398	0.408	O-O
	3.047	291	0.261	Si-Al
	3.304	337	0.379	Si-Si Al-Al
	3.643	329	0.346	Na-Si
	3.930	88	0.290	Na-Al Na-Na
	4.200	718	0.600	Si-O Al-O
	4.950	761	0.700	

Sample	Peak	Area	FWHM	Bond
1.5/1.0	1.600	587	0.200	Si-O
	1.750	283	0.200	Al-O
ρ	2.270	191	0.458	Na-O
0.06774	2.648	302	0.362	O-O
	3.050	396	0.304	Si-Al
	3.281	253	0.348	Si-Si Al-Al
	3.668	466	0.460	Na-Si
	3.930	22	0.184	Na-Al Na-Na
	4.216	742	0.604	Si-O Al-O
	4.950	746	0.700	
2.0/1.3	1.600	587	0.200	Si-O
	1.750	283	0.200	Al-O
ρ	2.266	199	0.419	Na-O
0.06682	2.632	289	0.320	O-O
	3.043	328	0.315	Si-Al
	3.292	394	0.492	Si-Si Al-Al
	3.675	320	0.369	Na-Si
	3.907	55	0.230	Na-Al Na-Na
	4.200	773	0.618	Si-O Al-O
	4.950	746	0.700	
2.0/2.0	1.600	565	0.200	Si-O
	1.750	261	0.200	Al-O
ρ	2.240	139	0.277	Na-O
0.06834	2.597	420	0.448	O-O
	3.051	296	0.288	Si-Al
	3.280	356	0.401	Si-Si Al-Al
	3.654	396	0.395	Na-Si
	3.912	42	0.214	Na-Al Na-Na
	4.215	743	0.635	Si-O Al-O
	4.950	738	0.700	
MK	1.600	587	0.200	Si-O
	1.750	370	0.200	Al^{IV}-O
ρ	1.953	181	0.299	Al^{VI}-O
0.07581	2.682	364	0.406	O-O
	3.048	344	0.284	Si-Al
	3.290	297	0.402	Si-Si Al-Al
	3.661	87	0.274	
	4.161	1139	0.800	Si-O Al-O
	4.950	579	0.560	
SF	1.590	1158	0.250	Si-O
	2.052	71	0.160	Zr-O
ρ	2.257	168	0.390	
0.06582	2.618	252	0.226	O-O
	3.052	519	0.368	Si-Si
	3.577	374	0.400	Zr-Zr
	4.096	775	0.568	Si-O

The Al^{VI}-O bond was used in the refinement of the MK PDF, as the NMR results had shown that MK had significant amounts of Al^{VI}. An Al^{V}-O bond was not utilised as it was not possible to produce a stable deconvolution when additional, unresolved peaks were added.

Examples of the gaussian fits to the PDFs and the assigned bonds are given in Figure 7.15. The main differences between the PDFs of MK and the final AIPs are the presence of 6-coordinate Al in the MK and the presence of Na-O/Al/Si/Na interactions in the AIP corresponding to nearest and next-nearest neighbours. *There were not any significant differences between the PDFs for the different AIPs*. While it was expected that the Na-O bond intensity would vary with the Na content of the AIP, this variation was not observed. Furthermore, differences were expected between the first Si-O/Al-O bonds of the AIPs. The difference was not able to be modelled as the peaks corresponding to the Si-O/Al-O bonds were not able to be resolved.

The first peak for the MK and AIP PDFs consists of a doublet Si-O/ Al-O peak at approximately 1.6 and 1.75 Å, respectively. As the two peaks were not resolved in the experimental data, refinement of the two components of this peak was very unstable. As a result, the peak refinement was constrained to intensity scaling only which did not enable any coordination information to be extracted from the refinement parameters. However, the peak positions used correspond to Si and Al tetrahedrally coordinated to oxygen.

Although trends were not seen in the first Si-O/Al-O peak when analysed with two Gaussians, trends were seen once the peak was fitted with a single asymmetric Gaussian. When a single peak is fitted to the Si-O/Al-O doublet in the PDFs, the position and FWHM of the peak vary with the composition of the AIP. The results are given in Figure 7.16.

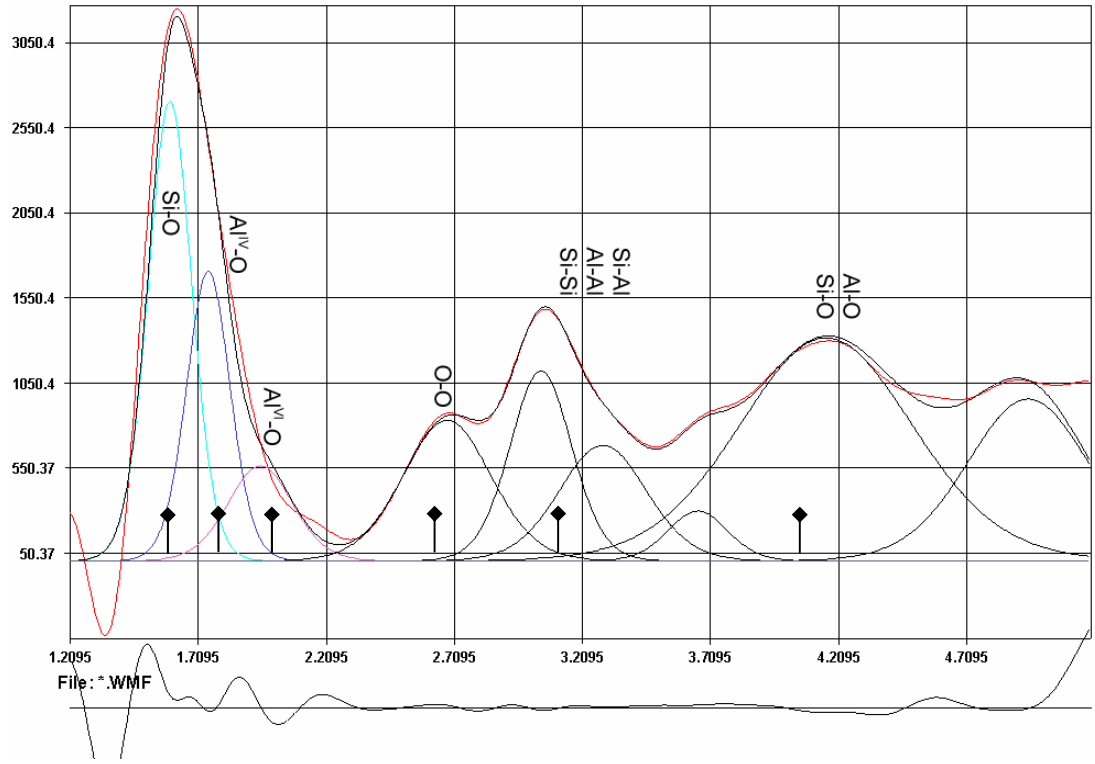

(a)

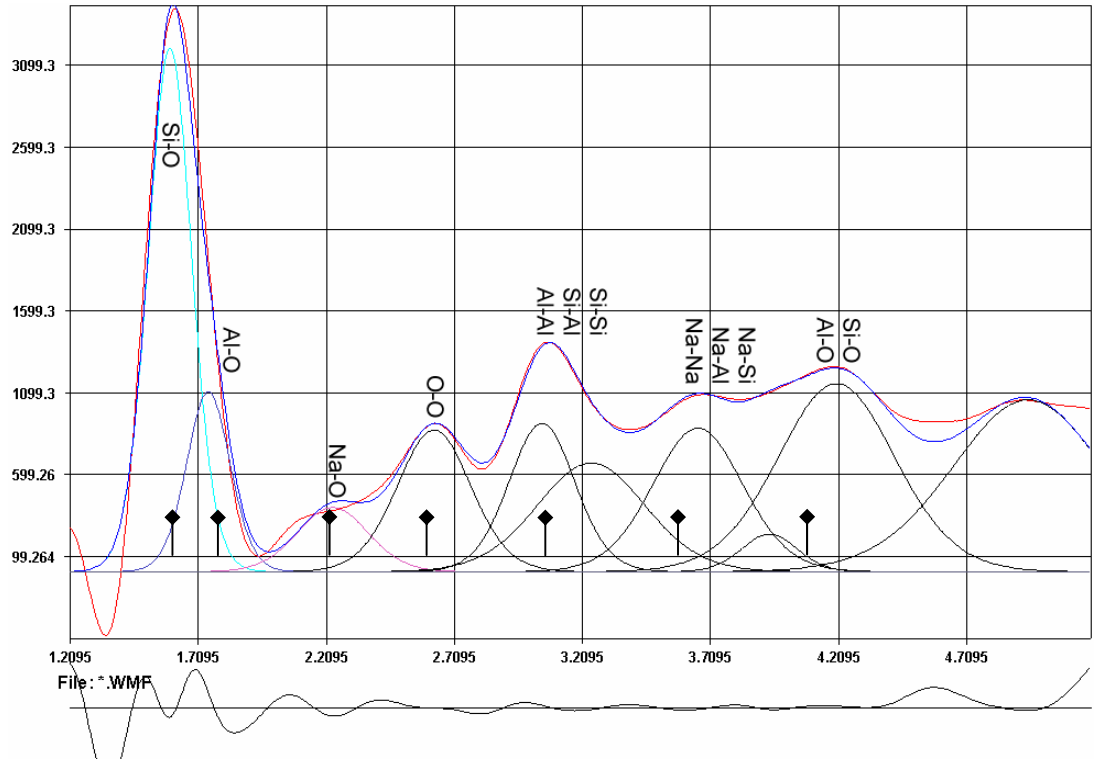

(b)

Figure 7.15: Pair distribution functions for **(a)** MK and **(b)** Sample 2.5/1.3. The Gaussians that make up the PDF have been labelled with the bonds to which they correspond. The horizontal axis is radius in ångstroms. Given below each PDF is a difference plot, showing the variation between the measured data and the fitted profiles.

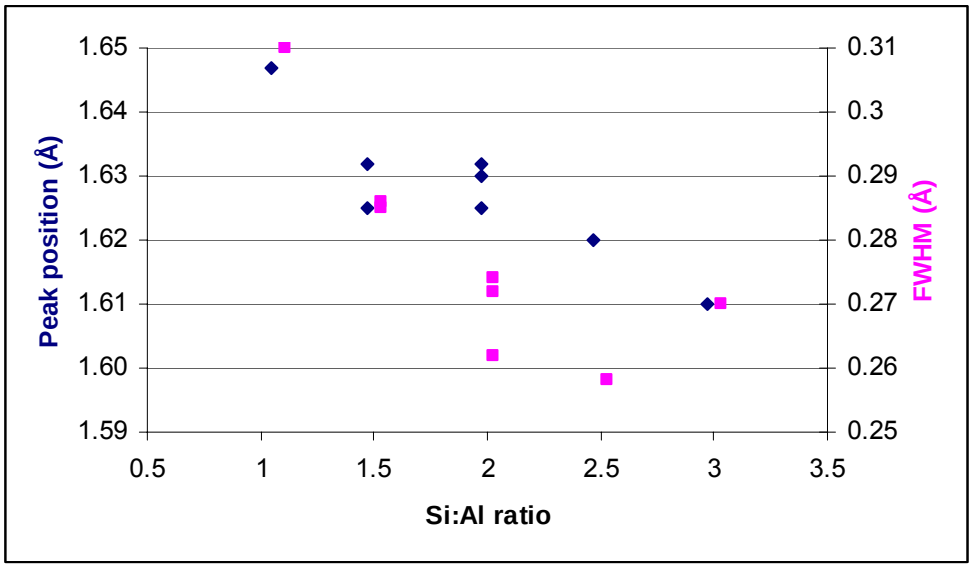

Figure 7.16: The peak position and full width half maximum from the single peak fit to the Si-O/Al-O doublet in the PDFs, showing that as the Si:Al ratio increases, the peak parameters become indicative of Si-O.

The single peak fitting results show that as the Si content of the AIP increases, the properties of the first peak tend towards Si-O. The peak position moves from a value that is indicative of an average Si-O/Al-O bond length in Sample 1.1/0.6, to a bond length that represents Si-O in Sample 3.0/2.0. The same phenomenon occurs with the FWHM of the peak. The width decreases as the Si content of the AIP increases. The decrease in width is due to the amount of Al-O present in the AIP dropping relative to the amount of Si-O, resulting in a peak that is more indicative of Si-O. This reasoning is corroborated by the results for Samples 2.0/1.0, 2.0/1.3 and 2.0/2.0. These samples have the same Si:Al ratio, and their peak position and width are all equivalent.

With the remainder of the peaks, there is little variation between the peaks of different samples. Unfortunately, the resolution of the data is such that unequivocal deconvolution of the data is not possible. The peak positions and intensities do not correlate with any compositional trends.

7.2.2 Attempt to extend the useable q_{max} for the measured data

As stated in §7.2.1, the measured diffracted intensity above 20.5 $Å^{-1}$ deviated significantly from the calculated independent scattering curve – see §3.2.2. In an attempt to rectify the intensity deviation, corrective calculations were applied to the scattered intensities.

For this trial, the scattering pattern of MK was used. A comparison between the independent scattering curve and the normalised experimental intensity was carried out at high *q*. The ratio of these two curves should be approximately one, as the scattered intensity tends towards the average of the square of the scattering factors for high *q* (see §3.2.2). As seen in Figure 7.17, this ratio decreases significantly below one indicating that the measured scattered intensity was less than predicted for the sample's composition.

As the angle through which the incident beam is diffracted increases, so to does the width of diffracted beam. The width of the diffracted beam is given by

$$b_2 = a\sin(2\theta + \phi) \qquad \textbf{Equation 7.1}$$

– see Figure 7.18. The reduction in the intensity of the measured scattering data correlates with an assumption of intensity loss due to incorrect slit widths – as the diffracted beam increased in width, the edges of the beam were cut off, and weren't recorded by the detector, resulting in a reduction in the measured scattered intensity.

Assuming an incident beam width of 1 mm and a sample thickness of 2 mm, the relationship between the diffracted beam width and the intensity ratio was found to be linear. Figure 7.19 shows the change in width of the diffracted beam, and the correlation between the beam width and the intensity ratio. The intensity ratio was used instead of the raw intensity, as the real diffracted intensity at high q can be approximated by the independent scattering curve. Use of the measured diffracted intensity would bias the

results, as this intensity is being reduced as a result of the experimental setup.

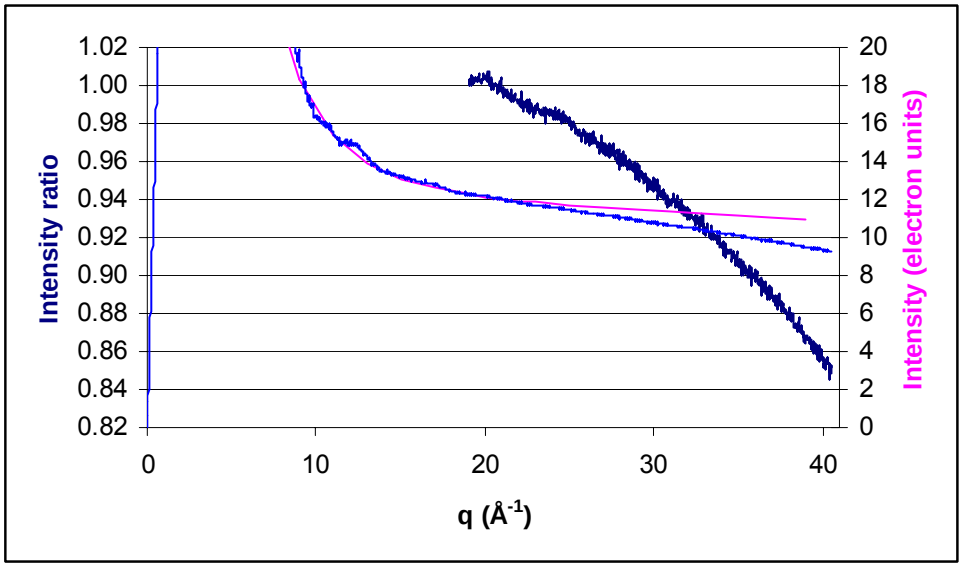

Figure 7.17: Plot showing the intensity ratio and the experimental scattering curve overlaid on the independent scattering curve. At high *q* values, the experimental and independent scattering curves should be approximately equal.

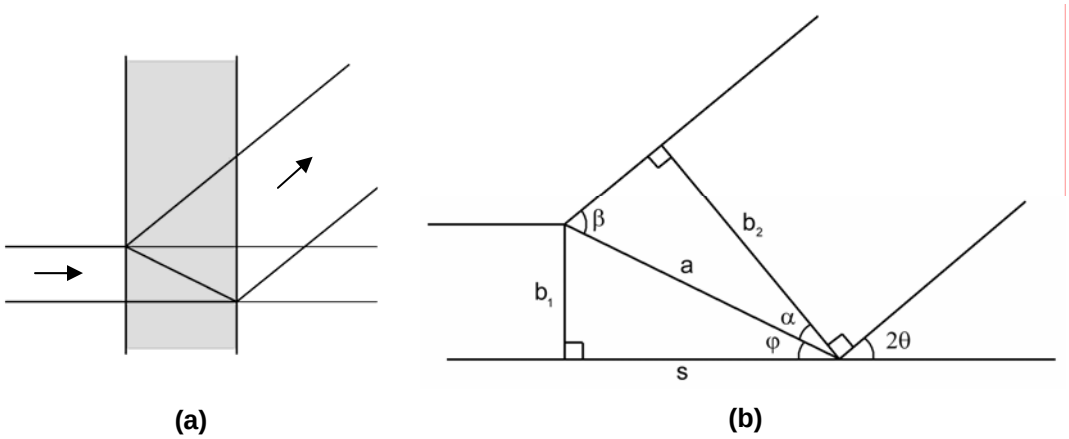

Figure 7.18: Schematic diagram showing the formulation of the diffracted beam width. (a) Shows the incident and diffracted beam passing through the sample (grey). (b) Details the variables used in Equation 7.1.

Having established that the decrease in intensity is most likely due to incorrect slit widths, the intensity ratio was fitted with a cubic curve, and the data above q = 20.5 Å^{-1} were modified by this curve to give an average intensity ratio of one. Both the modified and unmodified scattering data are given in Figure 7.20.

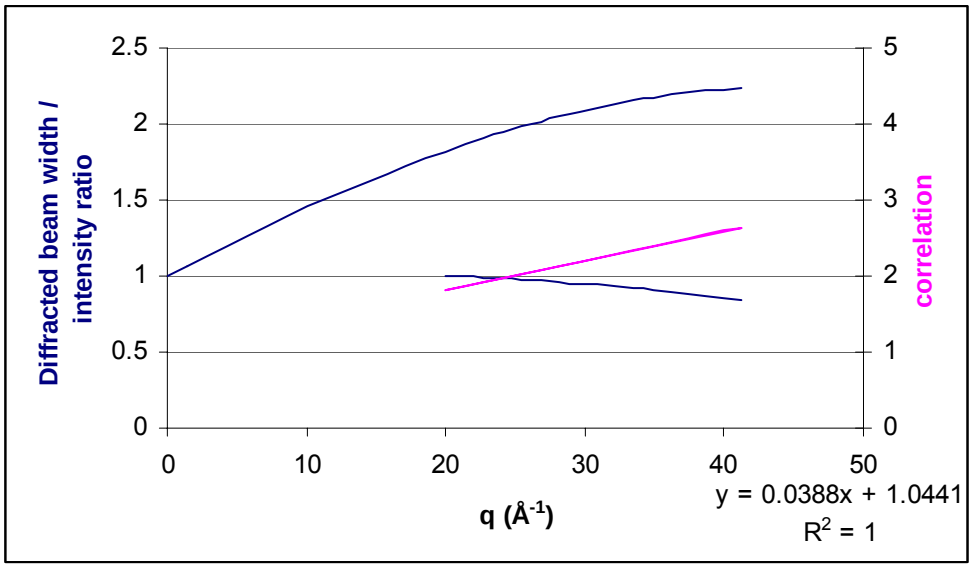

Figure 7.19: The upper blue curve shows the change in the diffracted beam width with increasing q. The lower blue curve gives the intensity ratio. The correlation between the beam width and intensity ratio is linear (pink), with a correlation coefficient of 1.

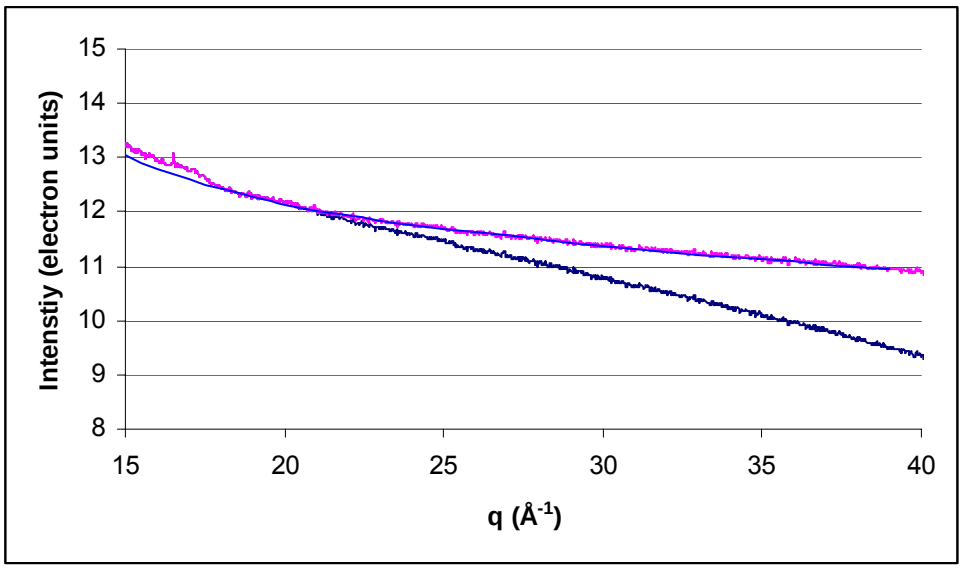

Figure 7.20: Modified (pink) and experimental (dark blue) scattered intensities. The independent scattering (royal blue) is also given.

The modified data were successfully transformed into a structure function; however, the noise present in the data at high q eliminates the gains made by increasing the q range. Figure 7.21 shows that the structure function of the corrected data diverges rapidly at higher *q*, negating any increase in resolution in the resultant RRDF. The scatter in the experimental structure function would have been reduced if data of adequate statistical quality had been collected.

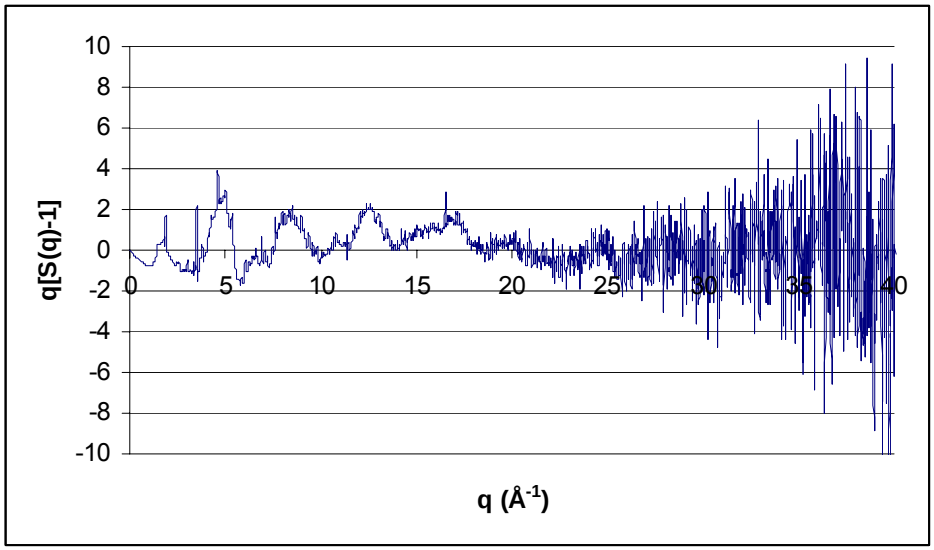

Figure 7.21: Structure function of MK calculated using the modified data, cf. Figure 7.12(i).

7.2.3 Summary

RDF analysis has been carried out on XRS patterns collected from both AIPs and precursor materials. The PDFs calculated from the scattering patterns show significant structural differences between the precursors and the AIP, as is to be expected. However, differences in the structures of the AIPs do not follow the trends in the chemical composition. *There were no significant observed structural differences between the AIPs*. The most significant difference between the PDFs of the AIPs should be found in the first Si-O/ Al-O peak, however, the two bonds were unable to be resolved due to experimental problems with the collection of high-angle data. The loss of the high angle data reduced the final resolution of the data from potentially 0.15 Å (q_{max} = 40 Å) to only 0.3 Å (q_{max} = 20.5 Å). The loss of resolution meant that the Si-O and Al-O bonds at 1.6 and 1.75 Å, respectively, were not able to be observed.

7.3 Concluding comments

7.3.1 Overview

The systematic change in Si coordination number, coupled with there being no significant change in the Al coordination with increased Na content, suggests that the growth of the tetrahedral network proceeds by the formation of Si-O-Na linkages, as has been reported in an x-ray study on calcium aluminosilicates (Petkov *et al.*, 2000). The coordination of both Si

and Al is consistent with 4-fold with respect to O by both NMR and RDF analysis.

The linewidths of the Si NMR spectra of the AIPs are in contrast to the linewidths of the Al spectra from the AIPs in terms of their relationship to the linewidth of kaolinite for the respective nuclei. Al has the same linewidth in the AIPs as in kaolinite, whereas the Si spectra of the AIPs have linewidths approximately 10 times that of kaolinite. Changes in the Si-O and Al-O bond lengths in the AIPs were not able to be confirmed by RDF analysis, due to insufficient resolution of the PDFs, however the combined lineshape of the Si/Al-O peak did vary systematically with composition. The disparity between the Si and Al NMR signals from the AIPs indicates that the amorphous character of the inorganic polymer is most likely due to a disordered Si sub-lattice. The Al sub-lattice can be considered to be constrained by the Loewenstein Avoidance Principle. If AlO_4 tetrahedra were constrained to bonding with SiO_4 tetrahedra, then the immediate structural environment of Al would be similar throughout different samples.

The change in Si coordination and the presence of residual MK in the inorganic polymer is an explanation for the change in the compressive strength of the material. The inverse relationship between residual MK content and compressive strength complicates the interpretation of compressive strength results in that the level of residual MK and the variations in the bonding network character with Si:Al ratio may both contribute to the observed trends in compressive strength. In short, it is not possible to unequivocally relate the maximisation of compressive strength to its inverse relationship with residual MK concentration. The change in the coordination of both Si and Al was not determined by RDF analysis due to insufficient PDF resolution. ^{29}Si MAS NMR showed that there was approximately 1% MK present in Sample 2.5/1.3, the highest strength sample. Microstructural analysis of the samples showed that this sample still had a significant amount of grain phase present, which leaves a question as to the exact nature of the grain phase. The presence of residual MK is not

revealed by NMR, yet SEM shows the presence of grain structures similar to those in samples which did contain residual MK.

The AIP structural models proposed by Barbosa, MacKenzie & Thaumaturgo (2000), Davidovits (1994b) and Li, Ding & Zhang (2004) (see §2.2.1 for discussion) all refer to the polymer network as being constructed of SiO_4 and AlO_4 tetrahedra, with the charge balancing cation, Na, being present in cage-like structures in the polymer. Furthermore, Davidovits (1994b) and Li, Ding & Zhang (2004) associate the Na cation directly with AlO_4 tetrahedra. The ^{29}Si MAS NMR results from the current study suggest that Na is associated preferentially with SiO_4 tetrahedra, and is also present in both hydrated and non-hydrated forms, indicating that Na may be actively involved in the forming and modifying of the polymer network.

A study into the structure of calcium aluminosilicate glasses (Petkov *et al.*, 2000) suggests that the calcium acts as network terminating species. As Ca is divalent, a terminal position would not serve to terminate the network. However, the Na used in the current study is monovalent, and if it were to occupy a terminal position, network termination would result. The position of Ca and Na in this model is outlined in Figure 7.22.

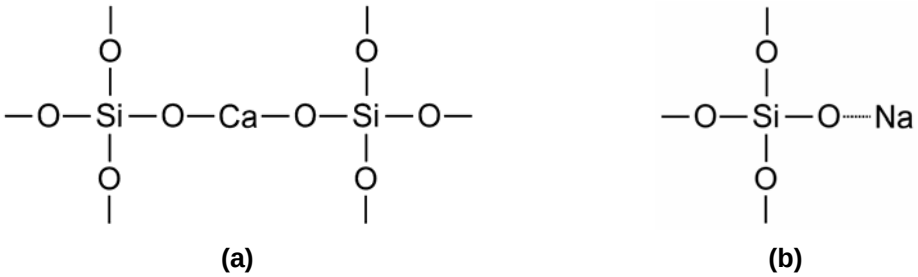

Figure 7.22: Location of the charge balancing ions, assuming network terminal positions. **(a)** Indicates that network growth is not interrupted by a terminal divalent anion. **(b)** Indicates that network growth is interrupted by a terminal monovalent anion.

In samples with high Na content, a terminal cation position would result in total disruption to the network structure as the presence of the cation would prevent further bonding with other SiO_4 or AlO_4 tetrahedra. As network disruption is not observed, an alternative model is proposed (Figure 7.23), in which the negative charge associated with the AlO_4 tetrahedra is localised on

an O atom, as it is more electronegative, allowing the Na atom to form an ionic bond with the oxygen, thus resulting in an Si-O-Na bond, without allowing network termination.

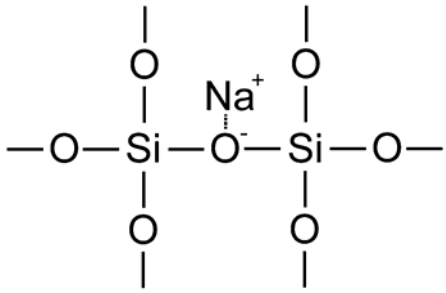

Figure 7.23: Model for the location of the charge balancing anion in AIPs. This model allows for Si-O-Na bonds to be formed without resulting in network termination.

In light of the ^{23}Na MAS NMR results presented in this chapter, a schematic modified structural model is proposed, see Figure 7.24. Based on the model of Barbosa, MacKenzie & Thaumaturgo (2000), the modified structure allows for the presence of various hydration states of Na, and tends to associate Na with Si-O-Si bonds.

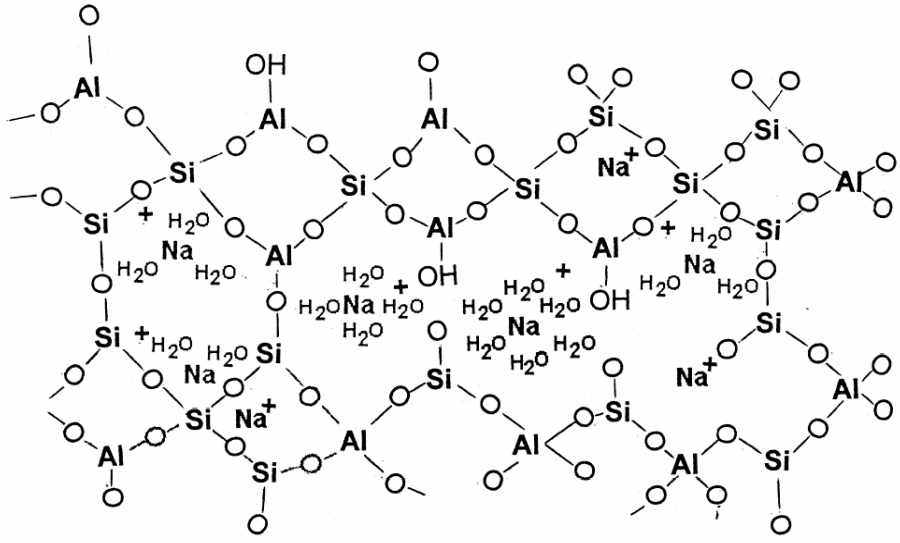

Figure 7.24: Proposed model for the structure of AIPs derived from Barbosa, MacKenzie & Thaumaturgo (2000).

The modified structure suggests that OH groups are present in the network. To elucidate the role, if any, OH has to play in the formation of the polymer network, ^{1}H MAS NMR and/or infra-red (IR) would have to be used, which will allow for the determination of the place that the OH groups take in

network formation. ^{1}H MAS NMR is able to differentiate between SiOH, AlOH and Si(OH)Al, and can give the relative amounts of these species present. IR is able to show the presence of OH, and by analysis of other absorption bands in the spectrum, the presence and coordination of Si and Al.

7.3.2 Conclusions

1) Analysis of the linewidths of the measured spectra showed that the immediate structural environment around Al in the inorganic polymers is regular, in contrast to the Si environment, which is irregular. The recorded Si linewidths are x10 the widths for kaolinite, whereas the Al linewidths are similar to that of kaolinite,
2) Initial analyses of the PDFs did not indicate a significant change in the structural environment past the nearest neighbour Si-O and Al-O bonds, however, the change in the size and shape of the first peak of the RRDF is commensurate with the change in the chemical composition,
3) The coordination of Si, as determined by NMR, changes progressively from 3.7 for Sample 1.1/0.6 to 2.2 for Sample 2.5/1.3, indicating that Na is incorporated into the polymer network as Si-O-Na. Al is present the AIPs in exclusively 4-coordinate state. The coordination of both Si and Al was unable to be determined by RDF analysis due to insufficient resolution of the PDFs,
4) A structural model for AIPs has been proposed which is consistent with results gleaned from NMR data,
5) Na signals were detected from both hydrated and non-hydrated Na sites, which indicate that Na may be taking an active role in the formation of the polymer network, as opposed to being present solely as a charge balancing cation,
6) The amount of residual MK has been quantified by ^{29}Si MAS NMR. The presence of residual MK is also revealed in the Al NMR spectra; however, quantification is not possible. Sample 1.1/0.6, the weakest sample, had 43% residual MK present,

whereas Sample 2.5/1.3, the strongest sample had 1% residual MK,

7) Changes in the compressive strength of the AIPs correlates with the variation in the coordination of the Si & the amount of residual MK present in the AIP. One, or both factors, may influence the compressive strength,

8) The presence of zeolites was revealed by ^{29}Si MAS NMR for Samples 1.1/0.6, 1.1/0.8 and 1.1/1.0. Zeolite features were not evident in the ^{27}Al MAS NMR spectra, and

9) The use of ^{1}H MAS NMR and/or IR is recommended to elucidate the role of OH groups in the formation of the polymer network.

8.0 CONCLUSIONS AND RECOMENDATIONS

8.1 Conclusions

The AIPs investigated in the current study were sodium aluminosilicate materials with applications in areas such as building and construction. Production of AIPs was carried out by mixing metakaolinite with a sodium silicate solution, followed by curing at elevated temperatures (< 100 ºC). The final properties of the AIP depend on the aluminosilicate used, the activating solution and the curing process.

The area of interest investigated, due to its technological and environmental importance, was the utilisation of AIPs as a substitute for Portland cement. Portland cement has been in use since the mid-1800s, and no substantial technological advance has been made in its manufacture and use since that time. Within this field of cement replacement research, the scope of the current study was further narrowed to study structure/property relationships in AIPs. The study of structure/property relationships was seen as a fruitful area of research, as elucidating the change in the material's structure as it varies with composition will allow for optimal compositions to be identified for different applications.

In understanding how the chemical composition impacts the material properties, the approach taken was to examine how the composition affects the structure of the polymers and endeavour to explain the material properties in terms of the structure. In light of this reasoning, the principal questions this research hoped to answer were:

1) How does the structure of these AIPs change with composition? and
2) How does this change in structure influence the material properties of the AIP?

The AIPs investigated had a composition range of Si:Al ratio = 1.1 – 3.0 and Na:Al ratio = 0.5 – 2.0. The Si content of the AIPs was altered by the addition of amorphous SiO_2 in the activating solution. The Na content of the

polymer was altered by changing the amount of NaOH present in the activating solution. The limits of the Si:Al ratio range were set in response results in the literature which stated that AIPs were best formed with Si:Al ratios between 1 and 3. AIPs prepared with Na:Al ratios less than 0.5 lacked any substantial material strength, and any silica added to the solutions was difficult to dissolve. The upper limit of the Na:Al ratio range was set by safety concerns as activating solutions with high Na levels tended to boil during the addition of silica fume.

Once the processing technique and sample composition had been established, the structural nature of the AIPs was investigated at multiple length scales. The nature of the AIPs in the macroscale was investigated by compressive strength testing, the structure of the AIPs in the microscale was studied by SEM and EDS and the nanostructure of the AIPs was examined by NMR and XRD/RDF.

How does the structure of these AIPs change with composition? It was found that the average coordination of Si changes progressively from 3.7 – 2.2 with change in the Al and Na content, which may be attributed to the formation of Si-O-Na linkages. The change in the Si coordination has not been reported previously. ^{23}Na MAS NMR revealed the presence of both hydrated and non-hydrated forms of Na, showing that Na may take an active role in the formation and modification of the polymer network. The presence of Na in multiple structural positions shows that designating Na a “charge balancing cation” is understating its role in the AIP network. To this end, *a structural model is proposed that takes the multiple Na states into account*.

Radial distribution function analysis of the x-ray scattering data for the AIPs does not indicate a significant change in the structural environment past the nearest neighbour Na-O bonds. However, *the change in the size and shape of the first peak of the RRDF is commensurate with the change in the chemical composition*. Unfortunately, the resolution of the RDFs was insufficient to enable the determination of changes in the nearest neighbour Si-O and Al-O bonds.

The microstructure of the AIPs showed that the samples consisted of two phases, grain and matrix. The grain phase is thought to arise from the incomplete dissolution of MK. The exact nature of the grain phase is not known, as its chemical composition, and NMR spectrum, has changed from that of MK, whilst its morphology remains reminiscent of MK. The amount of residual MK in the samples was able to be determined by ^{29}Si NMR. The relative amounts of the two phases in each sample were dependent on the Na:Al ratio of the sample with low Na:Al ratios resulting in a predominance of grains, except for the Si:Al = 1.08 samples, in which the grain microstructure was present for all Na:Al ratios.

Microanalysis of the AIPs confirmed the presence of Al and Si in the matrix phase, showing that it was formed from dissolved MK. *The matrix phase is the fully formed inorganic polymer*. It was also found that the Si:Al molar ratio of the grains increased with the increase of the nominal AIP composition, which was not expected, as it was originally thought that the grain phase was solely residual MK. The elevated Si:Al molar ratios of the grains can be explained by the preferential dissolution of Al from the grains, or by the initial stages of dissolution acting on the grains being stopped by the curing process. The Na content of the grains depends on both the Na:Al and Si:Al molar ratios. For samples with a Si:Al molar ratio ≥ 1.5, the Na content of the grains was virtually independent of both the Na:Al and Si:Al molar ratios. For the Si:Al = 1.08 samples, the Na content of the grains is only slightly less than the nominal Na:Al composition of the AIP. It is thought that Na is present in the grains in these materials at higher levels due to its greater availability due to the lack of Si in solution. The Na content of the matrix shows a generally increasing trend with increasing Na:Al ratio, largely independent of the Si:Al ratio. In general, the Na content of the matrix is apparently reduced from the nominal Na:Al ratio, most probably due to the soluble nature of Na in the preparation of the SEM samples. The matrix phase composition of the highest strength sample corresponded to a network formula of $Na_n[-(SiO_2)_{3.2}-(AlO_2)-]_n$.

Synchrotron x-ray diffraction analysis of the AIPs showed that the AIPs formed were entirely amorphous. It was also revealed that AIPs with the compositions Si:Al:Na = 1.1:1:0.6-1.5, 1.5:1:1.5-2.0 and 2.0:1:2.0 formed zeolites (zeolites A (LTA), X (LTA) & Y (FAU) and sodalite (SOD)) in conjunction with the amorphous AIP. Analysis of the microstructure of those AIPs did not reveal any features that could positively be identified as zeolitic. The location of the zeolites could be revealed by microdiffraction techniques such as electron back-scatter diffraction (EBSD). The observation of zeolites in the AIPs shows that zeolites can be made under the same processing conditions as AIPs. Furthermore, the formation mechanisms of zeolites may be adapted to explain the formation of AIPs, which could be a great help in elucidating the structural nature of AIPs.

How does the change in structure influence the material properties of the AIP? The compressive strength of the AIPs is significantly affected by their chemical composition. The maximum compressive strength was 64 ± 3 MPa for Sample 2.5/1.3, whilst the minimum compressive strength was 0.40 ± 0.02 MPa for Sample 1.1/0.6. The strength of the AIPs can be optimised by varying the composition. As the sample strength changed, so to did the way in which the samples failed. Samples with compressive strengths above 50 MPa resulted in catastrophic failure, whereas strengths below 5 MPa resulted in irreversible plastic deformation, and samples between these two extremes failed primarily by cone & split failure. These different mechanisms show that the highest strength AIPs exhibit almost ceramic-like failure behaviour, whilst the medium strength AIPs act as cement paste analogues.

The type of microstructure exhibited by the AIPs was found to correlate with the sample's compressive strength; an increase in the level of MK resulted in a decrease in the compressive strength. Low strength samples had a microstructure that consisted predominately of the grain phase, whilst the high strength samples had a more uniform microstructure, with a predominance of the matrix phase.

The microstructure of the AIPs does not solely determine the compressive strength of the material, which is shown by a comparison of Samples 1.5/1.0 and 2.0/1.0. These two samples have nearly identical microstructures, with the compressive strengths of the samples being 23.4 and 51.3 MPa, respectively. The composition of the matrix material of the higher strength samples (> 40 MPa) was in the range of $Na_n[-(SiO_2)_{2\text{-}3.5}-(AlO_2)-]_n$. There is also a correlation between the compressive strength of the AIP with the average coordination of Si.

There are two proposed causal factors for the observation of compressive strength maximisation, residual MK level and Si coordination. One, or both, of these factors may influence the results observed for compressive strength. Resolution of the question would require a further study of this type in which the particle size of the precursor MK is sufficiently fine as to permit complete dissolution.

In light of the experimental findings of this study, it is conjectured that a single-phase, MK-derived AIP would have a compressive strength of 80 – 100 MPa, a uniform microstructure with minimal porosity, elemental coordinations commensurate with the composition of the material and a structure that can be shown to be different to that of MK

In conclusion, it has been shown in the current study that:

1) The coordination of Si, as determined by NMR, changes progressively from 3.7 for Sample 1.1/0.6 to 2.2 for Sample 2.5/1.3, with change in the Al and Na content through the formation of Si-O-Na linkages. The coordination of both Si and Al was unable to be determined by RDF analysis due to insufficient PDF resolution,
2) Initial analyses of the PDFs do not indicate a significant change in the structural environment past the nearest neighbour Si-O and Al-O bonds, however, the change in the size and shape of the first peak in the PDF is commensurate with changes in the chemical composition,

3) The chemical composition has a direct effect on the compressive strength of the AIP. The occurrence of a maximum in the compressive strength shows that for given activation and curing regimes, the strength of the AIP can be optimised. The maximum compressive strength was 64 ± 3 MPa for Sample 2.5/1.3 (matrix network formula: $Na_n[-(SiO_2)_{3.2}-(AlO_2)-]_n$),
4) The AIPs exhibit a two-phase microstructure (AIP matrix and grain), in which the relative levels of the phases varies with the Na:Al molar ratio. As the ratio increases, so to does the relative amount of the matrix phase,
5) There is a correlation between the compressive strength of the AIP and with the coordination of the Si & the amount of residual MK present in the AIP. One, or both factors may contribute to the observed change in compressive strength,
6) Some of the AIPs synthesised co-formed zeolites during the curing process. The zeolites were observed for all samples with Si:Al = 1.08, regardless of the Na: level. AIPs with Si:Al = 1.5 and 2.0 also formed zeolites if the Na:Al ratio was sufficiently high. Visual evidence for these phases was not found in the microstructural investigation. The presence of zeolites has the potential to allow for the elucidation of formation mechanisms for the synthesis of AIPs,
7) As the nominal Si:Al ratio of the sample increases, the Si:Al ratio of the grain phase is increased from the MK value of 1.08. It is conjectured that the grains start to dissolve as they reach 'saturation' point, in terms of Si content. The grains observed in the micrographs were prevented from fully dissolving as the curing process halted further formation of the polymer, and
8) A structural model for AIPs has been proposed which is consistent with results gleaned from NMR data.

8.2 Recommendations

In the current study, effort was concentrated on investigating the properties of AIPs with a wide range of chemical compositions. The study has shown the wide range of composition produces an equally wide range of material properties. For example, the compressive strength, which varied from 0.4 to 64 MPa. It is recommended that the most promising samples from the suite studied be taken and further development carried out, including different curing regimes and precursor particle size. This work was not carried out in the current study due to time limitations. The question that this work would aim to answer is: what is the role and origin of the two phase microstructure? Would this change if the curing process was altered to try and make more of the grains dissolve? What would happen if we started with smaller particles? Hopefully, this foreshadowed work will result in single phase AIPs being produced, and would allow for a more definitive determination of the structure of the AIP.

The presence of zeolites in some of the AIPs is an outcome that needs to be investigated further, as the co-formation of zeolites shows that the conditions under which both zeolites and AIPs form is similar. As zeolite science is more mature than AIP science, can knowledge of the formation of zeolites be applied to the formation of AIPs? The location of the zeolites in the AIP may indicate how they have formed. Have they formed as a 'crust' around the grains, or are they evenly distributed through the matrix phase, or the grain phase? These questions could be answered by the use of microdiffraction techniques such as EBSD. Conversely, the presence of zeolites in these materials could be used to elucidate an alternative form of zeolite production. What processing conditions can be modified to increase or decrease the amount of zeolite produced? Can this low temperature route be exploited as an additional means of zeolite production?

The AIPs produced in the current study were relatively pure, with ~1 wt% of impurities such as Fe_2O_3 and TiO_2. As one potential use of these that is being investigated is toxic waste management, to effect of impurity elements on the structure of the AIP needs to be studied at a fundamental

level. The presence of zeolites also has implications for the use of AIPs as toxic waste repositories. Can the zeolites be used as molecular cages to trap toxic elements? Work has already been carried out looking at cause and effect, but nothing has been published on how the impurity elements interact with the polymer network to enable the enhancement or destruction of the polymer network.

The role of the “charge-balancing cation” and OH groups in the formation of the polymer network needs to be further elucidated. As has been shown in the current study, Na is present in different forms in the polymer network, showing that it may perform more than just a charge-balancing role. In order to clarify the role of Na as a charge balancing ion, it may be useful to carry out NMR analysis on heated samples in order to drive off any water present and remove the peaks due to aqueous Na. Also the use of ^{1}H NMR and/or IR to look at the presence of OH groups in the polymer network is recommended, as the presence of OH groups would modify the way in which the network grows.

Porosity may play a part in determining the properties of the AIPs. Large pores can be controlled through the AIP production route; however, micro and nanoporosity, formed in the synthesis process may affect the formation mechanisms. Small angle x-ray or neutron scattering (SAXS/ SANS) can be used to study pores in the size range of 50 Å – 1 μm. Use of small angle scattering, in conjunction with conventional x-ray diffraction will allow the determination of the structural nature of AIPs over the nano and microscales.

The area of research that needs the most input is the study of the formation mechanisms, and the development of structural models of AIPs. In this regard, the literature is lacking, relying on “hypothetical monomers” to explain the structures observed in the material. This area may benefit from input from the zeolite knowledge base. Also, the use of molecular simulations to model the polymerisation process would allow for the study of many different factors (e.g.: Si/Na:Al ratio, curing temperature, water content) and

their effects on the polymerisation process. *High resolution RDF analysis would allow for the determination bond length and angle distributions for the AIPs, which would help in the production of structural models*. Whilst NMR is able to give coordination information, it is a bulk technique. MicroXAS would be able to give coordination information on a local scale, allowing distribution maps of coordination and composition to be made. The distribution of the constituent atoms, and their coordination could also help shed light on the formation mechanisms of the AIP. In addition to these techniques, SEM/EDS could be used to investigate the possibility of “chemical zoning” in the grain phase. Any zoning of the constituent elements could shed light on the process by which the grains dissolve, and the inorganic polymer matrix forms.

There are great benefits to be gained from the use of AIPs in today’s society. Their current use may be small, but it is growing, and as it grows, so to must our understanding of the material. These materials show promise in their use for real-world applications, and as such, warrant the attention that is being paid to them.

9.0 REFERENCES

Allahverdi, A. & Skvára, F. 2001a, 'Nitric Acid Attack on Hardened Paste of Geopolymeric Cements, Part 1', *Ceramics-Silikáty* (Electronic), vol. 45, no. 3, pp. 81-88, Available: www.ceramics-silikaty.cz [2002, September 18].

Allahverdi, A. & Skvára, F. 2001b, 'Nitric Acid Attack on Hardened Paste of Geopolymeric Cements, Part 2', *Ceramics-Silikáty* (Electronic), vol. 45, no. 4, pp. 143-149, Available: www.ceramics-silikaty.cz [2002, September 19].

Alonso, S. & Palomo, A. 2001, 'Alkaline Activation of Metakaolin and Calcium Hydroxide Mixtures: Influence of Temperature, Activator Concentration and Solids Ratio', *Materials Letters* (Electronic), vol. 47, no. 1-2, pp. 55-62, Available: Elsevier/ScienceDirect S0167-577X(00)00212-3 [2001, March 28].

ASTM 1999, 'Standard Test Method for Compressive Strength of Cylindrical Concrete Specimens: C39-96', in *Annual Book of ASTM Standards*, pp. 18-22.

ASTM 2002, 'Standard Specification for Coal Fly Ash and Raw or Calcined Natural Pozzolan for Use as a Mineral Admixture in Concrete: C618-01', in *Annual Book of ASTM Standards*, vol. 4.02, pp. 318-321.

Atkins, M., Glasser, F. P. & Jack, J. J. 1995, 'Zeolite P in Cements: Its Potential for Immobilizing Toxic and Radioactive Waste Species', *Waste Management* (Electronic), vol. 15, no. 5, pp. 127-135, Available: Pergamon/ScienceDirect 0956-053X(95)00015-1 [2004, Febuary 2].

Bakharev, T., Sanjayan, J. G. & Cheng, Y.-B. 1999, 'Alkali Activation of Australian Slag Cements', *Cement and Concrete Research* (Electronic), vol. 29, no. 1, pp. 113-120, Available: Pergamon/ScienceDirect S0008-8846(98)00170-7 [2002, September 18].

Barbosa, V. F. F. & MacKenzie, K. J. D. 2003, 'Synthesis and Thermal Behaviour of Potassium Sialate Geopolymers', *Materials Letters* (Electronic), vol. 57, pp. 1477-1482, Available: Elsevier/ScienceDirect DOI:10.1016/S0167-577X(02)01009-1 [2003, Febuary 12].

Barbosa, V. F. F., MacKenzie, K. J. D. & Thaumaturgo, C. 2000, 'Synthesis and Characterisation of Materials Based on Inorganic Polymers of Alumina and Silica: Sodium Polysialate Polymers', *International Journal of Inorganic Materials* (Electronic), vol. 2, no. 4, pp. 309-317, Available: Elsevier/ScienceDirect S1466-6049(00)00041-6 [2001, March 5].

Basaldella, E. I., Kikot, A. & Tara, J. C. 1997, 'Effect of Aluminum Concentration on Crystal Size and Morphology in the Synthesis of a NaAl Zeolite', *Materials Letters* (Electronic), vol. 31, no. 1-2, pp. 83-86, Available: Elsevier/ScienceDirect S0167-577X(96)00256-X [2002, September 18].

Bazant, Z. P. 1984, 'Size Effect in Blunt Fracture: Concrete, Rock, Metal', *Journal of Engineering Mechanics,* vol. 110, no. 4, pp. 518-535.

Beyer, H. K., Pál-Borbély, G. & Karge, H. G. 1993, 'Assignment of ^{23}Na MAS NMR Signals of Ammonium- and Lanthanum-Exchanged Sodium Y Zeolites', *Microporous Materials* (Electronic), vol. 1, no. 1, pp. 67-71, Available: Elsevier/ScienceDirect 10.1016/0927-6513(93)80009-J [2003, Febuary 25].

Brinker, C. J. & Scherer, G. W. 1990, *Sol-Gel Science: The Physics and Chemistry of Sol-Gel Processing*, Academic Press, Inc., San Diego.

Brough, A. R. & Atkinson, A. 2002, 'Sodium Silicate-Based, Alkali-Activated Slag Mortars; Part I. Strength, Hydration and Microstructure', *Cement and Concrete Research* (Electronic), vol. 32, no. 6, pp. 865-879, Available: Pergamon/ScienceDirect DOI: 10.1016/S0008-8846(02)00717-2 [2002, September 24].

Brough, A. R., Katz, A., Sun, G.-K., Struble, L. J., Kirkpatrick, R. J. & Young, J. F. 2001, 'Adiabatically Cured, Alkali-Activated Cement-Based Wasteforms Containing High Levels of Fly Ash; Formation of Zeolites and Al-Substituted C-S-H', *Cement and Concrete Research* (Electronic), vol. 31, no. 10, pp. 1437-1447, Available: Pergamon/ScienceDirect DOI: 10.1016/S0008-8846(01)00589-0 [2002, September 18].

Bugosh, J. 1959, *Fibrous Alumina Monohydrate and Its Production,* US 2915475, (patent).

Callister, W. D. 1997, *Materials Science and Engineering: An Introduction,* 4th edn, John Wiley and Sons, Inc., New York.

Cartwright, M. 1990, *Fourier Methods for Mathematicians, Scientists and Engineers*, Ellis Horwood Limited, West Sussex.

Challa, G. 1993, *Polymer Chemistry: An Introduction*, Ellis Horwood, London.

Cromer, D. T. & Mann, J. B. 1967, 'Compton Scattering Factors for Spherically Symmetric Free Atoms', *Journal of Chemical Physics,* vol. 47, no. 6, pp. 1892-1893.

Cromer, D. T. & Mann, J. B. 1968, 'X-Ray Scattering Factors Computed from Numerical Hartree-Fock Wave Functions', *Acta Crystallographica,* vol. A24, pp. 321-324.

Davidovics, M., Martin, B. & Davidovits, J. 1999, 'Past and Present Experience on the Use of Carbon-Géopolymère Composite™ in Formula One and C.A.R.T. Racing Cars.' in *GEOPOLYMER '99*, eds. Davidovits, J., Davidovits, R. & James, C., Institut Géopolymère, pp. 141-142.

Davidovits, J. 1989, 'Geopolymers and Geopolymeric Materials', *Journal of Thermal Analysis,* vol. 35, no. 2, pp. 429-441.

Davidovits, J. 1991, 'Geopolymers: Inorganic Polymeric New Materials', *Journal of Thermal Analysis,* vol. 37, pp. 1633-1656.

Davidovits, J. 1994a, 'Global Warming Impact on the Cement and Aggregates Industries', *World Resource Review,* vol. 6, no. 2, pp. 263-278.

Davidovits, J. 1994b, 'Properties of Geopolymer Cements', in *Proceedings First International Conference on Alkaline Cements and Concretes*, Kiev State Technical University, Kiev, Ukraine, pp. 131-149.

Dove, M. T., Keen, D. A., Hannon, A. C. & Swainson, I. P. 1997, 'Direct Measurement of the Si-O Bond Length and Orientational Disorder in the High-Temperature Phase of Cristobalite', *Physics and Chemistry of Minerals,* vol. 24, pp. 311-317.

Duer, M. J. (ed.) 2002, *Solid-State NMR Spectroscopy: Principles and Applications*, Blackwell Science Ltd., Oxford.

Dwiggins Jr., C. W. & Park, D. A. 1971, 'Calculation of the Intensity of Secondary Scattering of X-Rays by Non-Crystalline Materials', *Acta Crystallographica,* vol. A27, pp. 264-272.

Engelhardt, G. & Michel, D. 1987, *High-Resolution Solid-State NMR of Silicates and Zeolites*, John Wiley & Sons, Chichester.

Engelhardt, G., Nofz, M., Forkel, K., Wihsmann, F. G., Mägi, M., Samoson, A. & Lippmaa, E. 1985, 'Structural Studies of Calcium Aluminosilicate Glasses by High Resolution Solid State ^{29}Si and ^{27}Al Magic Angle Spinning Nuclear Magnetic Resonance', *Physics and Chemistry of Glasses,* vol. 26, no. 5, pp. 157-165.

Escalante-García, J. I. & Sharp, J. H. 2001, 'The Microstructure and Mechanical Properties of Blended Cements Hydrated at Various Temperatures', *Cement and Concrete Research* (Electronic), vol. 31, no. 5, pp. 695-702, Available: Pergamon/ScienceDirect S0008-8846(01)00471-9 [2002, September 18].

Fernández-Jiménez, A., Palomo, J. G. & Puertas, F. 1999, 'Alkali-Activated Slag Mortars; Mechanical Strength Behaviour', *Cement and Concrete*

Research (Electronic), vol. 29, no. 8, pp. 1313-1321, Available: Elsevier/ScienceDirect S0008-8846(99)00154-4 [2002, September 18].

Garrett, R. E., Cookson, D. J., Lane, S. & Hunter, B. 2000, '*Python Powder Data Analysis*', ver: 1.5.

Gimblett, F. G. R. 1963, *Inorganic Polymer Chemistry*, Butterworth and Co., London.

Granizo, M. L. & Blanco, M. T. 1998, 'Alkaline Activation of Metakaolin. An Isothermal Conduction Calorimetry Study', *Journal of Thermal Analysis,* vol. 52, pp. 957-965.

Granizo, M. L., Blanco-Varela, M. T. & Palomo, A. 2000, 'Influence of the Starting Kaolin on Alkali-Activated Materials Based on Metakaolin. Study of the Reaction Parameters by Isothermal Conduction Calorimetry', *Journal of Materials Science,* vol. 35, no. 24, pp. 6309-6315.

Gutiérrez, G. 2002, *Atomistic Simulation of Densified Amorphous Alumina*, Available: [http://fisica.usach.cl/~ggutierr/reprints_gg/gg_sochi00_revisado.pdf] (October 20, 2003).

Hardjito, D., Wallah, S. E. & Rangan, B. V. 2002, 'Study on Engineering Properties of Fly Ash-Based Gropolymer Concrete', *Journal of the Australasian Ceramic Society,* vol. 38, no. 1, pp. 44-47.

Hos, J. P., McCormick, P. G. & Byrne, L. T. 2002, 'Investigation of a Synthetic Aluminosilicate Inorganic Polymer', *Journal of Materials Science* (Electronic), vol. 37, no. 11, pp. 2311-2316, Available: Kluwer Academic Publishers/Swetsnet [2002, September 24].

Hunter, D. N. 1963, *Inorganic Polymers*, Blackwell Scientific Publications, Oxford.

ICDD 2001, '*PCPDFWIN*', ver: 2.2, Available: http://www.icdd.com.

Iler, R. K. 1986, 'Silica Chemistry in Nature and Industry', *Chemistry in Australia,* vol. October, pp. 355-361.

Institute for Chemical Research *Principle and Application of Imaging Electron Energy Loss Spectroscopy* [Online], Available: http://eels.kuicr.kyoto-u.ac.jp/eels.en.html, Feburary 12].

Ispas, S., Benoit, M., Jund, P. & Jullien, R. 2001, 'Structural and Electronic Properties of the Sodium Tetrasilicate Glass $Na_2Si_4O_9$ from Classical and *Ab Initio* Molecular Dynamics Simulations', *Physical Review B,* vol. 64, pp. 214206-.

Iwahiro, T., Nakamura, Y., Komatsu, R. & Ikeda, K. 2001, 'Crystallization Behavior and Characteristics of Mullites Formed from Alumina–Silica Gels Prepared by the Geopolymer Technique in Acidic Conditions', *Journal of the European Ceramic Society* (Electronic), vol. 21, no. 14, pp. 2515-2519, Available: Elsevier/ScienceDirect 10.1016/S0955-2219(01)00273-4 [2002, September 24].

IZA Structure Commission 2004, *Database of Zeolite Structures*, Available: [http://www.iza-structure.org/databases/] (September 1, 2004).

Jahanian, S. & Rostami, H. 2001, 'Alkali Ash Material, a Novel Material for Infrastructure Enhancement', *Engineering Structures* (Electronic), vol. 23, no. 6, pp. 736-742, Available: Elsevier/ScienceDirect DOI: 10.1016/S0141-0296(00)00032-8 [2001, April 10].

James, R. W. 1962, *The Optical Principles of the Diffraction of X-Rays*, G. Bell and Sons Ltd, London.

Jaymes, I., Douy, A., Massiot, D. & Busnel, J.-P. 1995, 'Synthesis of a Mullite Precursor from Aluminum Nitrate and Tetraethoxysilane via Aqueous Homogeneous Precipitation: An ^{27}Al and ^{29}Si Liquid- and Solid-State NMR Spectroscopic Study', *Journal of the American Ceramic Society,* vol. 78, no. 10, pp. 2648-2654.

Jeong, I.-K., Mohiuddin-Jacobs, F., Petkov, V. & Billinge, S. J. L. 2000, 'Local Structure Study of $In_xGa_{1-x}As$ Semiconductor Alloys Using High Energy Synchrotron X-Ray Diffraction', *arXiv:cond-mat* (Electronic), vol. 0008079, [2002, October 9].

Jin, J., Sakida, S., Yoko, T. & Nogami, M. 2000, 'The Local Structure of Sm-Doped Aluminosilicate Glasses Prepared by Sol-Gel Method', *Journal of Non-Crystalline Solids* (Electronic), vol. 262, no. 1-3, pp. 183-190, Available: Elsevier/ScienceDirect S0022-3093(99)00696-1 [2002, September 18].

Kaplow, R., Rowe, T. A. & Averbach, B. L. 1968, 'Atomic Arrangement in Vitreous Selenium', *Physical Review,* vol. 168, no. 3, pp. 1068-1079.

Kaplow, R., Strong, S. L. & Averbach, B. L. 1965, 'Radial Density Functions for Liquid Mercury and Lead', *Physical Review A,* vol. 138, no. 5, pp. 1136-1345.

Keen, D. A. & Dove, M. T. 1999, 'Local Structures of Amorphous and Crystalline Phases of Silica, SiO_2, by Neutron Total Scattering', *Journal of Physics: Condensed Matter* (Electronic), vol. 11, pp. 9263-9273, Available: http://www.esc.cam.ac.uk/astaff/dove/publications/JPCM_LAD_2000.pdf S0953-8984(99)06785-5 [2003, October 20].

Klug, H. P. & Alexander, L. E. 1974, *X-Ray Diffraction Procedures: For Polycrystalline and Amorphous Materials*, Wiley, New York.

Koller, H., Engelhardt, G., Kentgens, A. P. M. & Sauer, J. 1994, '^{23}Na NMR Spectroscopy of Solids: Interpretation of Quadrupole Interaction Parameters and Chemical Shifts', *Journal of Physical Chemistry,* vol. 98, pp. 1544-1551.

Kriven, W. M., Bell, J. L. & Gordon, M. 2003, 'Microstructure and Microchemistry of Fully-Reacted Geopolymers and Geopolymer Matrix Composites', *Ceramic Transactions,* vol. 153, pp. 227-252.

Krumm, S. 1997, '*Winfit!*' ver: 1.2.1, Available: www.geol.uni-erlangen.de.

Lay, H. C. & Yarovsky, I. 2003, 'Effect of Water Concentration on Sol Formation in Synthesis of Organic/Inorganic Hybrid Materials', *Molecular Simulation* (Electronic), vol. 29, no. 3, p. 231–233, Available: Taylor & Francis 10.1080/0892702031000089696 [2004, September 27].

Léonard, A., Suzuki, S., Fripiat, J. J. & De Kimpe, C. 1964, 'Structure and Properties of Amorphous Silicoaluminas. 1. Structure from X-Ray Fluorescence Spectroscopy and Infrared Spectroscopy', *Journal of Physical Chemistry,* vol. 68, no. 9, pp. 2608-2617.

Li, Z., Ding, Z. & Zhang, Y. 2004, 'Development of Sustainable Cementitious Materials', in *Proceedings of the International Workshop on Sustainable Development and Concrete Technology*, ed. Wang, K., Iowa State University, Beijing, pp. 55-76.

Lippmaa, E., Mägi, M., Samoson, A., Tarmak, M. & Engelhardt, G. 1981, 'Investigation of the Structure of Zeolites by Solid-State High-Resolution ^{29}Si NMR Spectroscopy', *Journal of the American Chemical Society,* vol. 103, pp. 4992-4996.

Lippmaa, E., Samoson, A. & Mägi, M. 1986, 'High-Resolution Aluminum-27 NMR of Aluminosilicates', *Journal of the American Chemical Society,* vol. 108, no. 8, pp. 1730-1735.

Loewenstein, W. 1954, 'The Distribution of Aluminum in the Tetrahedra of Silicates and Aluminates', *American Mineralogist,* vol. 39, pp. 92-96.

Lyon, R. E. 2002, *Fire-Resistant Elastomers*, Federal Aviation Administration, DOT/FAA/AR-TN01/104.

Lyon, R. E., Balaguru, P. N., Foden, A., Sorathia, U., Davidovits, J. & Davidovics, M. 1997, 'Fire-Resistant Aluminosilicate Composites', *Fire and Materials* (Electronic), vol. 21, no. 2, pp. 67-73, Available: Wiley Interscience 10.1002/(SICI)1099-1018(199703)21:2<75::AID-FAM597>3.0.CO;2-P [2004, July 20].

MacGillavary, C. H. & Rieck, G. D. 1968, 'Physical and Chemcial Tables', in *International Tables for X-Ray Crystallography*, vol. 3, ed. Lonsdale, K., The Kynoch Press, Birmingham.

MacKenzie, K. J. D., Brown, I. W. M., Meinhold, R. H. & Bowden, M. E. 1985, 'Outstanding Problems in the Kaolinite-Mullite Reaction Sequence Investigated by ^{29}Si and ^{27}Al Solid-State Nuclear Magnetic Resonance: I, Metakaolinite', *Journal of the American Ceramic Society,* vol. 68, no. 6, pp. 293-297.

MacKenzie, K. J. D. & Smith, M. E. 2002, *Multinuclear Solid-State Nuclear Magnetic Resonance of Inorganic Materials*, Pergamon Press Inc, Oxford.

Materials Data Inc. 2004, '*Jade*', ver: 6.0.3.

May, M., Asomoza, M., Lopez, T. & Gomez, R. 1997, 'Precursor Aluminum Effect in the Synthesis of Sol-Gel Si-Ai Catalysts: FTIR and NMR Characterization', *Chemistry of Materials,* vol. 9, pp. 2395-2399.

McGreevy, R. L. & Pusztai, L. 1988, 'Reverse Monte Carlo Simulation: A New Technique for the Determination of Disordered Structures', *Molecular Simulation,* vol. 1, pp. 359-367.

McGreevy, R. L. & Zetterström, P. 2001, 'Reverse Monte Carlo Modelling of Network Glasses: Useful or Useless?,' *Journal of Non-Crystalline Solids* (Electronic), vol. 293-295, pp. 297-303, Available: Elsevier/ScienceDirect DOI: 10.1016/S0022-3093(01)00681-0 [2002, September 19].

Morrison, R. T. & Boyd, R. N. 1992, *Organic Chemistry,* 6th edn, Prentice Hall, New Jersey.

Mozzi, R. L. & Warren, B. E. 1969, 'The Structure of Vitreous Silica', *Journal of Applied Crystallography,* vol. 2, pp. 164-172.

Murayama, N., Yamamoto, H. & Shibata, J. 2002, 'Mechanism of Zeolite Synthesis from Coal Fly Ash by Alkali Hydrothermal Reaction', *International Journal of Mineral Processing* (Electronic), vol. 64, no. 1, pp. 1-17, Available: Elsevier/ScienceDirect DOI: 10.1016/S0301-7516(01)00046-1 [2002, September 24].

Newville, M. 2004, *Fundamentals of XAFS*, Available: [http://cars9.uchicago.edu/xafs/xas_fun/xas_fundamentals.pdf] (Febuary 24, 2004).

Nix, R. 1996, *Photoelectron Spectroscopy* [Online], Available: http://www.chem.qmw.ac.uk/surfaces/scc/scat5_3.htm [2004, Febuary 23].

Nofz, M., Engelhardt, G., Wihsmann, F.-G., Forkel, K., Mägi, M. & Lippmaa, E. 1986, 'Einfluß Des Netzwerkwandlerkations Auf Die ^{29}Si-NMR-Chemische Verschiebung in Alkali- Und Erdalkalialumosilicatgläsern', *Zeitschrift für Chemie,* vol. 26, pp. 221-222.

North, M. R. & Swaddle, T. W. 2000, 'Kinetics of Silicate Exchange in Alkaline Aluminosilicate Solutions', *Inorganic Chemistry* (Electronic)*,* vol. 39, no. 12, pp. 2661-2665, Available: American Chemical Society S0020-1669(00)00070-7 [2001, March 5].

O'Connor, B. H., van Riessen, A., Carter, J., Burton, G. R., Cookson, D. J. & Garrett, R. E. 1997, 'Characterization of Ceramic Materials with BIGDIFF: A Synchrotron Radiation Debye-Scherrer Powder Diffractometer', *Journal of the American Ceramic Society,* vol. 80, no. 6, pp. 1373-1381.

Palin, E. J., Trachenko, K. O. & Dove, M. T. 2002, 'Computer Simulation Study of Low-Energy Excitations of Silicate Glasses', *Journal of Physics: Condensed Matter,* vol. 14, p. 4857–4879.

Palomo, A., Blanco-Varela, M. T., Granizo, M. L., Puertas, F., Vazquez, T. & Grutzeck, M. W. 1999, 'Chemical Stability of Cementitious Materials Based on Metakaolin', *Cement and Concrete Research* (Electronic)*,* vol. 29, no. 7, pp. 997-1004, Available: Pergamon/ScienceDirect S0008-8846(99)00074-5 [2001, March 23].

Palomo, A. & de la Fuente, J. I. L. 2003, 'Alkali-Activated Cementitous Materials: Alternative Matrices for the Immobilisation of Hazardous Wastes: Part I. Stabilisation of Boron', *Cement and Concrete Research* (Electronic)*,* vol. 33, no. 2, pp. 281-288, Available: Pergamon/ScienceDirect 10.1016/S0008-8846(02)00963-8 [2003, January 30].

Palomo, A., Grutzeck, M. W. & Blanco, M. T. 1999, 'Alkali-Activated Fly Ashes; a Cement for the Future', *Cement and Concrete Research* (Electronic)*,* vol. 29, no. 8, pp. 1323-1329, Available: Pergamon/ScienceDirect S0008-8846(98)00243-9 [2001, March 23].

Palomo, A. & Palacios, M. 2003, 'Alkali-Activated Cementitious Materials: Alternative Matrices for the Immobilisation of Hazardous Wastes: Part II. Stabilisation of Chromium and Lead', *Cement and Concrete Research* (Electronic)*,* vol. 33, no. 2, pp. 289-295, Available: Pergamon/ScienceDirect 10.1016/S0008-8846(02)00964-X [2003, January 30].

Perera, D. S., Blackford, M. G., Vance, E. R., Hanna, J. V., Finnie, K. S. & Nicholson, C. L. 2004a, 'Geopolymers for the Immobilization of Radioactive Waste', in *MRS Proceedings - Scientific Basis for Nuclear Waste Management XXVIII*, p. in press.

Perera, D. S., Nicholson, C. L., Blackford, M. G., Fletcher, R. A. & Trautman, R. L. 2004b, 'Geopolymers Made Using New Zealand Flyash', *Journal of Ceramic Society of Japan,* vol. 112, no. 4, pp. S111-S118.

Perera, D. S., Vance, E. R., Aly, Z., Finnie, K. S., Hanna, J. V., Nicholson, C. L., Trautman, R. L. & Stewart, M. W. A. 2003, 'Characterisation of Geopolymers for the Immobilisation of Intermediate Level Waste', in *The 9th International Conference on Radioactive Waste Management and Environmental Remediation*, Examination School, Oxford, England.

Petkov, V. 1989, 'RAD, a Program for Analysis of X-Ray Diffraction Data from Amorphous Materials for Personal Computers', *Journal of Applied Crystallography,* vol. 22, pp. 387-389.

Petkov, V., Apostolov, A. & Skumryev, V. 1989, 'Radial Distribution Functions for RE_4Al_3 Metallic Glasses (RE = Pr, Gd, Tb, Dy)', *Journal of Non-Crystalline Solids,* vol. 108, pp. 75-79.

Petkov, V., Billinge, S. J. L., Shastri, S. D. & Himmel, B. 2000, 'Polyhedral Units and Network Connectivity in Calcium Aluminosilicate Glasses from High-Energy x-Ray Diffraction', *Physical Review Letters,* vol. 85, no. 16, pp. 3436-3439.

Pings, C. J. & Waser, J. 1968, 'Analysis of Scattering Data for Mixtures of Amorphous Solids or Liquids', *Journal of Chemical Physics,* vol. 48, no. 7, pp. 3016-3018.

Poulsen, H. F., Neumann, H.-B., Schneider, J. R., Neuefeind, J. & Zeidler, M. D. 1995, 'Amorphous Silica Studied by High Energy X-Ray Diffraction', *Journal of Non-Crystalline Solids* (Electronic)*,* vol. 188, no. 1-2, pp. 63-74, Available: Elsevier/ScienceDirect 0022-3093(95)00095-X [2002, September 23].

Proffen, T. & Billinge, S. J. L. 1999, 'PDFFIT, a Program for Full Profile Structural Refinement of the Atomic Pair Distribution Function', *Journal of Applied Crystallography,* vol. 32, pp. 572-575.

Proffen, T., Petkov, V., Billinge, S. J. L. & Vogt, T. 2002, 'Chemical Short Range Order Obtained from the Atomic Pair Distribution Function', *Zeitschrift für Kristallographie,* vol. 217, pp. 47-50.

Puertas, F., Martínez-Ramírez, S., Alonso, S. & Vázquez, T. 2000, 'Alkali-Activated Fly Ash/Slag Cements; Strength Behaviour and Hydration Products', *Cement and Concrete Research* (Electronic)*,* vol. 30, no. 10, pp. 1625-1632, Available: Pergamon/ScienceDirect S0008-8846(00)00298-2 [2001, March 23].

Rahier, H., Simons, W., van Mele, B. & Biesemans, M. 1997, 'Low-Temperature Synthesized Aluminosilicate Glasses. Part III: Influence of the Composition of the Silicate Solution on Production, Structure and Properties', *Journal of Materials Science,* vol. 32, no. 9, pp. 2237-2247.

Rahier, H., van Mele, B., Biesemans, M., Wastiels, J. & Wu, X. 1996, 'Low-Temperature Synthesized Aluminosilicate Glasses. Part I: Low-Temperature Reaction Stoichiometry and Structure of a Model Compound', *Journal of Materials Science,* vol. 31, no. 1, pp. 71-79.

Rahier, H., van Mele, B. & Wastiels, J. 1996, 'Low-Temperature Synthesized Aluminosilicate Glasses. Part II: Rheological Transformations During Low-Temperature Cure and High-Temperature Properties of a Model Compound', *Journal of Materials Science,* vol. 31, no. 1, pp. 80-85.

Rahier, H., Wullaert, B. & van Mele, B. 2000, 'Influence of the Degree of Dehydroxylation of Kaolinite on the Properties of Aluminosilicate Glasses', *Journal of Thermal Analysis and Calorimetry* (Electronic), vol. 62, pp. 417-427, Available: Kluwer Academic Publishers/Swetsnet 1418.2874/2000 [2002, October 9].

Rha, C. Y., Kang, S. K. & Kim, C. E. 2000, 'Investigation of the Stability of Hardened Slag Paste for the Stabilization/Solidification of Wastes Containing Heavy Metal Ions', *Journal of Hazardous Materials* (Electronic), vol. B73, no. 3, pp. 255-267, Available: Elsevier/ScienceDirect S0304-3894(99)00185-5 [2001, April 10].

Robello, D. R. 2002, *Chem 421: Examples of Ring Opening Polymerization* [Online], Available: http://www.chem.rochester.edu/%7Echem421/rop3.htm [2004, July 8].

Rocha, J. 1999, 'Single- and Triple-Quantum ^{27}Al MAS NMR Study of the Thermal Transformation of Kaolinite', *Journal of Physical Chemistry B* (Electronic), vol. 103, no. 44, pp. 9801-9804, Available: American Chemical Society DOI: 10.1021/jp991516b S1089-5647(99)01516-3 [2002, September 18].

Roy, D. M., Arjunan, P. & Silsbee, M. R. 2001, 'Effect of Silica Fume, Metakaolin, and Low-Calcium Fly Ash on Chemical Resistance of Concrete', *Cement and Concrete Research* (Electronic), vol. 31, no. 12, pp. 1809-1813, Available: Pergamon/ScienceDirect DOI: 10.1016/S0008-8846(01)00548-8 [2002, September 19].

Ruland, W. 1964, 'The Separation of Coherent and Incoherent Compton X-Ray Scattering', *British Journal of Applied Physics,* vol. 15, pp. 1301-1307.

Schneider, J., Cincotto, M. A. & Panepucci, H. 2001, '^{29}Si and ^{27}Al High-Resolution NMR Characterization of Calcium Silicate Hydrate Phases

in Activated Blast-Furnace Slag Pastes', *Cement and Concrete Research* (Electronic), vol. 31, no. 7, pp. 993-1001, Available: Pergamon/ScienceDirect S0008-8846(01)00530-0 [2002, September 24].

Shi, C. & Stegemann, J. A. 2000, 'Acid Corrosion Resistance of Different Cementing Materials', *Cement and Concrete Research* (Electronic), vol. 30, no. 5, pp. 803-808, Available: Pergamon/ScienceDirect S0008-8846(00)00234-9 [2001, April 10].

Siemens 1986, *X-Ray Spectrometers and Diffractometers*, Catalogue MP 42, Federal Republic of Germany, Order Number E86060-K6042A101-A2-7600.

Sinkó, K. & Mezei, R. 1998, 'Preparation Effects on Sol-Gel Aluminosilicate Gels', *Journal of Non-Crystalline Solids* (Electronic), vol. 231, no. 1-2, pp. 1-9, Available: Elsevier/ScienceDirect S0022-3093(98)00442-6 [2001, March 13].

Smith, M. E. 1993, 'Applications of ^{27}Al NMR Techniques to Structure Determination in Solids', *Applied Magnetic Resonance,* vol. 4, pp. 1-64.

SPSS 2001, '*SigmaPlot 2001 for Windows*', ver: 7.101.

Standards Australia 2001, 'Methods of Testing Concrete. Method 9: Determination of the Compressive Strength of Concrete Specimens: AS 1012.9-1999'.

Stebbins, J. F., Kroeker, S., Lee, S. K. & Kiczenski, T. J. 2000, 'Quantification of Five- and Six-Coordinated Aluminum Ions in Aluminosilicate and Fluoride-Containing Glasses by High-Field, High-Resolution ^{27}Al NMR', *Journal of Non-Crystalline Solids* (Electronic), vol. 275, pp. 1-6, Available: Elsevier/ScienceDirect S0022-3093(00)00270-2 [2003, March 6].

Subaer 2004, *Influence of Aggregate on the Microstructure of Geopolymer*, PhD, Curtin University of Technology.

Swanepoel, J. C. & Strydom, C. A. 2002, 'Utilisation of Fly Ash in a Geopolymeric Material', *Applied Geochemistry* (Electronic), vol. 17, no. 8, pp. 1143-1148, Available: Pergamon/ScienceDirect 10.1016/S0883-2927(02)00005-7 [2002, September 24].

Thijsse, B. 1984, 'The Accuracy of Experimental Radial Distribution Functions for Metallic Glasses', *Journal of Applied Crystallography,* vol. 17, pp. 61-76.

van Jaarsveld, J. G. S. & van Deventer, J. S. J. 1999a, 'The Effect of Metal Contaminants on the Formation and Properties of Waste-Based

Geopolymers', *Cement and Concrete Research* (Electronic), vol. 29, no. 8, pp. 1189-1200, Available: Pergamon/ScienceDirect S0008-8846(99)00032-0 [2001, March 5].

van Jaarsveld, J. G. S. & van Deventer, J. S. J. 1999b, 'Effect of the Alkali Metal Activator on the Properties of Fly Ash-Based Geopolymers', *Industrial and Engineering Chemistry Research* (Electronic), vol. 38, no. 10, pp. 3932-3941, Available: American Chemical Society S0888-5885(98)00804-5 [2001, April 2].

van Jaarsveld, J. G. S., van Deventer, J. S. J. & Lorenzen, L. 1997, 'The Potential Use of Geopolymeric Materials to Immobilise Toxic Metals: Part I. Theory and Applications', *Minerals Engineering* (Electronic), vol. 10, no. 7, pp. 659-669, Available: Pergamon/ScienceDirect S0892-6875(97)00046-0 [2001, March 20].

van Jaarsveld, J. G. S., van Deventer, J. S. J. & Lorenzen, L. 1998, 'Factors Affecting the Immobilization of Metals in Geopolymerized Flyash', *Metallurgical and Materials Transactions* (Electronic), vol. 29B, no. 1, pp. 283-291, Available: Elsevier/ScienceDirect [2001, March 28].

van Jaarsveld, J. G. S., van Deventer, J. S. J. & Lukey, G. C. 2002, 'The Effect of Composition and Temperature on the Properties of Fly Ash- and Kaolinite-Based Geopolymers', *Chemical Engineering Journal* (Electronic), vol. 89, no. 1-3, pp. 63-73, Available: Elsevier/ScienceDirect 10.1016/S1385-8947(02)00025-6 [2002, October 8].

van Jaarsveld, J. G. S., van Deventer, J. S. J. & Schwartzman, A. 1999, 'The Potential Use of Geopolymeric Materials to Immobilise Toxic Metals: Part II. Material and Leaching Characteristics', *Minerals Engineering* (Electronic), vol. 12, no. 1, pp. 75-91, Available: Pergamon/ScienceDirect S0892-6875(98)00121-6 [2001, March 20].

Waasmaier, D. & Kirfel, A. 1995, 'New Analytical Scattering-Factor Functions for Free Atoms and Ions', *Acta Crystallographica,* vol. A51, pp. 416-431.

Wagner, C. N. J. 1978, 'Direct Methods for the Determination of Atomic-Scale Structure of Amorphous Solids (X-Ray, Electron and Neutron Scattering)', *Journal of Non-Crystalline Solids,* vol. 31, pp. 1-40.

Warren, B. E. & Mozzi, R. L. 1966, 'Multiple Scattering of X-Rays by Amorphous Samples', *Acta Crystallographica,* vol. 21, pp. 459-461.

Xu, H. & van Deventer, J. S. J. 2000, 'The Geopolymerisation of Alumino-Silicate Minerals', *International Journal of Mineral Processing* (Electronic), vol. 59, no. 3, pp. 247-266, Available: Elsevier/ScienceDirect S0301-7516(99)00074-5 [2001, March 5].

I APPENDIX – SEM IMAGES

Appendix I gives SEM images of all the samples studied in this project. These images where taken during the collection of the EDS spectra and the sites of interest correspond directly to those given in Appendix II.

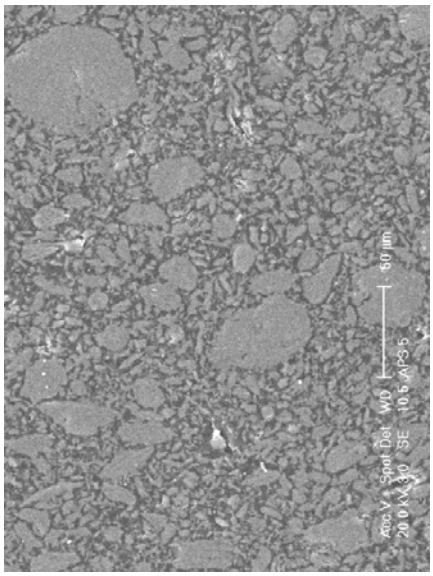

(a)

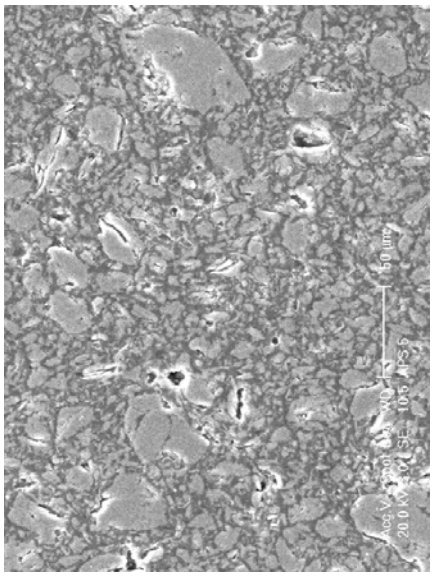

(b)

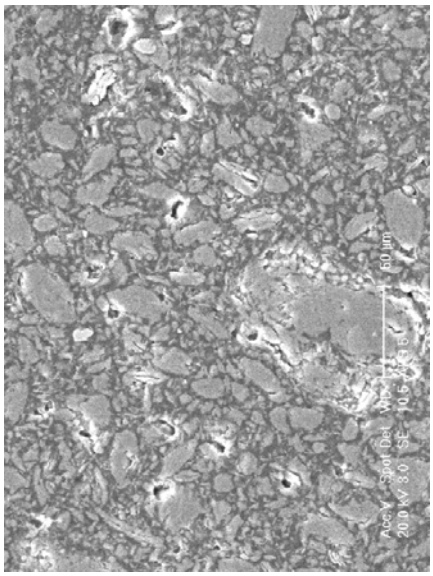

(c)

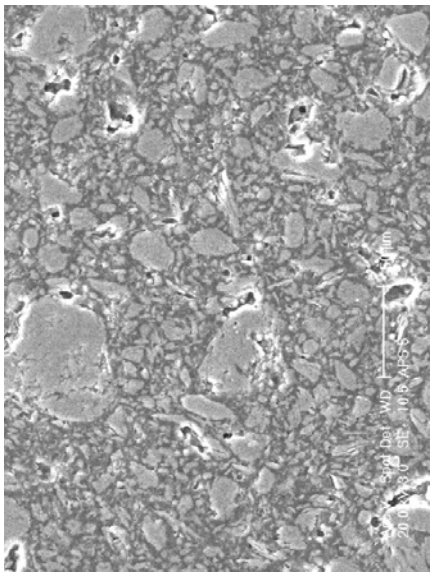

(d)

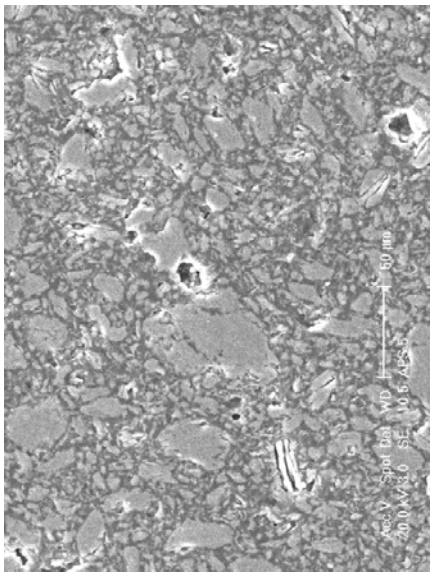

(e)

Figure AI.1: Sample 1.1/0.6.

(a) Site of interest 1

(b) Site of interest 2

(c) Site of interest 3

(d) Site of interest 4

(e) Site of interest 5

The images were collected with an accelerating voltage of 20 kV, a beam current of 60 pA and a working distance of 10.4 mm. The scale bar on the figures is 50 μm, and each micrograph is ~300 x 200 μm.

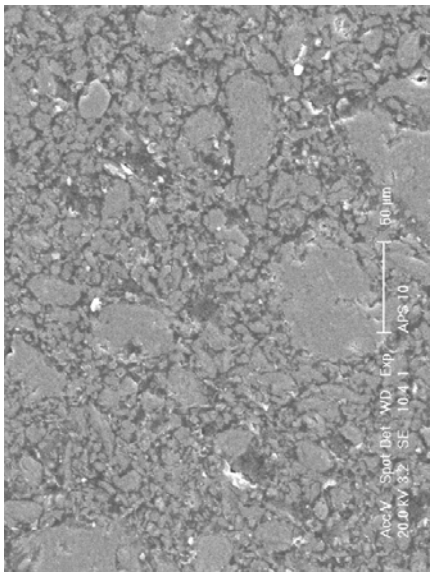

(a)

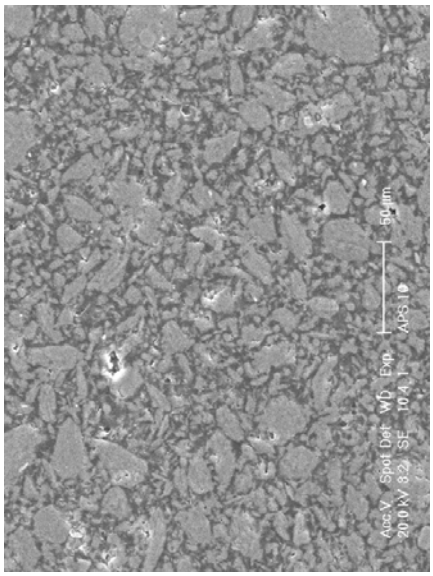

(b)

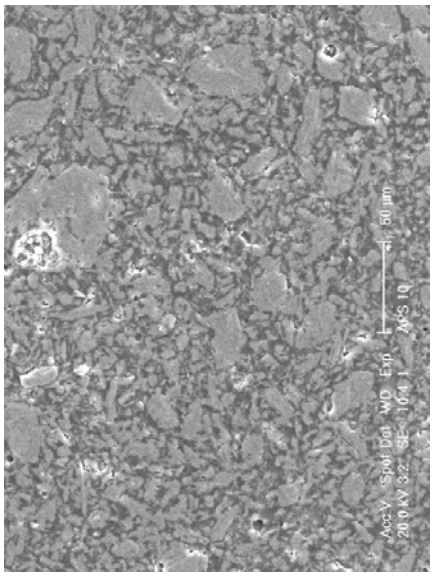

(c)

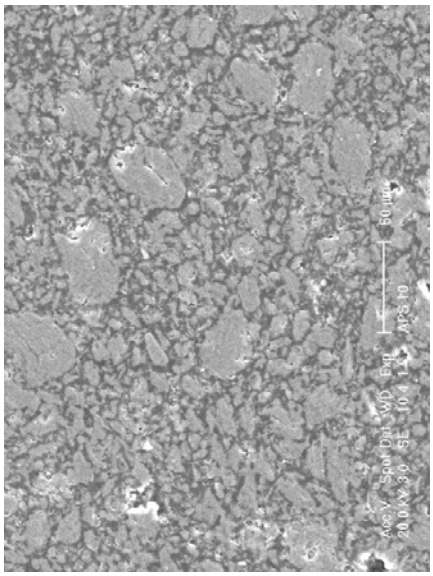

(d)

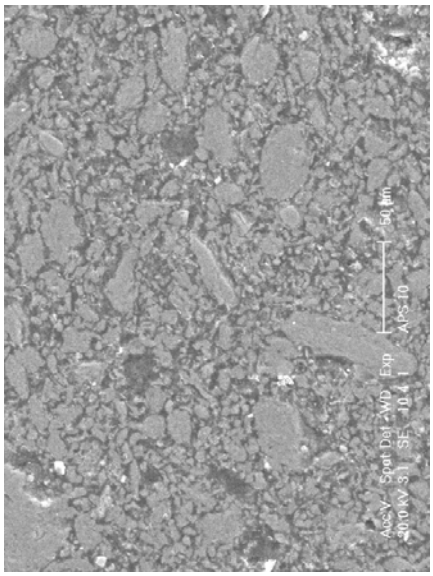

(e)

Figure AI.2: Sample 1.1/0.8.

(a) Site of interest 1

(b) Site of interest 2

(c) Site of interest 3

(d) Site of interest 4

(e) Site of interest 5

The images were collected with an accelerating voltage of 20 kV, a beam current of 60 pA and a working distance of 10.4 mm. The scale bar on the figures is 50 μm, and each micrograph is ~300 x 200 μm.

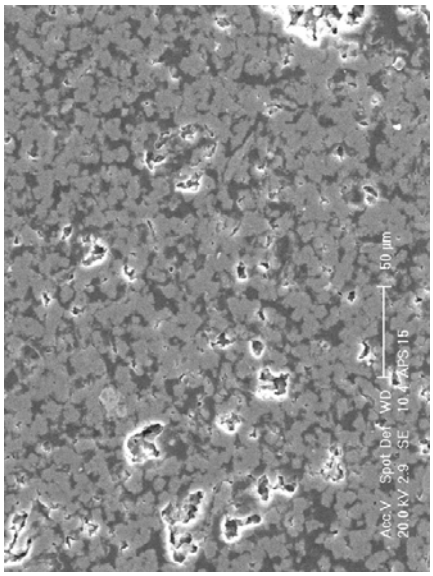

(a)

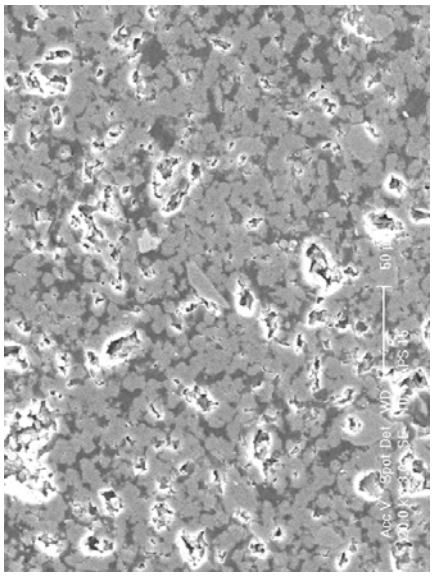

(b)

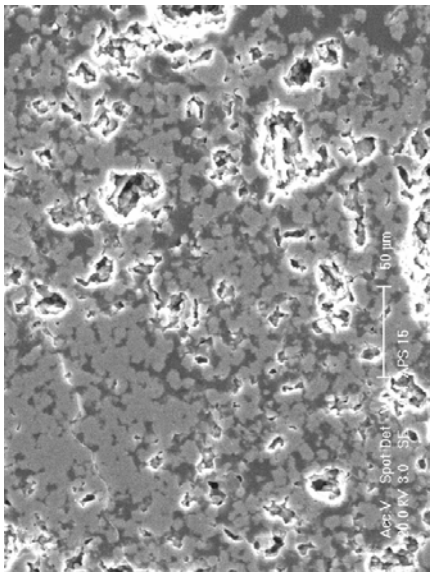

(c)

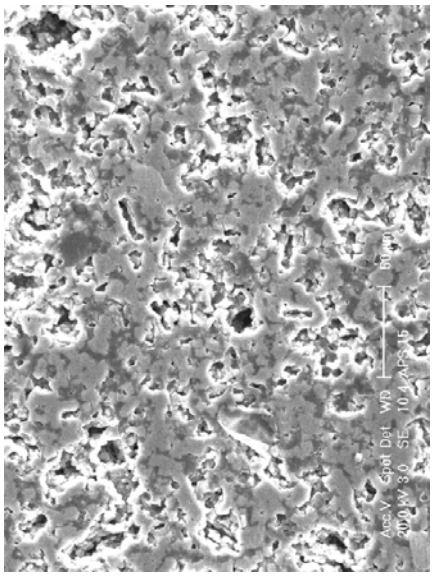

(d)

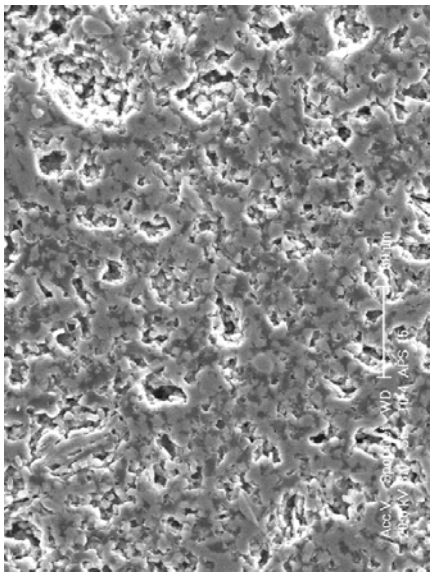

(e)

Figure AI.3: Sample 1.1/1.0.

(a) Site of interest 1

(b) Site of interest 2

(c) Site of interest 3

(d) Site of interest 4

(e) Site of interest 5

The images were collected with an accelerating voltage of 20 kV, a beam current of 60 pA and a working distance of 10.4 mm. The scale bar on the figures is 50 μm, and each micrograph is ~300 x 200 μm.

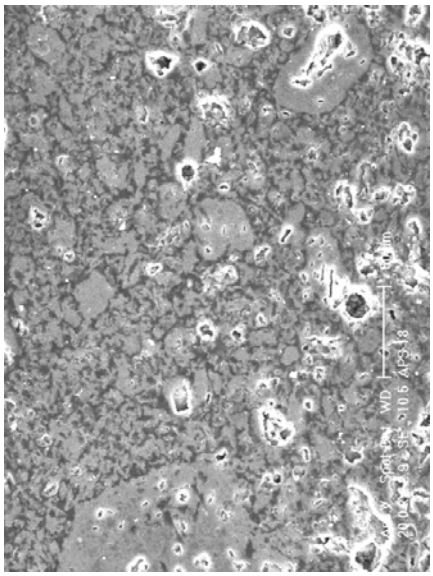

(a)

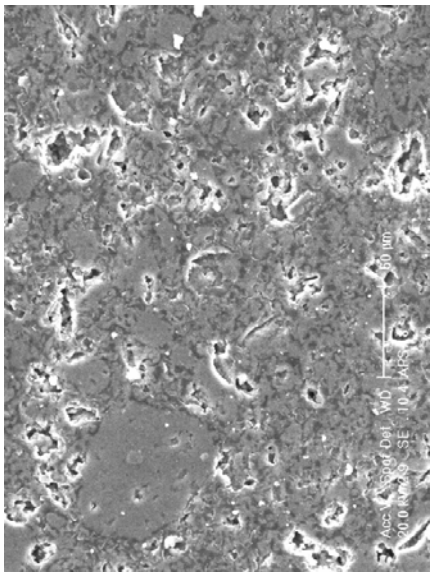

(b)

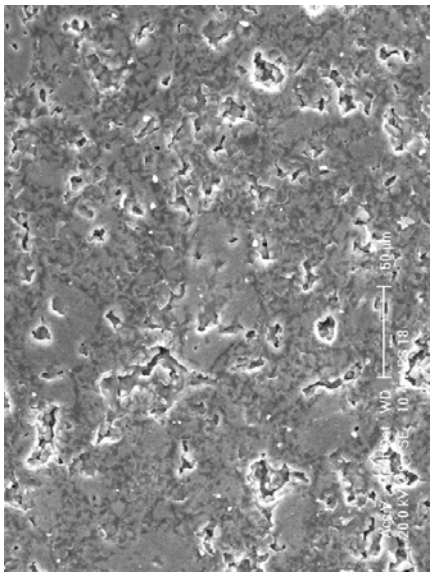

(c)

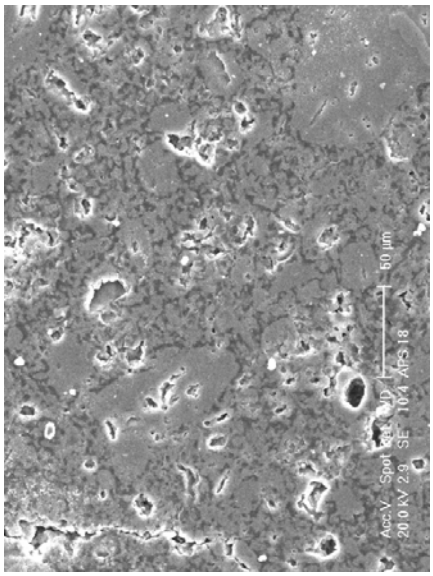

(d)

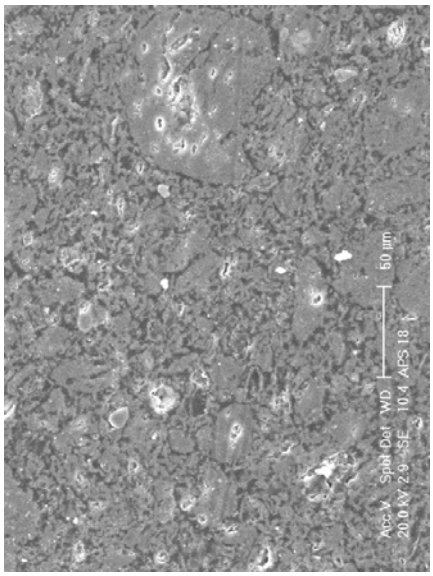

(e)

Figure AI.4: Sample 1.1/1.5.

(a) Site of interest 1

(b) Site of interest 2

(c) Site of interest 3

(d) Site of interest 4

(e) Site of interest 5

The images were collected with an accelerating voltage of 20 kV, a beam current of 60 pA and a working distance of 10.4 mm. The scale bar on the figures is 50 μm, and each micrograph is ~300 x 200 μm.

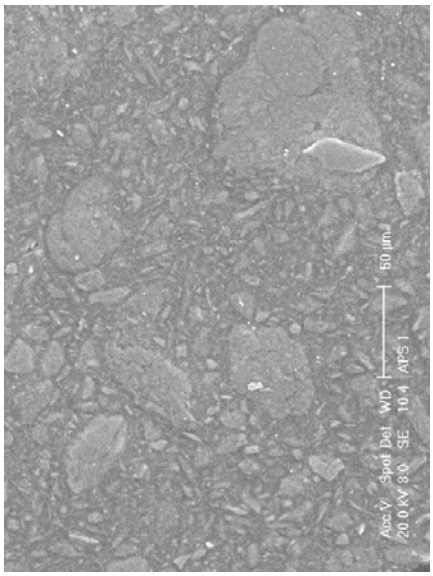

(a)

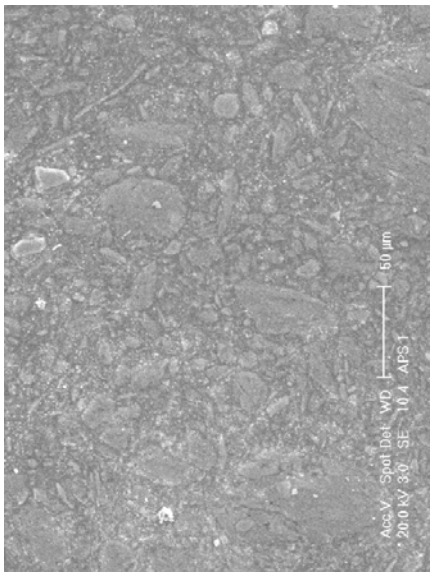

(b)

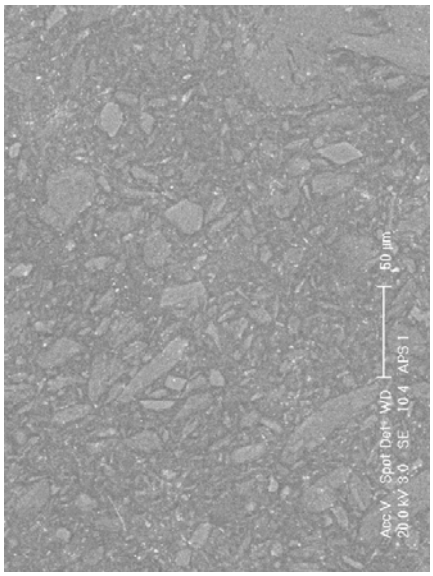

(c)

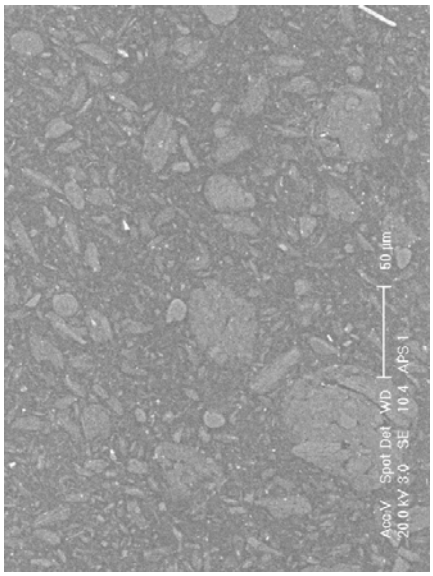

(d)

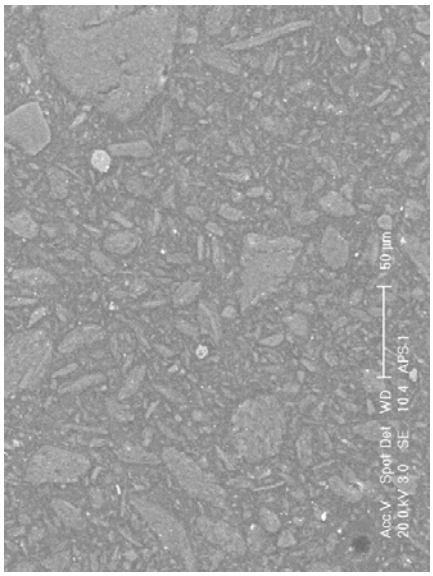

(e)

Figure AI.5: Sample 1.5/0.6.

(a) Site of interest 1

(b) Site of interest 2

(c) Site of interest 3

(d) Site of interest 4

(e) Site of interest 5

The images were collected with an accelerating voltage of 20 kV, a beam current of 60 pA and a working distance of 10.4 mm. The scale bar on the figures is 50 μm, and each micrograph is ~300 x 200 μm.

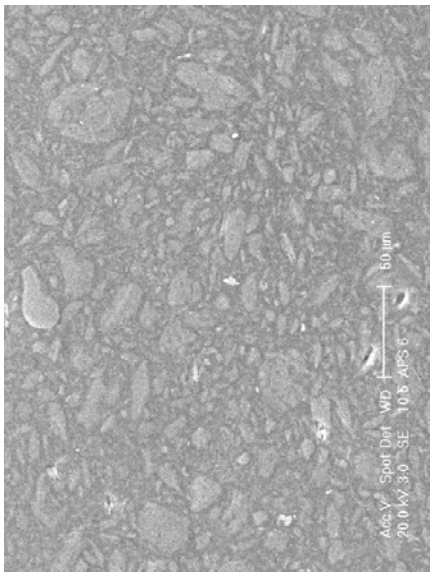

(a)

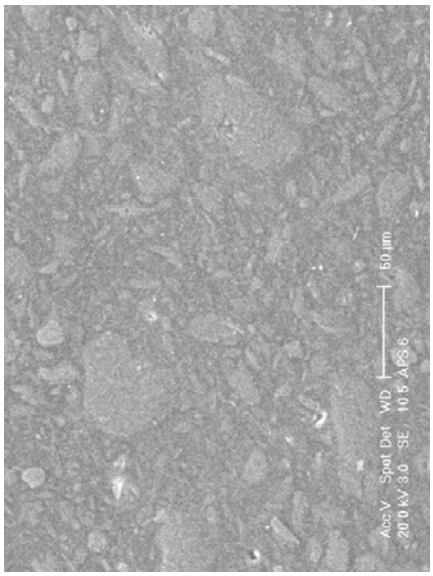

(b)

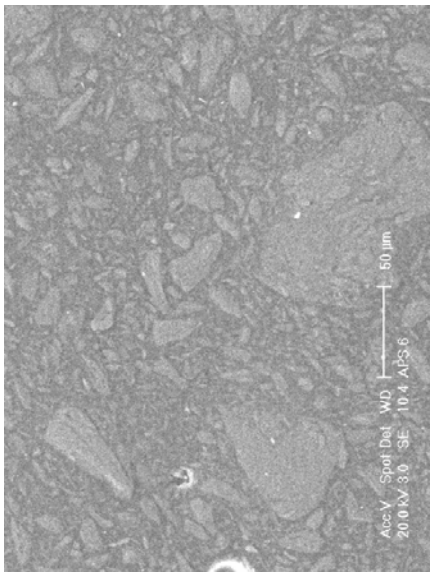

(c)

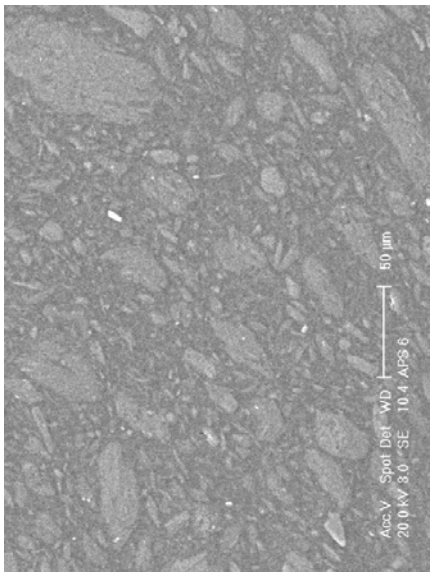

(d)

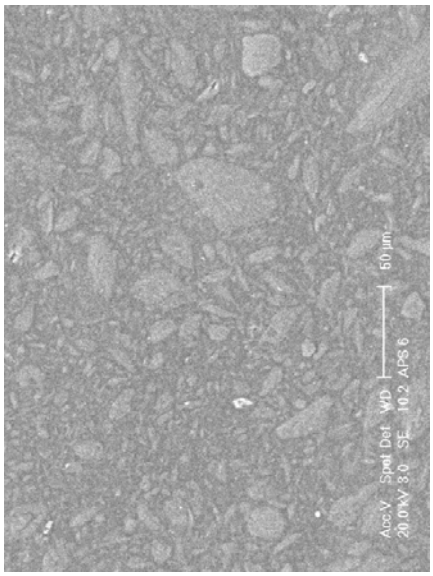

(e)

Figure AI.6: Sample 1.5/0.8.

(a) Site of interest 1

(b) Site of interest 2

(c) Site of interest 3

(d) Site of interest 4

(e) Site of interest 5

The images were collected with an accelerating voltage of 20 kV, a beam current of 60 pA and a working distance of 10.4 mm. The scale bar on the figures is 50 μm, and each micrograph is ~300 x 200 μm.

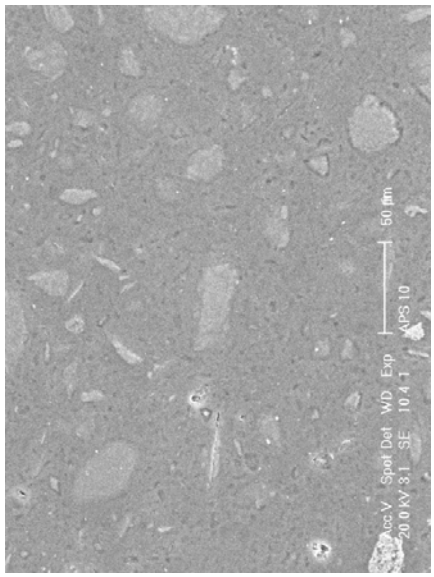

(a)

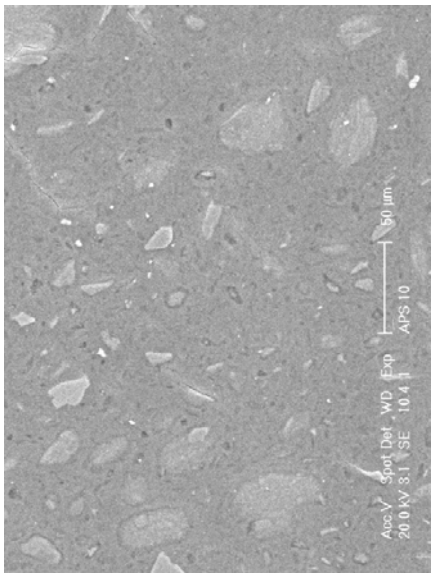

(b)

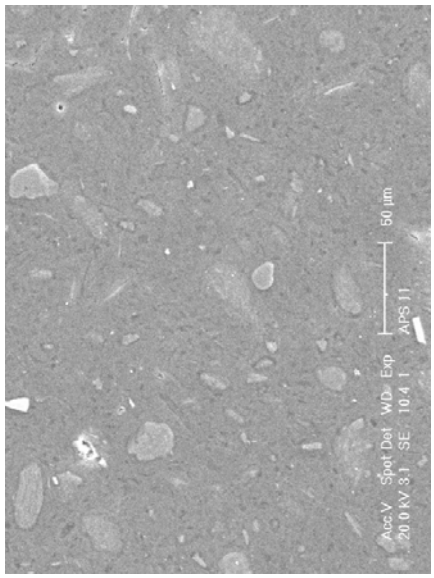

(c)

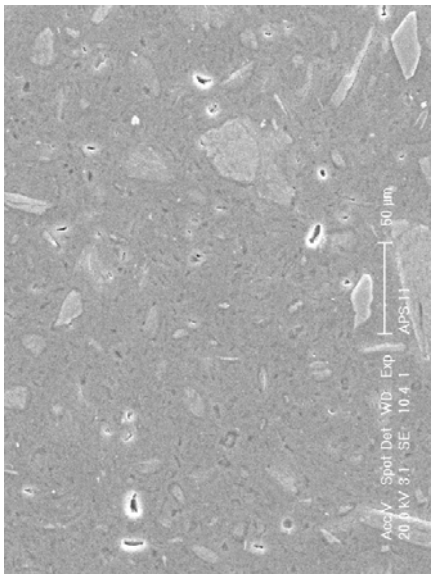

(d)

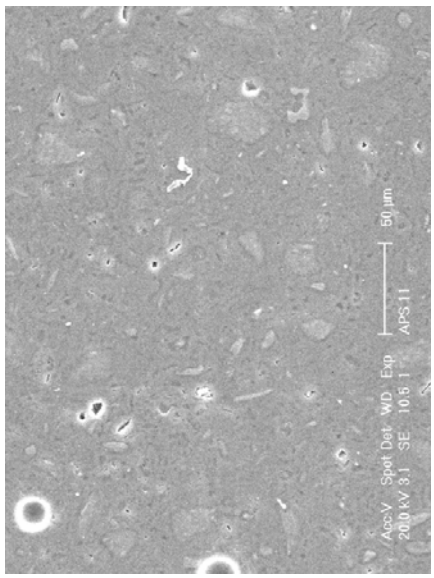

(e)

Figure AI.7: Sample 1.5/1.0.

(a) Site of interest 1

(b) Site of interest 2

(c) Site of interest 3

(d) Site of interest 4

(e) Site of interest 5

The images were collected with an accelerating voltage of 20 kV, a beam current of 60 pA and a working distance of 10.4 mm. The scale bar on the figures is 50 μm, and each micrograph is ~300 x 200 μm.

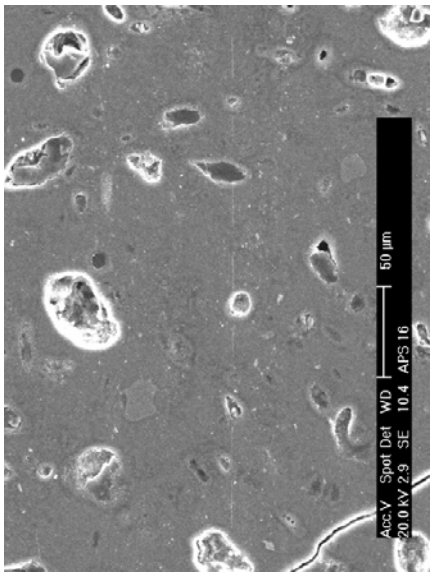

(a)

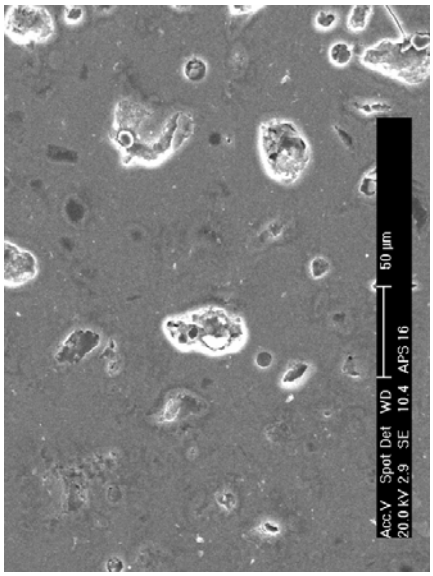

(b)

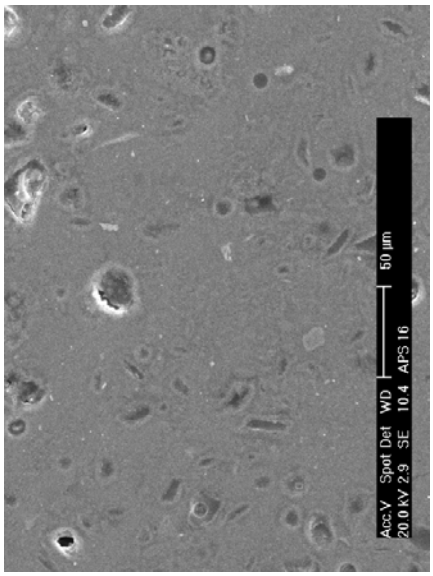

(c)

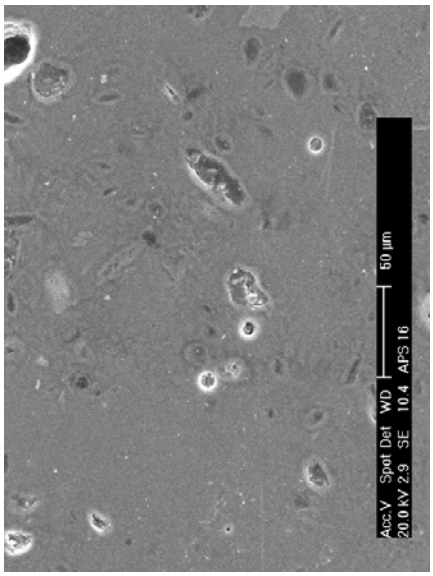

(d)

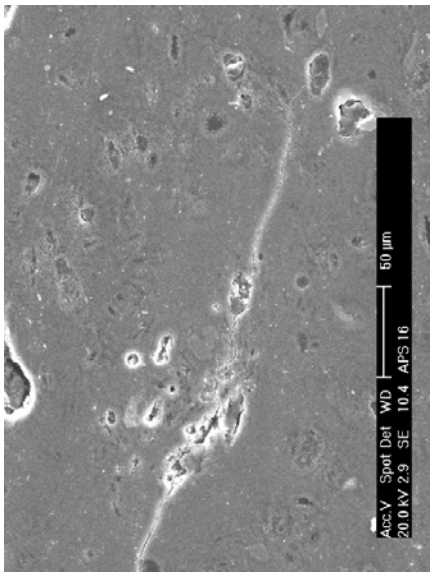

(e)

Figure AI.8: Sample 1.5/1.5.

(a) Site of interest 1

(b) Site of interest 2

(c) Site of interest 3

(d) Site of interest 4

(e) Site of interest 5

The images were collected with an accelerating voltage of 20 kV, a beam current of 60 pA and a working distance of 10.4 mm. The scale bar on the figures is 50 μm, and each micrograph is ~300 x 200 μm.

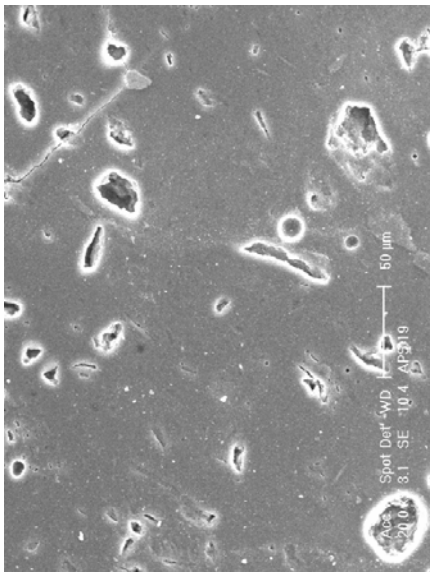

(a)

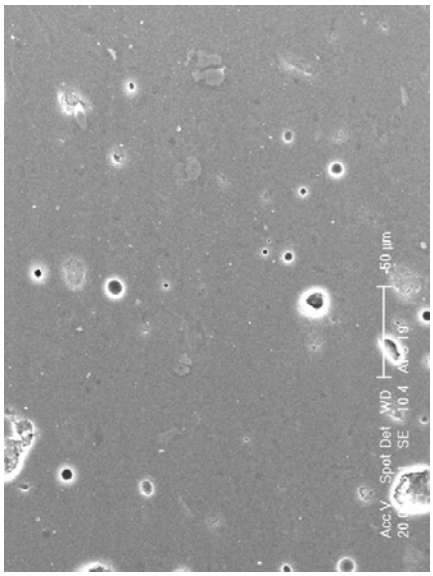

(b)

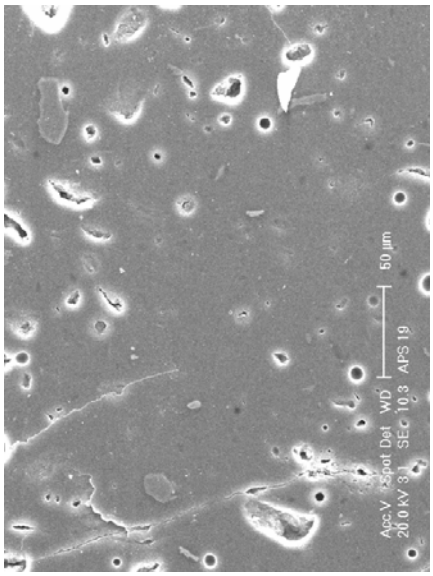

(c)

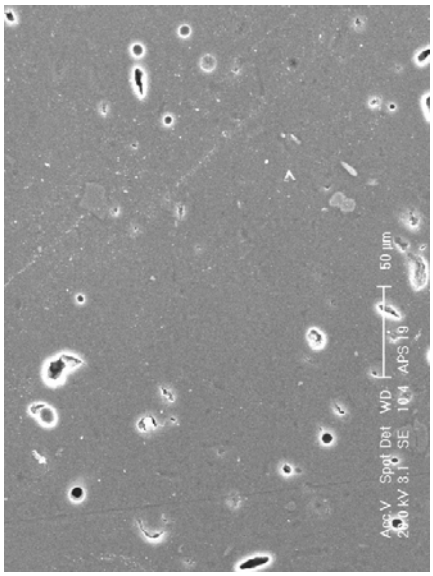

(d)

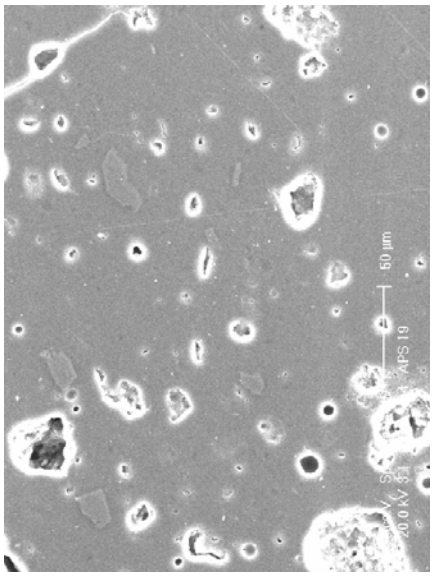

(e)

Figure AI.9: Sample 1.5/2.0.

(a) Site of interest 1

(b) Site of interest 2

(c) Site of interest 3

(d) Site of interest 4

(e) Site of interest 5

The images were collected with an accelerating voltage of 20 kV, a beam current of 60 pA and a working distance of 10.4 mm. The scale bar on the figures is 50 µm, and each micrograph is ~300 x 200 µm.

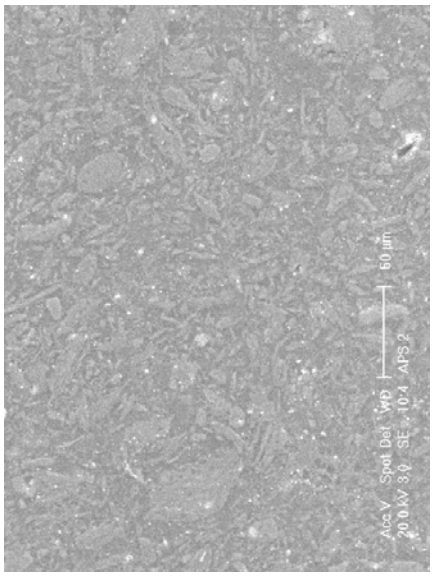

(a)

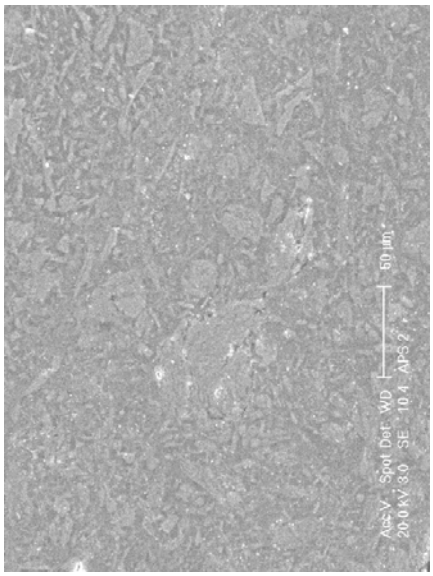

(b)

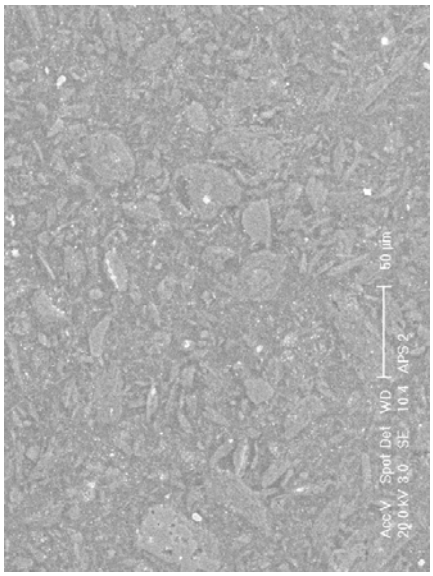

(c)

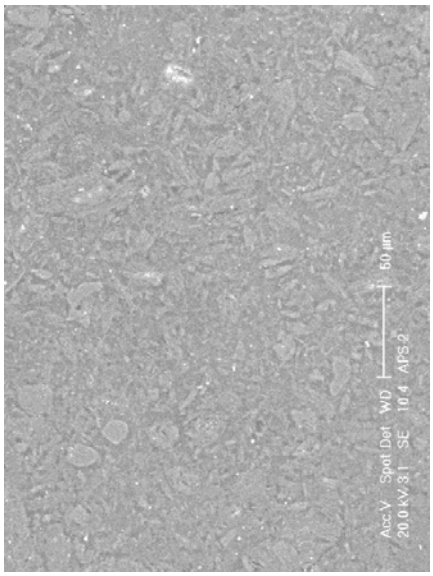

(d)

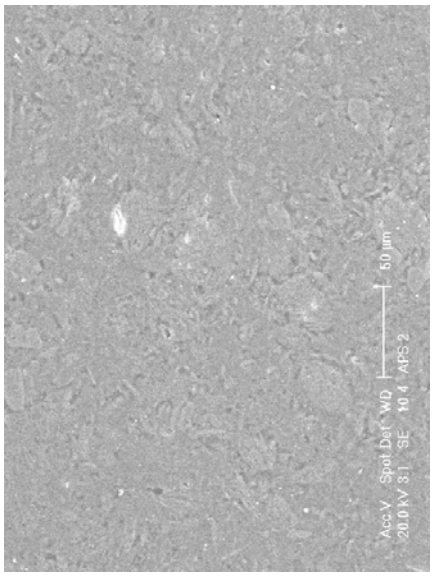

(e)

Figure AI.10: Sample 2.0/0.8.

(a) Site of interest 1

(b) Site of interest 2

(c) Site of interest 3

(d) Site of interest 4

(e) Site of interest 5

The images were collected with an accelerating voltage of 20 kV, a beam current of 60 pA and a working distance of 10.4 mm. The scale bar on the figures is 50 μm, and each micrograph is ~300 x 200 μm.

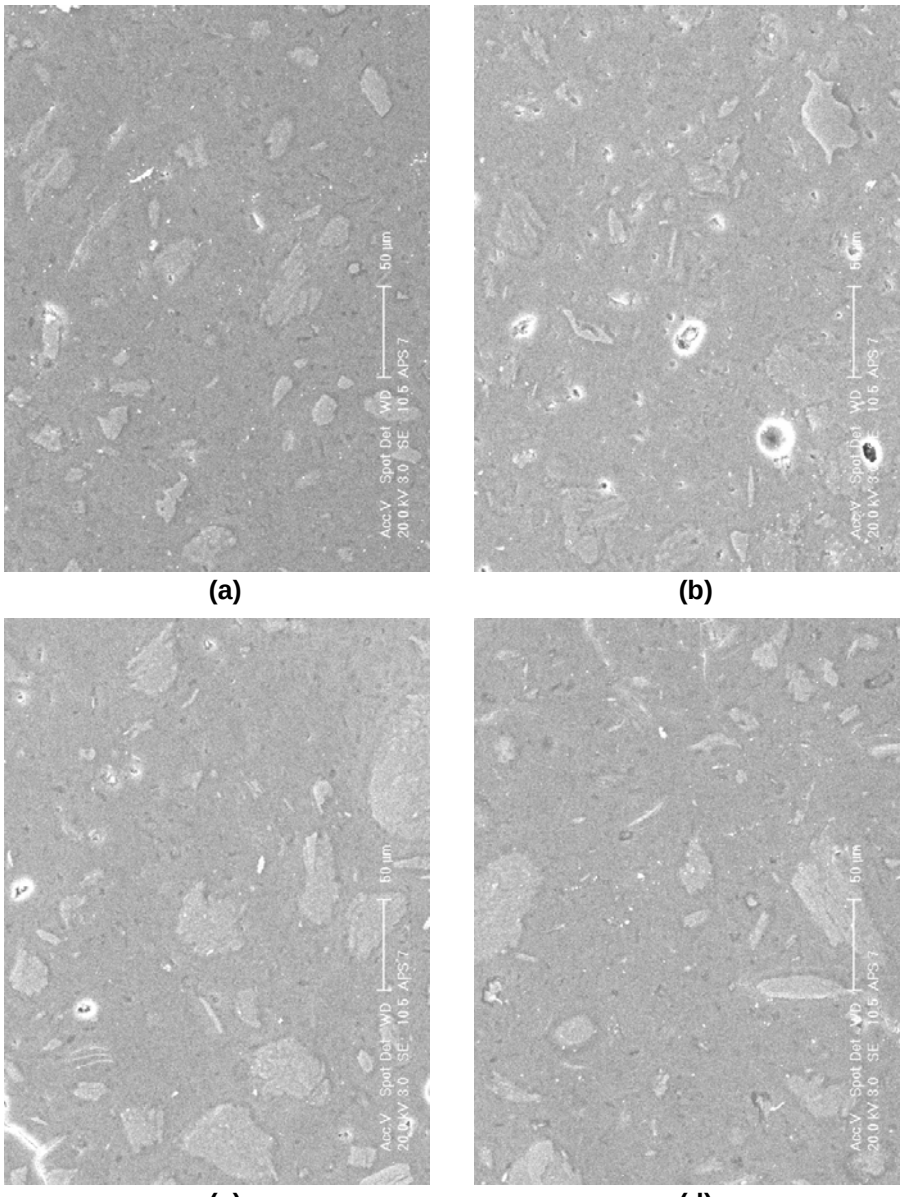

(a) **(b)**

(c) **(d)**

Figure AI.11: Sample 2.0/1.0.

(a) Site of interest 1

(b) Site of interest 2

(c) Site of interest 3

(d) Site of interest 5

The images were collected with an accelerating voltage of 20 kV, a beam current of 60 pA and a working distance of 10.4 mm. The scale bar on the figures is 50 μm, and each micrograph is ~300 x 200 μm.

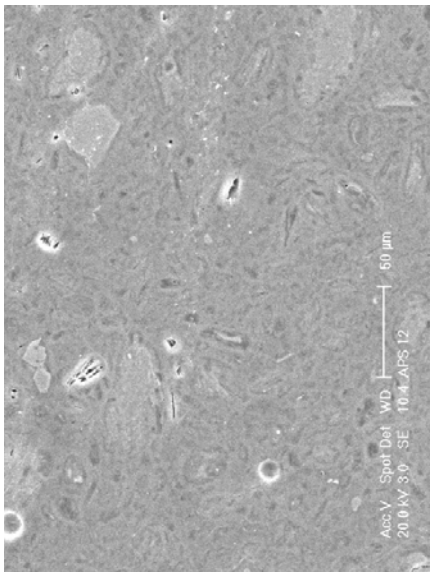

(a)

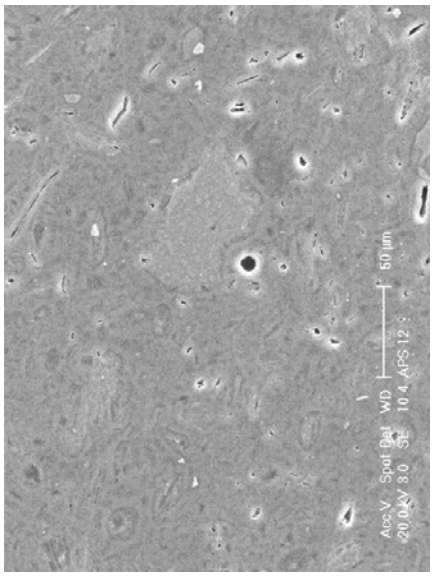

(b)

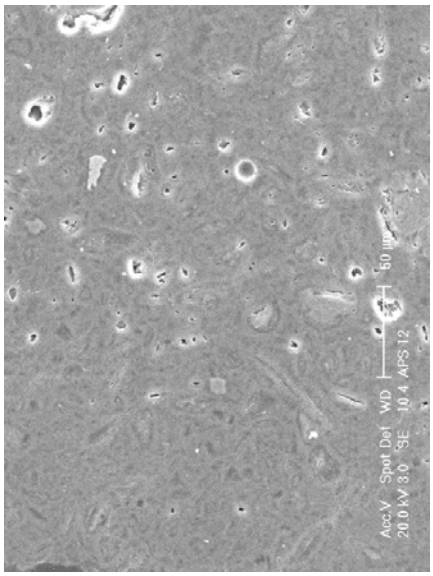

(c)

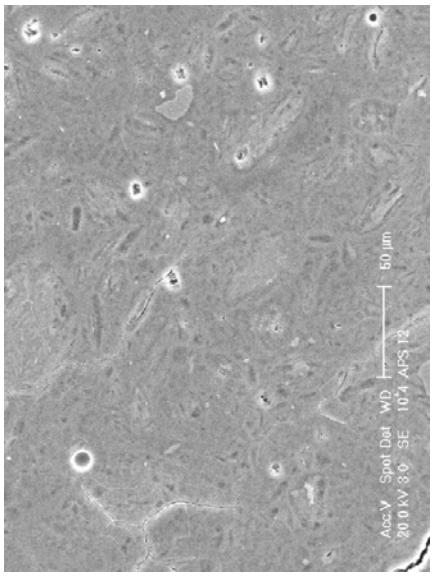

(d)

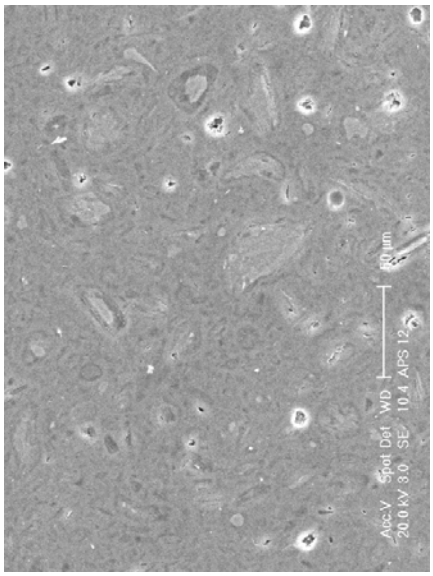

(e)

Figure AI.12: Sample 2.0/1.3.

(a) Site of interest 1

(b) Site of interest 2

(c) Site of interest 3

(d) Site of interest 4

(e) Site of interest 5

The images were collected with an accelerating voltage of 20 kV, a beam current of 60 pA and a working distance of 10.4 mm. The scale bar on the figures is 50 µm, and each micrograph is ~300 x 200 µm.

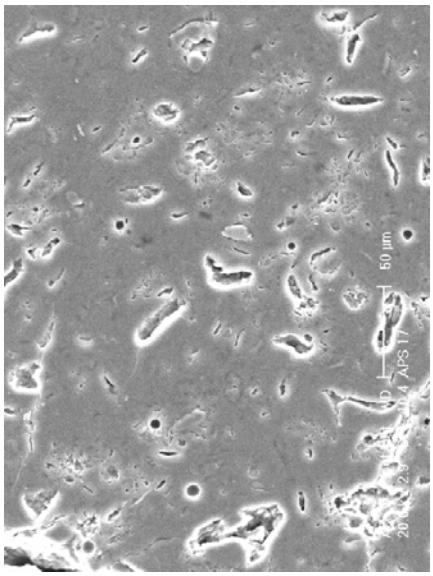

(a)

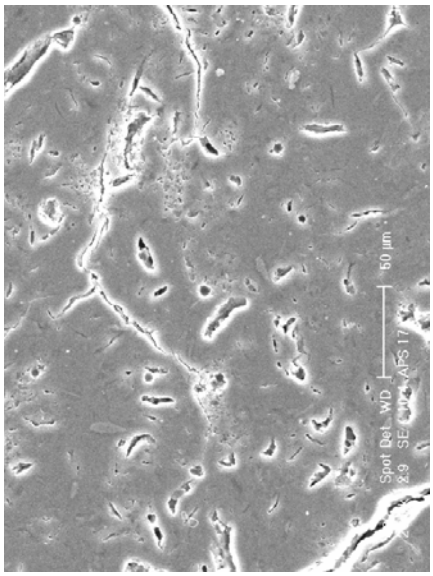

(b)

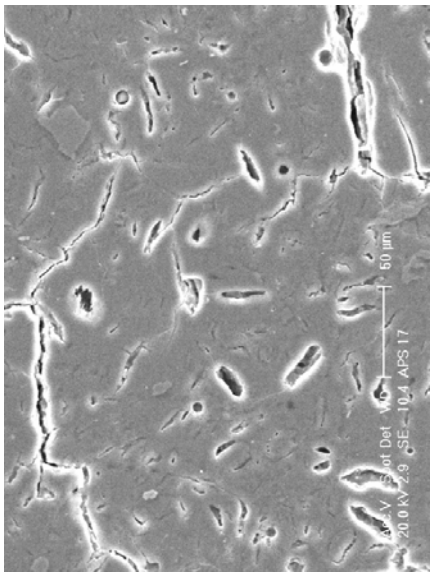

(c)

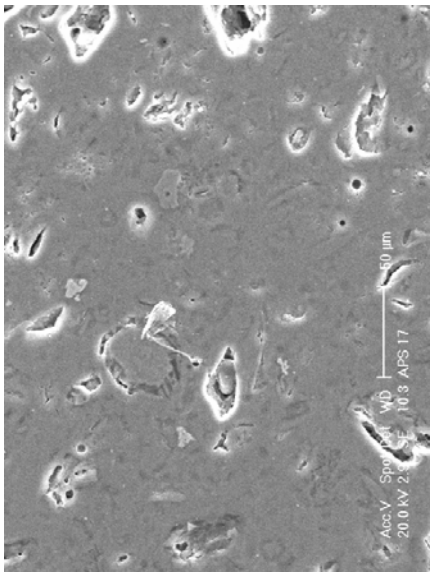

(d)

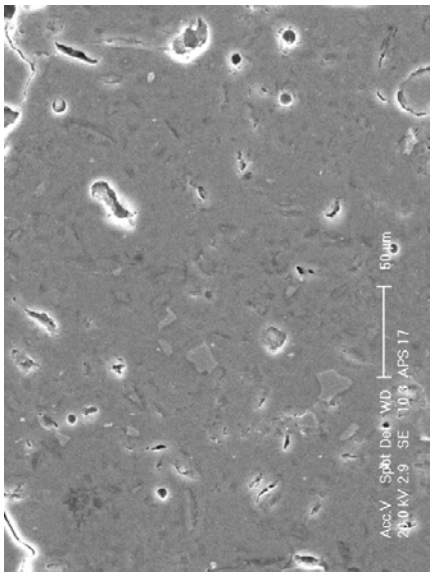

(e)

Figure AI.13: Sample 2.0/2.0.

(a) Site of interest 1

(b) Site of interest 2

(c) Site of interest 3

(d) Site of interest 4

(e) Site of interest 5

The images were collected with an accelerating voltage of 20 kV, a beam current of 60 pA and a working distance of 10.4 mm. The scale bar on the figures is 50 µm, and each micrograph is ~300 x 200 µm.

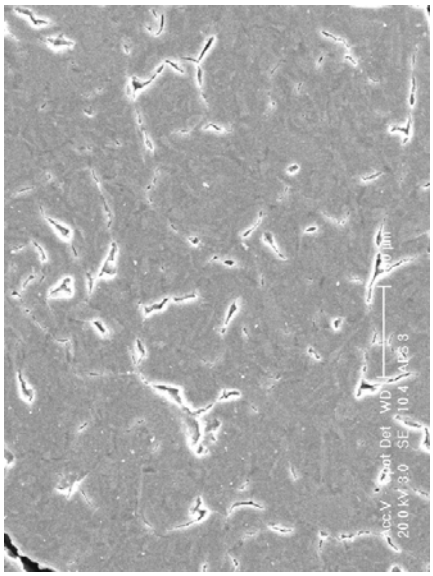

(a)

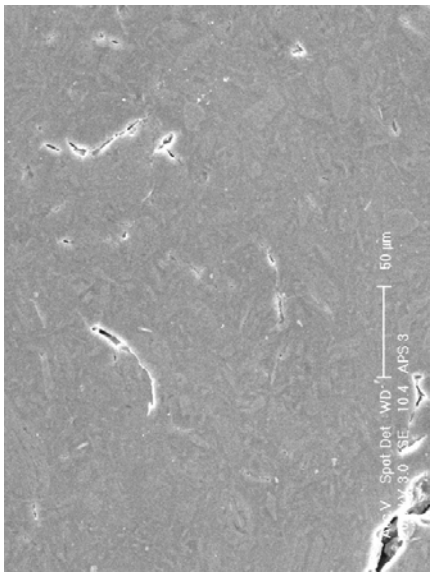

(b)

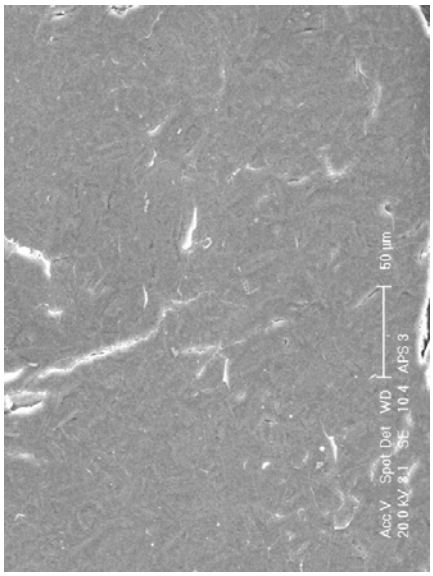

(c)

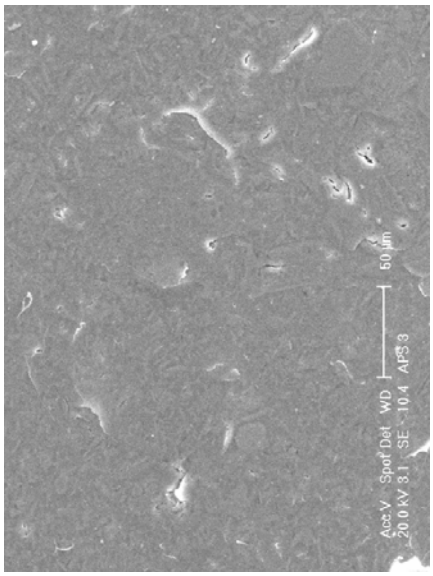

(d)

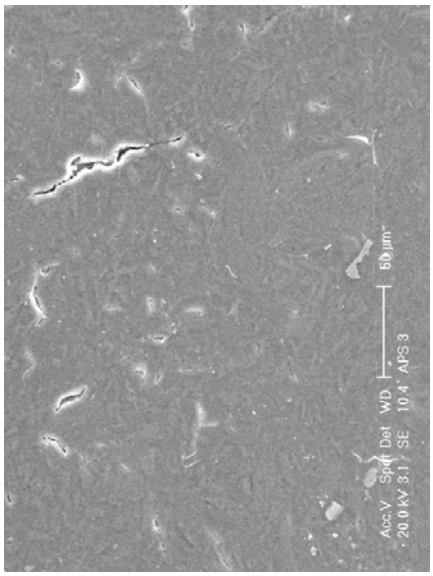

(e)

Figure AI.14: Sample 2.5/1.0.

(a) Site of interest 1

(b) Site of interest 2

(c) Site of interest 3

(d) Site of interest 4

(e) Site of interest 5

The images were collected with an accelerating voltage of 20 kV, a beam current of 60 pA and a working distance of 10.4 mm. The scale bar on the figures is 50 μm, and each micrograph is ~300 x 200 μm.

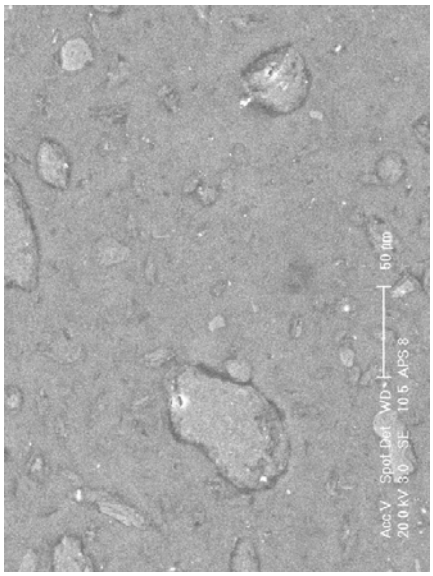

(a)

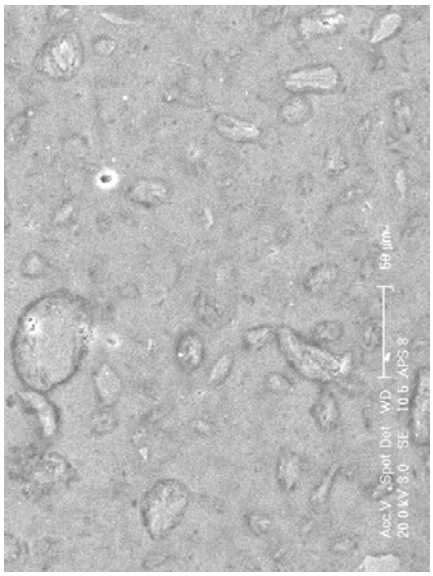

(b)

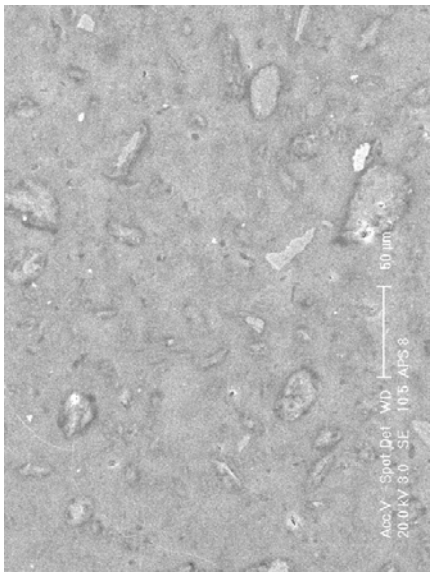

(c)

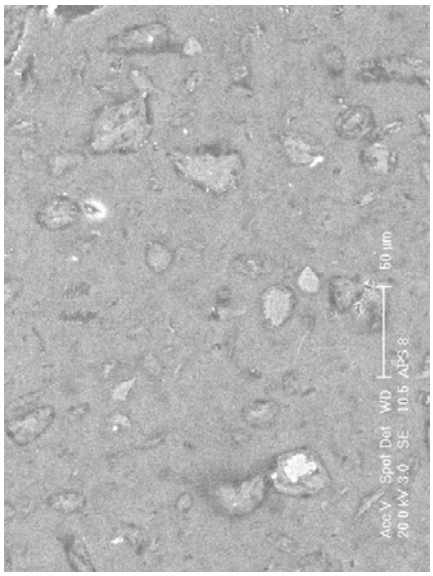

(d)

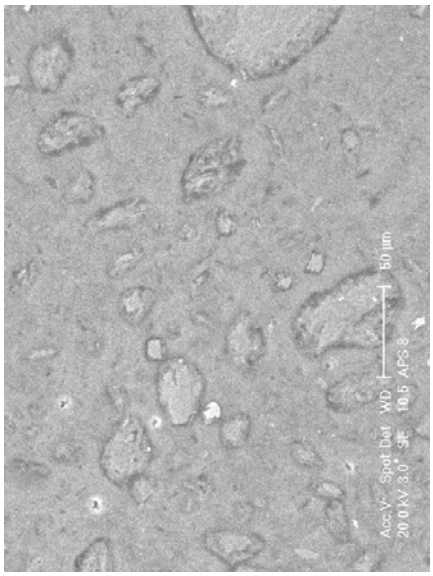

(e)

Figure AI.15: Sample 2.5/1.3.

(a) Site of interest 1

(b) Site of interest 2

(c) Site of interest 3

(d) Site of interest 4

(e) Site of interest 5

The images were collected with an accelerating voltage of 20 kV, a beam current of 60 pA and a working distance of 10.4 mm. The scale bar on the figures is 50 μm, and each micrograph is ~300 x 200 μm.

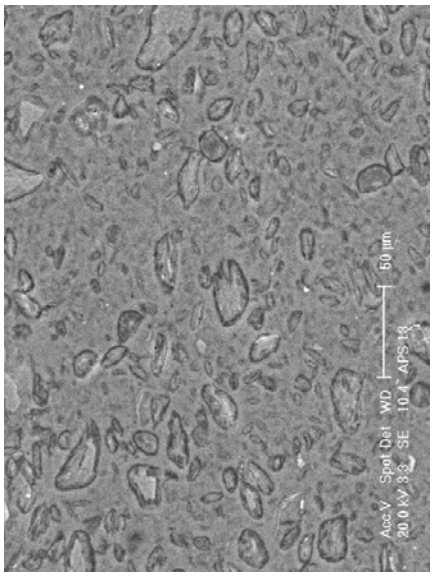

(a)

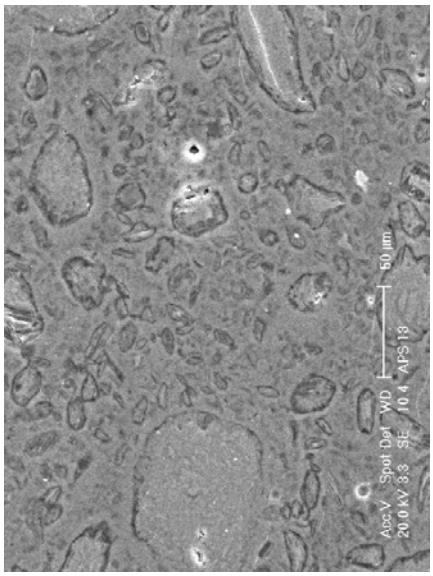

(b)

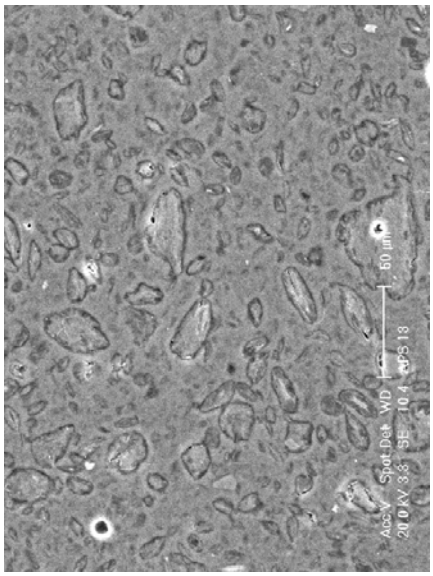

(c)

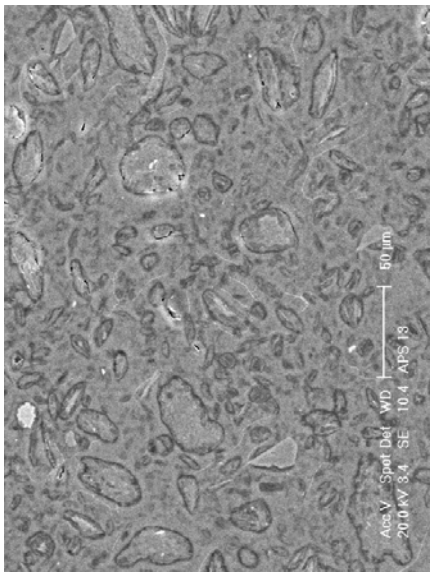

(d)

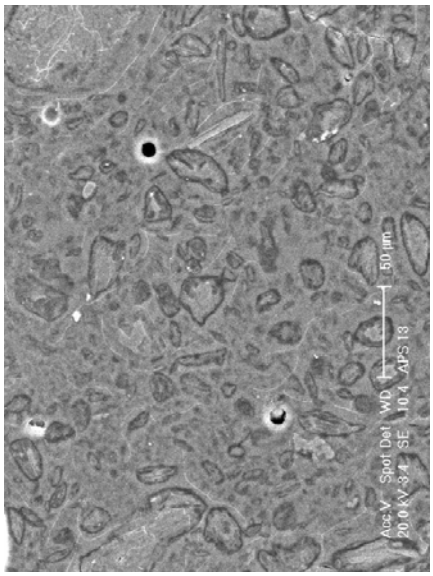

(e)

Figure AI.16: Sample 2.5/1.5.

(a) Site of interest 1

(b) Site of interest 2

(c) Site of interest 3

(d) Site of interest 4

(e) Site of interest 5

The images were collected with an accelerating voltage of 20 kV, a beam current of 60 pA and a working distance of 10.4 mm. The scale bar on the figures is 50 μm, and each micrograph is ~300 x 200 μm.

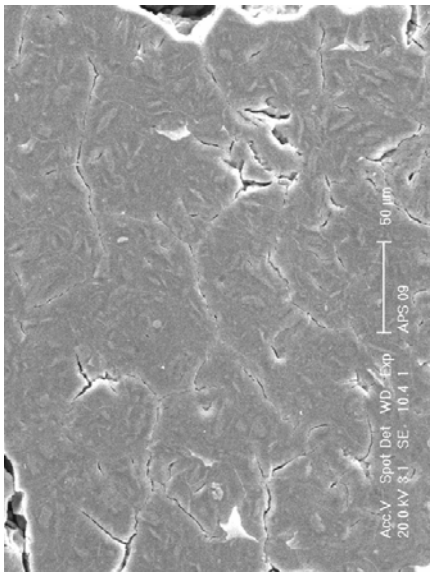

(a)

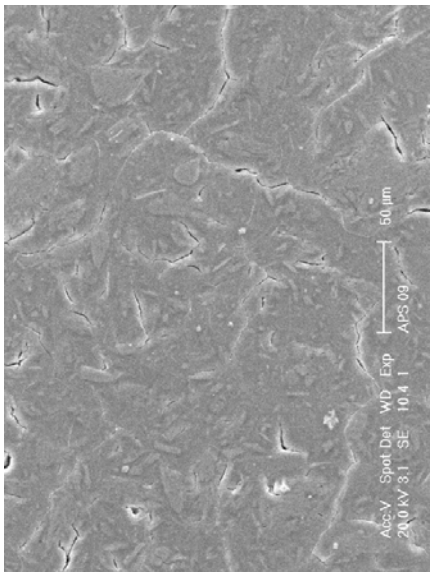

(b)

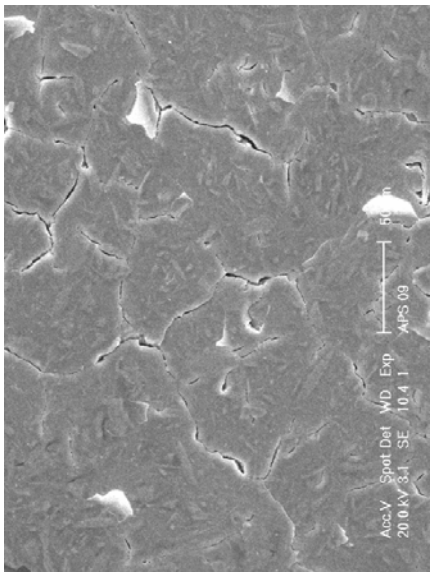

(c)

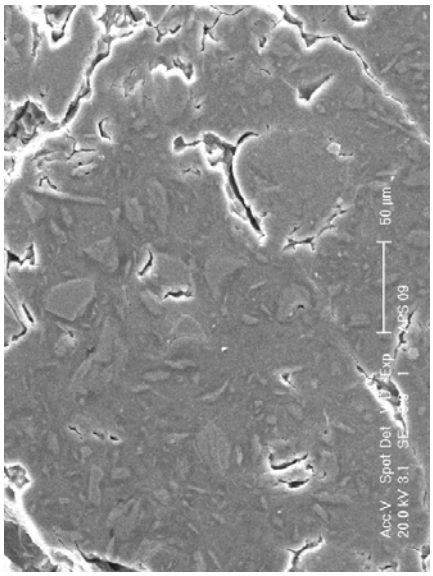

(d)

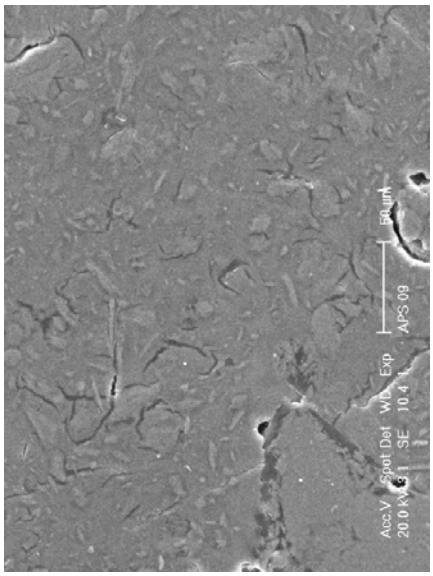

(e)

Figure AI.17: Sample 3.0/1.5.

(a) Site of interest 1

(b) Site of interest 2

(c) Site of interest 3

(d) Site of interest 4

(e) Site of interest 5

The images were collected with an accelerating voltage of 20 kV, a beam current of 60 pA and a working distance of 10.4 mm. The scale bar on the figures is 50 μm, and each micrograph is ~300 x 200 μm.

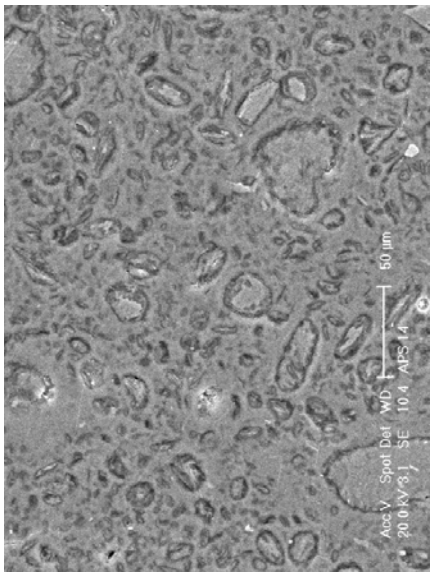

(a)

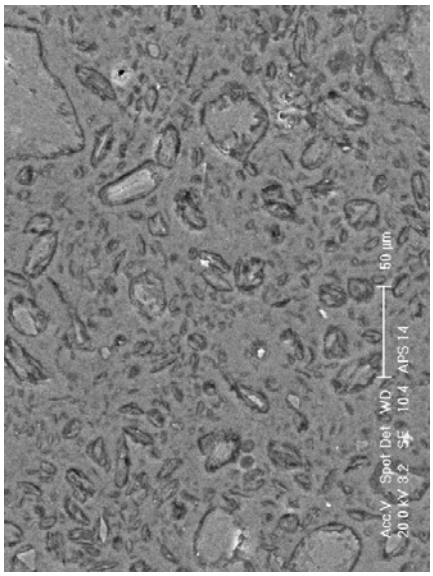

(b)

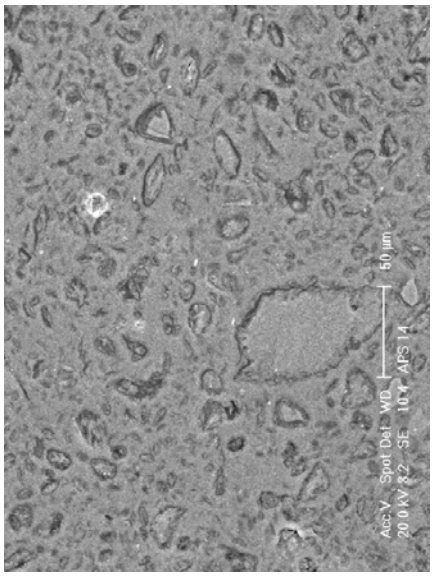

(c)

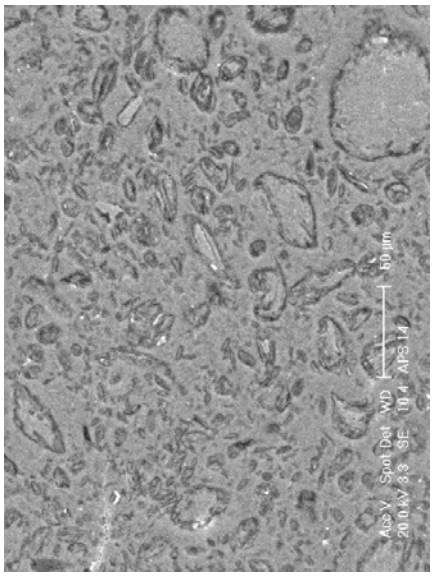

(d)

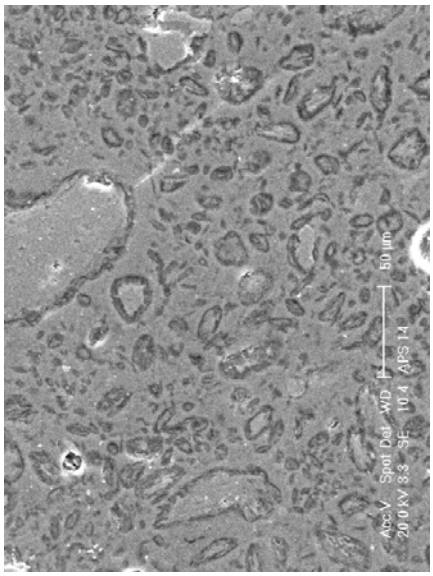

(e)

Figure AI.18: Sample 3.0/2.0.

(a) Site of interest 1

(b) Site of interest 2

(c) Site of interest 3

(d) Site of interest 4

(e) Site of interest 5

The images were collected with an accelerating voltage of 20 kV, a beam current of 60 pA and a working distance of 10.4 mm. The scale bar on the figures is 50 μm, and each micrograph is ~300 x 200 μm.

II APPENDIX – MOLAR RATIOS

Appendix II lists the Si:Al and Na:Al molar ratios measured from the EDS spectra taken from the SEM micrographs shown in Appendix I. In these tables, '#' gives the sample number used in the identification of the samples for this experiment, 'St' denotes the site of interest and 'Sp' gives the spectrum number. In general, 25 spectra were taken of each grain and matrix composition for each sample; any "missing" spectra are those of silica grains. In these tables, the set of numbers of the left correspond to the grain composition, whilst those on the right correspond to the matrix.

Table AII.1: Si:Al and Na:Al molar ratios of selected grain and matrix phases of Sample 1.1/0.6.

#	St	Sp	Si:Al	Na:Al	#	St	Sp	Si:Al	Na:Al
5	2	2	1.04	0.38	5	2	7	1.02	0.51
5	2	3	1.12	0.19	5	2	8	0.64	0.33
5	2	4	0.85	0.26	5	2	9	0.65	0.40
5	2	5	1.00	0.34	5	2	10	0.91	0.41
5	2	6	1.04	0.39	5	2	11	0.90	0.37
5	3	2	1.08	0.35	5	3	7	0.81	0.48
5	3	3	1.07	0.31	5	3	8	0.80	0.39
5	3	4	0.95	0.44	5	3	9	0.75	0.67
5	3	5	1.01	0.28	5	3	10	0.70	0.43
5	3	6	1.09	0.39	5	3	11	0.85	0.41
5	4	2	1.10	0.39	5	4	7	0.91	0.40
5	4	3	1.00	0.38	5	4	8	1.13	0.39
5	4	4	1.12	0.12	5	4	9	0.99	0.48
5	4	5	1.05	0.11	5	4	10	0.93	0.31
5	4	6	0.91	0.31	5	4	11	0.76	0.41
5	5	2	1.05	0.46	5	5	7	0.73	0.38
5	5	3	0.95	0.40	5	5	8	0.83	0.45
5	5	4	1.15	0.30	5	5	9	0.79	0.50
5	5	5	0.98	0.54	5	5	10	0.69	0.44
5	5	6	1.01	0.41	5	5	11	0.91	0.33

Table AII.2: Si:Al and Na:Al molar ratios of selected grain and matrix phases of Samples 1.1/0.8 and 1.1/1.0.

#	St	Sp	Si:Al	Na:Al
10	1	2	1.20	0.47
10	1	3	1.26	0.64
10	1	4	1.27	0.57
10	1	5	1.18	0.56
10	1	6	1.09	0.79
10	2	2	1.15	0.46
10	2	3	1.23	0.51
10	2	4	1.13	0.57
10	2	5	1.19	0.50
10	2	6	1.21	0.67
10	3	2	1.22	0.60
10	3	3	1.20	0.45
10	3	4	1.14	0.44
10	3	5	1.19	0.16
10	3	6	1.17	0.45
10	4	2	1.08	0.92
10	4	3	1.15	0.51
10	4	5	1.13	0.63
10	4	6	1.15	0.42
10	5	2	1.21	0.96
10	5	3	1.25	0.51
10	5	4	1.18	0.52
10	5	5	1.15	0.67
10	1	7	1.63	1.41
10	1	8	1.51	2.03
10	1	9	1.39	0.71
10	1	10	1.36	1.07
10	1	11	1.42	1.12
10	2	7	1.44	0.45
10	2	8	1.47	0.49
10	2	9	1.43	0.40
10	2	10	1.04	0.69
10	2	11	1.31	1.40
10	3	7	1.31	0.69
10	3	8	1.41	0.00
10	3	9	1.47	0.72
10	3	10	1.38	0.81
10	3	11	1.45	0.59
10	4	7	1.35	0.50
10	4	8	1.17	0.71
10	4	9	1.31	0.58
10	4	10	1.51	0.60
10	4	11	1.27	0.66
10	5	7	1.25	0.96
10	5	8	0.82	3.34
10	5	9	1.50	1.06
10	5	10	1.11	0.60
10	5	11	1.90	1.88
15	1	2	1.18	0.86
15	1	3	1.21	0.88
15	1	4	1.10	0.76
15	1	5	0.98	0.82
15	1	6	1.15	0.76
15	2	2	1.13	0.84
15	2	4	1.16	0.61
15	2	5	1.15	0.65
15	2	6	1.15	0.85
15	3	2	1.21	0.79
15	3	3	1.11	0.78
15	3	4	1.14	0.71
15	3	5	1.20	0.71
15	3	6	1.15	0.72
15	4	3	1.23	0.67
15	4	4	1.15	0.72
15	4	5	1.17	0.96
15	4	6	1.11	0.65
15	5	2	1.14	0.62
15	5	3	1.12	0.54
15	5	5	1.17	0.64
15	5	6	1.22	0.72
15	1	7	2.19	2.92
15	1	8	1.15	1.65
15	1	9	1.23	0.82
15	1	10	1.12	0.87
15	1	11	1.08	0.81
15	2	7	1.31	0.91
15	2	8	1.22	1.94
15	2	9	1.44	1.27
15	2	10	1.20	0.93
15	2	11	1.32	0.87
15	3	7	1.40	0.59
15	3	8	1.24	0.70
15	3	9	1.28	1.29
15	3	10	1.47	0.57
15	3	11	1.14	0.67
15	4	8	1.72	2.73
15	4	9	1.24	1.24
15	4	10	1.26	3.45
15	4	11	1.25	1.66
15	5	7	1.42	0.72
15	5	8	1.53	0.67
15	5	9	1.33	0.72
15	5	10	1.24	0.82
15	5	11	1.18	0.75

Table AII.3: Si:Al and Na:Al molar ratios of selected grain and matrix phases of Samples 1.1/1.5 and 1.5/0.6.

#	St	Sp	Si:Al	Na:Al	#	St	Sp	Si:Al	Na:Al
18	1	2	1.04	0.99	18	1	7	1.35	1.62
18	1	3	1.14	1.29	18	1	8	1.22	1.74
18	1	4	1.28	1.34	18	1	9	1.10	2.36
18	1	5	1.21	1.58	18	1	10	1.18	1.44
18	1	6	2.57	1.28	18	1	11	1.21	1.52
18	2	2	1.12	1.64	18	2	7	1.34	1.59
18	2	3	1.10	1.46	18	2	8	1.12	1.84
18	2	4	1.18	1.24	18	2	9	1.16	1.84
18	2	5	1.14	1.26	18	2	10	1.21	1.63
18	2	6	1.09	1.73	18	2	11	1.18	1.64
18	3	2	1.16	1.28	18	3	7	1.25	1.86
18	3	3	1.19	1.49	18	3	8	1.38	2.17
18	3	4	1.14	1.37	18	3	9	1.27	2.36
18	3	5	1.09	1.21	18	3	10	1.24	1.86
18	3	6	1.33	1.43	18	3	11	1.13	1.62
18	4	2	1.26	1.34	18	4	7	1.39	1.53
18	4	3	1.11	1.21	18	4	8	1.17	1.83
18	4	4	1.15	1.11	18	4	9	1.09	1.79
18	4	5	1.25	1.20	18	4	10	1.15	1.68
18	4	6	1.04	2.22	18	4	11	1.06	1.72
18	5	2	1.16	1.34	18	5	7	1.34	1.49
18	5	3	1.30	1.26	18	5	8	1.16	3.14
18	5	4	1.17	1.58	18	5	9	1.29	1.76
18	5	5	1.17	1.13	18	5	10	1.19	1.59
18	5	6	1.24	1.35	18	5	11	1.22	1.65
1	1	2	1.35	0.21	1	1	7	2.12	0.67
1	1	3	1.46	0.21	1	1	8	1.90	0.59
1	1	4	1.41	0.27	1	1	9	1.93	0.46
1	1	5	1.13	0.00	1	1	10	1.64	0.42
1	1	6	1.37	0.20	1	1	11	2.12	0.62
1	2	2	1.36	0.25	1	2	7	1.90	0.92
1	2	3	1.17	0.08	1	2	8	1.88	1.17
1	2	4	1.19	0.09	1	2	9	2.16	1.16
1	2	5	1.28	0.19	1	2	10	1.94	1.25
1	3	2	1.34	0.37	1	2	11	1.96	0.85
1	3	3	1.27	0.19	1	3	7	2.19	2.11
1	3	4	1.13	0.00	1	3	8	2.02	1.59
1	3	5	1.49	0.38	1	3	9	2.20	2.38
1	3	6	1.47	0.38	1	3	10	1.80	1.39
1	4	2	1.19	0.07	1	3	11	1.86	1.73
1	4	3	1.35	0.28	1	4	7	2.17	1.82
1	4	4	1.41	0.33	1	4	8	2.23	1.84
1	4	5	2.09	0.43	1	4	9	1.80	1.30
1	4	6	1.41	0.24	1	4	10	2.08	1.50
1	5	2	1.43	0.43	1	4	11	2.01	1.21
1	5	3	1.42	0.40	1	5	7	2.06	1.50
1	5	4	1.40	0.49	1	5	8	2.48	2.24
1	5	5	1.24	0.27	1	5	9	2.06	1.37
1	5	6	1.40	0.22	1	5	10	1.79	1.26
					1	5	11	1.96	1.22

Table AII.4: Si:Al and Na:Al molar ratios of selected grain and matrix phases of Samples 1.5/0.8 and 1.5/1.0.

#	St	Sp	Si:Al	Na:Al	#	St	Sp	Si:Al	Na:Al
6	1	2	1.42	0.64	6	1	7	1.80	1.89
6	1	3	1.53	0.50	6	1	8	1.97	1.96
6	1	4	1.51	0.54	6	1	9	1.91	1.16
6	1	5	1.47	0.49	6	1	10	2.05	1.47
6	1	6	1.52	0.80	6	1	11	2.00	1.39
6	2	2	1.38	0.45	6	2	7	1.41	0.75
6	2	3	1.48	0.91	6	2	8	1.95	2.38
6	2	4	1.49	0.45	6	2	9	1.86	1.57
6	2	5	1.52	0.45	6	2	10	1.98	1.90
6	2	6	1.55	0.57	6	2	11	1.73	2.29
6	3	2	1.29	0.54	6	3	7	1.91	1.51
6	3	3	1.43	0.31	6	3	8	2.04	1.82
6	3	4	1.17	0.19	6	3	9	1.73	1.96
6	3	5	1.47	0.65	6	3	10	1.73	1.96
6	3	6	1.19	0.10	6	3	11	1.81	1.59
6	4	2	1.50	0.56	6	4	7	1.93	1.09
6	4	3	1.28	0.24	6	4	8	1.95	1.01
6	4	4	1.20	0.10	6	4	9	1.85	1.30
6	4	5	1.55	0.43	6	4	10	1.50	0.56
6	4	6	1.53	0.33	6	4	11	1.66	0.82
6	5	2	1.45	0.53	6	5	7	1.77	1.79
6	5	3	1.42	0.69	6	5	8	1.96	2.35
6	5	4	1.53	0.49	6	5	9	1.85	2.01
6	5	5	1.27	0.18	6	5	10	1.66	1.72
6	5	6	1.29	0.23	6	5	11	1.62	1.73
11	1	2	1.12	0.14	11	1	7	1.83	0.67
11	1	3	1.48	0.49	11	1	8	1.81	0.66
11	1	4	1.08	0.06	11	1	9	1.76	0.73
11	1	5	1.48	0.47	11	1	10	1.90	0.70
11	1	6	1.42	0.30	11	1	11	1.80	0.70
11	2	2	1.36	0.37	11	2	7	1.66	0.62
11	2	3	1.53	0.51	11	2	8	1.84	0.67
11	2	4	1.40	0.37	11	2	9	1.75	0.56
11	2	5	1.27	0.22	11	2	10	1.68	0.69
11	2	6	1.36	0.26	11	2	11	1.75	0.69
11	3	2	1.62	0.68	11	3	7	1.64	0.68
11	3	3	1.33	0.22	11	3	8	1.58	0.51
11	3	4	1.43	0.39	11	3	9	1.69	0.69
11	3	5	1.63	0.63	11	3	10	1.57	0.47
11	3	6	1.18	0.24	11	3	11	1.76	0.73
11	4	2	1.41	0.18	11	4	7	1.82	0.76
11	4	3	1.43	0.46	11	4	8	1.75	0.89
11	4	4	1.49	0.46	11	4	9	1.65	0.90
11	4	5	1.63	0.53	11	4	10	1.82	0.76
11	4	6	1.28	0.20	11	4	11	1.68	0.65
11	5	2	1.58	0.44	11	5	7	1.80	0.67
11	5	3	1.55	0.52	11	5	8	1.82	0.87
11	5	4	1.44	0.41	11	5	9	1.76	0.74
11	5	5	1.62	0.59	11	5	10	1.90	0.76
11	5	6	1.44	0.41	11	5	11	1.64	0.73

Table AII.5: Si:Al and Na:Al molar ratios of selected grain and matrix phases of Samples 1.5/1.5 and 1.5/2.0.

#	St	Sp	Si:Al	Na:Al
16	1	2	2.02	1.54
16	1	3	1.83	1.40
16	1	4	2.45	2.06
16	1	5	2.12	2.88
16	1	6	9.94	11.29
16	2	2	1.90	2.47
16	2	3	2.34	1.93
16	2	4	1.88	1.24
16	2	5	2.14	3.22
16	2	6	2.09	1.44
16	3	2	2.89	1.12
16	3	3	1.79	0.90
16	3	4	1.92	1.06
16	3	5	1.79	0.98
16	3	6	1.84	0.81
16	4	2	1.57	0.14
16	4	3	1.78	0.98
16	4	4	1.73	0.87
16	4	5	1.99	1.20
16	4	6	1.63	0.79
16	5	2	1.79	1.19
16	5	3	1.78	1.42
16	5	4	1.76	0.95
16	5	5	5.46	1.34
16	5	6	1.91	1.04
16	1	7	1.94	1.15
16	1	8	1.74	1.08
16	1	9	1.66	0.99
16	1	10	1.76	1.61
16	1	11	1.76	1.21
16	2	7	1.67	1.00
16	2	8	1.80	1.03
16	2	9	1.92	1.04
16	2	10	1.64	1.08
16	2	11	1.67	0.96
16	3	7	1.62	1.03
16	3	8	1.68	1.04
16	3	9	1.71	1.03
16	3	10	1.64	0.95
16	3	11	1.73	1.02
16	4	7	1.68	0.97
16	4	8	1.45	0.92
16	4	9	1.75	0.97
16	4	10	1.54	0.84
16	4	11	1.57	0.84
16	5	7	1.61	0.94
16	5	8	1.49	0.95
16	5	9	1.68	0.99
16	5	10	1.61	0.96
16	5	11	1.69	1.07
19	1	3	1.91	1.07
19	1	5	2.62	1.21
19	1	6	1.67	1.01
19	2	2	2.11	1.30
19	2	3	32.01	1.54
19	2	4	1.83	1.11
19	2	5	7.29	0.00
19	2	6	59.23	0.00
19	3	2	1.56	1.01
19	3	3	1.62	0.81
19	3	4	1.57	0.91
19	3	5	1.34	0.99
19	4	4	2.03	1.29
19	4	5	1.83	1.43
19	4	6	1.78	1.34
19	5	3	1.57	0.94
19	5	4	1.62	1.30
19	5	5	1.69	1.23
19	5	6	1.69	1.28
19	1	7	1.58	1.11
19	1	8	1.58	1.12
19	1	9	1.62	1.08
19	1	10	1.61	1.25
19	1	11	1.70	1.14
19	2	7	1.79	1.03
19	2	8	1.73	0.96
19	2	9	1.61	0.91
19	2	10	1.75	1.09
19	2	11	1.70	0.97
19	3	7	1.54	0.96
19	3	8	1.56	1.01
19	3	9	1.57	0.91
19	3	10	1.64	0.96
19	3	11	1.66	1.00
19	4	7	1.88	1.17
19	4	8	2.25	1.30
19	4	9	1.89	1.20
19	4	10	1.99	1.28
19	4	11	2.01	1.21
19	5	7	1.81	1.32
19	5	8	1.76	1.32
19	5	9	1.70	1.22
19	5	10	1.77	1.20
19	5	11	1.72	1.23

Table AII.6: Si:Al and Na:Al molar ratios of selected grain and matrix phases of Samples 2.0/0.8 and 2.0/1.0.

#	St	Sp	Si:Al	Na:Al
2	1	2	1.83	0.42
2	1	3	1.57	0.32
2	1	4	1.58	0.21
2	1	5	1.36	0.19
2	1	6	1.67	0.37
2	2	2	1.29	0.18
2	2	3	1.69	0.42
2	2	4	1.68	0.18
2	2	5	1.74	0.21
2	2	6	1.75	0.29
2	3	2	1.82	0.32
2	3	5	1.53	0.30
2	3	6	1.48	0.16
2	4	2	1.66	0.28
2	4	3	1.74	0.24
2	4	4	1.35	0.07
2	4	5	1.07	0.00
2	4	6	1.53	0.29
2	5	2	1.61	0.87
2	5	3	1.36	0.14
2	5	4	1.67	0.50
2	5	5	1.75	0.36
2	5	6	26.41	0.00

#	St	Sp	Si:Al	Na:Al
2	1	7	6.55	3.61
2	1	8	4.51	3.32
2	1	9	5.17	3.79
2	1	10	3.89	2.43
2	1	11	3.94	3.01
2	2	7	3.52	0.96
2	2	8	2.32	0.82
2	2	9	4.30	2.91
2	2	10	2.57	1.11
2	2	11	4.31	2.24
2	3	7	4.17	2.53
2	3	8	3.31	1.66
2	3	9	4.72	2.43
2	3	10	4.18	2.32
2	3	11	3.21	1.87
2	4	7	5.43	1.49
2	4	8	3.09	1.37
2	4	9	3.95	1.91
2	4	10	4.45	1.26
2	4	11	4.87	2.70
2	5	7	3.65	3.13
2	5	8	3.46	1.58
2	5	9	3.82	2.65
2	5	10	3.68	1.98
2	5	11	4.66	4.00

#	St	Sp	Si:Al	Na:Al
7	1	2	1.80	0.45
7	1	3	1.45	0.21
7	1	4	1.67	0.33
7	1	5	1.30	0.09
7	1	6	1.34	0.14
7	2	2	1.67	0.35
7	2	3	1.72	0.30
7	2	4	1.88	0.50
7	2	5	1.54	0.29
7	2	6	1.60	0.25
7	3	2	1.47	0.29
7	3	3	1.29	0.14
7	3	4	1.58	0.31
7	3	5	1.50	0.30
7	3	6	1.60	0.32
7	4	2	1.56	0.21
7	4	3	1.51	0.25
7	4	4	1.60	0.26
7	4	5	1.29	0.05
7	4	6	1.93	0.49
7	5	2	1.53	0.29
7	5	3	2.06	0.35
7	5	4	1.25	0.13
7	5	5	1.49	0.28
7	5	6	1.58	0.26

#	St	Sp	Si:Al	Na:Al
7	1	7	2.40	1.26
7	1	8	2.11	1.08
7	1	9	2.51	1.09
7	1	10	2.50	1.18
7	1	11	2.40	1.08
7	2	7	2.38	0.85
7	2	8	2.25	0.82
7	2	9	2.25	0.90
7	2	10	2.35	0.88
7	2	11	2.41	0.92
7	3	7	2.46	0.80
7	3	8	2.37	0.79
7	3	9	2.57	1.07
7	3	10	2.40	0.91
7	3	11	2.45	0.99
7	4	7	2.47	0.95
7	4	8	2.47	0.70
7	4	9	2.43	0.79
7	4	10	2.20	0.74
7	4	11	1.59	0.41
7	5	7	2.51	1.03
7	5	8	2.57	1.07
7	5	9	2.47	1.08
7	5	10	2.05	0.71
7	5	11	2.32	0.93

Table AII.7: Si:Al and Na:Al molar ratios of selected grain and matrix phases of Samples 2.0/1.3 and 2.0/2.0.

#	St	Sp	Si:Al	Na:Al
12	1	2	1.57	0.34
12	1	4	1.64	0.44
12	1	5	1.54	0.36
12	1	6	1.82	0.52
12	2	2	1.65	0.41
12	2	3	1.45	0.34
12	2	4	1.50	0.30
12	2	5	1.99	0.55
12	2	6	2.41	0.81
12	3	2	1.30	0.17
12	3	3	1.67	0.39
12	3	4	2.08	0.64
12	3	5	2.37	0.70
12	3	6	2.17	0.59
12	4	2	1.51	0.34
12	4	3	1.89	0.57
12	4	4	1.63	0.39
12	4	5	1.79	0.51
12	4	6	1.81	0.47
12	5	2	1.49	0.28
12	5	3	1.33	0.24
12	5	4	1.20	0.07
12	5	5	5.59	0.72
12	5	6	1.29	0.15
12	1	7	2.47	0.74
12	1	8	2.36	0.61
12	1	9	2.24	0.56
12	1	10	2.32	0.71
12	1	11	2.16	0.76
12	2	7	2.22	0.57
12	2	8	2.49	0.69
12	2	9	2.40	0.61
12	2	10	2.27	0.70
12	2	11	2.57	0.58
12	3	7	2.40	0.74
12	3	8	2.18	0.72
12	3	9	2.36	0.90
12	3	10	2.39	0.96
12	3	11	2.22	0.93
12	4	7	2.37	0.72
12	4	8	2.28	0.85
12	4	9	2.16	0.70
12	4	10	2.30	0.74
12	4	11	2.10	0.83
12	5	7	2.43	0.73
12	5	8	2.29	0.58
12	5	9	2.41	0.76
12	5	10	2.45	0.83
12	5	11	2.31	0.71
17	1	3	2.10	1.19
17	1	4	2.04	1.25
17	1	5	2.02	1.26
17	1	6	2.56	1.25
17	2	2	40.20	1.47
17	2	3	2.10	1.02
17	2	4	1.88	1.05
17	2	5	1.84	1.19
17	2	6	2.07	1.14
17	3	2	1.85	1.08
17	3	3	1.81	0.47
17	3	4	2.84	1.20
17	3	5	2.27	1.22
17	3	6	2.48	1.31
17	4	2	1.24	0.20
17	4	3	2.03	1.16
17	4	4	2.02	1.20
17	4	5	2.11	1.14
17	4	6	2.09	1.09
17	5	2	2.05	1.09
17	5	3	2.30	1.12
17	5	4	2.24	1.07
17	5	5	2.26	1.09
17	5	6	2.01	0.92
17	1	7	2.11	1.10
17	1	8	2.38	1.16
17	1	9	2.03	1.02
17	1	10	2.11	1.15
17	1	11	2.14	1.13
17	2	7	2.08	1.00
17	2	8	2.08	1.09
17	2	9	2.06	1.01
17	2	10	2.09	1.07
17	2	11	2.15	1.00
17	3	7	2.46	1.26
17	3	8	2.27	1.24
17	3	9	2.20	1.16
17	3	10	1.97	1.09
17	3	11	2.15	1.05
17	4	7	2.02	1.01
17	4	8	2.06	1.00
17	4	9	2.05	1.02
17	4	10	2.03	1.06
17	4	11	2.20	1.08
17	5	7	2.36	1.21
17	5	8	2.15	1.15
17	5	9	2.11	1.09
17	5	10	2.01	0.97
17	5	11	2.06	0.97

Table AII.8: Si:Al and Na:Al molar ratios of selected grain and matrix phases of Samples 2.5/1.0 and 2.5/1.3.

#	St	Sp	Si:Al	Na:Al
3	1	2	2.16	0.23
3	1	3	1.91	0.21
3	1	4	1.95	0.24
3	1	5	2.27	0.24
3	1	6	6.64	0.89
3	2	4	1.56	0.14
3	2	6	3.54	0.65
3	3	2	1.22	0.06
3	3	3	1.61	0.21
3	3	4	2.95	0.53
3	3	5	1.77	0.29
3	3	6	4.67	1.39
3	4	3	1.70	0.36
3	4	4	1.86	0.23
3	4	5	1.23	0.00
3	4	6	2.05	0.28
3	5	2	1.75	0.27
3	5	3	18.09	1.00
3	5	4	1.31	0.09
3	5	5	2.74	0.53
3	5	6	1.86	0.28
3	1	7	3.82	0.56
3	1	8	4.83	0.60
3	1	9	1.86	0.17
3	1	10	2.02	0.24
3	1	11	2.32	0.21
3	2	7	3.63	0.59
3	2	8	4.31	0.67
3	2	9	5.10	0.77
3	2	10	1.56	0.21
3	2	11	4.81	0.77
3	3	7	3.49	0.69
3	3	8	3.01	0.65
3	3	9	1.86	0.26
3	3	10	3.86	1.02
3	3	11	3.18	0.67
3	4	7	3.62	0.81
3	4	8	2.70	0.62
3	4	9	3.14	0.59
3	4	10	4.92	1.13
3	4	11	3.92	0.91
3	5	7	5.64	1.15
3	5	8	3.77	0.86
3	5	9	3.87	0.75
3	5	10	4.23	1.18
3	5	11	3.23	0.61
8	1	2	1.76	0.44
8	1	3	1.63	0.32
8	1	4	1.96	0.60
8	1	5	1.61	0.26
8	1	6	2.30	0.73
8	2	2	1.60	0.29
8	2	3	1.78	0.37
8	2	4	2.50	0.87
8	2	5	1.44	0.16
8	2	6	1.17	0.09
8	3	2	2.03	0.39
8	3	3	1.81	0.34
8	3	4	2.63	0.96
8	3	5	2.76	0.87
8	3	6	1.73	0.34
8	4	2	1.79	0.39
8	4	3	1.45	0.23
8	4	4	1.55	0.42
8	4	5	1.27	0.08
8	4	6	1.77	0.47
8	5	2	1.65	0.36
8	5	3	1.23	0.06
8	5	4	1.45	0.22
8	5	5	1.74	0.38
8	5	6	1.61	0.29
8	1	7	3.57	1.68
8	1	8	2.72	1.15
8	1	9	3.30	1.60
8	1	10	3.25	1.54
8	1	11	3.27	1.49
8	2	7	3.35	1.16
8	2	8	3.09	1.24
8	2	9	3.33	1.19
8	2	10	3.45	1.25
8	2	11	3.20	1.17
8	3	7	3.20	1.16
8	3	8	3.13	1.05
8	3	9	3.09	1.04
8	3	10	3.31	1.14
8	3	11	3.25	0.95
8	4	7	3.28	1.48
8	4	8	3.25	1.47
8	4	9	3.17	1.35
8	4	10	3.44	1.65
8	4	11	3.30	1.53
8	5	7	3.19	1.54
8	5	8	3.41	1.66
8	5	9	3.07	1.61
8	5	10	3.32	1.68
8	5	11	3.29	1.71

Table AII.9: Si:Al and Na:Al molar ratios of selected grain and matrix phases of Samples 2.5/1.5 and 3.0/1.5.

#	St	Sp	Si:Al	Na:Al
13	1	2	1.67	0.30
13	1	3	2.63	0.63
13	1	4	1.34	0.10
13	1	5	1.72	0.39
13	1	6	1.53	0.30
13	2	2	1.29	0.10
13	2	3	1.92	0.52
13	2	4	1.57	0.28
13	2	5	1.22	0.09
13	2	6	1.65	0.35
13	3	2	1.86	0.42
13	3	3	1.38	0.26
13	3	4	1.69	0.37
13	3	5	1.88	0.49
13	3	6	1.87	0.37
13	4	2	2.51	0.75
13	4	3	1.90	0.34
13	4	4	1.61	0.35
13	4	5	1.26	0.12
13	4	6	1.88	0.38
13	5	2	1.24	0.15
13	5	3	1.64	0.33
13	5	4	1.79	0.36
13	5	5	2.00	0.42
13	5	6	1.57	0.20
13	1	7	3.09	1.16
13	1	8	3.38	1.43
13	1	9	3.26	1.24
13	1	10	3.32	1.19
13	1	11	2.90	1.17
13	2	7	3.03	1.12
13	2	8	3.17	1.18
13	2	9	3.20	1.14
13	2	10	3.20	1.23
13	2	11	2.90	1.26
13	3	7	3.10	1.04
13	3	8	3.50	1.18
13	3	9	3.04	1.10
13	3	10	3.12	1.13
13	3	11	2.98	1.06
13	4	7	3.26	1.06
13	4	8	3.08	1.01
13	4	9	3.18	1.08
13	4	10	2.92	1.00
13	4	11	3.22	1.05
13	5	7	3.29	0.99
13	5	8	3.20	1.04
13	5	9	3.18	0.91
13	5	10	8.13	0.95
13	5	11	3.23	1.01
9	1	2	5.20	1.12
9	1	3	4.48	0.80
9	1	4	5.09	1.02
9	1	5	3.72	0.78
9	1	6	3.94	0.80
9	2	2	1.26	0.07
9	2	3	1.45	0.11
9	2	5	1.31	0.10
9	2	6	1.92	0.25
9	3	2	61.71	0.00
9	3	3	1.61	0.19
9	3	4	3.20	0.43
9	3	5	4.95	0.99
9	3	6	1.54	0.14
9	4	3	1.47	0.09
9	4	4	1.69	0.14
9	4	5	2.27	0.34
9	4	6	1.55	0.10
9	5	2	2.26	0.28
9	5	3	1.51	0.12
9	5	4	2.43	0.37
9	5	5	2.36	0.29
9	5	6	2.18	0.24
9	1	7	4.23	0.86
9	1	8	1.37	0.10
9	1	9	5.01	0.45
9	1	10	2.36	0.35
9	1	11	1.48	0.13
9	2	7	4.27	0.85
9	2	8	4.72	0.85
9	2	9	3.45	0.62
9	2	10	3.30	0.68
9	2	11	4.09	0.74
9	3	7	5.33	0.94
9	3	8	3.59	0.70
9	3	9	4.77	1.00
9	3	10	4.57	0.95
9	3	11	4.06	0.72
9	4	7	4.04	0.53
9	4	8	4.72	0.68
9	4	9	4.60	0.82
9	4	10	3.95	0.52
9	4	11	3.84	0.64
9	5	7	5.45	0.93
9	5	8	5.21	0.69
9	5	9	3.17	0.51
9	5	10	5.91	0.90
9	5	11	5.16	0.79

Table AII.10: Si:Al and Na:Al molar ratios of selected grain and matrix phases of Samples 3.0/2.0

#	St	Sp	Si:Al	Na:Al
14	1	2	1.89	0.36
14	1	3	1.57	0.23
14	1	4	1.91	0.48
14	1	5	1.78	0.36
14	1	6	1.30	0.10
14	2	2	1.49	0.29
14	2	3	1.86	0.49
14	2	4	1.40	0.22
14	2	5	1.77	0.37
14	2	6	1.76	0.34
14	3	2	1.43	0.21
14	3	3	1.43	0.24
14	3	4	2.74	0.99
14	3	5	2.60	0.91
14	3	6	2.24	0.69
14	4	2	1.55	0.26
14	4	3	1.16	0.06
14	4	4	1.77	0.38
14	4	5	1.66	0.29
14	4	6	1.35	0.18
14	5	2	1.54	0.27
14	5	3	1.70	0.38
14	5	4	1.24	0.12
14	5	5	1.76	0.38
14	5	6	3.50	1.45

#	St	Sp	Si:Al	Na:Al
14	1	7	3.47	1.22
14	1	8	3.40	1.55
14	1	9	3.51	1.23
14	1	10	3.65	1.84
14	1	11	3.98	1.65
14	2	7	3.50	1.34
14	2	8	3.45	2.11
14	2	9	3.64	1.45
14	2	10	3.75	1.46
14	2	11	3.95	1.45
14	3	7	3.79	1.45
14	3	8	3.63	1.70
14	3	9	3.63	1.57
14	3	10	3.22	1.30
14	3	11	3.96	1.61
14	4	7	3.66	1.55
14	4	8	3.71	1.53
14	4	9	3.19	1.36
14	4	10	3.72	1.48
14	4	11	3.60	1.55
14	5	7	3.83	1.70
14	5	8	3.76	1.64
14	5	9	3.82	1.72
14	5	10	3.37	1.51
14	5	11	4.48	2.07

III APPENDIX – GRAPHICAL MOLAR RATIOS

The following figures show the molar ratios reported in Appendix II. Each of the figures has a data point with a value of zero at approximately position 25 dividing the data in two. The grain composition is given by the values on the left, the matrix by those on the right.

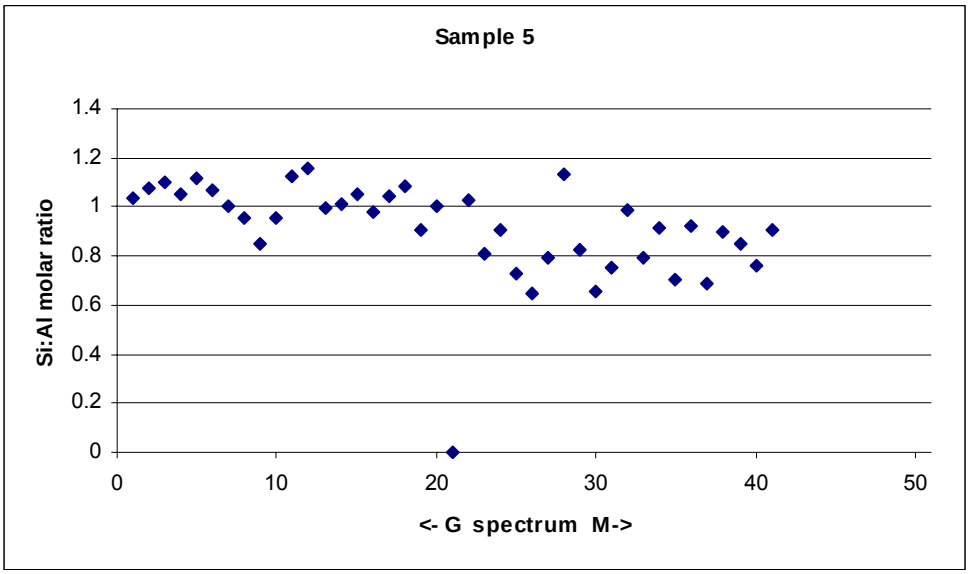

(a)

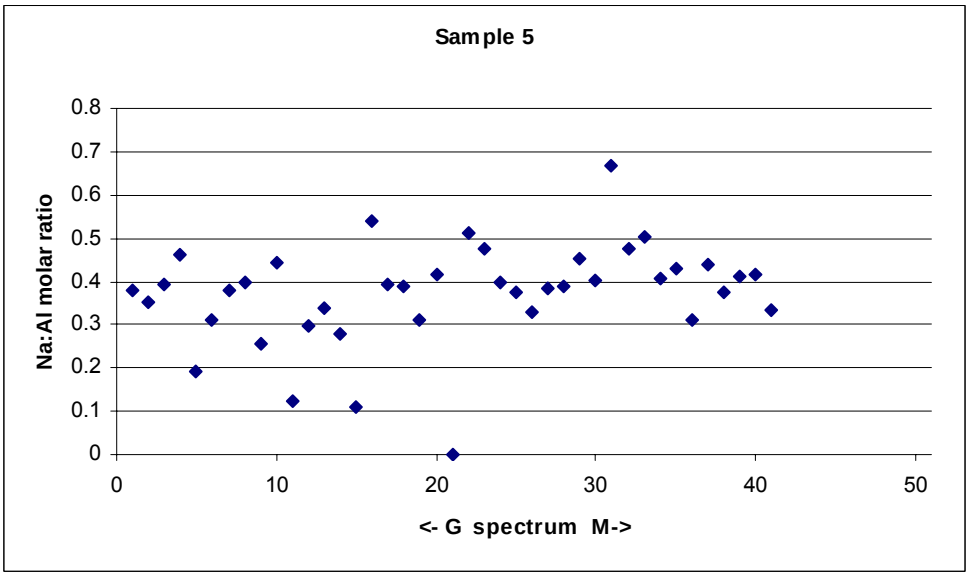

(b)

Figure AIII.1: Graphical depiction of the **(a)** Si:Al and **(b)** Na:Al molar ratios of Sample 1.1/0.6.

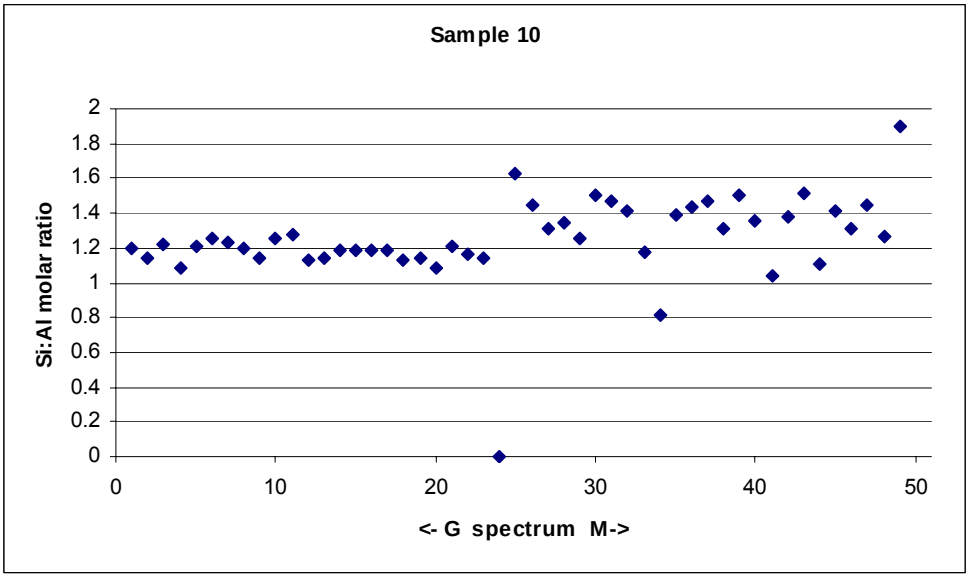

(a)

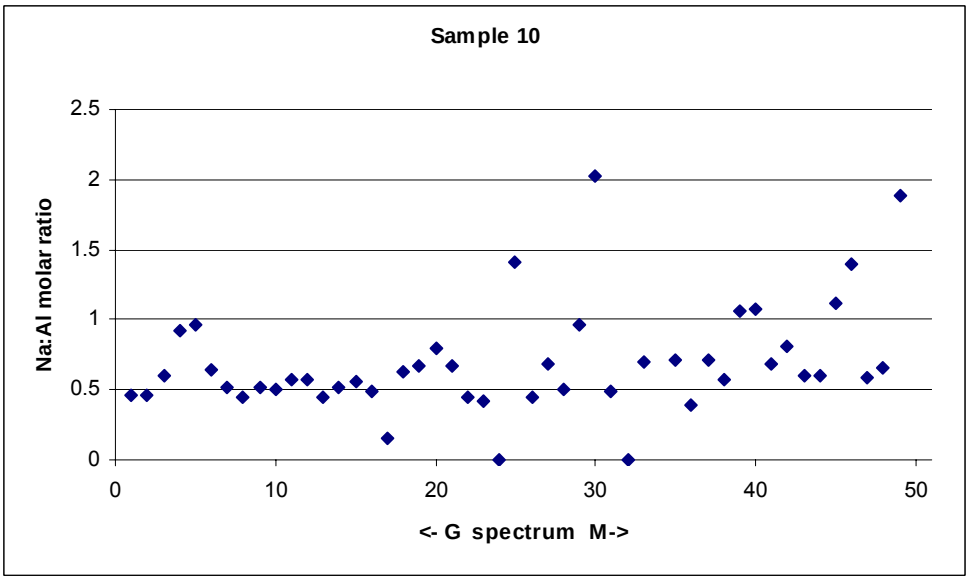

(b)

Figure AIII.2: Graphical depiction of the **(a)** Si:Al and **(b)** Na:Al molar ratios of Sample 1.1/0.8. One data point has been excluded from the matrix in **(b)** for scaling clarity. Its value is 3.3.

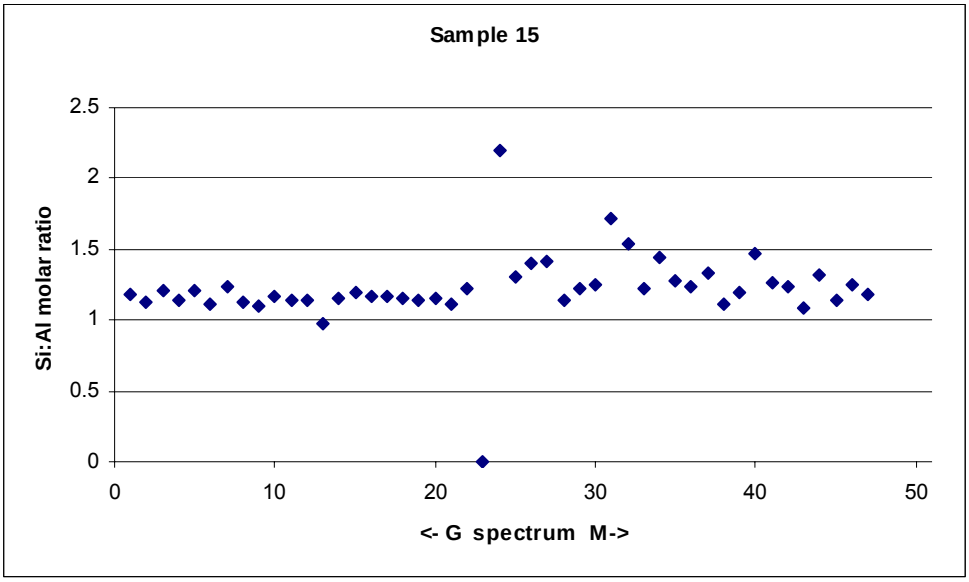

(a)

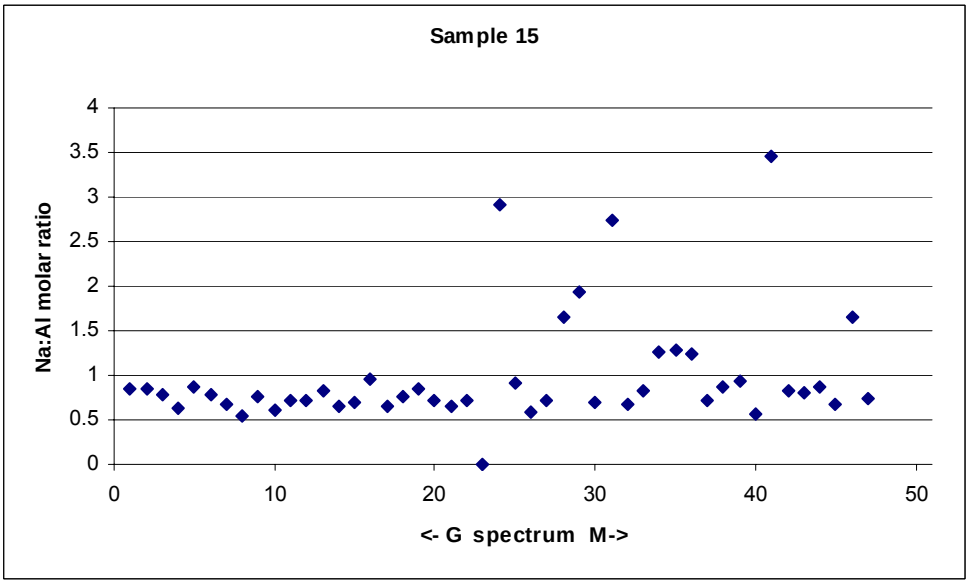

(b)

Figure AIII.3: Graphical depiction of the **(a)** Si:Al and **(b)** Na:Al molar ratios of Sample 1.1/1.0.

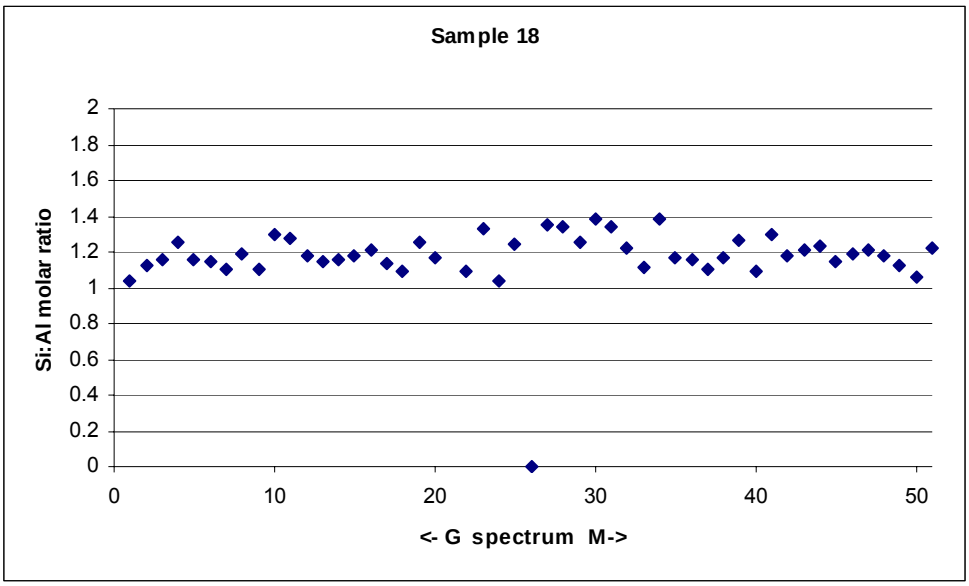

(a)

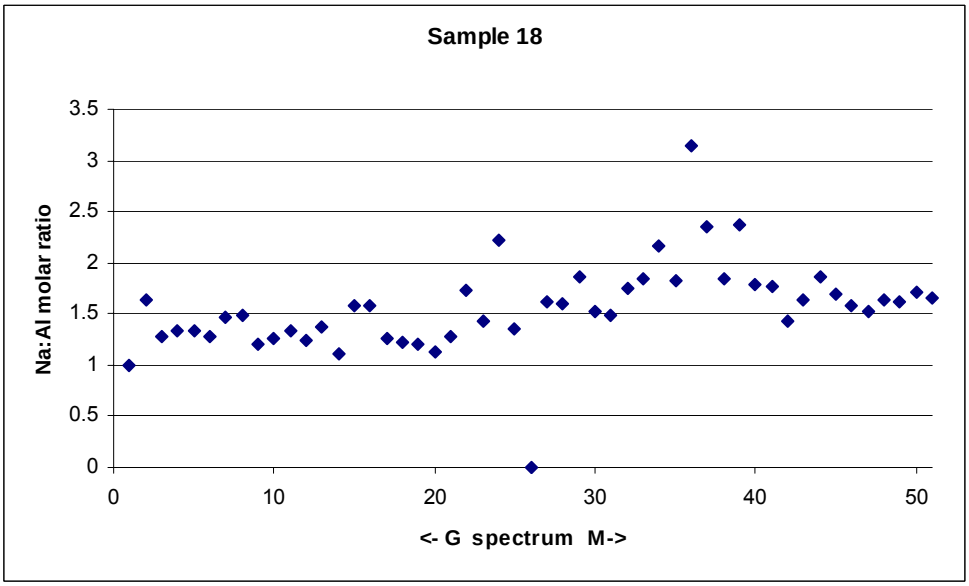

(b)

Figure AIII.4: Graphical depiction of the **(a)** Si:Al and **(b)** Na:Al molar ratios of Sample 1.1/1.5. One data point has been excluded from the grains in **(a)** for scaling clarity. Its value is 2.8.

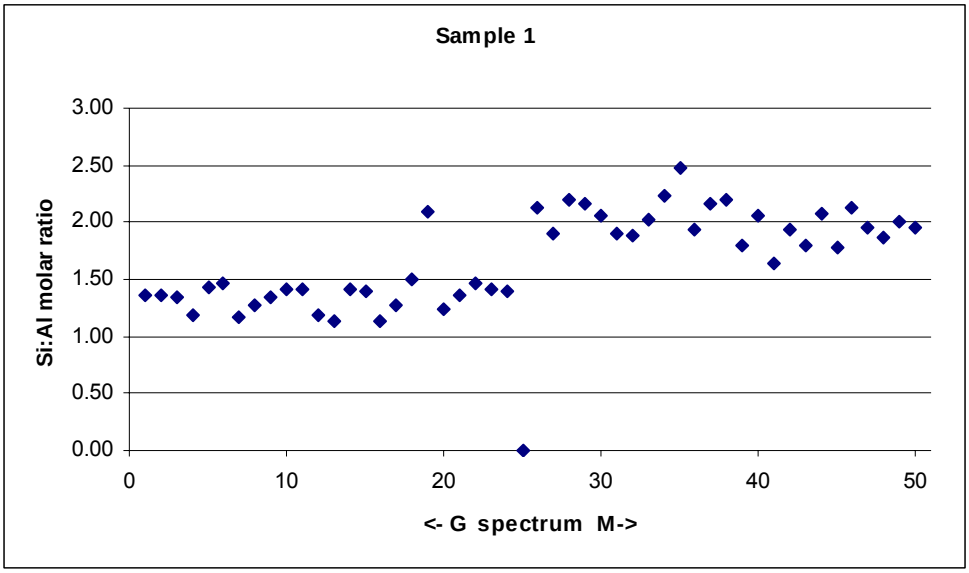

(a)

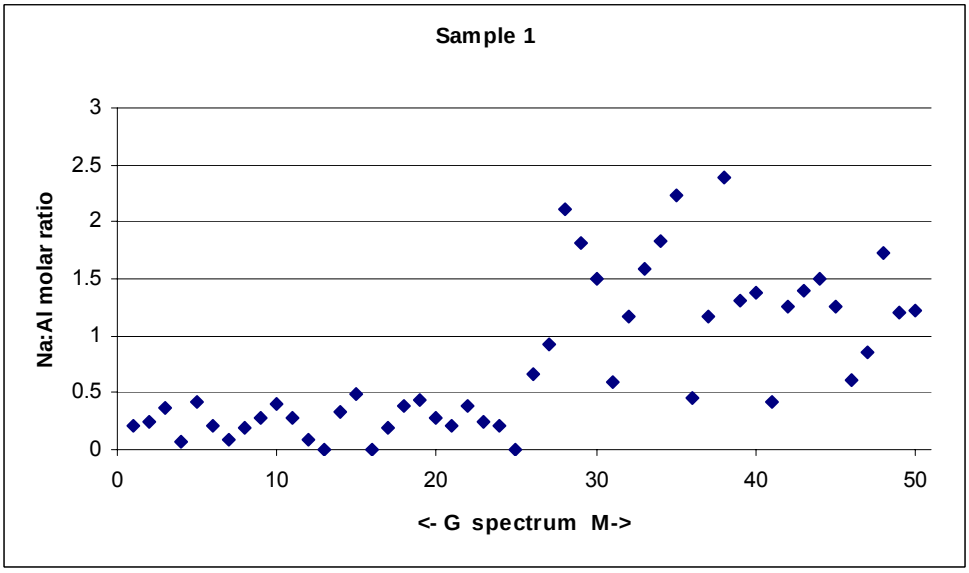

(b)

Figure AIII.5: Graphical depiction of the **(a)** Si:Al and **(b)** Na:Al molar ratios of Sample 1.5/0.6.

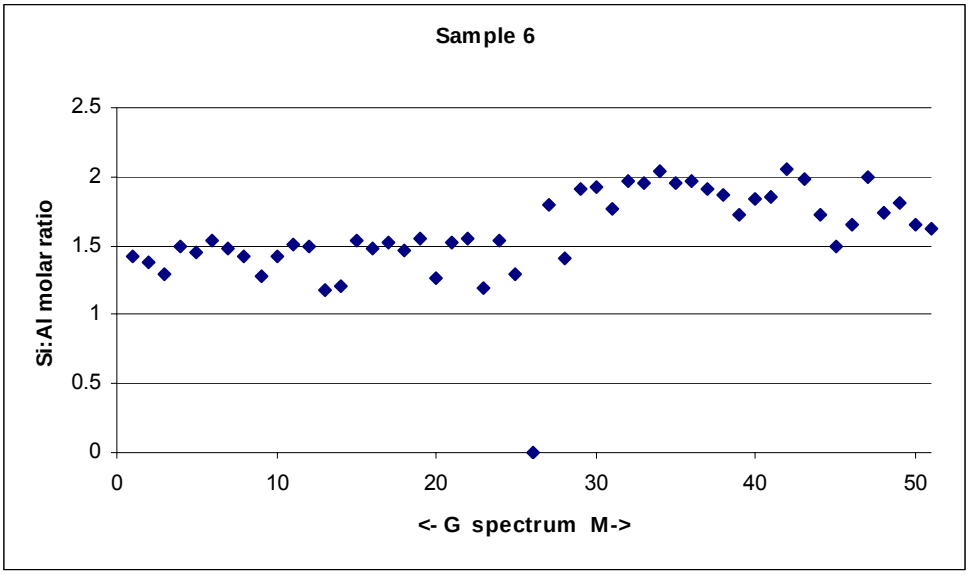

(a)

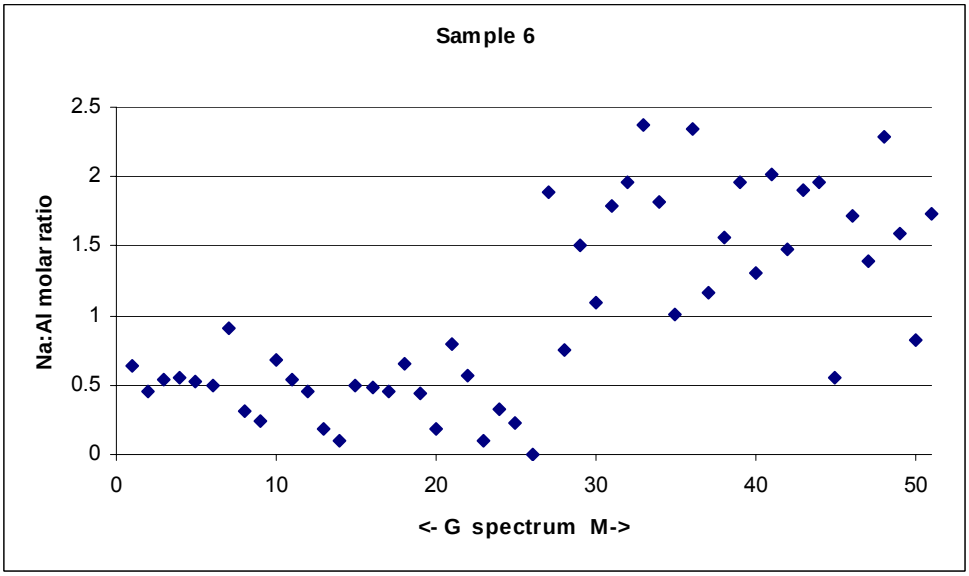

(b)

Figure AIII.6: Graphical depiction of the **(a)** Si:Al and **(b)** Na:Al molar ratios of Sample 1.5/0.8.

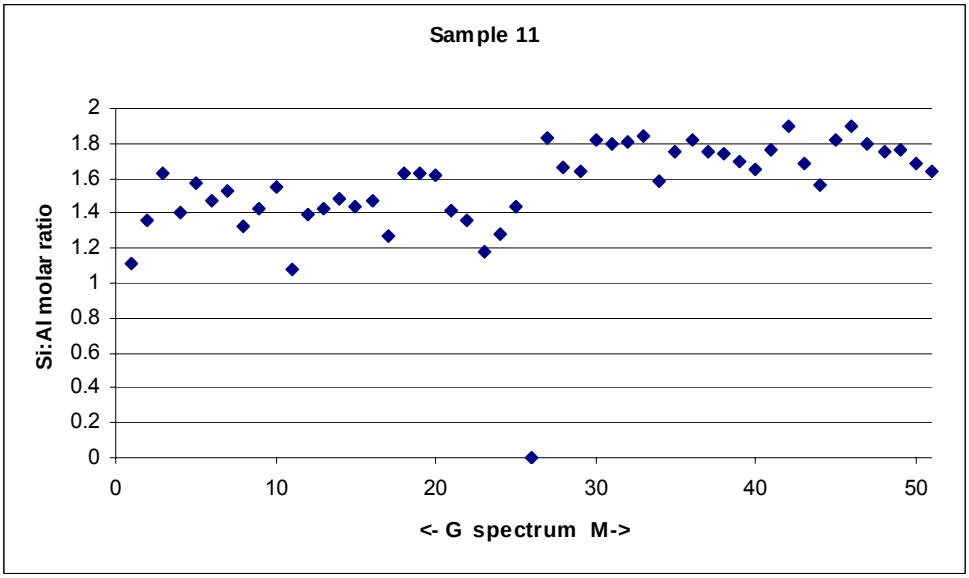

(a)

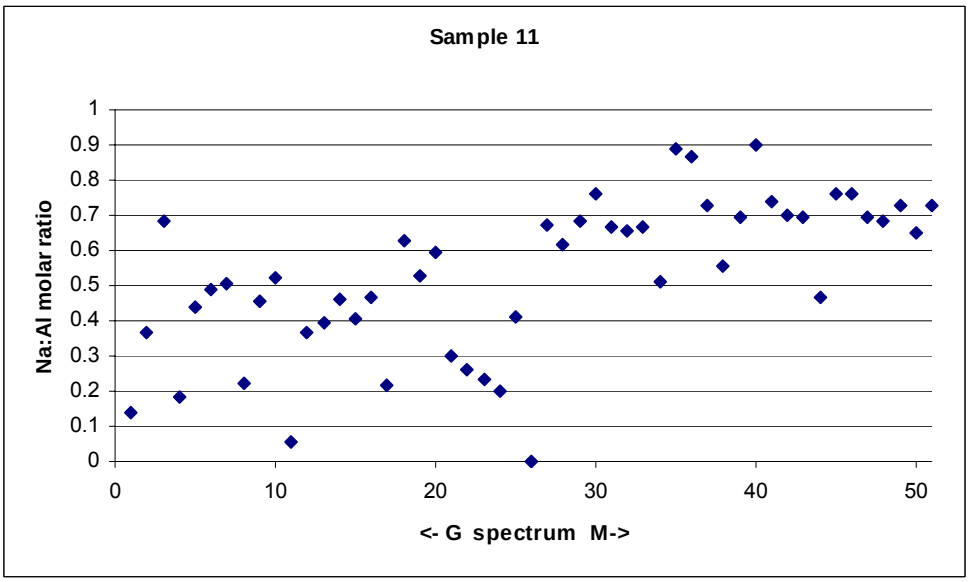

(b)

Figure AIII.7: Graphical depiction of the **(a)** Si:Al and **(b)** Na:Al molar ratios of Sample 1.5/1.0.

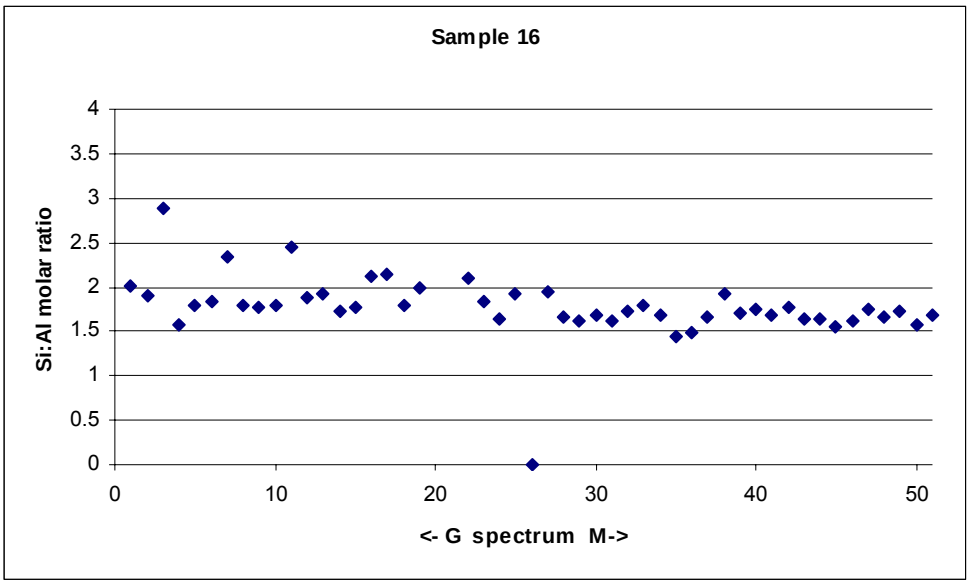

(a)

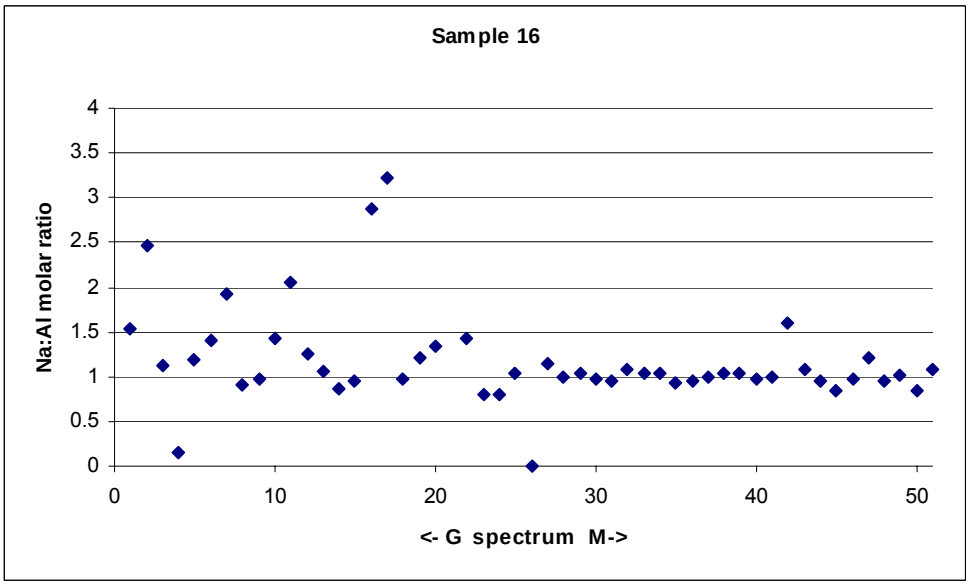

(b)

Figure AIII.8: Graphical depiction of the **(a)** Si:Al and **(b)** Na:Al molar ratios of Sample 1.5/1.5. Two data points have been excluded from **(a)** for scaling clarity. Their values are 5.5 and 9.9.One data point has been excluded from the grains in **(b)** for scaling clarity. Its value is 11.

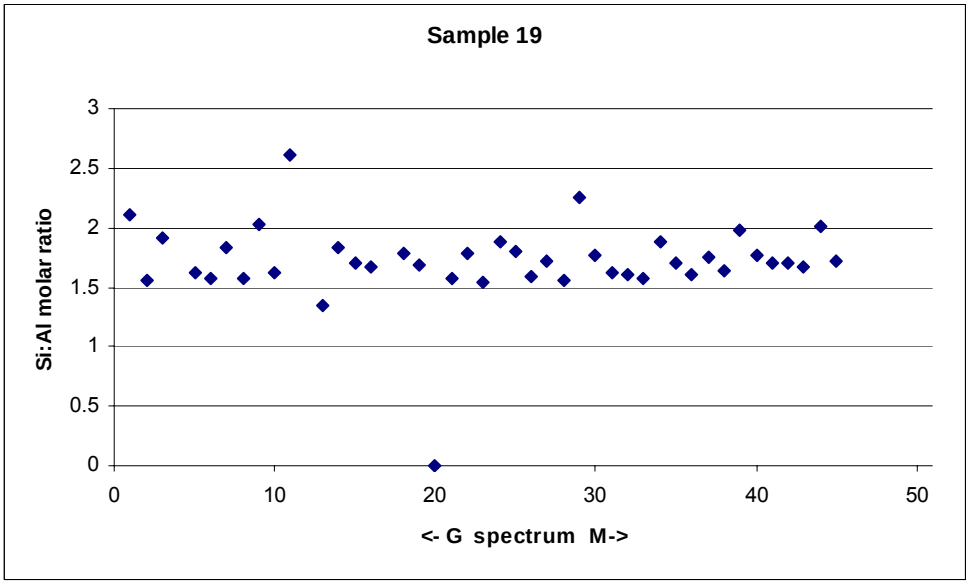

(a)

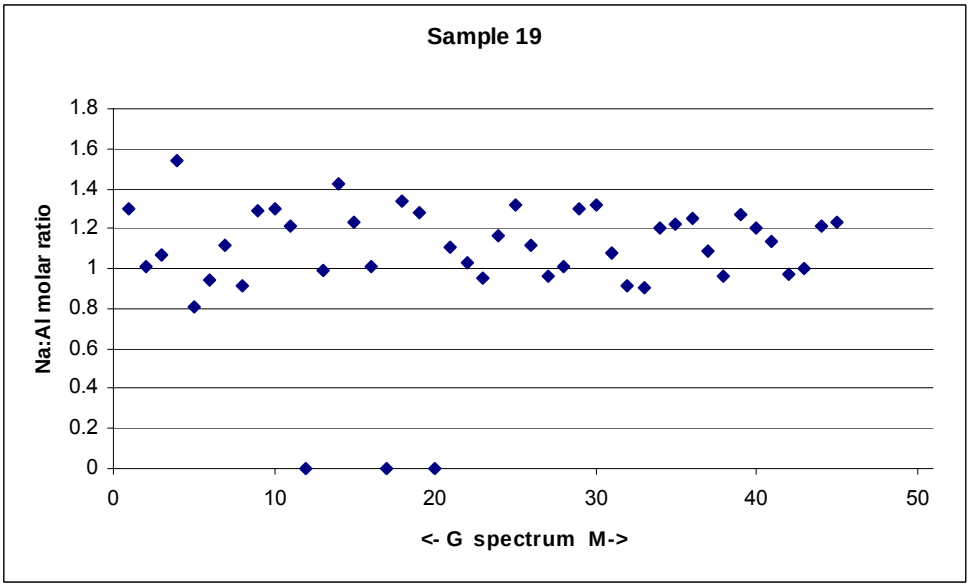

(b)

Figure AIII.9: Graphical depiction of the **(a)** Si:Al and **(b)** Na:Al molar ratios of Sample 1.5/2.0. Three data points have been excluded from the grains in **(a)** for scaling clarity. Their values are 32, 7.3 and 59.

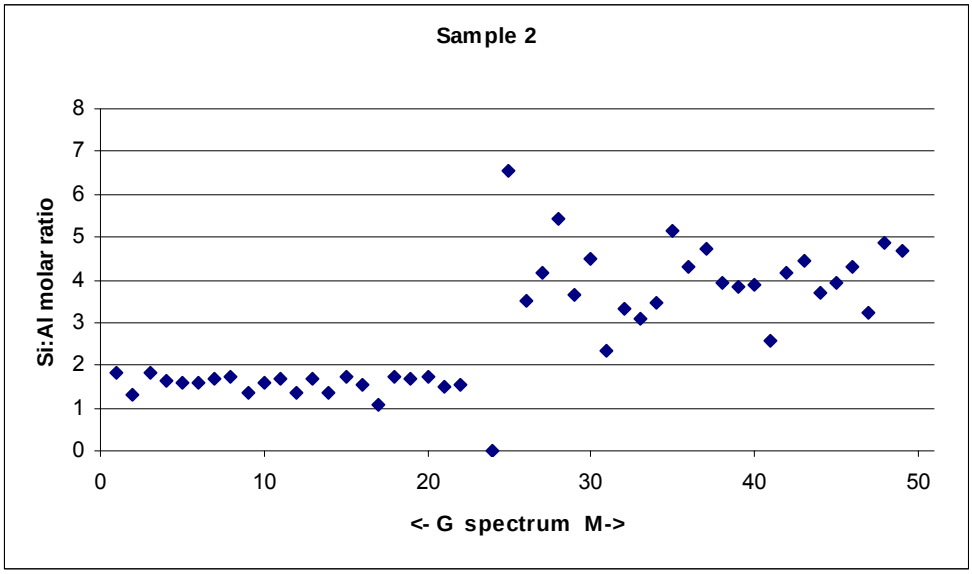

Figure AIII.10: Graphical depiction of the **(a)** Si:Al and **(b)** Na:Al molar ratios of Sample 2.0/0.8. One data point has been excluded from the grains in **(a)** for scaling clarity. Its value is 26.

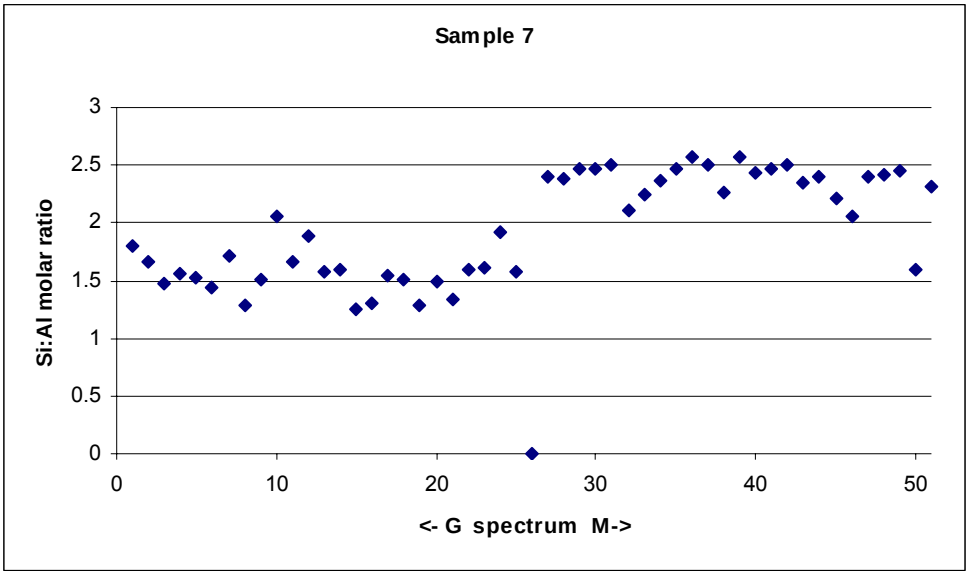

(a)

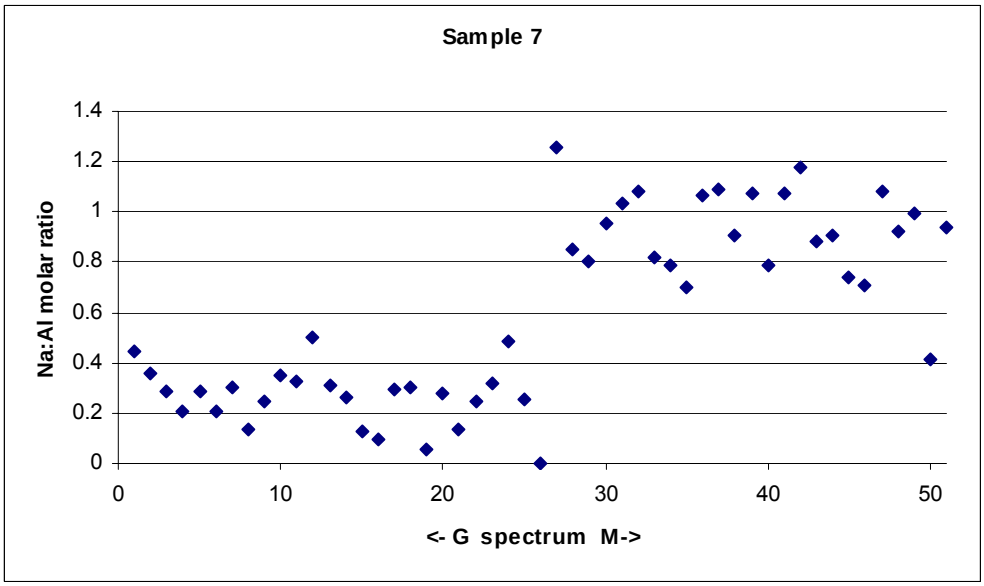

(b)

Figure AIII.11: Graphical depiction of the **(a)** Si:Al and **(b)** Na:Al molar ratios of Sample 2.0/1.0.

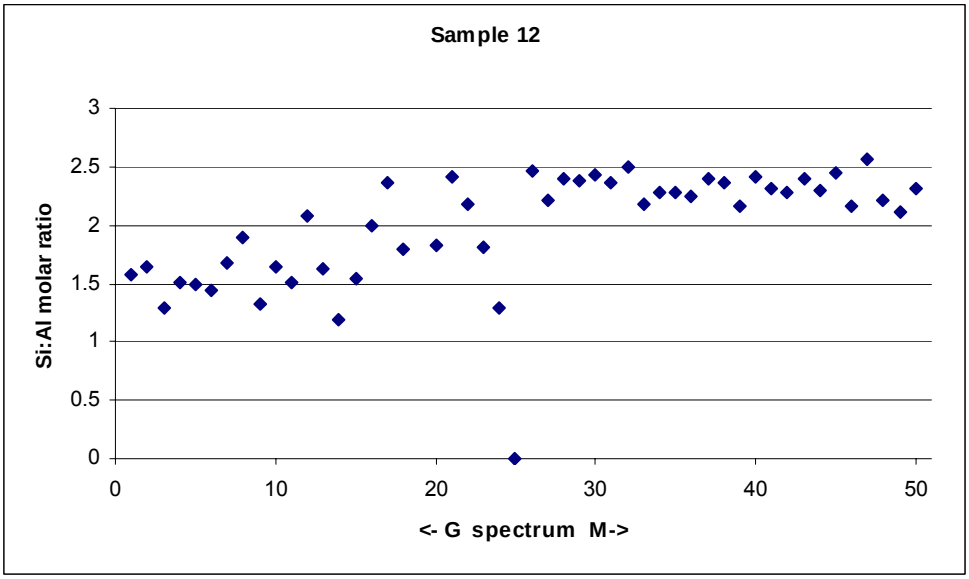

(a)

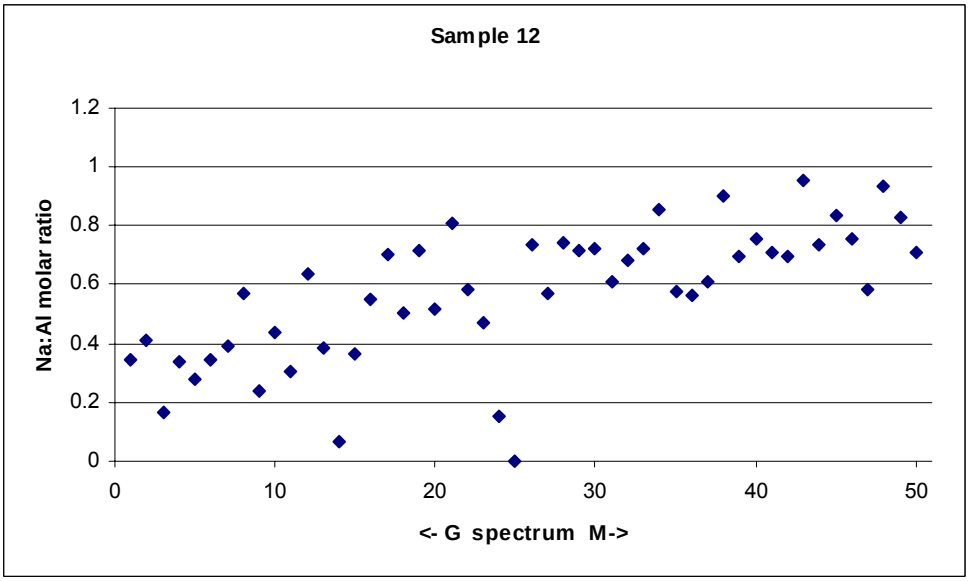

(b)

Figure AIII.12: Graphical depiction of the **(a)** Si:Al and **(b)** Na:Al molar ratios of Sample 2.0/1.3. One data point has been excluded from the grains in **(a)** for scaling clarity. Its value is 5.6.

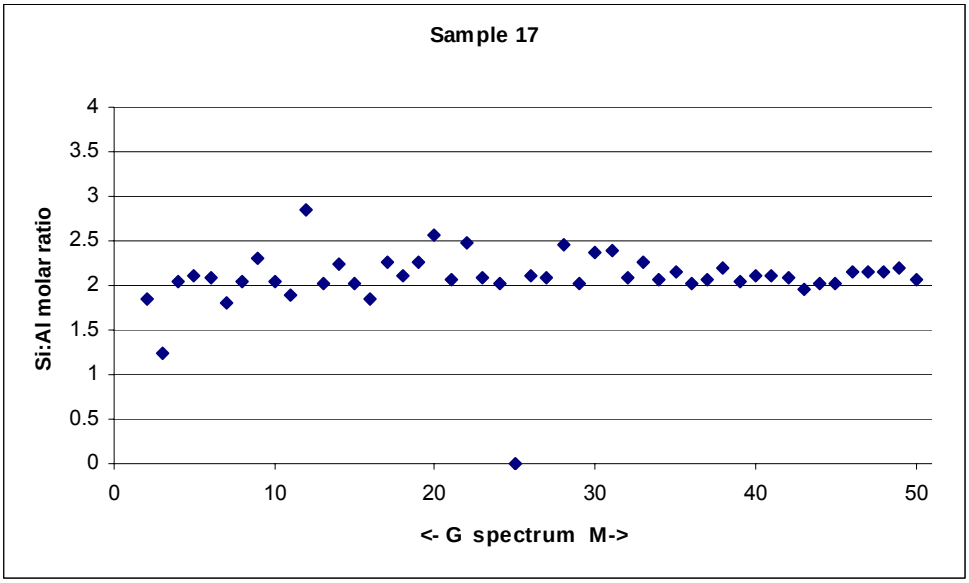

(a)

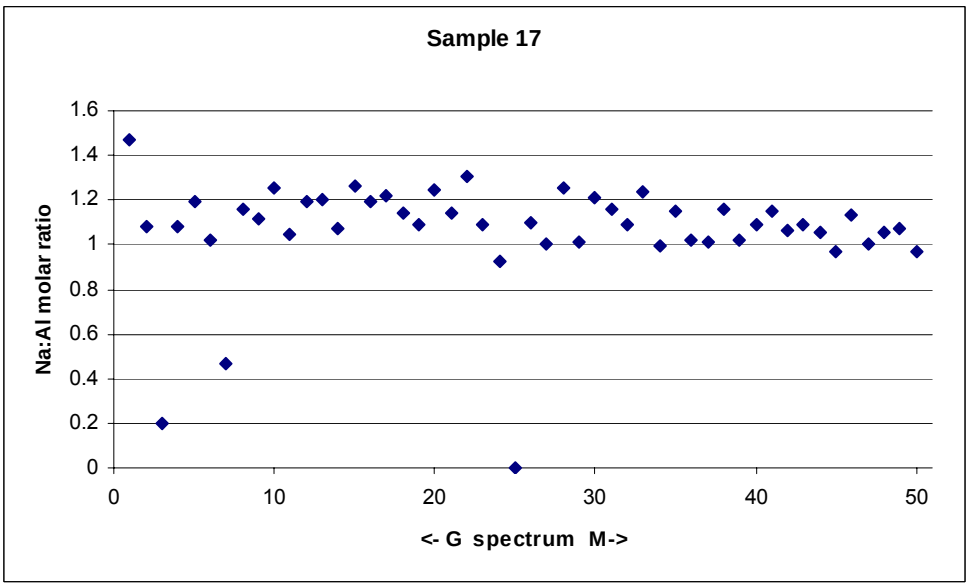

(b)

Figure AIII.13: Graphical depiction of the **(a)** Si:Al and **(b)** Na:Al molar ratios of Sample 2.0/2.0. One data point has been excluded from the grains in **(a)** for scaling clarity. Its value is 40.

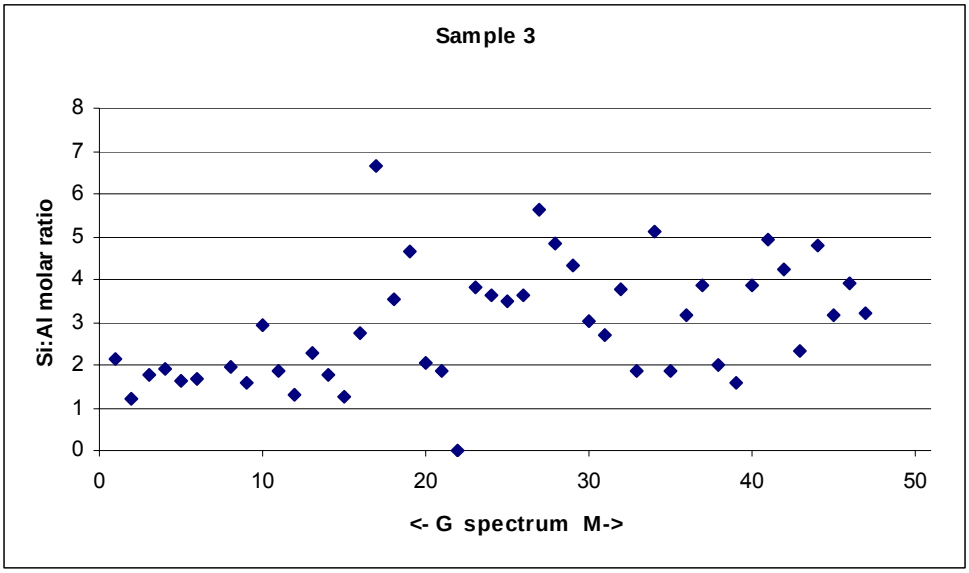

(a)

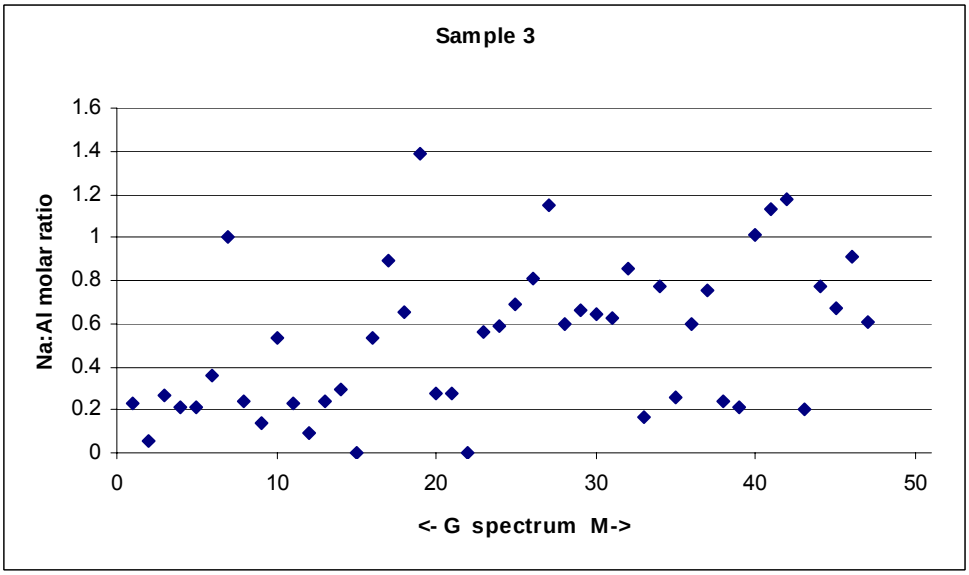

(b)

Figure AIII.14: Graphical depiction of the **(a)** Si:Al and **(b)** Na:Al molar ratios of Sample 2.5/1.0. One data point has been excluded from the grains in **(a)** for scaling clarity. Its value is 18.

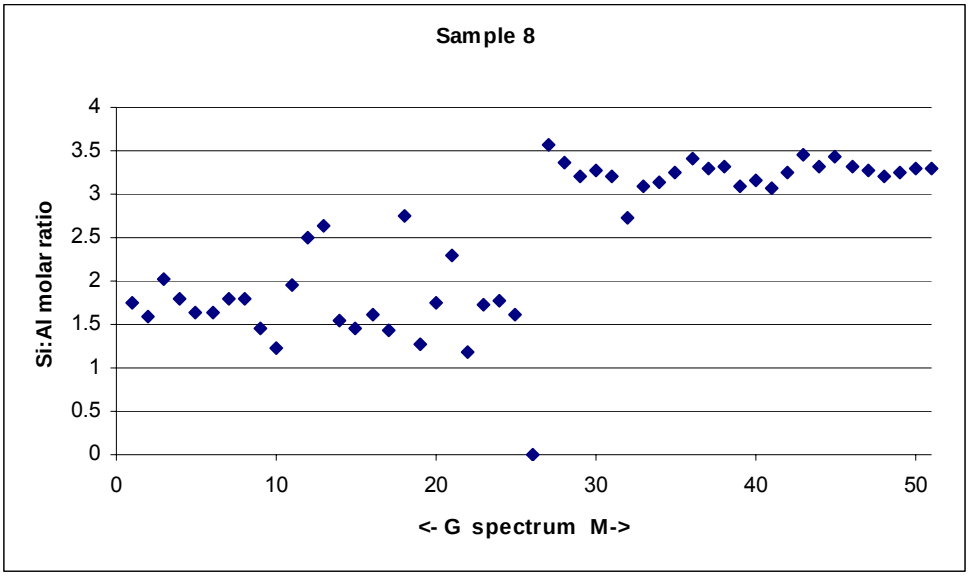

(a)

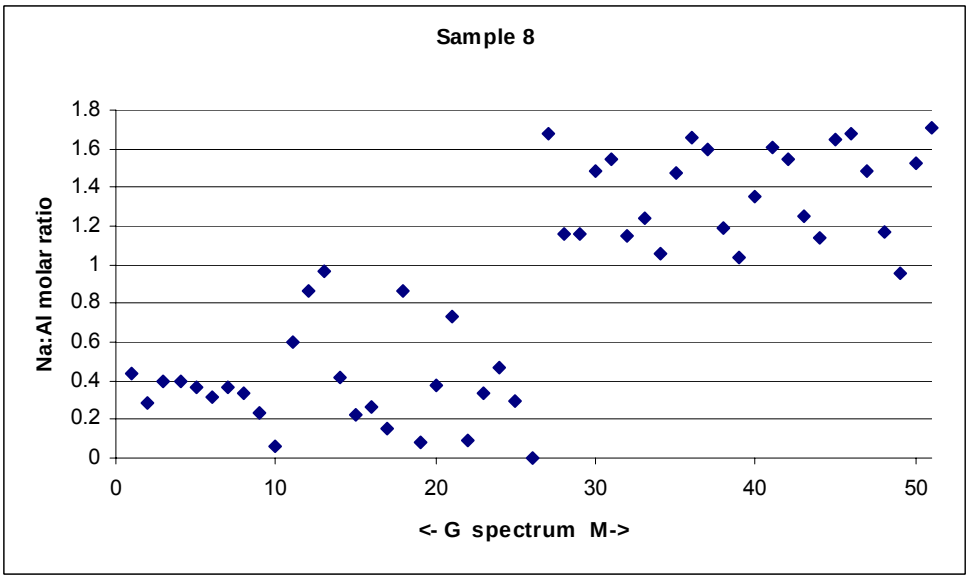

(b)

Figure AIII.15: Graphical depiction of the **(a)** Si:Al and **(b)** Na:Al molar ratios of Sample 2.5/1.3.

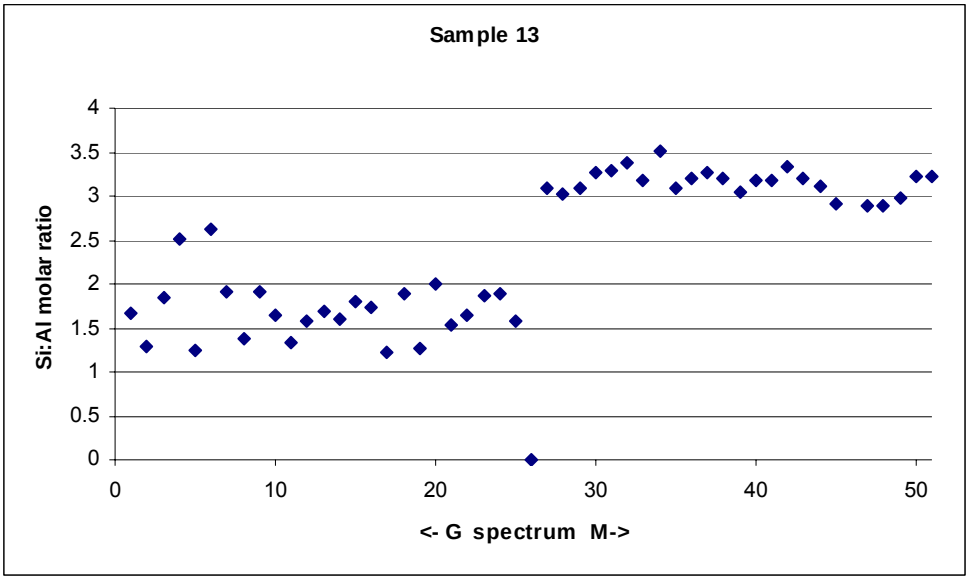

(a)

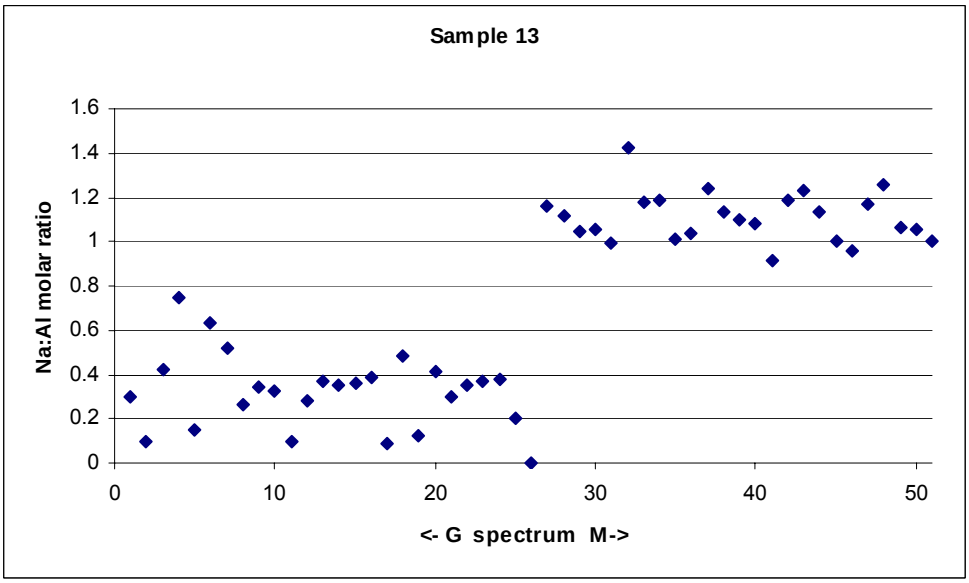

(b)

Figure AIII.16: Graphical depiction of the **(a)** Si:Al and **(b)** Na:Al molar ratios of Sample 2.5/1.5. One data point has been excluded from the matrix in **(a)** for scaling clarity. Its value is 8.1.

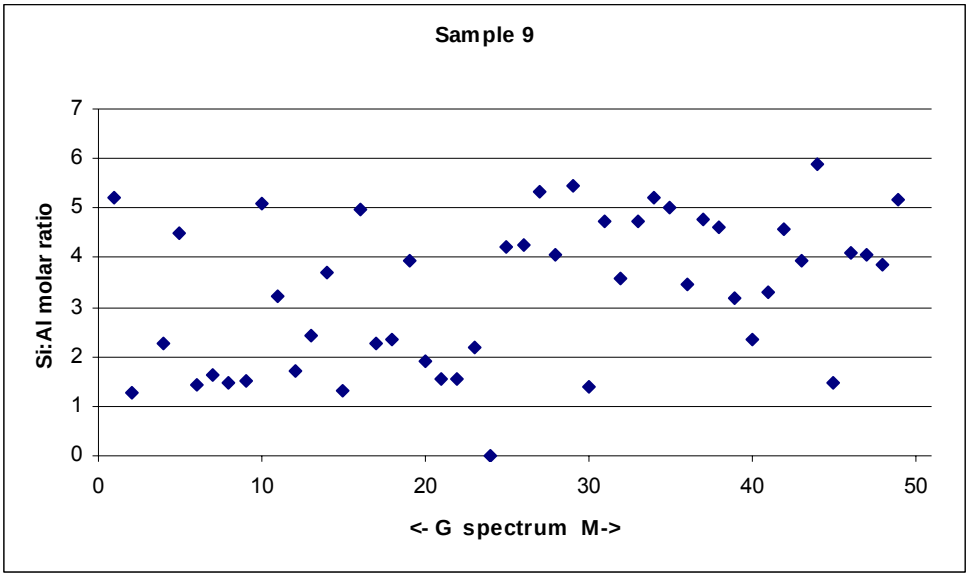

Figure AIII.17: Graphical depiction of the **(a)** Si:Al and **(b)** Na:Al molar ratios of Sample 3.0/1.5. One data point has been excluded from the grains in **(a)** for scaling clarity. Its value is 62.

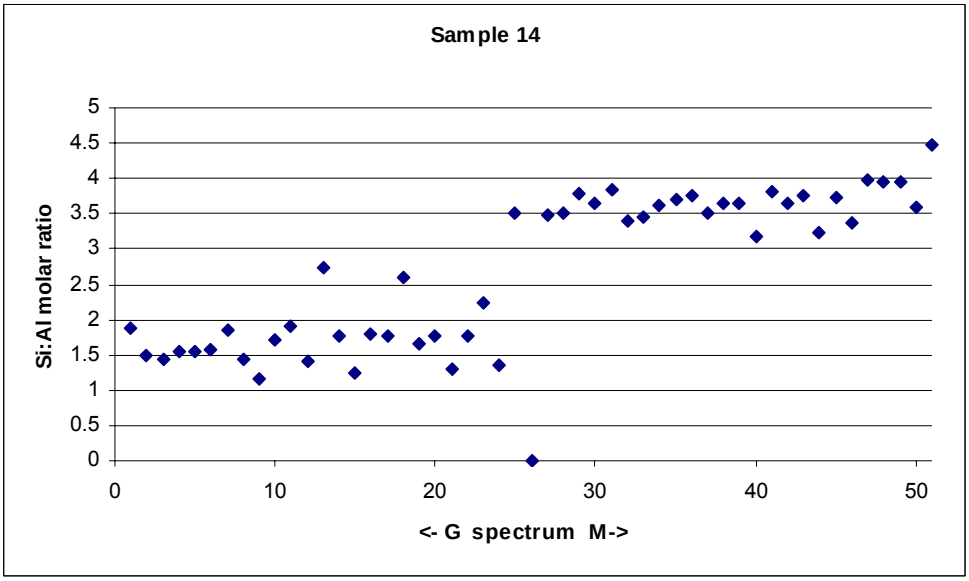

(a)

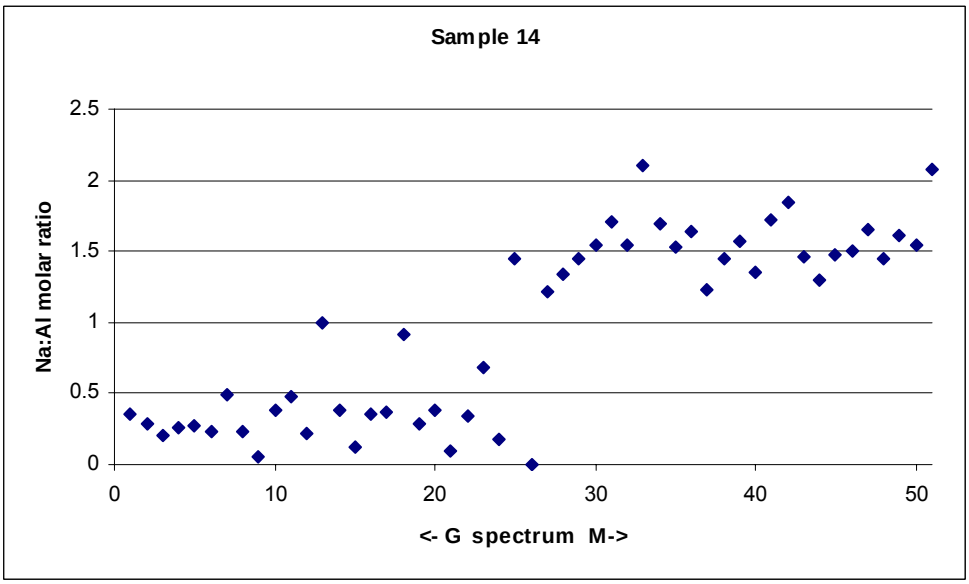

(b)

Figure AIII.18: Graphical depiction of the **(a)** Si:Al and **(b)** Na:Al molar ratios of Sample 3.0/2.0.

IV APPENDIX – EXPANDED IMAGES

Appendix IV gives the expanded versions of Figures 6.1 and 6.15.

Figure AIV.1: Expanded version of Figure 6.1

This uses the same image as given in the thesis, just expanded to fit A3.

Figure AIV.2: Expanded version of Figure 6.15.

This uses the same image as given in the thesis, just expanded to fit A3.

V APPENDIX – PUBLICATIONS ARISING FROM THE THESIS

- *Refereed papers*

Rowles, M. & O'Connor, B. 2003, 'Chemical Optimisation of the Compressive Strength of Aluminosilicate Geopolymers Synthesised by Sodium Silicate Activation of Metakaolinite', *Journal of Materials Chemistry,* vol. 13, no. 5, pp. 1161-1165.

- *Refereed papers in preparation*

Rowles, M. R., Hanna, J. V. & O'Connor, B., 'NMR Study of Bonding Character in Aluminosilicate Inorganic Polymers According to Chemical Composition', *Journal of Materials Chemistry* (to be submitted).

Rowles, M. R. & O'Connor, B., 'Microstructural Character of Aluminosilicate Inorganic Polymers According to Chemical Composition', *Journal of Materials Chemistry* (to be submitted).

Rowles, M. R., O'Connor, B., van Riessen, A. & Shastri, S., 'Variation in the Bonding Network of Aluminosilicate Inorganic Polymers with Chemical Composition', *Journal of Materials Chemistry* (to be submitted).

- *Conference papers and abstracts*

Rowles, M. & O'Connor, B. 2004, 'Zeolite Formation in the Synthesis of Aluminosilicate Inorganic Polymers: Combining the Power of the PDF and Synchrotron Data', International Centre for Diffraction Data – Spring Meeting, Newtown Square, Philadelphia USA, *Powder Diffraction*, vol. 19, pp. 303-304.

Rowles, M. & O'Connor, B. 2003, 'Microstructural Characterisation of Aluminosilicate Inorganic Polymers by Scanning Electron Microscopy', in *2003 Materials Research Society Fall Meeting*, ed. Materials Research Society, Boston, USA.

Rowles, M., O'Connor, B. & van Riessen, A. 2003, 'Microstructural Characterisation of Aluminosilicate Inorganic Polymers', in Proceedings of the 2003 Joint Australian X-Ray Analytical Association (WA) and West Australian Society for Electron Microscopy Conference, eds. Saunders, M., Hart, R. D., Fallon, P. & Clode, P., Western Australia.

Rowles, M. & O'Connor, B. 2002, 'Zeolite Formation in the Synthesis of Aluminosilicate Inorganic Polymers', in *Austceram 2002*, eds. Low, I. M. & Phillips, D. N., Perth, Western Australia, pp. 41-42.

Rowles, M. & O'Connor, B. 2002, 'The Effect of Composition and Preparation on the X-Ray Scattering Patterns of Aluminosilicate Inorganic Polymers', in *Australian X-Ray Analytical Association 2002 Analytical X-rays for Industry and Science*, Newcastle, New South Wales, p. 100.

Rowles, M., O'Connor, B. H., Buckley, C. & van Riessen, A. 2001, 'Preliminary X-Ray Study of Aluminosilicate Inorganic Polymers', in *Proceedings of the 2001 Joint Australian X-Ray Analytical Association (WA) and West Australian Society for Electron Microscopy Conference*, eds. Saunders, M., Kirby, N., Paglia, G., Browne, J. & Hart, R., Australian X-Ray Analytical Association – Mandurah, Western Australia, pp. 82-89.